

Structural performance of FRP-concrete hybrid beams with flexible shear connection

Thesis by:

Cătălin Andrei Neagoe

Directed by:

Lluís Gil Espert

Barcelona, May 2016

Universitat Politècnica de Catalunya, BarcelonaTECH
Escola Tècnica Superior d'Enginyeries Industrial i Aeronàutica de Terrassa
Departament de Resistència de Materials i Estructures a l'Enginyeria
Laboratori per a la Innovació Tecnològica d'Estructures i Materials

TESIS DOCTORAL



UNIVERSITAT POLITÈCNICA
DE CATALUNYA
BARCELONATECH

Ph.D. Thesis

***Structural performance of FRP-concrete hybrid beams
with flexible shear connection***

Author:

Cătălin Andrei Neagoe

Directed by:

Lluís Gil Espert

Tesi presentada per obtenir el títol de Doctor per la Universitat Politècnica de Catalunya

Programa de doctorat d'Anàlisi Estructural. Departament de Resistència de Materials i
Estructures a l'Enginyeria

Escola Tècnica Superior d'Enginyeria Industrial i Aeronàutica de Terrassa. Universitat
Politécnica de Catalunya, BarcelonaTECH

Barcelona, May 2016

Abstract

Sustainability of buildings and public infrastructure is a relatively recent topic put into discussion by the engineering community. A solution to designing structures that have long-term durability and low maintenance requirements is to introduce new construction materials or to implement new structural systems. In this regard, fiber reinforced polymers (FRP) represent one of the novel solutions in the civil engineering field that offer promising results.

To optimize the use of FRP shapes, researchers have proposed to form hybrid structural systems by combining the composite materials with conventional materials, such as concrete, in order to improve on the stiffness, ductility, and buckling resistance of single FRP members. However, due to the novelty and wide variety of hybrid elements, the technology demands further experimental testing to prove its viability. In addition, because there is a current lack of mandatory codes for the design of structures built with composite profiles and consequently FRP-concrete members, reliable predictive models have to be developed. Addressing the above-mentioned issues is essential in lessening the introduction of advanced composite materials in common types of public works and constructions.

The present research aimed thus to study the structural performance of hybrid beams made of FRP pultruded profiles attached to concrete slabs by carrying an experimental, analytical, and numerical investigation. Since interface slip effects had been largely overlooked in the past, the thesis focused also on the influence of the connection flexibility over bending behavior.

With respect to the developed experimental campaign, eight glass FRP-concrete hybrid beams with mechanical shear connectors were fabricated and their flexural behavior was assessed against that of equivalent reinforced concrete beams and single GFRP structural profiles. The variables of the research were the type of hybrid cross-section and the concrete strength class. The laboratory campaign was divided in two phases depending on the specific test setup configuration, and observations were made regarding the short-term behavior of the novel elements under positive bending moments. Previous to the experimental tests, a nondestructive characterization procedure was proposed for obtaining the elastic properties of the constitutive materials of hybrid members in a reduced amount of time, by using an analysis of the free vibration response. Overall, the bending tests have demonstrated the high structural efficiency of the hybrid beam solution and have underlined the importance of accounting for shear connection deformability.

An analytical procedure was introduced for the design of FRP-concrete beams under short-term loading. Design equations for the serviceability and ultimate limit states were proposed in function of complete or partial shear interaction assumptions. The feasibility of using simplified formulas to quantify for interlayer slip effects was studied in evaluating deflections, flexural stiffness, bending

capacities, normal and shear stress distributions. Due to the improved precision of the expressions that had considered the shear connection flexibility, the proposed analytical procedure was able to capture appropriately the structural behavior and performance of the specimens.

Finally, referring to the numerical analyses, predictive finite element models capable of simulating the fundamental behavior of FRP-concrete beams with bolted joints were developed. The model that included material, contact, and geometry nonlinearities offered the best results in comparison with the experimental data and analytical estimations. Concrete slab crushing and cracking, tension stiffening effects, interface friction, and the elasto-plastic behavior of the shear connectors were all taken under consideration.

Keywords: fiber-reinforced polymers; composite materials; FRP-concrete; hybrid beam; composite structures; flexural behavior; analytical procedure; finite element model; nonlinear analysis; partial interaction.

Resumen

La sostenibilidad de los edificios y de las infraestructuras públicas es un tema de importancia reciente puesto en discusión por la comunidad de ingeniería. La necesidad de diseñar estructuras con bajos requerimientos de mantenimiento y durabilidad a largo plazo puede ser resuelta mediante la introducción de nuevos materiales de construcción o la implementación de sistemas estructurales innovadores. En este sentido, los polímeros reforzados con fibras (FRP) representan una de las soluciones en el campo de la ingeniería civil que ofrecen resultados prometedores.

Para optimizar el uso de secciones de FRP los investigadores han propuesto la creación de sistemas estructurales híbridos donde se combinan materiales compuestos con materiales convencionales, tales como el hormigón. Las soluciones híbridas mejoran la rigidez, la ductilidad y la resistencia a pandeo de los elementos aislados de material compuesto. Debido a la novedad y a la variedad de soluciones híbridas, la tecnología requiere de la realización de más ensayos experimentales para valorar su viabilidad. Además, en la actualidad hay una falta de códigos prescriptores y normas que ayuden al diseño de estructuras construidas con perfiles compuestos y, por consiguiente, los elementos mixtos requieren del desarrollo de modelos predictivos fiables. Abordar las cuestiones antes mencionadas es esencial para facilitar la introducción de materiales compuestos avanzados en tipologías comunes de obras públicas y de construcciones donde, actualmente, todavía se están utilizando materiales tradicionales.

Por lo tanto, la presente investigación tiene como objetivo estudiar el comportamiento estructural de vigas híbridas hechas de perfiles pultrusionados de FRP unidos a losas de hormigón, mediante la realización de una investigación experimental, analítica y numérica. Puesto que los efectos de deslizamiento en la interfaz han sido mayoritariamente ignorados en el pasado, la tesis se centra también en la influencia de la flexibilidad de la conexión sobre el comportamiento de flexión.

Con respecto a la campaña experimental, se han fabricado y ensayado a flexión ocho vigas de perfiles de FRP de fibra de vidrio (GFRP) y hormigón, con conectores mecánicos en el rasante. También se ha comparado su comportamiento con respecto a vigas de hormigón armado equivalentes y perfiles estructurales individuales de GFRP. Las variables de la investigación fueron el tipo de sección transversal y la clase de resistencia del hormigón. La campaña de laboratorio se dividió en dos fases en función de la configuración de ensayo, y se hicieron observaciones sobre el comportamiento de los nuevos elementos a corto plazo bajo la flexión de momentos positivos. Previamente a dichos ensayos, se propuso un procedimiento eficaz de caracterización no destructiva para la obtención de las propiedades elásticas de los materiales que componían los especímenes, mediante el uso de un análisis de la respuesta a la vibración libre. En general, los ensayos de flexión han demostrado la alta eficiencia

estructural de la solución de viga híbrida y han subrayado la importancia de tener en cuenta la flexibilidad de conexión del rasante.

También se ha desarrollado un procedimiento analítico para el diseño de vigas mixtas de FRP-hormigón bajo cargas a corto plazo. Se han propuesto ecuaciones de diseño para los estados límite de servicio y último en función de la interacción completa o parcial del rasante. Además, se ha analizado la viabilidad de utilizar fórmulas aproximadas para cuantificar los efectos del deslizamiento entre capas y su repercusión en la evaluación de los desplazamientos, la rigidez a flexión, la capacidad de flexión y las distribuciones de tensiones. Debido a la mejora de la precisión de las expresiones que representan la flexibilidad de la conexión del rasante, el procedimiento analítico propuesto ha sido capaz de capturar de manera adecuada el comportamiento estructural. Por otro lado, la aplicabilidad de utilizar un enfoque simplificado ha sido probada.

Por último, en referencia a los análisis numéricos, se han desarrollado modelos de elementos finitos capaces de simular el comportamiento fundamental de vigas híbridas con conectores tipo perno. El modelo que representó las no linealidades en el material, en los contactos y en la geometría fue el que ofreció los mejores resultados en comparación con los datos experimentales y las estimaciones analíticas. El aplastamiento del hormigón en la losa y su fisuración, los efectos de rigidización post-fisuración, la fricción de la interfaz y el comportamiento elasto-plástico de los conectores de rasante fueron tomados en consideración.

Palabras clave: polímeros reforzados con fibras; materiales compuestos; FRP-hormigón; viga híbrida; estructuras mixtas; comportamiento a flexión; procedimiento analítico; modelo de elementos finitos; análisis no lineal; interacción parcial.

Publications

The following peer-reviewed publications have resulted from the main investigation carried by the author in the present doctoral thesis:

Neagoie, C.A., Gil, L. (2015). Analytical procedure for the design of PFRP-RC hybrid beams including shear interaction effects. *Composite Structures*, 132, 122–135.
<http://doi.org/10.1016/j.compstruct.2015.04.054>

Neagoie, C.A., Gil, L., Pérez, M.A. (2015). Experimental study of GFRP-concrete hybrid beams with low degree of shear connection. *Construction and Building Materials*, 101, 141–151.
<http://doi.org/10.1016/j.conbuildmat.2015.10.024>

Neagoie C.A. (2014). Diseño y análisis de vigas híbridas de PFRP y hormigón. In M.A. Pérez (Ed.), *Aplicaciones avanzadas de los materiales compuestos en la obra civil y la edificación* (pp. 205–236). OmniaScience Monographs. <http://doi.org/10.3926/oms.207>

Neagoie, C.A., Gil, L. (2014). Evaluation of Deflections for PFRP-RC Hybrid Beams with Complete and Partial Shear Connection. In C.G. Chiorean (Ed.), *Proceedings of the Second International Conference for PhD Students in Civil Engineering and Architecture (CE-PhD 2014)* (pp. 57–64). Cluj-Napoca, Romania: UTPRESS.

Neagoie, C.A., Gil, L. (2013). Experimental study of GFRP-concrete hybrid beams with partial interaction. In *Book of Abstracts – 17th International Conference on Composite Structures (ICCS17)*. Porto, Portugal.

Neagoie, C.A., Pérez, M.A., Gil, L. (2013). Determining the elastic properties of GFRP-concrete hybrid beams through the use of a non-destructive technique. In *Book of Abstracts – 17th International Conference on Composite Structures (ICCS17)*. Porto, Portugal.

Acknowledgements

First of all, I would like to express my sincere appreciation to my thesis supervisor, Prof. Lluís Gil, for giving me the opportunity to work and study under his direction, for all the guidance, trust and support provided along these years. His advice, enthusiasm and creative thinking have constituted a personal source of inspiration and have contributed to my formation as a researcher.

I am very thankful to the Polytechnic University of Catalonia and the Laboratory for the Technological Innovation of Structures and Materials (LITEM) for the granted FPI-UPC scholarship which allowed me to follow the Ph.D. program. Part of the present experimental work has also been developed with the financial support of PIGRA Engineering S.L. obtained through the Centre for the Development of Industrial Technology (CDTI).

Furthermore, I would like to thank from the bottom of my heart my current and former colleagues from the department and research group – Ernest Bernat, Christian Escrig, Roger Serra López, Marco Antonio Pérez, Francesc Puigvert, and Sònia Segura – for their invaluable help in realizing this work and for the wonderful moments that we shared together. At the same time, the support of laboratory technician Vicenç Andreu in preparing experimental tests is greatly acknowledged. A special mention is also addressed to the rest of the department staff, for accepting me with open arms in their collective.

Additional recognition goes to Prof. Tudor Postelnicu from the Technical University of Civil Engineering of Bucharest, for his cordial assistance and the productive discussions we had; to Mercedes Escusa from the UPC Electron Microscopy Service, for aiding us with the inspection of the internal structure of the composite materials employed in the experimental campaign; and to fellow researcher Ștefan Buru from the Technical University of Cluj-Napoca, for his collaboration with the advanced finite element modelling.

Finally, I would like to express my deepest gratitude to my family, my beloved fiancée Ivy, and to my friends, for their unconditional support and encouragement to succeed.

Table of Contents

CHAPTER 1. INTRODUCTION	1
1.1. CONTEXT AND MOTIVATION	1
1.2. AIM AND OBJECTIVES	3
1.3. RESEARCH METHODOLOGY	4
1.4. THESIS OUTLINE	5
CHAPTER 2. STATE OF THE ART	7
2.1. INTRODUCTION	7
2.2. FIBER-REINFORCED POLYMER PROFILES	8
2.2.1. DESCRIPTION	8
2.2.2. FABRICATION	11
2.2.3. CHARACTERISTICS	12
2.2.4. APPLICATIONS	15
2.3. HYBRID BEAM SOLUTIONS	16
2.3.1. CONCEPT AND STRUCTURAL APPLICATIONS	16
2.3.2. CONNECTION TECHNOLOGY	19
2.3.3. EXPERIMENTAL RESEARCH STUDIES	22
2.3.4. ANALYTICAL DESIGN FORMULATIONS	29
2.3.5. NUMERICAL SIMULATIONS	36
2.4. SUMMARY AND RESEARCH NEEDS	45
CHAPTER 3. EXPERIMENTAL CAMPAIGN	49
3.1. INTRODUCTION	49
3.2. MATERIALS	50
3.2.1. COMPOSITE PROFILE	50
3.2.2. REINFORCED CONCRETE SECTION	56
3.2.3. SHEAR CONNECTORS	57
3.3. HYBRID BEAM MODELS AND FABRICATION	57
3.4. NONDESTRUCTIVE HYBRID BEAM CHARACTERIZATION	60
3.4.1. INTRODUCTION	60
3.4.2. METHODOLOGY	64
3.4.3. RESULTS AND DISCUSSION	71
3.5. BENDING TEST SETUPS AND PROCEDURE	74
3.6. BENDING TEST RESULTS AND DISCUSSION	77
3.6.1. FLEXURAL BEHAVIOR AND FAILURE MODES	77
3.6.2. COMPOSITE ACTION AND INTERLAYER SLIP	85
3.6.3. COMPARATIVE ANALYSIS	90
3.7. CONCLUSIONS	93

CHAPTER 4. ANALYTICAL PROCEDURE	97
4.1. INTRODUCTION	97
4.2. SCOPE	98
4.3. SERVICEABILITY LIMIT STATES (SLS)	100
4.3.1. DEFLECTION AND FLEXURAL STIFFNESS	100
4.3.2. VIBRATIONS	113
4.4. INTERNAL ACTIONS AND STRESS DISTRIBUTIONS	113
4.4.1. COMPLETE SHEAR INTERACTION	113
4.4.2. PARTIAL SHEAR INTERACTION	114
4.5. INTERLAYER SLIP	115
4.6. ULTIMATE LIMIT STATES (ULS)	118
4.6.1. FLEXURAL CAPACITY	118
4.6.2. ADDITIONAL FAILURE CRITERIA	121
4.7. VALIDATION WITH PREVIOUS EXPERIMENTAL DATA	124
4.7.1. DESCRIPTION OF SPECIMENS	124
4.7.2. SERVICEABILITY ANALYSIS	126
4.7.3. FAILURE ANALYSIS	127
4.7.4. FLEXURAL BEHAVIOR	130
4.7.5. STRAIN AND STRESS DISTRIBUTIONS	132
4.8. VALIDATION WITH EXPERIMENTAL CAMPAIGN RESULTS	134
4.8.1. REFERENCE SPECIMENS	134
4.8.2. SERVICEABILITY AND FAILURE ANALYSIS	135
4.8.3. FLEXURAL BEHAVIOR	137
4.8.4. STRAIN AND STRESS DISTRIBUTIONS	140
4.9. CONCLUSIONS	144
CHAPTER 5. NUMERICAL MODELS	149
5.1. INTRODUCTION	149
5.2. INITIAL FINITE ELEMENT MODELS	150
5.2.1. GFRP PROFILE CALIBRATION	150
5.2.2. LINEAR ELASTIC MODEL FOR HYBRID BEAMS	152
5.2.3. PRELIMINARY NONLINEAR MODEL FOR HYBRID BEAMS	156
5.3. ADVANCED NONLINEAR FINITE ELEMENT MODEL	159
5.3.1. MATERIAL CONSTITUTIVE LAWS	160
5.3.2. GEOMETRY AND MESH	163
5.3.3. INTERACTIONS AND CONSTRAINTS	165
5.3.4. BOUNDARY AND LOAD CONDITIONS	166
5.3.5. ANALYSIS PROCEDURE AND OUTPUTS	166
5.3.6. VALIDATION WITH EXPERIMENTAL AND ANALYTICAL RESULTS	167
5.4. CONCLUSIONS	183
CHAPTER 6. CONCLUSIONS AND OUTLOOK	187
6.1. CONCLUSIONS	187
6.1.1. EXPERIMENTAL CAMPAIGN	188
6.1.2. ANALYTICAL PROCEDURE	190
6.1.3. NUMERICAL MODELS	192
6.2. FUTURE LINES OF INVESTIGATION	193

APPENDIX A. PROFILE CHARACTERIZATION TESTS	207
A.1. INTRODUCTION	207
A.2. FLEXURAL CHARACTERIZATION TESTS	207
A.2.1. SCOPE AND PRINCIPLE	207
A.2.2. TESTING PROCEDURE	208
A.2.3. RESULTS	210
A.3. TENSILE CHARACTERIZATION TESTS	212
A.3.1. SCOPE AND PRINCIPLE	212
A.3.2. TESTING PROCEDURE	213
A.3.3. RESULTS	215
A.4. IN-PLANE COMPRESSIVE CHARACTERIZATION TESTS	218
A.4.1. SCOPE AND PRINCIPLE	218
A.4.2. TESTING PROCEDURE	218
A.4.3. RESULTS	221
A.5. INTERLAMINAR SHEAR STRENGTH CHARACTERIZATION TESTS	225
A.5.1. SCOPE AND PRINCIPLE	225
A.5.2. TESTING PROCEDURE	225
A.5.3. RESULTS	227
A.6. IN-PLANE SHEAR STRENGTH CHARACTERIZATION TESTS	229
A.6.1. SCOPE AND PRINCIPLE	229
A.6.2. TESTING PROCEDURE	229
A.6.3. RESULTS	231
A.7. FULL-SECTION CHARACTERIZATION TESTS	232
A.7.1. SCOPE AND PRINCIPLE	232
A.7.2. TESTING PROCEDURE	233
A.7.3. RESULTS	235
APPENDIX B. ADDITIONAL EXPERIMENTAL DATA	239
B.1. INTRODUCTION	239
B.2. TEST SETUPS	239
B.3. REFERENCE SPECIMENS	240
B.4. GFRP-CONCRETE HYBRID BEAMS	243
APPENDIX C. ADDITIONAL ANALYTICAL RESULTS	251
C.1. INTRODUCTION	251
C.2. VALIDATION OF ANALYTICAL RESULTS FOR REFERENCE PROFILES	251
C.3. VALIDATION OF EXPERIMENTAL CAMPAIGN RESULTS	253

List of Figures

Figure 2.1: Current applications of FRP composites in civil engineering.....	9
Figure 2.2: Various types of rovings used in pultruded FRP profiles [9].	9
Figure 2.3: Various types of fiber mats used in pultruded FRP profiles [9].	10
Figure 2.4: Typical internal structure of a pultruded FRP specimen [10]......	10
Figure 2.5: Pultrusion process of FRP profiles (image courtesy of GDP SA).	12
Figure 2.6: Typical shapes of pultruded FRP structural profiles (image courtesy of Strongwell Corporation).	12
Figure 2.7: Uniaxial behavior of pultruded GFRP profiles versus common materials (graph courtesy of GDP SA).	13
Figure 2.8: Degradation of GFRP profile elastic modulus under fatigue loading (graph courtesy of GDP SA).	13
Figure 2.9: General view of the all-FRP footbridge from Lleida, Spain [19].	15
Figure 2.10: Examples of pultruded GFRP profiles used in new structures and rehabilitation projects: (a) the Eyecatcher office building, Basel, Switzerland (image courtesy of Fiberline Composites); (b) the 19 th century “Paludo” pedestrian bridge, Venice, Italy [20]; (c) the temporary roof structure of the Santa Maria Paganica Church, L'Aquila, Italy [21].	16
Figure 2.11: Examples of infrastructure projects incorporating hybrid FRP-concrete beams: (a) the Cantábrico highway overpass bridge; (b) the M-111 highway overpass bridge (both images courtesy of ACCIONA Infraestructuras); (c) the marine pier of the Downeast Institute for Applied Marine Research and Education (courtesy of Downeast Institute).	18
Figure 2.12: Hybrid beam designs investigated by Fam <i>et al.</i> [36]	23
Figure 2.13: Hybrid FRP-concrete girder sections designed by Manalo <i>et al.</i> [50].	25
Figure 2.14: Hybrid FRP-concrete beams tested by El-Hacha <i>et al.</i> [58].	26
Figure 2.15: Hybrid cross-sections analyzed by Hulatt <i>et al.</i> [63].	28
Figure 2.16: Hybrid FRP-concrete girders analyzed by Fam <i>et al.</i> [71].	29
Figure 2.17: Uniaxial stress-strain curve of concrete, adapted from [109]. Compressive curve model from Eurocode 2.	43
Figure 2.18: Uniaxial stress-strain curve of concrete, adapted from [134]. Rüsçh’s compressive parabola-rectangle curve....	43
Figure 2.19: Tensile stress-strain relationship of concrete simulated in [127].	44
Figure 2.20: Tensile stress-strain relationship of concrete introduced in [151].	44
Figure 2.21: Idealized trilinear shear connector force-slip relationship from [153].	45
Figure 2.22: Exponential force-slip relationship for steel studs, adopted from Model Code 2010 [77].	45
Figure 3.1: Cross-section geometry of the GFRP IPE 120 pultruded profile.....	50
Figure 3.2: GFRP profiles used in the experimental campaign.	50
Figure 3.3: Internal macrostructure of the GFRP profile: (a) cross-section layers (emphasized colors); (b) fiber rovings; (c) non-woven continuous strand mats (CSM).	51
Figure 3.4: Internal microstructure of the GFRP profile: (a) flange sample; (b) unidirectional fibers; (c) multidirectional fibers (CSM); (d) a single glass fiber covered in resin.	51
Figure 3.5: Internal microstructure of the GFRP web-flange region: (a) junction sample; (b) lengthwise view; (c) transverse view; (d) structural pores.	52
Figure 3.6: GFRP profile material characterization tests: (a) flexure; (b) tension; (c) in-plane compression; (d) interlaminar shear; (e) in-plane shear; (f) full section effective moduli.	54
Figure 3.7: Constructive details of the proposed models: cross-sections, lateral views and combined top view of M1 and M2 hybrid beams (mm) – not to scale.....	58
Figure 3.8: Fabrication process of the hybrid beams: (a) installment of steel bolts; (b) completed formwork; (c) concrete casting; (d) specimens prior to instrumentation and testing.	59

Figure 3.9: Composite material with transverse isotropy.....	62
Figure 3.10: Flowchart of the experimental and numerical procedure used in evaluating the elastic properties of the GFRP profiles and corresponding hybrid beams.....	64
Figure 3.11: Experimental modal analysis test setup for the GFRP profile.....	65
Figure 3.12: GFRP profile model used to visualize the experimental modal results.....	65
Figure 3.13: Experimental modal analysis test setup for the GFRP-concrete hybrid beams.....	66
Figure 3.14: GFRP-concrete hybrid beam model used to visualize the experimental modal results.....	66
Figure 3.15: Curve fitting for a single magnitude experimental FRF of the GFRP profile.....	67
Figure 3.16: Imaginary shapes of all the experimental FRFs of the GFRP profile (three accelerometer references, colored in red, black and green).....	67
Figure 3.17: GFRP profile finite element model.....	67
Figure 3.18: GFRP-concrete hybrid beam finite element model.....	67
Figure 3.19: Correlation matrices for the three first vibrational modes of the GFRP profile in longitudinal and transverse bending and in torsion.....	68
Figure 3.20: Numerical (FEA) and experimental (EXP) matching mode shapes of the profile.....	69
Figure 3.21: Numerical (FEA) and experimental (EXP) matching mode shapes of the M2 hybrid beams.....	70
Figure 3.22: MAC values of the first normal modes of the tested specimens.....	70
Figure 3.23: GFRP profile design candidates and evaluation samples.....	71
Figure 3.24: Comparative charts of the experimentally and numerically estimated natural frequencies.....	73
Figure 3.25: Schematic of load arrangements and instrumentation of tested specimens (mm).....	75
Figure 3.26: Laboratory setups and instrumentation: (a) M1 or M0 beams in test setup I; (b) M1 or M0 beams in test setup II; (c) Profile 1 in test setup I; (d) M2 beams in test setup I; (e) M2 beams in test setup II; (f) Profile 2 in test setup I.....	76
Figure 3.27: Failure characteristics of reference specimens: (a) M0-RCB1; (b) M0-RCB2; (c) Profile 1; (d) Profile 2.....	77
Figure 3.28: Experimental bending results under test setup I: load-midspan deflection curves until failure.....	78
Figure 3.29: Deflection profiles of hybrid beams at maximum load in test setup I.....	78
Figure 3.30: Failure characteristics of hybrid beams model M1 in test setup I: (a) concrete crushing and flexural cracks; (b) inward slip and flange delaminations; (c) bottom flange separation.....	79
Figure 3.31: Failure characteristics of hybrid beams model M2 in test setup I: (a) profile web-flange shear delamination preceded by concrete slab crushing; (b) post-failure local buckling of the web; (c) transverse crushing of the profile's web.....	80
Figure 3.32: Visible crack patterns of hybrid beams in test setup I. Failure cracks and crushing areas are indicated in bright red.....	81
Figure 3.33: Experimental bending results under test setup II: load-midspan deflection curves until failure.....	82
Figure 3.34: Deflection profiles of hybrid beams at maximum load in test setup II.....	82
Figure 3.35: Failure characteristics of hybrid beams model M1 and M2 in test setup II: (a) M1 – profile top web-flange shear delamination; (b) M2 – profile top web-flange shear failure followed by global web buckling.....	83
Figure 3.36: Visible crack patterns of hybrid beams in test setup II. Failure cracks are indicated in bright red.....	84
Figure 3.37: Hybrid beam M2-HB4, section S1: variation of axial strains in function of the applied load.....	86
Figure 3.38: Hybrid beam M2-HB4, section S1: normal strain distribution at different load levels (kN).....	86
Figure 3.39: Hybrid beam M2-HB4, section S2: variation of axial strains in function of the applied load.....	87
Figure 3.40: Hybrid beam M2-HB4, section S2: normal strain distribution at different load levels (kN).....	87
Figure 3.41: Hybrid beam M2-HB2: bottom flange axial strain variations.....	87
Figure 3.42: Hybrid beam M2-HB4: bottom flange axial strain variations.....	87
Figure 3.43: Hybrid beam M2-HB4, section S2: in-plane shear stress variation in function of the applied shear load.....	88

Figure 3.44: Hybrid beam M2-HB4, section S2: shear percentile carried by the profile in function of the applied total load.	88
Figure 3.45: High-speed camera images taken during the shear delamination failure of M2-HB1.	89
Figure 3.46: M2 hybrid beams: slip strain variation in function of the applied bending moment.	89
Figure 3.47: Relative end slip of the profiles versus load ratio.	89
Figure 3.48: Visual evidence of partial shear interaction and shear failure: (a) occurrence of slip and junction shear; (b) deformation of bolts; (c) distortion of connector holes; (d) web-flange rupture; (e) top and bottom flange delaminations of M1-HB2; (f) radial inclination of bolts in M2-HB2 (concrete slab removed).	90
Figure 3.49: Bending capacity increase in hybrid beams vs. equivalent RC beam M0-RCB1, in test setup I.	91
Figure 3.50: Bending capacity increase in hybrid beams vs. equivalent RC beam M0-RCB2, in test setup II.	91
Figure 3.51: Bending capacity increase in hybrid beams vs. single GFRP profiles, under test setup I.	91
Figure 3.52: Structural efficiency of investigated beam models under test setup I.	92
Figure 3.53: Structural efficiency of investigated beam models under test setup II.	92
Figure 4.1: Analytical models for the flexural behavior of a hybrid beam: (a) Euler-Bernoulli composite beam with complete shear interaction; (b) Timoshenko composite beam with partial shear interaction.	98
Figure 4.2: Generic hybrid cross-section geometry with corresponding strain (ϵ) and stress (σ) distributions, at SLS and ULS, considering: (a) complete or (b) partial shear interaction.	99
Figure 4.3: Static cases analyzed. Simply-supported hybrid beams subjected to: (a) a midspan point load; (b) two symmetrically applied point loads; (c) a uniformly distributed load.	99
Figure 4.4: Typical load ratio-slip curve for a steel shear stud.	105
Figure 4.5: Differential element for a hybrid pultruded FRP-concrete beam with partial interaction.	105
Figure 4.6: Variation of composite action parameter αL in function of connection shear stiffness K_c .	109
Figure 4.7: Variation of partial interaction parameter ξ to relative coordinates $x_r = x/L$ and $b_r = b/L$.	110
Figure 4.8: Influence of composite action parameter αL over partial interaction parameter ξ , at beam midspan.	111
Figure 4.9: Variation of complete and partial normalized deflections to relative coordinates $x_r = x/L$.	111
Figure 4.10: Variation of partial interaction parameter ξ in function of the degree of shear connection η , according to several design code formulations for composite beams. Corresponding inferior limits for η are also plotted.	112
Figure 4.11: Normalized longitudinal distributions of slip and slip strain for the three static cases discussed.	117
Figure 4.12: Variation of maximum slip strain in function of the connection's shear stiffness for hybrid beam M2-HB4.	118
Figure 4.13: Cross-sections of the hybrid beams used in the validation analysis.	124
Figure 4.14: Analytically computed load versus experimental load at SLS.	127
Figure 4.15: Analytically estimated midspan deflection versus experimental deflection at 50% of the maximum sustained load.	127
Figure 4.16: Analytically computed midspan deflections versus experimental deflections at ULS.	129
Figure 4.17: Validation diagram for the proposed analytical models in terms of flexural capacity and maximum deflection at ULS.	129
Figure 4.18: Validation diagrams for the proposed analytical models, at SLS and ULS, for the six hybrid beams used in the procedure. Numbers indicate the ratio between the analytical and experimental results.	129
Figure 4.19: Experimental and analytical load-deflection curves of hybrid beam specimens. Partial and complete interaction considered.	130
Figure 4.20: Comparative chart of the estimated partial interaction parameters ξ for the six hybrid beams used in the validation procedure.	131
Figure 4.21: Comparative chart of the percentile difference of analytical versus experimental flexural stiffness EI for the six hybrid beams used in the validation procedure.	132
Figure 4.22: Experimental and analytical load-strain curves of hybrid beam specimens. Only partial interaction considered.	133

Figure 4.23: Analytical in-plane shear stress distribution over the depth of hybrid beam HB1.	134
Figure 4.24: Bottom flange axial strain variations of Profile 2: experimental and analytical curves.	135
Figure 4.25: In-plane shear stress variation in Profile 2, section S2, in function of the applied shear load: experimental and analytical curves with or without longitudinal warping.	135
Figure 4.26: Hybrid beams model M1: analytical and experimental load-midspan deflection curves.	137
Figure 4.27: Hybrid beams model M2: analytical and experimental load-midspan deflection curves.	138
Figure 4.28: Analytical and experimental flexural stiffness of hybrid beams with concrete mix C1. Various design code and proposed formulations are compared.	138
Figure 4.29: Analytical and experimental flexural stiffness of hybrid beams with concrete mix C2. Various design code and proposed formulations are compared.	139
Figure 4.30: Comparative chart of the percentile difference of analytical versus experimental flexural stiffness EI for the four hybrid beams tested under three-point bending (test setup I).	140
Figure 4.31: Comparative chart of the percentile difference of analytical versus experimental flexural stiffness EI for the four hybrid beams tested under four-point bending (test setup II).	140
Figure 4.32: Neutral axis depth variation in function of the applied load for hybrid beam M2-HB1 in section S1. Experimental curves and analytical predictions.	141
Figure 4.33: Experimental and analytical axial strain distribution in hybrid beam M2-HB4, in section S1, at an intermediate load level of 50 kN.	141
Figure 4.34: Analytical longitudinal slip distribution in hybrid beam M2-HB4 at an intermediate load level of 50 kN, versus the registered experimental data slip point.	142
Figure 4.35: In-plane shear stress variation in hybrid beam M2-HB4, section S2, in function of the applied shear load. Experimental and analytical curves with or without warping.	143
Figure 4.36: In-plane shear stress distribution in M2-HB4, in section S2, at an intermediate load of 50 kN. Analytical curves under complete (τ_{co}) and partial (τ_{eff}) shear interaction assumptions versus experimental data points (τ_{exp}).	143
Figure 5.1: Three-dimensional model of GFRP Profile 2 including stiffeners and loading plate.	150
Figure 5.2: Load-midspan deflection response of Profile 1: experimental, analytical and numerical curves.	151
Figure 5.3: Load-midspan deflection response of Profile 2: experimental, analytical and numerical curves.	151
Figure 5.4: Axial strain variations of Profile 2 in section S1: experimental, analytical and numerical values.	151
Figure 5.5: In-plane shear stress variation in Profile 2, section S2, in function of the applied shear load: experimental, analytical and numerical curves.	151
Figure 5.6: Schematic view of the deformed hybrid beam M2 finite element base model.	152
Figure 5.7: Numerically predicted flexural responses of referenced hybrid beams versus experimental curves and analytical estimations. Concrete cracking and partial interaction were accounted for in the analytical model.	154
Figure 5.8: Numerically predicted flexural responses of hybrid beams M2 versus experimental curves and analytical estimations. Concrete cracking and partial interaction were accounted for in the analytical model.	155
Figure 5.9: Numerically computed longitudinal slip distributions in hybrid beams M2, at an intermediate load level of 50 kN, versus experimental data points and analytical predictions.	156
Figure 5.10: Assembly view of the nonlinear finite element model of FRP-concrete hybrid beam B7.	157
Figure 5.11: Shear connector behavior models for hybrid beam M2-HB1.	158
Figure 5.12: Comparison between experimental and numerical flexural responses. Linear and nonlinear finite element models considered.	159
Figure 5.13: GFRP modeled constitutive behavior for the two principal material directions.	160
Figure 5.14: Concrete mixtures constitutive behavior model for compression.	161
Figure 5.15: Concrete mixtures constitutive behavior model for tension.	161
Figure 5.16: Steel reinforcement constitutive behavior model.	162
Figure 5.17: Steel bolt constitutive behavior model.	163

Figure 5.18: Assembly view of the hybrid beam finite element model in function of the applied load setup (three-point bending or four-point bending).....	164
Figure 5.19: Spatial and cross-section view of the meshed finite element model (central part of slab removed for visualization reasons).....	164
Figure 5.20: Boundary and load conditions for the hybrid beam finite element model.	166
Figure 5.21: Numerically predicted global flexural responses of M2 hybrid beams versus experimental curves and analytical estimations.....	167
Figure 5.22: Numerically predicted deflection profiles versus experimental curves and analytical estimations, at an intermediate load of 50 kN.	168
Figure 5.23: Longitudinal normal stress distributions at the ultimate load, for hybrid beams M2-HB1 and M2-HB3 (MPa).169	
Figure 5.24: Numerical (solid line) versus experimental (dotted line) axial strain variations in section S1.	170
Figure 5.25: Numerical (solid line) versus experimental (dotted line) bottom flange axial strain variations.	170
Figure 5.26: Experimental, analytical and numerical axial strain distributions of hybrid beams M2 in section S1, at an intermediate load level of 50 kN.....	171
Figure 5.27: Concrete slab axial compressive strain at section S1 for hybrid beam M2-HB1 (load in kN).....	173
Figure 5.28: Concrete slab axial compressive strain at section S1 for hybrid beam M2-HB3 (load in kN).....	173
Figure 5.29: Transverse normal stress distribution at the ultimate load, for hybrid beam M2-HB2 (MPa).....	173
Figure 5.30: Midspan sectional transverse normal stress distribution at failure, for hybrid beam M2-HB2 (MPa).....	173
Figure 5.31: Transverse compressive stress in the GFRP profile versus material determined strength.	173
Figure 5.32: Comparison between the experimental and numerical plastic deformations of the concrete slab.	174
Figure 5.33: Axial stress distributions of the concrete slab at failure, for hybrid beams M2-HB1 and M2-HB3 (MPa).	175
Figure 5.34: Longitudinal in-plane shear stress distributions at the ultimate load, for beams M2-HB1 and M2-HB3 (MPa).176	
Figure 5.35: Cross-sectional (S2) in-plane shear stress distribution at failure, for beams M2-HB1 and M2-HB3 (MPa).....	176
Figure 5.36: Experimental, analytical and numerical curves of the web in-plane shear stress variation in hybrid beams M2, section S2, in function of the applied shear load.	177
Figure 5.37: In-plane shear stress distributions in hybrid beams M2, in section S2, at an intermediate load of 50 kN. Numerical and analytical estimated distributions versus experimental data points.	178
Figure 5.38: Simulated longitudinal in-plane shear stress distributions for M2-HB1 in test setup I, at the maximum load, at different coordinate levels across the profile.	179
Figure 5.39: Simulated longitudinal in-plane shear stress distributions for M2-HB3 in test setup II, at the maximum load, at different coordinate levels across the profile.	179
Figure 5.40: Numerical (solid line) versus experimental (dotted line) bending moment-slip strain variations near the midspan for the M2 specimens of test setup I.	180
Figure 5.41: Numerical (solid line) versus experimental (dotted line) bending moment-slip strain variations at the midspan for the M2 specimens of test setup II.	180
Figure 5.42: Numerical (solid line) versus experimental (dotted line) profile end slip variation in function of the applied load ratio for the M2 specimens of test setup I.	181
Figure 5.43: Numerical (solid line) versus experimental (dotted line) profile end slip variation in function of the applied load ratio for the M2 specimens of test setup II.	181
Figure 5.44: Numerical longitudinal slip distributions in hybrid beams M2, at an intermediate load level of 50 kN, versus registered experimental data points and analytical results.	182
Figure 5.45: Longitudinal shear connector load variation at the maximum load, for specimen M2-HB1.	182
Figure 5.46: Longitudinal shear connector load variation at the maximum load, for specimen M2-HB3.	182

Figure A.1: Specimen nominal dimensions and sampling area for flexural tests (mm).	208
Figure A.2: Test setup scheme for flexural characterization tests [155].....	209
Figure A.3: Experimental test setup configuration for flexural characterization tests.....	209
Figure A.4: Tensile fracture and compression fracture of fibers due to flexure [155].....	210
Figure A.5: Bottom-up view of the flexural failure of the GFRP specimens.	211
Figure A.6: Lateral view of the failed specimens in flexure.	211
Figure A.7: Stress-strain curves of the longitudinal flexural characterization tests.....	211
Figure A.8: Nominal dimensions of Type 2 specimens and sampling area for tensile tests (mm).	213
Figure A.9: Tensile failure of specimen W1 in the proximity of one of the action grips.	213
Figure A.10: Nominal dimensions of Type 1B specimens used for the tensile tests (mm).	214
Figure A.11: Experimental test setup configuration for tensile characterization tests.....	214
Figure A.12: Tensile GFRP specimen positioned in the action grips.	214
Figure A.13: Tensile failure of a Type 1B GFRP specimen.....	216
Figure A.14: Tensile splintering of GFRP fibers.	216
Figure A.15: Type 1B specimens after tensile testing.	216
Figure A.16: Load-displacement curves of the longitudinal tensile characterization tests.	216
Figure A.17: Stress-strain curves of the longitudinal tensile characterization tests.....	217
Figure A.18: Lengthwise and crosswise coupon nominal dimensions and sampling areas for in-plane compressive tests (mm).	219
Figure A.19: Isometric views of the designed compressive supporting jig.	219
Figure A.20: Schematic of the loading fixture for compressive characterization tests (mm).	220
Figure A.21: Experimental test setup configuration for compressive tests.	220
Figure A.22: Acceptable compressive failure mode: delamination [158].	221
Figure A.23: Acceptable compressive failure mode: through-thickness shear failure [158].	221
Figure A.24: Compressive failure of the GFRP lengthwise specimens.....	221
Figure A.25: Through-thickness shear failure of a crosswise GFRP specimen.....	222
Figure A.26: Compressive failure of the GFRP crosswise specimens.	222
Figure A.27: Load-displacement curves of the longitudinal compressive tests.....	222
Figure A.28: Load-displacement curves of the transverse compressive tests.....	222
Figure A.29: Stress-strain curves of the longitudinal compressive tests.	223
Figure A.30: Stress-strain curves of the transverse compressive tests.	223
Figure A.31: Coupon nominal dimensions and sampling area for interlaminar shear tests (mm).	225
Figure A.32: Test setup scheme for interlaminar shear tests [159].	226
Figure A.33: Test setup configuration for interlaminar shear tests.....	226
Figure A.34: Loading and support arrangement for interlaminar shear tests.	226
Figure A.35: Single shear and multiple shear interlaminar failure modes [159].	227
Figure A.36: Interlaminar single shear failure at the right end of a GFRP web specimen.	227
Figure A.37: Lateral view of the interlaminar shear failure of all coupons.	227
Figure A.38: Load-midspan displacement curves of the interlaminar shear tests.	228
Figure A.39: Coupon nominal dimensions and sampling area for in-plane shear tests (mm).	230
Figure A.40: GFRP profile coupons used for in-plane shear characterization tests.	230

Figure A.41: Test setup configuration for in-plane shear tests.	230
Figure A.42: Loading jig and specimen for in-plane shear tests.	230
Figure A.43: In-plane shear failure of a GFRP specimen.	231
Figure A.44: Post-failure image of a ruptured GFRP specimen.	231
Figure A.45: Load-displacement curves of the in-plane shear tests.	231
Figure A.46: Loading configuration for method A [15].	233
Figure A.47: Profile bending setup for a test span of 2500 mm.	233
Figure A.48: Profile bending setup for a test span of 1800 mm.	233
Figure A.49: Flexural test scheme used for determining the elastic properties of the GFRP profiles.	234
Figure A.50: Load-midspan deflection curves of the tested GFRP profiles.	235
Figure A.51: Slope-intercept form for the evaluation of the effective flexural stiffness of P1.	237
Figure A.52: Slope-intercept form for the evaluation of the effective shear stiffness of P1.	237
Figure A.53: Slope-intercept form for the evaluation of the effective flexural stiffness of P2.	237
Figure A.54: Slope-intercept form for the evaluation of the effective shear stiffness of P2.	237
Figure A.55: Slope-intercept form for the evaluation of the effective flexural stiffness of P3.	237
Figure A.56: Slope-intercept form for the evaluation of the effective shear stiffness of P3.	237
Figure B.1: Deformation behavior of elastomeric supports.	239
Figure B.2: Schematic of load arrangements and instrumentation of reference specimens (mm).	240
Figure B.3: Flexural behavior of M0-RCB1: load-midspan deflection curve.	240
Figure B.4: Deflection profile of M0-RCB1 at different load levels (kN; P_y – yielding load; P_{max} – maximum load; P_f – final load).	240
Figure B.5: Flexural behavior of M0-RCB2: load-midspan deflection curve.	241
Figure B.6: Deflection profile of M0-RCB2 at different load levels (kN).	241
Figure B.7: Reference beam M0-RCB1: variation of axial compressive strain in section S1.	241
Figure B.8: Reference beam M0-RCB2: variation of axial compressive strains in section S1 and S1'.	241
Figure B.9: Flexural behavior of reference beam Profile 1: load-midspan deflection curve.	241
Figure B.10: Flexural behavior of reference beam Profile 2: load-midspan deflection curve.	241
Figure B.11: Reference beam Profile 2: variation of axial strains in section S1.	242
Figure B.12: Reference beam Profile 2: variation of axial strains in section S2.	242
Figure B.13: Reference beam Profile 2: axial strain distribution at different load levels (kN), in section S1.	242
Figure B.14: Reference beam Profile 2: axial strain distribution at different load levels (kN), in section S2.	242
Figure B.15: Reference beam Profile 2: bottom flange axial strain variations.	242
Figure B.16: Reference beam Profile 2: in-plane shear stress variation.	242
Figure B.17: Flexural behavior of hybrid beams: complete load-midspan deflection curves until final collapse.	243
Figure B.18: Deflection profiles of hybrid beams at different load levels until failure (kN).	244
Figure B.19: Axial strain variations of hybrid beams in section S1 until failure.	245
Figure B.20: Axial strain distributions of hybrid beams in section S1 at different load levels until failure (kN).	246
Figure B.21: Axial strain variations and axial strain distributions of the M2 hybrid beams in section S2 until failure (kN).	247
Figure B.22: Bottom flange axial strain variations of hybrid beams until failure.	248
Figure B.23: In-plane shear stress variation and shear force percentile carried by the profile in function of the applied shear load or total load, for the M2 hybrid beams.	249

Figure B.24: Relative profile end slip variation of the hybrid beams in function of the applied load ratio, until failure.	250
Figure C.1: Load-midspan deflection response of Profile 1: experimental and analytical curves.	251
Figure C.2: Load-midspan deflection response of Profile 2: experimental and analytical curves.	251
Figure C.3: Axial strain variations of Profile 2 in section S1: experimental and analytical curves.	252
Figure C.4: Axial strain variations of Profile 2 in section S2: experimental and analytical curves.	252
Figure C.5: Bottom flange axial strain variations of Profile 2: experimental and analytical curves.	252
Figure C.6: In-plane shear stress variation in Profile 2, section S2, in function of the applied shear load: experimental and analytical curves with or without warping.	252
Figure C.7: Neutral axis depth variation in function of the applied load for hybrid beams M2 in section S1. Experimental curves and analytical predictions.	253
Figure C.8: Experimental and analytical axial strain distributions of hybrid beams M2 in section S1, at an intermediate load level of 50 kN.	253
Figure C.9: Analytical estimation of the slip strain variation in hybrid beams M2, in function of the applied bending moment.	254
Figure C.10: Analytical estimation of the interlayer slip variation in hybrid beams M2, in function of the applied bending load ratio.	254
Figure C.11: Analytical longitudinal slip distributions in hybrid beams M2, at an intermediate load level of 50 kN, versus registered experimental data points.	254
Figure C.12: In-plane shear stress variation in hybrid beams M2 section S2 in function of the applied shear load: experimental and analytical curves with or without warping.	255
Figure C.13: In-plane shear stress distributions in hybrid beams M2, in section S2, at an intermediate load of 50 kN. Analytical curves under complete (τ_{co}) and partial (τ_{eff}) shear interaction assumptions versus experimental data points (τ_{exp}).	255

List of Tables

Table 2.1: Typical property values of GFRP pultruded profiles and minimum requirements specified for structural members.	14
Table 2.2: Summary of FRP-concrete hybrid beam finite element models.	39
Table 3.1: Declared properties of the GFRP PR500 pultruded shapes.	52
Table 3.2: Declared chemical resistance of the GFRP PR500 pultruded shapes.	53
Table 3.3: Experimentally determined mechanical properties of the GFRP profile (average \pm standard deviation values).	55
Table 3.4: Concrete compressive strength characterization results.....	57
Table 3.5: Mechanical properties of concrete mixes.	57
Table 3.6: Beam designation and description.	59
Table 3.7: Elastic constants of orthotropic and transverse isotropic materials.....	62
Table 3.8: Optimization domain and constraints for the GFRP profile.....	69
Table 3.9: Optimization domain for the M2 GFRP-concrete hybrid beams.	70
Table 3.10: Experimental (EXP) and numerical (FEA) modal frequency results for the GFRP profile.	72
Table 3.11: Experimental (EXP) and numerical (FEA) modal frequency results for the GFRP-concrete hybrid beams.....	72
Table 3.12: Comparison between the estimated elastic properties using the proposed nondestructive method and the properties offered by the manufacturer or obtained from the destructive static tests.	73
Table 3.13: Overview of flexural tests carried out.....	74
Table 3.14: Experimental results of tested specimens at failure (u subscript): bending moment (M), midspan deflection (w), sustained load (P), shear load (V), bottom flange maximum axial stress (σ), average in-plane web shear stress (τ), and relative end slip (s).	90
Table 4.1: Deflection functions for simply supported beams.	101
Table 4.2: Exact analytical expressions for the partial interaction parameter ξ and corresponding midspan values.....	107
Table 4.3: Exact analytical solutions for the maximum slip and slip strain in a hybrid beam with partial shear interaction. .	117
Table 4.4: Characteristics of the hybrid beam specimens chosen for validation analysis.	124
Table 4.5: Computed parameters of partial interaction.....	125
Table 4.6: Participation percentages of hybrid beam sub-systems.....	125
Table 4.7: Computed loads at SLS considering various hypotheses.....	126
Table 4.8: Experimental failure characteristics and maximum computed moments.	128
Table 4.9: Maximum loads and total deflections considering various hypotheses at ULS.	128
Table 4.10: Timoshenko shear coefficient of the GFRP pultruded profile.	135
Table 4.11: Results for hybrid beams at the serviceability (SLS) and ultimate limit states (ULS/u): bending moment (M), midspan deflection (w), and bottom flange ultimate axial stress (σ).....	136
Table 4.12: Flexural responses of hybrid beams considering concrete crushing: bending moment (M) and midspan deflection (w).....	137
Table 4.13: Strain and stress results at an intermediate load of 50 kN: interlayer slip strain at section S1 (ϵ_s), maximum GFRP axial strain (ϵ_{max}) and corresponding maximum longitudinal tensile stress (σ_{max}).	142
Table 5.1: Comparison between experimental, analytical and finite element analysis midspan deflections (wt) computed at failure considering a state of complete (wtco) or partial (wtpa) shear interaction.....	153
Table 5.2: Composite profile engineering data for the advanced FE model.	160

Table 5.3: Concrete engineering data for the advanced FE model.	161
Table 5.4: Steel reinforcement engineering data for the advanced FE model.	162
Table 5.5: Comparison between experimental results and analytical and numerical estimates for serviceability bending moments (MSLS) and midspan deflections (w) measured at an intermediate load of 50 kN and at the ultimate failure load.	169
Table 5.6: Concrete compressive strain (ϵ_1, u^1 – section S1) and bottom flange maximum axial strain (ϵ_f, \max, u) and stress (σ_f, \max, u) at an intermediate load of 50 kN.	172
Table 5.7: Concrete compressive strain (ϵ_1, u^1 – section S1) and bottom flange maximum axial strain (ϵ_f, \max, u) and stress (σ_f, \max, u) at failure load.	172
Table 5.8: Comparative web in-plane shear stresses at rosette positions ($r1, r2$), at an applied total load of 50 kN.	178
Table 5.9: Comparative web in-plane shear stresses at rosette positions ($r1, r2$), at failure load.	179
Table 5.10: Evaluation of interlayer slip strain at an applied load of 50 kN and at the ultimate load, in section S1.	180
Table 5.11: Measured and predicted extreme interlayer slip at an applied load of 50 kN and at the ultimate load.	181
Table A.1: Main results and statistical interpretation of the flexural characterization tests.	212
Table A.2: Main results and statistical interpretation of the longitudinal tensile tests.	217
Table A.3: Main results and statistical interpretation of the longitudinal compressive tests.	224
Table A.4: Main results and statistical interpretation of the transverse compressive tests.	224
Table A.5: Main results and statistical interpretation of the interlaminar shear tests.	228
Table A.6: Main results and statistical interpretation of the in-plane shear tests.	232
Table A.7: Registered and calculated data values for GFRP profile P1.	235
Table A.8: Registered and calculated data values for GFRP profile P2.	236
Table A.9: Registered and calculated data values for GFRP profile P3.	236
Table A.10: Main results and statistical interpretation of the full-section tests.	238

1

Introduction

1.1. Context and motivation

In the past two decades a lot of research effort has been invested in updating the current structural design codes in order to cover durability, conservation and environmental aspects. Furthermore, since the construction sector is the largest single economic activity in Europe and the biggest industrial employer, new and improved construction standards are currently being developed, in line with the European Union strategy for smart, sustainable and inclusive growth.

The new EN Eurocodes, which are due to be published by 2020, are bound to embrace new construction materials and technological solutions. In this regard, design specifications for structures built with composite materials made of fiber-reinforced polymers (FRPs) are intended to be officially introduced, as many engineering applications have already confirmed their usefulness. The major advantages of FRP products are related to the high strength, faster installation times, reduced transportation costs, increased durability, and low maintenance requirements that they possess. At first, the proposed technical specifications will not be mandatory and will allow for a trial period for use and commenting. Therefore, comprehensive investigations are still required to fully understand the behavior and performance of these fairly novel materials.

From the generic group of composites, pultruded FRP profiles have gained popularity over the years because of their lower manufacturing costs and shape resemblance to conventional profiles. Still, due to their inherent brittle behavior, moderate flexural stiffness, and sensitivity to instability failure modes, researchers have started to look for other solutions that could exploit the characteristics of the material in a better way. One of the novel alternatives is represented by the hybrid type of element which combines the outstanding properties of the pultruded composite shapes with the low cost and reliability of concrete. Hybrid FRP-concrete beams typically consist of a concrete section working in compression that is mechanically connected or adhesively bonded to a composite shape working mostly in tension. The hybrid beam system has been successfully employed especially in infrastructure projects and has demonstrated its potential also in other civil engineering applications. The benefits over single pultruded

profiles include increased strength and stiffness, superior structural redundancy and ductility, better resistance to buckling phenomena and impact loading, as well as enhanced vibrational characteristics.

An in-depth review of the principal researches published thus far has indicated that there is still a great need to investigate experimentally the flexural behavior of FRP-concrete beams and to identify structural designs with lower costs. Besides, the influence of the flexibility of the connection system over structural response has been largely ignored. Due to the novelty of the subject and the wide diversity of proposed hybrid beam solutions, the viability of the technology demands further experimental tests and comparative analyses against conventional members.

Secondly, many theoretical studies have limited their analyses by considering a state of complete shear interaction although slip phenomena had been previously observed during testing. To add, there are currently no available design recommendations for FRP-concrete members, while for pultruded FRP structural profiles, there have been a number of standards, guides and manuals issued. Besides, the main codes that regulate the design of steel-concrete composite members deal with the slip effects only from the perspective of the shear capacity of the connectors or neglect them as a whole through the use of appropriate detailing measures. Nevertheless, shear connections in hybrid beams are known to be more flexible and thus the same design principles established may not be valid.

Thirdly, in contrast to the research developments in simulating steel-concrete composite beams, hybrid FRP-concrete numerical models have preponderantly relied on simplified material, contact and geometry considerations, limiting in consequence the precision required for obtaining reliable predictive data for computer-aided design.

Ultimately, the present doctoral research has also been motivated by the previous investigations carried on composite materials at the Laboratory for the Technological Innovation of Structures and Materials (LITEM) from the Polytechnic University of Catalonia (UPC – BarcelonaTech).

To summarize, the observations derived from the completed state of the art have emphasized the need for supplementary laboratory tests on hybrid FRP-concrete beams with mechanical shear connectors, with special emphasis on the flexibility of the connection system and its effects. Corresponding analytical formulations and advanced numerical models are also required for estimating judiciously the structural performance of this novel type of members.

The conclusions of the proposed research will further lessen the introduction of advanced composite materials in common types of public works and constructions currently built with traditional materials. Furthermore, knowledge in this area is considered strategic and can provide a competitive advantage as the industry veers toward identifying innovative constructive solutions for the future.

1.2. Aim and objectives

The present work aimed to investigate the structural performance of hybrid beams made of fiber reinforced polymer pultruded profiles attached to concrete slabs, with highlight on the effects of the connection flexibility over bending behavior.

In order to achieve this aim, the following primary and secondary objectives were defined:

- Characterize the experimental flexural response of GFRP-concrete hybrid beams with mechanical shear connectors.
 - Perform an extensive series of in-house characterization tests on the FRP material.
 - Develop a nondestructive technique which can be used to determine the elastic properties of hybrid members and composite profiles.
 - Design several GFRP-concrete beams and investigate their flexural behavior under different configurations and in a comparative manner against single GFRP profiles and equivalent reinforced concrete beams.
- Propose an analytical procedure for the design of FRP-concrete hybrid beams under short-term loading.
 - Offer design equations for the serviceability and ultimate limit states in function of complete or partial shear interaction assumptions.
 - Study the viability of using simplified or approximate formulas to account for interlayer slip effects.
 - Validate the analytical procedure with experimental data.
- Develop a predictive finite element model capable of simulating the fundamental behavior of FRP-concrete beams with bolted joints.
 - Trial initial numerical models with a low level of complexity to better understand the influence of material, connection and geometry characteristics.
 - Carry out nonlinear finite element simulations and validate the obtained results against experimental data and analytical estimations.

1.3. Research methodology

According to the objectives set, a number of research tasks and activities were defined which are outlined next.

- Document past and current hybrid beam solutions where FRP profiles were used as structural elements and identify possible deficiencies of the current systems. Review the most significant published experimental, analytical and numerical investigations in this field and summarize their main observations.
- Characterize the flexural, tensile, compressive, shear, and full-section properties of the GFRP profile to be used in an experimental campaign.
- Design and fabricate a number of eight GFRP-concrete specimens with two different cross-section models, and an additional two reinforced concrete beams with similar features.
- Use an experimental modal analysis to acquire the dynamic properties of the fabricated specimens and then a finite element analysis coupled with a parameter identification method so as to obtain the elastic properties of the hybrid members. Validate the proposed method with the results of the previous static tests.
- Instrument the beams, carry out the bending tests under two different load configurations and post-process the results. Investigate the flexural behavior, possible failure modes and their causes, analyze the partial interaction between the concrete and the profile and evaluate its influence. To finish, compare the structural performance of the hybrid beams to that of the single GFRP profiles and equivalent reinforced concrete beams.
- Propose analytical relations for the serviceability and ultimate limit state conditions. Derive “exact” and simplified expressions for estimating deflections, flexural stiffness, interlayer slip, bending capacities, and normal and shear stress distributions under different interaction conditions. Validate the analytical procedure against previous experimental data from recognized studies and against gathered laboratory results from the preceding campaign.
- Start with a fairly simple finite element model that intends to capture the flexural behavior of hybrid beams with bolted joints, and continue to improve its accuracy by adding advanced material definitions, interface contact features, and second order effects. In this respect, explore also various modelling techniques. Compare the predictions of the numerical models with the experimental results and with the analytical estimations using simplified assumptions in order to assess their correctness.
- Summarize the main conclusions of the investigation and sketch out further research tasks.

1.4. Document outline

The doctoral thesis is divided into six chapters and three appendices, the contents of which are briefly summarized below.

Chapter 1. Introduction

The current chapter contextualizes the subject of the present work and briefly exposes the reasons which led to the investigated topic. The principal aim of the thesis and its main objectives are described next, followed by the employed research methodology and the document structure in view.

Chapter 2. State of the art

The second chapter consists of an initial overview of the fiber-reinforced polymer materials for civil engineering, and the fabrication, characteristics and applications of pultruded FRP profiles. The chapter continues with the current state of knowledge regarding hybrid FRP-concrete beams, in which the structural concept, practical applications and existing connection technologies are discussed. In direct correspondence, the published key experimental investigations, analytical formulations and numerical finite element simulations are amply examined and compared in order to highlight some of the research needs at this moment.

Chapter 3. Experimental campaign

In the commencing part of the third chapter, the properties of the constitutive materials to be used in the design of hybrid beam specimens are noted and commented. The planned beam models are then described together with their fabrication process. The section is followed by the introduction of a nondestructive method for obtaining the elastic properties of FRP profiles and FRP-concrete beams, and its validation results. Next off, the laboratory setups, testing procedure, and experimental results are discussed in the main part of the chapter. The outcomes of the experimental campaign are analyzed in terms of flexural behavior and failure modes, developed composite action and interlayer slip, as well as in a comparative manner versus reference specimens.

Chapter 4. Analytical procedure

The fourth chapter refers to the proposed analytical procedure for the design of hybrid FRP-concrete beams. It includes serviceability and ultimate limit state formulations for estimating deflections, flexural stiffness, and vibration limits, respectively, maximum bending capacities. Relations for determining internal actions, stress distributions and interlayer slip are also offered. In the last part of the chapter, the validation of the analytical procedure with previous experimental data and with the outcomes of the laboratory tests is illustrated. The validation incorporates serviceability and failure analyses, and assessments of flexural behavior with strain and stress distribution comparisons.

Chapter 1 | Introduction

Chapter 5. Numerical models

The development of predictive finite element models for hybrid beams with mechanical shear connectors is revealed within the fifth chapter of the thesis. Several preliminary models are detailed first, followed by a final one with advanced nonlinear characteristics. In this regard, employed material constitutive curves, interface characteristics and modelling techniques are commonly detailed. Each section of a proposed numerical model concludes with the results of a validation process against experimental data and analytical estimations.

Chapter 6. Conclusions and outlook

The last chapter summarizes the main findings of the investigation and indicates possible research lines for future studies.

Appendix A. Profile characterization tests

In the first appendix of the document, the results of the laboratory characterization tests performed on the GFRP coupons of the composite profiles used in the experimental investigation are listed. The results are preceded by the scope, principles and specifics of the testing procedure discussed.

Appendix B. Additional experimental data

The second appendix includes additional information regarding the specimen instrumentation and laboratory setups, as well as supplementary experimental results for the investigated hybrid beams and reference specimens.

Appendix C. Additional analytical results

The last appendix contains complementary analytical results from the validation process of the derived mathematical relations, for the reference profiles and the GFRP-concrete beams.

2

State of the art

2.1. Introduction

A solution to designing structures that have long-term durability and low maintenance requirements is to introduce new construction materials or to implement new structural systems. In this regard, fiber-reinforced polymers (FRPs) represent one of the novel solutions in the civil engineering field that offer promising results. Thus, the initial part of the present chapter describes briefly the introduction of FRP materials in structural applications and their basic constituent components. The discussion transitions then to the pultruded composite profiles and their corresponding fabrication, structural behavior, properties, typical shapes, and uses.

To optimize the use of composite materials, researchers have proposed to form hybrid structural systems with conventional materials such as concrete. The concept and design principles of hybrid FRP-concrete beams are subsequently presented, and their competitive advantages over simple pultruded profiles and classic reinforced concrete beams are analyzed. In direct correlation, the available connection technologies are explained together with their notable benefits and drawbacks.

A review of the most representative experimental studies carried so far on FRP-concrete beams is performed, where the discussed examples are split into five categories depending on the design of the hybrid cross-section. The references are illustrated in chronological order to highlight how the designs evolved over the years, and their reported outcomes are generally examined with emphasis on the influence of the shear connection system.

Afterwards, related design guidelines for hybrid beams are indicated and the factors which affect the composite action in members with mechanical joints are commented. Later on, the specifications of the major design codes for conventional composite beams regarding the allowance of incomplete shear connections and the effects of partial interaction over stiffness and deflection are inspected. The last section on this topic deals with the analytical relations reported so far for hybrid beams, and with the more complete design formulations proposed for conventional composite beams with partial shear interaction.

At the end of the state of the art, noteworthy numerical simulations used to predict the structural behavior of hybrid beams and composite beams with mechanical shear connectors are reviewed with focus on the modelling techniques, nonlinear considerations and validation results. In addition, material constitutive curves for FRP profiles, steel reinforcements, and especially for concrete and shear connectors are studied.

To conclude, the whole bibliographic research helped to identify the current knowledge gaps in the research field of hybrid FRP-concrete beams, where additional investigations are needed.

2.2. Fiber-reinforced polymer profiles

2.2.1. Description

A composite material is defined as a mechanically separable combination of two or more constituent materials with significantly different chemical or physical properties that are purposefully mixed in order to obtain a new material with dissimilar characteristics from the individual components. Composites are usually preferred over conventional materials due to their desirable properties, such as strength, cost, or weight that makes them more attractive for specific applications.

Since ancient times, composite materials have been used in construction with great success. Currently, however, the notion of composites refers primarily to fiber-reinforced polymer (FRP) materials that have appeared at the beginning of the 20th century, in the 1930s, with the development of the plastic industry. Although initially designed and targeted specifically for the aerospace and defense industries, FRPs have evolved over the last four decades into economically and structurally viable construction materials for civil engineering applications [1]. Their introduction in other domains of activities and industries was lessened by the research carried toward the end of the 1970s, when advanced composites with superior strength, stiffness, dimensional stability, and chemical resistance were developed [2]. The decrease in costs due to the perfection of manufacturing methods also accelerated their introduction.

FRP composite materials used in structural engineering today typically consist of continuous or discontinuous strong fibers arranged in a reinforcement system that is embedded in a weaker material called the matrix, which is typically made of a thermosetting polymer resin. The resulting composite material is highly heterogeneous, anisotropic, and capable of intermediate mechanical performance (superior to the matrix but lower to the fibrous reinforcement) [3]. Fiber concentrations in structural composites are usually greater than 30% by volume to provide sufficient strength and stiffness.

At an early stage, the use of fiber-reinforced polymers in civil engineering was mainly limited to demonstrative rehabilitation projects because of high costs, lack of design codes, and limited experience.

Rehabilitation comprises repair, strengthening and seismic retrofit, and many researchers still study it because of the exceptional advantages that FRP composites offer compared to the traditional strengthening methods [4–6]. Nevertheless, in recent years, researchers have also proposed to form new structures entirely from FRP, or hybrid new structures from combining FRP with other materials, including concrete, metal or timber. In fact, it is believed that hybrid members represent the future in civil infrastructure projects [7]. To better illustrate the current applications of FRP composites in civil engineering, Figure 2.1 classifies the possible utilizations in a tree diagram.

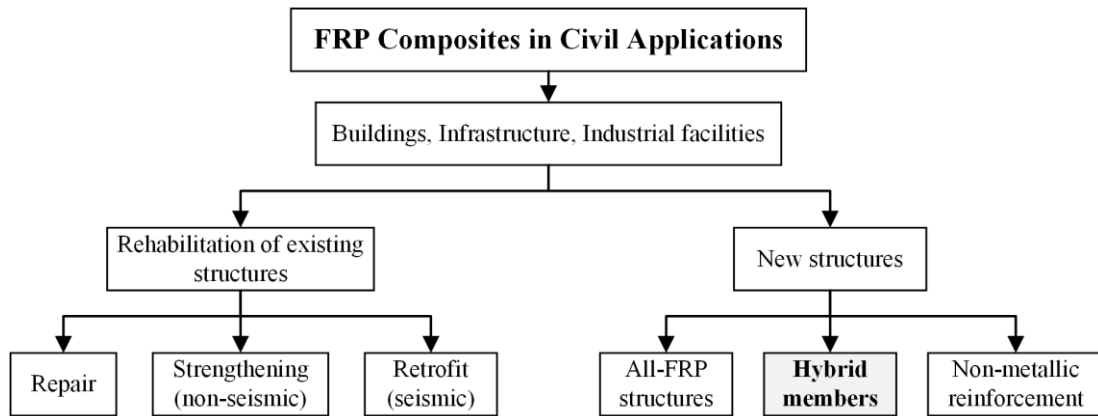


Figure 2.1: Current applications of FRP composites in civil engineering.

With respect to the hybrid members, the majority of the beam designs rely on pultruded FRP profiles given their relatively low cost and suitability for structural applications.

As previously mentioned, FRP composites have a reinforcement system and a matrix system that grant them their unique characteristics. The main functions of the fiber reinforcements are to carry the applied load and to provide strength, stiffness, and thermal stability to the composite. Commonly, pultruded FRP profiles employ glass or carbon fibers, and occasionally aramid, basalt or hybrid combinations of fibers. The selection of the fiber types is normally performed according to the design specifications and taking into consideration the advantages and weaknesses involved. More details about various fiber characteristics are offered in ref. [1,8].

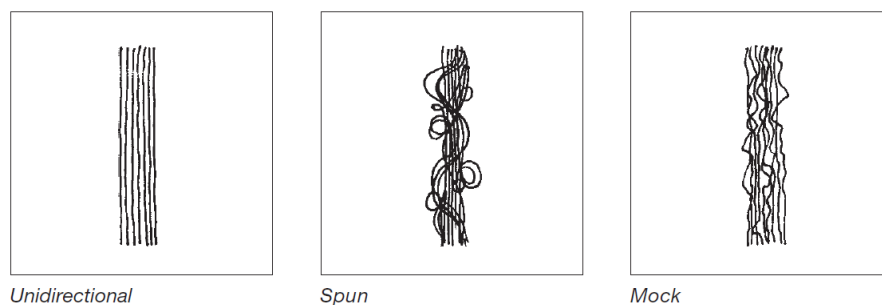


Figure 2.2: Various types of rovings used in pultruded FRP profiles [9].

Primarily, the fibers in a pultruded FRP profile are arranged in the longitudinal direction to offer the product high tensile and flexural capabilities, and to greatly contribute to the overall section stiffness.

The rovings are typically made of unidirectional or twisted filaments as shown in Figure 2.2, and constitute more than half of the total fiber content.

The rest of the fiber content is mainly disposed in the form of continuous strand mats (CSM) which are used to provide the desired transverse strength and stiffness of the profile. Their structure is composed of randomly oriented fibers, and constitutes the most economical method of attaining high transverse mechanical properties. In situations in which the design requirements are not satisfied by conventional mats, selected products such as woven and non-woven fabrics, stitched fabrics, grids and meshes can be used instead. Several examples of special mats are illustrated in Figure 2.3 adjacent to the common type of CSM.

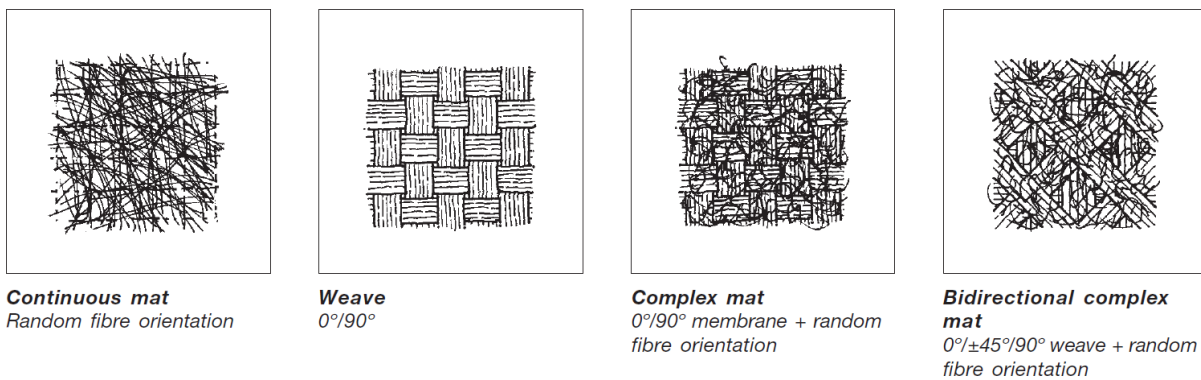


Figure 2.3: Various types of fiber mats used in pultruded FRP profiles [9].

The fiber rovings and the continuous strand mats are protected by an exterior veil that is used to enhance the surface of the pultruded profiles. The veil consists of a resin-rich layer that affects the appearance, durability and handling of the product. Its low roughness and porosity provide a high quality finish and a proper resistance to chemical agents, ultraviolet radiation, and weatherability.

In a representative fiber arrangement of a pultruded FRP, as depicted in Figure 2.4, the mats are disposed near the outside faces and, in certain situations, at the center of the composite material. The continuous rovings fill generously the remaining space, while the surface veils are positioned on top of the exterior mats. Noticeably, polymer cores are not used in pultruded shapes, so the ratio between the rovings and the mats determines the relationship of the longitudinal to transverse properties.

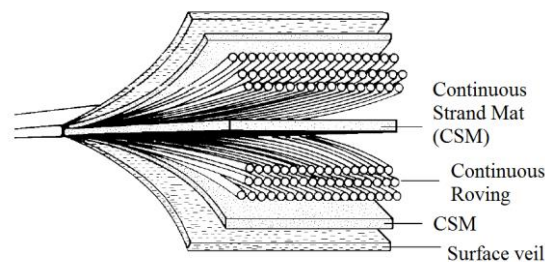


Figure 2.4: Typical internal structure of a pultruded FRP specimen [10].

Next to the reinforcement system, the second major component of the composite material is represented by the matrix system which transfers the loads between the fibers and forms a protective barrier against moisture, oxidation and harmful chemical agents. Furthermore, it protects the fibers from abrasion and shocks, and governs the shear, transverse tensile and compression behavior of the composite [11]. The fire response is also greatly influenced by the matrix performance.

There are two categories of polymer resins used in pultrusion established according to the effects caused by heat on their properties. For structural FRP profiles, the most common matrix systems are of the thermosetting type, based on unsaturated polyester, vinyl ester, epoxy, phenolic or methacrylate resins. Their distinctive trait is that after heating to a certain temperature, known as the glass transition temperature, their mechanical and physical properties degrade severely and irreversibly. Thermoplastic resins on the other hand can be softened and hardened repeatedly without affecting significantly their inherent properties. Nevertheless, they are usually avoided in civil engineering applications due to their reduced stiffness and strength, difficulty to process, and low fiber impregnation and adhesion.

In addition to the polymer resin, the matrix system contains additional components called fillers and additives that have the purpose to reduce costs, to aid with the fabrication process and to provide additional capabilities to the finished product. The list usually includes inorganic fillers, chemical catalysts and accelerators, fire and flame retardants, pigments, ultraviolet retardants, inhibitors, low shrink additives, release agents, and other various items [12].

2.2.2. Fabrication

Structural FRP profiles are normally manufactured through a process called pultrusion which is essentially a continuous and highly cost-effective technology for producing heat constant cross-section members. Pultrusion started in the 1950s in the USA, and until the late 70s its products were mostly used in non-structural applications. It has been recently reported [13] that pultrusion is the second most important manufacturing process for composites, yielding the second highest quantity of produced materials.

Inside the process, fiber rovings are pulled from a creel and brought about through a special bath where they are slowly impregnated by the matrix. At the same time, the mats, fabrics or complexes are reeled off coils and rolls, impregnated, and fed into a former system to be processed in the correct configuration. The composite material is then joined by the surface veil and pulled through a high temperature heated die to be polymerized, which matches the desired geometry of the profile. At the end of the production line, the cured material is cut to the specified length to be packaged. A schematic of the whole fabrication process can be seen in Figure 2.5.

The main advantages of the pultrusion technology are represented by the very fast, and therefore economic, way of impregnating and curing materials; by the accurate resin and fiber control with

minimum waste; by the high volume concentration of fibers that can be achieved; and by the ability to coextrude other polymer materials or elastomers in conjunction with the base components. The fabrication process is limited by the constant or near constant cross-sections obtained that are ideally suited mostly for axial and flexural members.

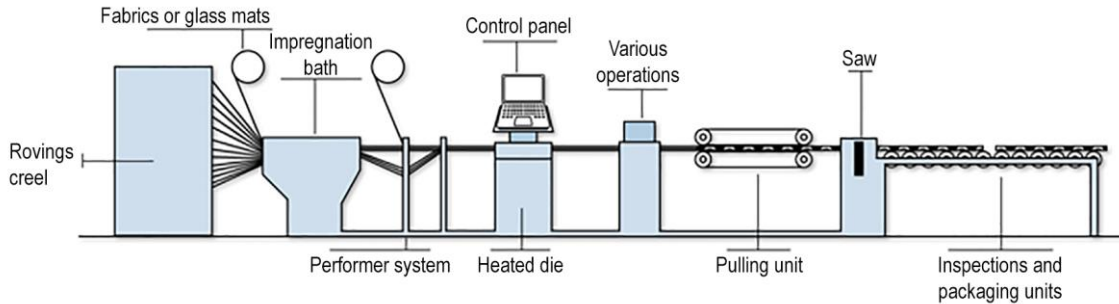


Figure 2.5: Pultrusion process of FRP profiles (image courtesy of GDP SA).

The majority of commercial, off-the-shelf, profiles have been designed by imitating thin-walled metallic cross-sections, which is not necessarily beneficial due to the material’s anisotropy. Pultruded profiles have common geometries such as angle, channel, tube, or I shapes, as displayed in Figure 2.6. More advanced structural shapes have been developed specifically for composite decks or composite panels, but are not discussed in the present document.

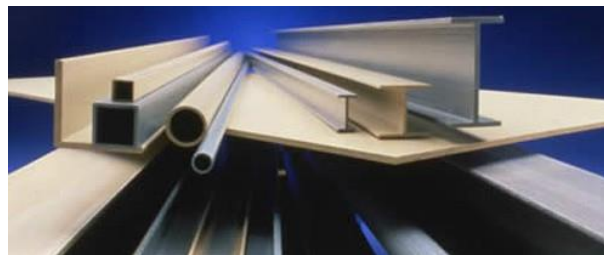


Figure 2.6: Typical shapes of pultruded FRP structural profiles (image courtesy of Strongwell Corporation).

At the current time, no standard geometries or material recipes are employed by manufacturers for structural pultruded profiles. There are, however, a number of industry groups that represent the interests of pultrusion manufacturers and coordinate some of the activities in the field. Leading associations are the European Pultrusion Technology Association (EPTA) and the American Composites Manufacturers Association (ACMA).

Product prices may vary from 2-10 €/kg or 5-30 €/m for glass FRP (GFRP) profiles, while custom shapes made of high-performance carbon fibers and resin systems are more expensive.

2.2.3. Characteristics

Referring to the structural behavior, FRP pultruded profiles possess a linear elastic stress-strain relationship until failure, a higher axial strength when compared to steel profiles, lower transverse

strength, and a relatively low modulus of elasticity. The advantages of the composite pultruded material over traditional materials include: low self-weight, high fatigue and environmental resistance, long-term durability, high strength-to-weight ratio, tailored properties and geometry, thermal insulation, electromagnetic transparency, low maintenance, and ease of transportation and assembly.

The uniaxial elastic behavior of a glass FRP (GFRP) pultruded profile is illustrated in Figure 2.7, in comparison to that of conventional materials. Because of their linear response, the profiles are well suited for applications that involve cyclical mechanical stresses, vibrations or repeated impacts. To exemplify, the chart shown in Figure 2.8 displays the degradation of the elastic modulus of a GFRP profile under 3-point bending, subjected to a dynamic regime with a frequency of 10 Hz. A slight decrease of 10% is observed only after half a million cycles under an imposed elongation at 80% of the ultimate stress, confirming thus the good fatigue performance of pultruded FRP members.

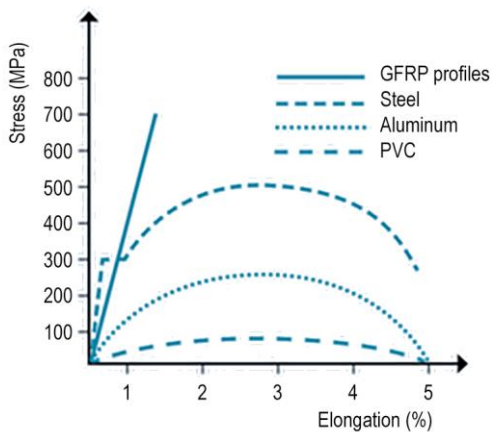


Figure 2.7: Uniaxial behavior of pultruded GFRP profiles versus common materials (graph courtesy of GDP SA).

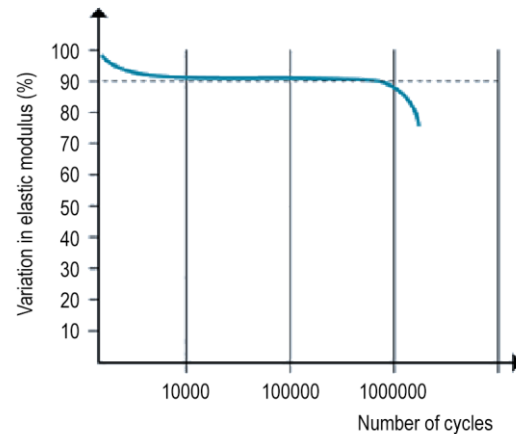


Figure 2.8: Degradation of GFRP profile elastic modulus under fatigue loading (graph courtesy of GDP SA).

The properties of FRP pultruded profiles, as in most composites, depend fundamentally on the characteristics of their constituent materials, on the orientation and content of the fiber reinforcement and also on the fiber-matrix interaction. In addition, the response is further influenced by external factors such as the loading conditions and environmental factors.

Currently, there are no standard properties defined that the manufacturers can follow. However, in 2002, the European Committee for Standardization published the EN 13706 [14–16] which introduced specifications for FRP profiles, including minimum property requirements. The normative designates two grades for classifying structural profiles in function of the effective elastic modulus of the full section. In 2010, the American Society of Civil Engineers (ASCE) published a more extensive design pre-standard [17] that also specifies minimum required physical and mechanical properties for FRP pultruded shapes.

Table 2.1 summarizes the typical mechanical and physical properties of currently available GFRP profiles from the major manufacturers, together with the minimum requirements specified by the

aforementioned standards. As seen from the tabular data, the American specifications are more rigorous than the European ones, and provide minimum values for additional properties. Moreover, it was noted that the majority of the manufacturers report for design the interlaminar shear strength instead of the in-plane shear strength.

Table 2.1: Typical property values of GFRP pultruded profiles and minimum requirements specified for structural members.

Property	Units	Typical values	EN 13706-3		ASCE Pre-Standard
			E23 Grade	E17 Grade	
<i>Mechanical</i>					
Full section elastic modulus ^a	GPa	17-35	23	17	n/s
Tensile modulus – axial	GPa	17-35	23	17	21
Tensile modulus – transverse	GPa	5-11	7	5	5.5
Tensile strength – axial	MPa	200-500	240	170	207
Tensile strength – transverse	MPa	50-100		n/s	48
Compressive modulus – axial	GPa	17-35		n/s	21
Compressive modulus – transverse	GPa	6-13		n/s	6.9
Compressive strength – axial	MPa	200-500		n/s	207
Flexural strength – axial	MPa	200-500	240	170	n/s
In-plane shear modulus	GPa	3-4		n/s	2.8
Interlaminar shear strength – axial	MPa	25-35	25	15	24
In-plane shear strength	MPa	n/s		n/s	55
Pin-bearing strength – axial	MPa	100-260	150	90	145
Pin-bearing strength – transverse	MPa	120-180	70	50	124
Pull-through strength per fastener	kN	n/s		n/s	2.9-5.6 ^b
Poisson ratio – axial		0.23-0.35		n/s	n/s
Poisson ratio – transverse		0.09-0.15		n/s	n/s
<i>Physical</i>					
Fiber Volume Fraction	%	45-75		n/s	> 30
Density	kg/dm ³	1.6-2.1		n/s	n/s
Barcol hardness		40-55		n/s	> 40
Moisture equilibrium content	%	0.25-1.25		n/s	< 2
Glass transition temperature	°C	80-130		n/s	> 82
Coefficient of thermal expansion	/°C	9-14.5		n/s	< 13.5·10 ⁻⁶

^a Effective flexural modulus.

^b In function of base thickness.

n/s – not specified.

Generally, common pultruded FRP shapes can be used without any restriction between -20 °C and +80 °C, while for harsher conditions, special formulations are necessary. The durability of the composite material is also linked with the sensitivity to time-dependent effects from creep, relaxation, ultraviolet radiation, alkalinity, moisture, and fire resistance. The chemical resistance to various solutions is usually indicated by manufacturers through the use of compatibility guides. To resist some of the abovementioned factors, pultruded profiles are often protected with surface veils, coatings, gels, or special mixtures added to the matrix formulation during fabrication.

Regarding the environmental impact of pultruded FRP profiles, it is worthwhile to say that the manufacturing process is friendly to the environment due to the closed molds that minimize the evaporation of volatile substances and to the exothermic reaction of the polymerization. It was observed that the energy consumption used in the production of a glass FRP composite profile is 1/4 of that required for steel, and 1/6 that for aluminum [9]. Furthermore GFRP profiles are made from inexpensive, widespread raw materials, while cured polyester or phenolic resins are stable and do not pollute. It also helps that structures built with pultruded FRP profiles are easy to erect, require a low maintenance, and can benefit from additional thermal insulation. Lastly, at the end of the life cycle, composite structures are relatively easy to decommission, however, the biggest drawback is still related to the limited recyclability of the materials, which is still under investigation [18].

2.2.4. Applications

Pultruded profiles have been used in the past 40 years in a significant number of structures, including pedestrian and road bridges, building floors, frames, roofs, stair structures, cooling towers, offshore platforms, walkways, trusses, joists, structure supports, and so on. They have also been employed in non-structural applications to serve as railings, panels, claddings, containment systems, covers, gratings, planks, or ladders.

From the 1950s to the 1970s, FRP profiles were mostly used in non-structural applications, however, starting with the 1980s, the first structural systems that included composite shapes began to appear, such as single-story gable frames for electromagnetic interference laboratories, building claddings or “stick” systems for cooling towers, as well as pedestrian and vehicular bridges with composite decks. The last couple of decades saw a wide introduction of pultruded composites in rehabilitation projects, multi-story buildings, floors, piers and especially footbridges. The quantity and quality of fabricated pultruded profiles has also grown remarkably.

A notable example of an all-FRP composite bridge is the Lleida footbridge from Spain, built in 2001, which spans 38 m over a high-speed railway and a roadway that connects Madrid to Barcelona. The main requirements for the design were minimum maintenance, quick and easy erection and no electromagnetic interference [19]. The completed infrastructure project is depicted in Figure 2.9.



Figure 2.9: General view of the all-FRP footbridge from Lleida, Spain [19].

Other great examples of constructions that relied on the exceptional advantages possessed by pultruded FRP profiles are illustrated in Figure 2.10. The examples represent pilot projects, rehabilitation works, or temporary structures used for the restoration of historic monuments.

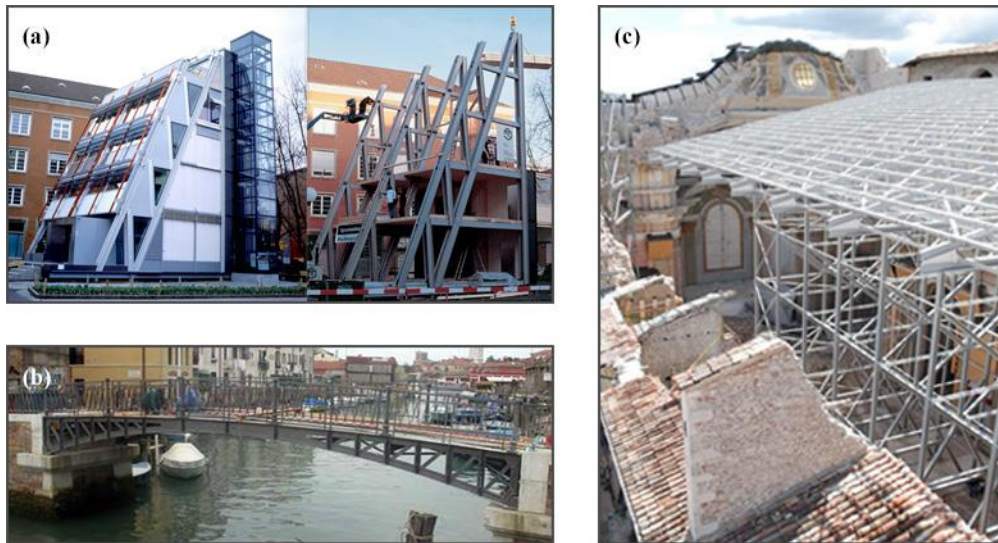


Figure 2.10: Examples of pultruded GFRP profiles used in new structures and rehabilitation projects: (a) the Eyecatcher office building, Basel, Switzerland (image courtesy of Fiberline Composites); (b) the 19th century “Paludo” pedestrian bridge, Venice, Italy [20]; (c) the temporary roof structure of the Santa Maria Paganica Church, L'Aquila, Italy [21].

2.3. Hybrid beam solutions

2.3.1. Concept and structural applications

Despite their great potential, fiber-reinforced polymer profiles present several drawbacks when compared to their steel counterparts: a relatively low stiffness (especially for glass FRP), which can lead to design constraints due to instability or large deformations, an inherent brittle behavior, and a partially developed connection technology. In addition, the lack of authoritative codes as well as the current high initial costs of these advanced materials prevent a widespread use of composite profiles in civil engineering applications. To overcome some of these issues, researchers have proposed the introduction of new hybrid elements that combine the advantages of FRP profiles with those of conventional materials in order to obtain superior structural members.

Most of the hybrid members designed up to date have been built by combining fiber-reinforced polymer shapes with concrete, given the lower cost and higher structural efficiency of the resulting constructive solution. Concrete is also preferred because it can provide confinement, increase flexural stability, strength and stiffness. Besides, the added weight from the concrete part may be beneficial in the sense that the system will have better damping, as light structures are normally predisposed to unacceptable vibrations. Because composite materials can be tailored in function of expected needs, the

FRP-concrete combined solution allows engineers to take advantage of the preeminent properties of each component and to optimize the use of both materials.

After a thorough analysis of the available and possible applications of advanced polymer composites in civil infrastructure, it has been suggested that hybrid FRP-concrete members represent the future in this field [7], as they possess great in-service properties and mechanical characteristics. Moreover, these novel elements can be employed in a wide variety of situations, and based on their promising results, extensive investigations have been undergone in North America [22], Europe and Asia [23].

In a recent review of the present and future utilization of FRP composites in construction [2], the author recommended that the following three criteria should be met for a successful implementation of hybrid systems in new structures:

- Cost effectiveness in terms of the most advantageous combination of whole-life cost and of high quality and performance.
- The composite material should be used ideally in areas subjected to tension.
- The fire resistance should not be critical.

Regarding FRP-concrete beams, the large majority of the proposed designs rely on pultruded FRP sections connected to concrete slabs. The main role of the composite profile is to carry the tension and shear in the member, while the concrete top serves to resist compression and to stabilize the flexural behavior. Most of the designs favor glass FRP (GFRP) pultruded profiles due to their lower production costs, whereas the top slabs are generally made from normal strength reinforced concrete. The FRP profiles and the concrete layers can be connected using a bonded joint, mechanical joint, or combined joint, as will be detailed further on.

The major advantages of the FRP-concrete beams over conventional reinforced concrete beams are:

- Higher strength-to-weight ratio
- Extended service life and reduced maintenance
- Resistance to aggressive external factors
- Lower transportation and installation costs
- Reduced formwork

Compared to single pultruded FRP profiles, the hybrid beams possess the following benefits:

- Enhanced strength and stiffness
- Better resistance to instability phenomena and impact loading
- Improved vibrational characteristics

- Elevated structural redundancy and ductility

Some of the notable disadvantages of hybrid FRP-concrete beams at the present time are related to:

- Interface/connection problems
- Little available data and experience
- High initial costs and environmental concerns (*i.e.*, recycling of FRPs)

Initial applications of hybrid FRP-concrete beams in civil infrastructure commenced in the 1980s with a few experimental projects and grew substantially along the years, as the technology evolved and the price of the advanced polymer composites decreased. More recently, there has been a tremendous attention provided to the use of hybrid solutions and to broadening their application range. At the current moment, FRP-concrete beams may be employed in designing bridge superstructures, building floors, industrial platforms, and offshore structures. Extensive reviews of pedestrian and vehicular bridges utilizing hybrid solutions may be found in ref. [24–27].

To exemplify a few practical cases, a joint project developed in 2003 in Spain led to the completion of three highway overpass bridges with hybrid superstructures [28]. One of the bridges, spanning a four-lane highway and designed to carry 60 ton traffic, has a total length of 46 m and four continuous spans, as illustrated in Figure 2.11(a).



Figure 2.11: Examples of infrastructure projects incorporating hybrid FRP-concrete beams: (a) the Cantábrico highway overpass bridge; (b) the M-111 highway overpass bridge (both images courtesy of ACCIONA Infraestructuras); (c) the marine pier of the Downeast Institute for Applied Marine Research and Education (courtesy of Downeast Institute).

The superstructure of the first bridge is made of three carbon fiber sandwich beams with a polymer foam that support the roadway deck which is formed from reinforced concrete and asphalt. Installation of the beams and concreting of the deck took place in under two days due to the reduced weight of the beams at 1 kN/m. The other two bridges were built identical, each made up of three simply supported spans with a 20.40 m wide box-girder deck, as seen in Figure 2.11(b). The former design was improved by combining GFRP with CFRP layers to reduce the costs of the composite girders, and by using a different manufacturing and assembly method. The overall objective of the research project was the development of a new high performance and cost-effective construction concept for bridges based on the application of rapid-renewal and long-life service infrastructures [29].

As a last case study, the composite marine pier depicted in Figure 2.11(c) was commissioned to replace an old wooden pier that was damaged due to the harsh environmental conditions present at the location. The project demanded the structure to necessitate a minimal maintenance and to support important supply loads. Thus, an innovative solution was applied, where 10 m long hybrid FRP-concrete beams were mounted on top of composite piles, over three spans.

2.3.2. Connection technology

There are three major types of connections that can be used to guarantee an effective shear transfer mechanism between the concrete and the FRP shape in a hybrid beam. Henceforth, the connection can be formed with a bonded joint, mechanical joint, or with a combination of the two. The selection of the joint type is usually determined by several factors such as the geometry of the members to be joined, the loads that need to be transferred, and the serviceability, fabrication and cost requirements, to name just a few.

2.3.2.1. Bonded joints

Briefly, bonded joints are generally realized with high-strength adhesive agents which are classified in function of their type, form, and curing process. The epoxy resins stand out as the most encountered solution for gluing FRP profiles to concrete as they provide strong joints and excellent creep properties. Furthermore, the epoxies have a suitable resistance to weathering agents, oils, chemical solvents, and elevated temperatures. They are essentially thermosetting resins which cure by polymerization, and come available either as two-part mixtures (resin plus hardener) or as a one-part resin, depending on the curing process involved. The limitations of the epoxy resins are embodied by the precise formulation requirements, exothermic reaction, and short pot life.

There are two possible application methods for bonding FRP and concrete, the first being the dry bond, where the adhesive is applied on a cured concrete surface, respectively the wet bond, where fresh concrete is cast on top of the adhesive agent before it has cured. Notwithstanding, there is also a third

variant where no adhesive is utilized in which concrete grout is poured around and/or inside the composite shape, connection known as pure bond.

Adhesive bonding technique is the most efficient way of achieving composite action between the FRP and concrete as it leads to connections with high strength and high stiffness. Because the load is distributed over a large interface area, there is a more uniform distribution of stresses and higher resistance to flexural, dynamic, and fatigue induced stresses [12]. Bonded joints are relatively inexpensive, are light and fast to apply, and are more appropriate for connecting irregular surfaces and obtaining esthetic forms. Lastly, they offer a good electrical and thermal insulation, and they act as a sealant, minimizing water ingress effects.

Nevertheless, bonded joints require special tools, materials and installation conditions, all which increase application costs; are difficult to inspect and disassemble, while time-dependent environmental factors (*i.e.*, temperature, humidity, air composition, etc.) can possibly affect their properties and durability. Perhaps the most important drawback is that the failure in glued joints takes place suddenly, exhibiting a brittle behavior. It must be noted also that the load-bearing capacity is not proportional to the surfaces of the adhered components, and that the bonded connection takes a long time to develop strength.

The flexibility of bonded joints is affected by the thickness of the adhesive, its elastic properties, and the eventual local stiffeners disposed near the joined area. In addition, the connection is sensitive to the stiffness of the hybrid beam components and to the joint configuration.

2.3.2.2. *Mechanical joints*

Similar to the case of conventional composite members, mechanical joints in FRP-concrete hybrid beams can be realized with dowels, fasteners, bolts, threaded rods, or profiles of various shapes and sizes. The connectors are usually made from steel (galvanized or stainless, to prevent corrosion) or from fiber-reinforced polymers. Normally, one end of the mechanical connector is attached to the profile while the other is embedded into the concrete.

Because FRP composites are heterogeneous, anisotropic and brittle, every discontinuity of the fibers can reduce the pin bearing capacity of the element. Furthermore, the connection capacity is greatly influenced by the fiber orientation, thickness of the FRP, edge distance, hole clearance, and clamping force, among many other factors.

Mechanical connections are usually preferred over bonded joints due to the ease of inspection, installation and disassembly, due to the short time they take to fully develop their strength capacity, and to the ductile behavior they can possess. Moreover, no surface preparation of the base materials is required and the connection solution can turn out to be more economical when the cost of both shop and field labor work is taken into account [1]. Lastly, minor misfits generated by hole sizes or positions are easily correctable for mechanical connectors using simple hand tools.

The bolting technique produces high stress concentrations at the holes since FRP materials have a linear elastic behavior and no local plastic deformations are permitted. These important stress concentrations coupled with the anisotropy of the composite material lead in most situations to overly-conservative designs. Apart from this aspect, bolt tension can decrease over time due to strain relaxation, and shear stresses may not be distributed evenly to multiple rows of fasteners.

The use of FRP connectors can assure a thermal and electrical insulation of the joint, however, the resulting connection has a brittle failure mode. On the other hand, metallic fasteners, although ductile, can lead to insulation and corrosion problems, and increase the weight of the structure. Other issues of mechanical connections are related to the time needed for realizing the assembly, the raw finished aspect of the joint, and the modest fatigue endurance. As a final point, because drilled holes in FRP profiles can provide a way for moisture and chemical agents to degrade the performance of the base material, the openings should be ideally sealed with resins.

The flexibility of bolted joints is notably influenced by the flexibility of the fasteners, slip, and bearing of fastener holes. As in the case of bonded joints, the flexibility is also susceptible to the mechanical properties of the constituent materials of the hybrid beam, and to the joint configuration.

2.3.2.3. Combined joints

Shear connectors may be added to bonded joints in order to deter the occurrence of brittle failure modes and to assure a backup solution for the initial connection system. The resulting combined joint is characterized by high strength and stiffness, and by potential post-elastic capacity. In addition, bolt connectors can provide support and pressure during assembly and curing of the adhesive, and can hinder the growth of bondline defects [12]. To emphasize, hybrid FRP-concrete beams with combined joints have a high degree of composite action and manifest little to no slip.

Regardless, combined joints are a costly constructive solution given their build complexity and the fact that the performance of the mechanical joint is only utilized after the adhesive's capacity has been exhausted.

Various experimental tests on bonded, mechanical, and combined joints for FRP-concrete beams have been reported in ref. [30,31]. In the absence of standardized tests for characterizing the performance of pultruded FRP-concrete connections, Albiol Ibáñez [32] has recently studied the bond between GFRP laminates and concrete by analyzing the influence of a series of surface treatments applied to the composite's surface and combined with mechanical fasteners, with the aim of identifying a suitable ductile connection for hybrid beams.

2.3.3. Experimental research studies

In the past decades, numerous hybrid beam designs have been proposed and analyzed experimentally. From the published investigations, the most important have been selected for review and comparison. The FRP-concrete beams were grouped in function of the composite's shape to better illustrate the available leading designs at the current moment.

2.3.3.1. Examples of hybrid beams with concrete-filled FRP tubes

One of the first possibilities in combining FRP with concrete in creating new structural members came at the beginning of the 1980s, following the successful use of FRP sheets in strengthening concrete columns. The principal idea was to fill entirely or partially FRP shapes with concrete to obtain hybrid elements with superior mechanical characteristics and performance. An early study carried by Fardis and Khalili [33] investigated the flexural performance of a beam formed from a rectangular glass fiber-reinforced plastic (GFRP) box filled with concrete. The purpose of the GFRP shape was to provide partial confinement in the compressive zone and to carry tensile and shear forces, while the concrete fill contributed to the compressive strength, ductility and rigidity of the member, preventing the local buckling of the FRP shape. Since concrete was restrained at both ends by the sides of the box, the bond was not a critical factor in the bending response.

Around the late 1990s, the *Carbon Shell System* was introduced as an alternative structural technology for short and medium span bridges. The concept uses prefabricated composite carbon fiber-reinforced polymer (CFRP) tubes as girders which are filled with lightweight concrete and then joined with a conventional precast, cast-in-place, or advanced composite deck system to form the bridge superstructure. Karbhari *et al.* [34] have reported experimental results from testing the hybrid girders, anchorages, and girder-deck assemblies for both serviceability and ultimate limit states, confirming the potential of the proposed structural solution. The innovative system was employed in building the Kings Stormwater Channel Bridge in 2001.

In order to reduce the weight of the concrete filled shapes, Fam *et al.* [35,36] investigated the flexural response of partially filled circular and rectangular GFRP tubes. Twenty circular beams were tested in bending under four-point loading. A number of nine different configurations of GFRP tubes were used and one was made entirely from steel. The design differed also by the existence or position of an internal tube or by the placement of concrete. Results showed that the flexural behavior is highly dependent on the stiffness and diameter-to-thickness ratio of the tube, and, to a much less extent, on the concrete strength. The contribution of concrete confinement to the flexural strength was insignificant; however, the ductility of the member was improved. Furthermore, it was demonstrated that if no connection is provided between the two different materials, slip will occur, diminishing the structural performance of the hybrid element. For the rectangular GFRP-concrete beams illustrated in Figure 2.12, the results indicated that although the concrete-filled pultruded tubes showed higher stiffness than the concrete-

filled filament-wound tubes of the same thickness, they failed prematurely by horizontal shear due to the lack of fibers in the hoop direction.

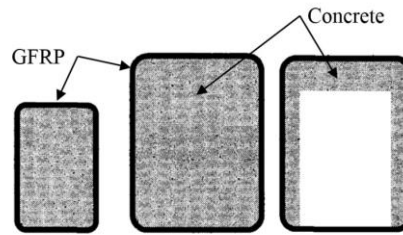


Figure 2.12: Hybrid beam designs investigated by Fam *et al.* [36]

Improved designs of the concrete-filled hybrid solutions were proposed in recent years by several authors. To exemplify, Li and Wu [37] suggested bonding the concrete core to the outside shell by using epoxy resins, so as to prevent significant slippage. CFRP sheets were then considered to increase the flexural stiffness of the system, and GFRP sheets with high rupture strains were wrapped in the hoop direction of the beam to bear the shear load and provide confinement. Lastly, a minimum reinforcement ratio of steel rebars was included to control the localization and propagation of flexural cracks.

The rationale and advantages of hybrid FRP-concrete-steel double-skin tubular members were discussed in a paper by Teng *et al.* [38] where the authors suggested potential applications in structures exposed to harsh environments, such as bridges, costal structures and various tower structures. The shear connection between the internal tube and the concrete core, and the joint between the tubular member and concrete decks were highlighted as key features in assuring the performance of the hybrid members.

Finally, a novel hybrid tubular solution was developed and analyzed by Chakraborty *et al.* [39], which consists of a pultruded GFRP profile, a CFRP bottom laminate, and a concrete block, all wrapped up using filament winding. The experimental results showed that the outside composite layer prevented the concrete part from debonding from the pultruded box and enhanced the stiffness and load capacity of the beam. In addition, it was observed that the hybrid beams with normal concrete or steel fiber-reinforce concrete had greater ductility than the beams with high strength concrete, all at the cost of slightly lower stiffness and flexural capacity.

2.3.3.2. Examples of hybrid beams with open section FRP profiles

An alternative design for combining concrete with pultruded FRP profiles started to appear at the beginning of the 1990s, when composite shapes with open section that resembled conventional steel profiles were employed in creating new structural hybrid members. One of the first theoretical studies was reported by Hillman and Murray [40] which conceptualized a novel lightweight floor system and compared its effectiveness against common or alternative low weight systems. The composite slab was constructed using a fiber reinforced plastic (FRP) deck with deep inverted T-beams connected by

intermediate flanges, and a concrete top fill. Besides the increase in strength, the authors reported a reduction in weight of over 50%, and by assuming full composite action with the concrete, the rigidity of the pultruded section was at least doubled. Despite the impressive weight reduction of this type of floor system, there were several disadvantages highlighted such as the high raw material costs, possible excessive deflections due to the low elastic moduli of the materials, and poor vibration characteristics.

An initial experimental campaign regarding hybrid beams of the aforementioned type was performed by Saiidi *et al.* [41] on graphite/epoxy concrete composite beams for bridge decks and floor slabs. The investigation focused on the flexural behavior of custom-made I-shaped profiles connected to concrete slabs with an epoxy layer, and studied the composite action and the effects of concrete strength on bond, flexural stiffness and capacity. Fragile failure modes were observed that consisted of shear debonding followed by longitudinal delaminations of the web. Analytical calculations based on the assumption of complete shear interaction and an estimated bond strength proved to be inexact. The study emphasized the need for pultruded shapes with better fiber orientation, lower costs, and more effective shear transfer mechanisms.

Hall and Mottram [42] designed and tested under four-point bending a dozen FRP-concrete beams. The hybrid members were formed from two or four T-shaped FRP profiles attached to an FRP base that was joined or embedded in a concrete section. Different geometries and orientations were investigated, and half of the tested specimens had an epoxy mortar applied between the two constitutive materials. Results showed that the hybrid specimens that had the adhesive applied had a superior structural response compared to the others and did not suffer from debonding. However, the majority of the beams experienced a shear failure of the unreinforced concrete top.

Given the observed deficiencies of the bonded joints in hybrid members (especially the lack of ductility and sensitivity to concrete cracking), researchers have started to design FRP-concrete beams with embedded mechanical shear connectors. To illustrate, Sekijima *et al.* [43,44] investigated the behavior of GFRP-concrete beams made with H-shaped profiles, where the shear transfer mechanism consisted of conventional studs which had been used for steel-concrete composite beams, arranged in a cross stitch pattern to prevent cracking between holes. There was no buckling of the hybrid specimens observed; however, the failure was sudden and occurred in the web of the profiles. The experimental behavior was linear elastic up to failure and slip between the two materials was noted. Studies carried out by Biddah [45], and by Fam and Skutezky [46] demonstrated that by surrounding the connectors with concrete, the registered deformations and slippage decrease while the flexural strength and dead load increase.

The viability of using hybrid FRP-concrete structural members with I-shaped profiles was further validated by Nordin and Täljsten [47], and by Correia *et al.* [48]. The investigations proved that the instability phenomenon associated with open section profiles may be impeded by providing web

stiffeners at the reaction points, and that the composite beams with mechanical shear connectors tend to possess a better flexural performance. In contrast, the specimens which had a bonded shear connection exhibited brittle, premature failures, but at the same time, an increased bending stiffness due to the notable absence of interlayer slip. Furthermore, apart from simply supported members, the use of GFRP-concrete sections in multi-span beams was demonstrated to be more advantageous given the structural redundancy of the system [49].

In recent years, researchers have proposed various ways of improving the characteristics of the hybrid system by tailoring the properties and microstructure of the composite profiles, or by using high performance or fiber-reinforced concrete layers. The behavior of hybrid GFRP-CFRP pultruded girders used in conjunction with normal strength concrete (NSC) decks [50] or ultra-high performance fiber-reinforced concrete (UHPFRC) decks [51] was assessed from flexural tests, and the conclusions indicated that the hybrid beams with NSC had a more ductile response due to the crushing failure of the concrete slab, while the ones with UHPFRC slabs exhibited a linear elastic response up to failure, accompanied by a more fragile collapse. Nonetheless, the studies showed that the use of UHPFRC is more effective in terms of structural stiffness and weight, and that the flexural capacity of the hybrid beams is still limited by the mechanical characteristics of the composite profiles or connection. Regarding the shear transfer mechanism, different connection designs were investigated for the beams with NSC slabs, as illustrated in Figure 2.13. The steel u-bolts combined with epoxy resin and gravel chips provided a more effective shear connection than that of the epoxy resin adhesive alone, by assuring a full composite action and leading to a non-catastrophic type of failure. The double-nut steel bolts also performed better than the bonded joint but the connection was less stiff than the first trialed design.

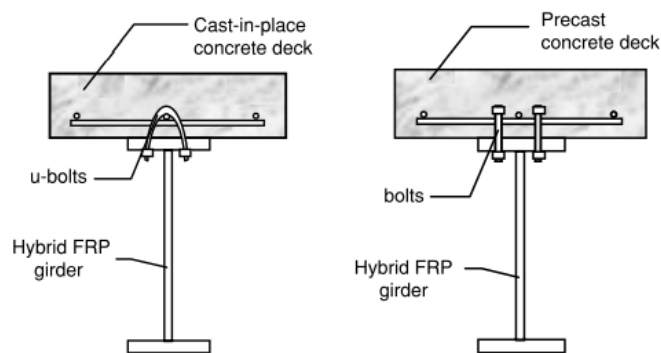


Figure 2.13: Hybrid FRP-concrete girder sections designed by Manalo *et al.* [50].

Additional information about the experimental flexural behavior of hybrid girders for prototype bridge structures with fiber-reinforced concrete decks and open section FRP profiles may be found in ref. [52–54], where various shear transfer mechanisms have also been studied.

2.3.3.3. Examples of hybrid beams with FRP box sections

In order to provide additional shear strength and torsional stiffness, hybrid beams with FRP box sections have been investigated. The downside of this type of composite member is that, compared to the beams with open section profiles, mechanical connections are more difficult to install, inspect, and replace. Even so, tests have been made also on specimens with bonded or combined joints. Initial experiments performed by Saiidi *et al.* [41] and by Kavlicoglu *et al.* [55] analyzed the flexural response of graphite-concrete beams joined with epoxy resins and observed that debonding constituted the primary mode of failure. The first study utilized double box profiles attached to concrete slabs, while the second employed an internal FRP tube surrounded by a reinforced concrete tube and by an exterior FRP U-shell. Because of the box shapes, the hybrid beams continued to work even after complete separation and total loss of composite action. Subjecting the beams to cyclic loading, Kavlicoglu *et al.* [56] noted that the epoxy interface slipped after 150,000 cycles of fatigue loading, exposing a weakness of the bond shear mechanism. Consequently, the following hybrid beam designs were built mostly with shear stud connectors.

Fam and Skutezky [46] connected rectangular GFRP profiles with concrete slabs, by means of GFRP dowels forced into pre-drilled holes in the composite top flange. In the absence of a sufficient fixity, the dowels became subjected to bending in addition to shear, and the hybrid beams ultimately failed from the loss of strength of the connection system. The authors also investigated the web buckling phenomenon, which is likely to occur in tubular shapes, and proposed a critical shear span-to-depth ratio to avoid such issues.

In recent works carried by Elmahdy *et al.* [57], and by El-Hacha and Cheng [58], the beams were constructed from a ultra-high performance concrete (UHPC) slab connected with bonded GFRP shear studs and an epoxy resin layer to a box GFRP profile that had the bottom flange strengthened with CFRP sheets or steel fiber-reinforced polymer (SFRP) sheets, as depicted in Figure 2.14. The use of advanced materials with superior strength, stiffness and durability characteristics allowed obtaining a composite section with much smaller dimensions than traditional sections.

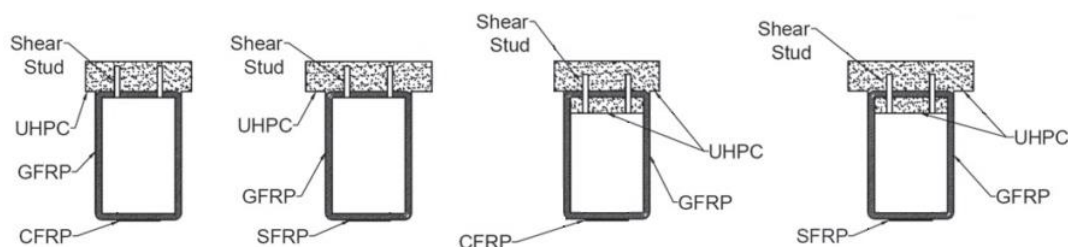


Figure 2.14: Hybrid FRP-concrete beams tested by El-Hacha *et al.* [58].

The load-midspan deflection and the strain distribution across the depth of the hybrid beams remained linear until failure and there was no slippage observed between the two parts. The failure of

the proposed designs was sudden and did not display any ductility. In addition, the members reinforced with SFRP showed better cost effectiveness than the beams reinforced with CFRP. The authors concluded that the web buckling and web-flange delamination constituted the main reasons of the collapse, and that the performance of the hybrid members is still governed by the inherent material properties of the individual components making up the cross-section.

2.3.3.4. Examples of hybrid beams with FRP shapes as concrete formwork

This type of construction technology, developed alongside the other previously mentioned hybrid member designs in the 1990s, features the FRP shape as an effective formwork for casting the concrete slab, eliminating thus the need for additional supports. Most of the hybrid cross-sections proposed have also included a thin layer of CFRP sheets or laminates bonded to the soffit of the FRP shape to enhance the beam's flexural stiffness.

At the Swiss EPFL laboratories, Deskovic *et al.* [59,60] examined the short-term and long-term behavior of a novel hybrid FRP-concrete beam design. A cost-effective solution was introduced by bonding a concrete layer on top of an outside filament-wound GFRP box profile with upper margins. Furthermore, a thin CFRP strip was attached on the tension face of the composite member. The key idea was that the hybrid beam would fail in a predetermined sequence: first the concrete top will crash, then the carbon FRP strip will fail in tension, and finally, the GFRP box will break. In this way, a pseudo-ductile and rigid structural member could be obtained compared to simple FRP profiles. The experimental results acquired from testing in flexure large scale specimens confirmed the superior performance of the innovative solution in terms of load capacity, stiffness and ductility. The study suggested that the ideal connection between GFRP and concrete should be realized by combining an adhesive layer with mechanical connectors so as to deter debonding. As for the long-term behavior, the authors concluded that the hybrid beam design was viable, obtaining good structural responses from the tested specimens.

Canning *et al.* [61] fabricated comparable hybrid structural members, and investigated the performance of six different shear transfer mechanisms which relied on indentations, horizontal bolts, adhesive bonding or resin injection. To avoid buckling, the webs were manufactured from a sandwich construction of face materials made of $\pm 45^\circ$ GFRP layers and a polymer foam core. The concrete top was restrained by the permanent shuttering of the composite shape. It was determined that the most practical technique for achieving a high composite action in the hybrid beams is by using the wet adhesive bonding method between the fresh concrete and the FRP permanent shuttering.

Two designs of FRP-concrete hybrid beams were investigated by Hulatt *et al.* [62,63], as shown in Figure 2.15. The authors studied the failure mechanisms under short-term and long-term loading, and under fatigue. The two T-shape sections described were projected to fail either by shear failure of the walls or by debonding between the concrete top and the GFRP shape. From the experimental analyses,

it was observed that both types of hybrid beams experienced a brittle failure, but none of them occurred in the adhesive layer. Furthermore, it was determined that the advanced polymeric composite had an appreciable resistance to sustained loads and fatigue, whilst the effects of the long-term loading caused a typical reduction in the properties of the concrete.

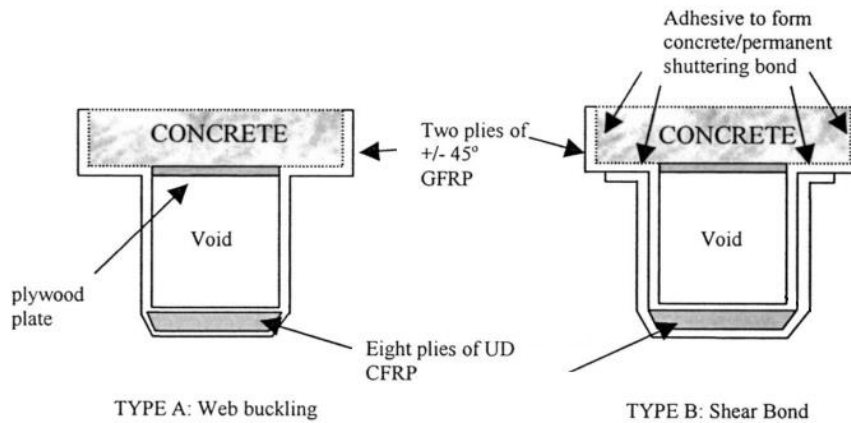


Figure 2.15: Hybrid cross-sections analyzed by Hulatt *et al.* [63].

The advantages of using FRP shapes as permanent formworks in a hybrid concept were further investigated by Bloodworth and Szczerbicki [64], Euring [65], and by Li *et al.* [66]. In recent years, however, the interest for this kind of beams has diminished as the fabrication of the assemblies requires a large amount of work and expertise.

2.3.3.5. Examples of hybrid beams with trapezoidal FRP sections

Lastly, a special category of hybrid FRP-concrete beams was created explicitly for building short-span vehicular bridge superstructures. This type of composite beams generally possess a trapezoidal FRP shape that makes part of the girder system, joined with a reinforced concrete slab at the top that serves the role of the deck system.

Mieres *et al.* [67] and Gutiérrez *et al.* [68] have detailed the characteristics, respectively the short-term behavior, of the Cantábrico highway overpass composite bridge inaugurated in 2004 in Spain. The bridge's girders were formed from carbon fibers with low elastic modulus and high strength that were pre-impregnated with epoxy resin. In addition, the trapezoidal closed section of the beams had a polyurethane core to resist web buckling. Alkali-resistant GFRP pultruded I profiles that served as shear connectors were bonded uniformly on the top of the CFRP beams, in crosswise direction. The deck was realized from cast-in-place reinforced concrete with normal strength. The outcomes of the quasi-static tests performed on independent, statically indeterminate hybrid beams indicated that the bridge design amply met the prescribed serviceability and safety criteria, and that under increasing loading, the distribution of the shear and bending moment profiles along the length of the member changed from the hyperstatic to the isostatic cases. It was observed that the dominant failure mechanisms at the reaction points and joint sections were shear controlled, and may have caused more than one failure mode,

including delamination of the reinforced concrete slab from the main load-bearing beam, joint separation, and support diaphragm buckling.

Ziehl *et al.* [69] commented on the design and field evaluation of a hybrid FRP-concrete superstructure system employed in a prototype vehicular bridge built in Texas, USA. The structure featured a succession of a dozen GFRP trapezoidal shapes with an open side at the top to allow for concrete casting. Horizontal braces were installed at the superior part of the profiles to prevent the webs from deforming. The concrete deck was then poured down to the middle of the profiles, embedding the metal braces and assuring the development of an effective composite action in the hybrid members. After two years of monitoring, the results showed no significant degradation in stiffness and composite action, demonstrating the validity and advantages of this novel construction system.

More recently, multiple studies have been conducted by Fam *et al.* [70–72] on hybrid girders in which commercially available GFRP sheet-pile trapezoidal pultruded shapes were combined with reinforced concrete, as illustrated in Figure 2.16. The authors sought to demonstrate the potential of the novel composite material in acting as the primary load-bearing material in new bridge superstructure designs.

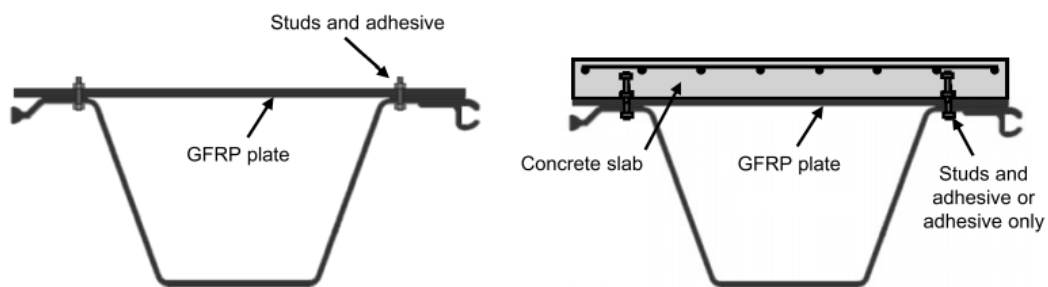


Figure 2.16: Hybrid FRP-concrete girders analyzed by Fam *et al.* [71].

Various cross-sections were investigated, where the composite shapes were filled completely or partially with concrete, and both adhesive bond and shear stud systems were trialed. The efficiency of the girders was demonstrated against that of common girders, where the new box beam was shown to have an equivalent flexural strength to similar size, heavily reinforced, conventional concrete box girders. Nevertheless, debonding represented the principal mode of failure of the hybrid beams, so further research is required on that topic.

2.3.4. Analytical design formulations

2.3.4.1. Design codes and guides

At the present time there are no European or American authoritative codes for designing structures with pultruded FRP profiles or hybrid FRP-concrete elements. Nonetheless, several guides and manuals

were published in the last decades, which amass recommended rules of good practice for FRP structural shapes generally made of thermoset resins strengthened with long glass fibers. Thus, in 1984, the American Society of Civil Engineers (ASCE) published the *Structural Plastics Design Manual* [73], followed later, in 2010, by the *Pre-Standard for Load & Resistance Factor Design (LRFD) of Pultruded Fiber Reinforced Polymer (FRP) Structures* [17]. Meanwhile, in 1996, the European Structural Polymeric Composites Group issued the *EUROCOMP Design Code and Handbook* [12] for the structural design of polymeric composites, which was intended to serve as basis for a future Eurocode. Finally, in 2008, the National Research Council of Italy published the *Guide for the Design and Construction of Structures made of FRP Pultruded Elements (CNR-DT 205/2007)* [74]. Commonly, the guides and manuals specify a design philosophy, partial safety factors or resistance factors, as well as rules and equations for the design of members and their corresponding connections in framed structures. Analytical relations are provided for the design of elements subjected to compression, tension, flexure, shear, torsion or combined loading. In addition, equations for global and local instability, vibration limits and long-term behavior characteristics are also frequently included.

Apart from the previous sources, a number of companies from the pultrusion industry have produced their own design manuals [9–11,75], some of them even preceding by several years the aforementioned guides. Usually, the manuals include the properties of the pultruded shapes sold by the manufacturers, the equations and load tables needed for design, rules and relations for bonded and/or bolted connections, fabrication and construction technique details, and environmental considerations. Most of the referred topics relate, however, with the FRP profiles produced by the companies and are not regarded as generally valid.

Design considerations for flexural and axial pultruded FRP profiles and their corresponding connections have also been discussed by Bank [1] which compared provisions for the following design bases: allowable stress design, load and resistance factor design, limit states design, and performance based design. The author indicated that even though analytical equations for conventional structural members have been thoroughly developed and validated over the years, there is less consensus over the expressions proposed for designing connections, which are still mostly empirically based. On this matter, more recently, the ASCE published the *Design Guide for FRP Composite Connections* authored by Mosallam [76] that covers design rules for bolted, adhesively bonded, and combined composite joints. As a final point, safety coefficients used in the design of FRP profile structures are likely to be changed or adjusted in the near future after additional experimental validation.

As stated before, there are no current guidelines for the design of hybrid FRP-concrete beams, and thus, the considerations provided for conventional composite beams were reviewed, with special attention to the shear connection system and partial interaction effects over flexibility.

The *fib Model Code for Concrete Structures 2010* [77] classifies the interaction between concrete and steel components in the following categories, where the choice of interaction mechanisms depends mainly on the type of structural elements and on the type of loading:

- adhesion (*i.e.*, pure bond);
- frictional interlock provided by peculiar shapes of the interface profile;
- mechanical interlock provided by specific treatments and deformations of the steel interface (*i.e.*, indentations and embossments); and
- dowel action provided by anchor devices and systems.

For steel-concrete composite beams, due to the characteristics of the connection system, partial interaction can occur at the interface between the concrete slab and the steel profile. It has been observed after numerous push-out tests that the determined load-slip relationships are influenced by many factors [78], such as:

- joint configuration;
- number, capacity and stiffness of shear connectors;
- concrete slab strength and cracking phenomena;
- size, arrangement and strength of slab reinforcement in the proximity of the connectors;
- thickness, mean longitudinal stress and degree of compaction of the concrete surrounding the connectors;
- uplift forces on the connectors; and
- chemical bond and friction.

Normally, construction codes specify design rules that aim at limiting interface shear slip, as this phenomenon strongly influences the overall structural response of composite members, especially in critical regions where high internal forces appear. Alternatively, it has been indicated that fully composite beams are not always the most efficient solution in terms of costs and that in some situations full shear connections are difficult to achieve [79]. Therefore, lower numbers of connectors may be used in design. In fact, Eurocode 4 [80] states that if all cross-sections are in Class 1 or Class 2, partial shear theory may be used for beams in buildings, but only in regions of sagging bending moment and only for equivalent spans smaller than 20/25 m. It also dictates that the calculation of stresses at the serviceability limit state must take into account the increased flexibility resulting from significant incomplete interaction due to slip of shear connection. Nevertheless, the effects of incomplete interaction may be ignored where full shear connection is provided and where, in case of partial shear connection in buildings: (i) the design of the shear connection is in accordance with the normative rules; (ii) either not less shear connectors are used than half the number for full shear connection, or the forces resulting

from an elastic behavior and which act on the shear connectors in the serviceability limit state do not exceed the connector's design shear capacity; and (iii) in case of a ribbed slab with ribs transverse to the beam, the height of the ribs does not exceed 80 mm. Under these circumstances, the deformations of a composite beam may be determined assuming a rigid shear connection. The code states that the effects on deflection of concrete cracking in hogging moment regions should also be taken into account.

Because deflections may govern design, especially when beams are built unpropped, an early draft version of the Eurocode 4, DD ENV 1994-1-1:1994 [81], offered an empirical relation for estimating the deflections of simply supported or continuous beams with partial shear connection in function of the construction method employed, when $0.4 \leq \eta < 0.5$:

$$\delta = \delta_c + c(\delta_a - \delta_c)(1 - \eta) \quad (2.1)$$

where η represents the degree of shear connection, $c = 0.3$ for unpropped construction and 0.5 for propped construction, δ_c is the deflection for the composite beam with complete interaction, and δ_a is the deflection of the steel beam acting alone. The equation was borrowed from BS 5950-3.1:1990 [82], which in its turn, adopted the method from a summary [83] of research studies performed before 1975 on this topic. The arbitrary nature of the relation, which arises from the difficulty of predicting accurately deflections in a simple manner, was the cause of its omission from the final form of the Eurocode.

In the Commentary part I3 of the current *Specification for Structural Steel Buildings* developed by the American Institute of Steel Construction, ANSI/AISC 360-10 [84], it is stated that when a composite beam is controlled by deflection, the design should limit the behavior of the beam to the elastic range under serviceability load combinations, or otherwise consider the amplification effects of inelastic behavior over deflection. The following formula is proposed therein for calculating the equivalent elastic moment of inertia of a partially composite steel-concrete beam:

$$I_{equiv} = I_s + \sqrt{\eta}(I_{tr} - I_s) \quad (2.2)$$

where I_s designates the moment of inertia for the structural steel section, and I_{tr} the moment of inertia for the fully composite uncracked transformed section.

As it is often impractical to calculate accurate flexural stiffness values that include inelastic effects, the standard states that for short-term deflections, an effective value of the moment of inertia should be used instead, as 75% of the equivalent elastic moment of inertia. The minimum degree of shear connection for the application of this formula is set to 0.25 in order to avoid excessive slippage and significant stiffness reduction.

The Australian standard for steel-concrete composite structures that deals with the design of simply supported beams, AS 2327.1-2003 [85], indicates in the normative Appendix B that the effective moment of inertia for partially composite members ($\eta < 1$) should be taken as:

$$I_{eff} = I_{tr} + 0.6(1 - \eta)(I_s - I_{tr}) \quad (2.3)$$

at the cross-sections under maximum bending subjected to short-term or long-term loads. The effective stiffness is used afterwards in estimating the magnitude of the relevant deflection components in a simplified manner, assuming a linear elastic behavior.

Other design codes have preferred to provide relations for determining the effective stiffness of composite beams in function of the flexibility of the shear connection systems. One such case is represented by Eurocode 5 [86] which introduces a simple procedure in the informative Annex B for estimating the deflections of mechanically jointed timber beams. Thus, the effective stiffness of a simply supported two-part ($i = 1, 2$) composite member is expressed by:

$$EI_{eff} = \sum_{i=1}^2 (E_i I_i + \gamma_i E_i A_i a_i^2) \quad (2.4)$$

where E_i , I_i , A_i , and a_i designate the elastic modulus of part i , the corresponding moment of inertia, the cross-sectional area, and respectively, the distance from the part's centroid to the beam's principal neutral axis. The γ_i parameter is computed from:

$$\gamma_i = \left[1 + \frac{\pi^2 E_i A_i s_c}{K_c L^2} \right]^{-1} \quad (2.5)$$

where s_c constitutes the spacing of the mechanical fasteners along the interface, K_c the slip modulus, and L the beam's span. Eurocode 5 notes that for continuous beams or other supporting conditions, the value of the span should be changed according to provisions. Furthermore, the method offered is valid only for the linear elastic analysis of composite beams with constant or uniformly varying connector spacing, and for the situations in which the vertical acting loads produce a sinusoidally or parabolically bending moment distribution.

A second example was found in the Chinese Code for the Design of Steel Structures, GB 50017-2003 [87], which proposes a different formula for calculating the deflection of steel-concrete composite beams that is also based on the elastic stiffness of the shear connection system. The code affirms that interlayer slip effects should be considered regardless of the shear capacity of the connectors installed, by using a reduced flexural stiffness. Furthermore, it specifies that partial composite design is allowed only in continuous beams with uniform cross-section and with spans ≤ 20 m, and that the reduced bending stiffness has to be applied only in sagging moment regions. Thus, the expression of the reduced flexural stiffness given is:

$$B = \frac{EI_{eq}}{1 + \zeta} \quad (2.6)$$

where EI_{eq} represents the equivalent flexural stiffness of the composite beam under complete interaction assumptions, and ζ a reduction coefficient of stiffness adapted here in a clearer form as:

$$\zeta = \frac{EI_{eq}}{EI_0} \left[\frac{7.2}{(\alpha L)^2} - \frac{54}{(0.9\alpha L)^4} \right]; \zeta \leq 0 \rightarrow \zeta = 0 \quad (2.7)$$

where EI_0 is the flexural stiffness of the composite beam considering no shear interaction, and αL the composite action parameter which will be detailed further on, in Chapter 4 of the present document.

2.3.4.2. Analytical research studies

Given the lack of guides and codes for designing and checking FRP-concrete hybrid beams, researchers have started to develop their own analytical procedures. To exemplify, Deskovic *et al.* [59] proposed a series of mathematical relations aimed to characterize the nonlinear flexural behavior of hybrid FRP-concrete rectangular beams. Equations for estimating the failure sequence, the displacements, the brittle web shear fracture and the web shear buckling load were presented and validated successfully against experimental data. The web shear buckling phenomenon was also analyzed by Fam and Skutezky [46] in a study regarding composite T-beams using reduced-scale rectangular FRP tubes and concrete slabs, and by Chakraborty *et al.* [39] in researching the performance of outside filament-wound hybrid FRP-concrete beams, with emphasis on the moment-deflection response. To add to the examples of analytical studies, serviceability and failure aspects of hybrid GFRP-concrete footbridge girders were described mathematically by Santos Neto and La Rovere [88], and by Gonilha *et al.* [53].

In all the aforementioned investigations, the effects of interlayer slip and flexibility of shear connection were neglected. In contrast, Correia *et al.* [49,89] presented analytical equations for calculating the bending responses of single-span and multi-span hybrid GFRP-concrete beams that took into account the slip strain developing at the interface and the additional deflection due to partial shear interaction. The slip strain was estimated from a formulation indicated by Knowles [90] which evaluates the property for a simply supported beam submitted to a point load. At the same time, the deflection contribution was estimated as recommended by Wang [91], from the equation of the simply supported, uniformly-loaded Euler-Bernoulli composite beam. More recently, Nguyen *et al.* [92] proposed an effective moment of inertia for obtaining the reduced flexural stiffness of special high-performance hybrid beams with mechanical shear connectors:

$$I_{eff} = I_F + \eta^2(I_{tr} - I_F) \quad (2.8)$$

where I_F designates the moment of inertia of the FRP girder, I_{tr} the moment of inertia of the fully composite FRP-concrete transformed section, and η the degree of shear connection. The equation was derived from the general form presented by Grant *et al.* [93], with $m = 2$:

$$I_{eff} = I_F + \eta^m (I_{tr} - I_F) \quad (2.9)$$

For steel-concrete girders with or without a formed steel deck, Grant *et al.* suggested $m = 0.5$, as found later in the AISC 360-10 specifications for composite beams with steel headed studs or steel channel anchors. For the partial interaction analysis of composite beams with profiled sheeting and non-welded shear connectors, Crisinel [94] indicated a unity value for m .

Many researchers have studied the problem of partial shear interaction especially for composite beams made of conventional materials like steel, concrete and timber. The first analytical relations for layered structural members were provided independently by Stüssi [95], Granholm [96], Newmark *et al.* [97], and Pleshkov [98]. The static analysis carried by Newmark *et al.* was based on the Euler-Bernoulli composite beam theory and became a basis for subsequent investigations, where the main hypothesis established states that the connection system is represented by an elastic uniform medium with constant stiffness where the interlayer shear stress is proportional to the developed interface slip. Consequently, Girhammar *et al.* [99–102] analyzed the static and dynamic behavior of beam-column elements with interlayer slip and deduced exact and simplified first and second order closed-form solutions for the displacement functions and various internal actions of composite beams. A formula for the effective bending stiffness was introduced, similar to the one presented in Eurocode 5 but with the γ_i parameter defined as below:

$$\gamma_i = \left[1 + \frac{\pi^2 E_i A_i s_c}{K_c (\mu L)^2} \right]^{-1} \quad (2.10)$$

In Eq. (2.10) the span of the beam, L , is affected by Euler's buckling length coefficient, μ , to take into consideration the correct effective length of the beam.

Researching the shear slip effects in steel-concrete composite beams subjected to positive and negative bending moments, Nie *et al.* [103–105] proposed a simplified analytical model that was validated against experimental data and design code specifications. The study revealed that a universal flexural stiffness reduction parameter can be employed regardless of the load and supporting conditions.

Faella *et al.* [106,107] developed a displacement-based finite element model for steel-concrete composite beams with flexible shear connection and a simplified analytical procedure that accounts for concrete slab cracking and the resulting tension stiffening effect, nonlinear connection behavior, and the reduction of connection stiffness in hogging bending moment regions. The simplified procedure relies on the connector's stiffness and yielding slip, and was adapted from the formula proposed by McCutcheon [108]. Nevertheless, the method has a more empirical character and thus may need further calibration. For composite beams with high strength steel, Ban and Bradford [109] suggested adopting a modified elastic modulus for the concrete slab so as to quantify for the effects of incomplete interaction.

Regarding timber-concrete composite beams with ductile connections, Frangi and Fontana [110] introduced an elasto-plastic model that is based on the capacity of shear connectors in order to avoid the difficulties in determining the stiffness of the shear transfer mechanism. The model was compared successfully to experimental data and further validated by Persaud and Symons [111].

In the previous sources, the analytical models were built on the Euler-Bernoulli composite beam theory, however, in certain situations a more accurate procedure based on the Timoshenko beam theory may be needed. In particular, Schnabl *et al.* [112] and Xu *et al.* [113,114] considered also the effect of transverse shear deformation on displacements in each layer of a composite beam and concluded that shear deformations are more important to be evaluated for two-layer beams having a high connection stiffness, high flexural-to-shear moduli ratio, and short span. Martinelli *et al.* [115] carried out a comparative study of analytical models for steel-concrete composite beams with partial interaction by employing a dimensionless formulation. Shear-rigid and shear-flexible models were considered using the Timoshenko beam theory and the study indicated possible threshold values beyond which certain effects become negligible, so that a simpler theory may be used.

To conclude, some of the formulations that were proposed for characterizing the flexural behavior of conventional composite beams may be extended in a straightforward manner and calibrated for the design of pultruded FRP-concrete hybrid beams, so as to take into account the shear interaction effects associated with the nature of the mechanical connections in such members.

2.3.5. Numerical simulations

2.3.5.1. Hybrid beam models

Although numerous experimental tests have been performed to characterize the mechanical behavior of various FRP-concrete hybrid member designs, accompanying complex numerical simulations have been rarely executed and reported. To illustrate, several relevant finite element (FE) analyses published in the last two decades are discussed in the following paragraphs.

Some of the first simulations were reported in the studies of Deskovic *et al.* [59,116], in which the numerically predicted short-term behavior of an innovative FRP-concrete beam design was compared successfully against experimental curves and analytical results. The computer model was built considering the concrete slab to be formed from eight node brick elements with isotropic material properties, and the GFRP box profile and CFRP bottom strip from thick shell elements with orthotropic elasticity. Nonlinearities were accounted for in the compressive behavior of the high-strength concrete which was modeled as a hypoelastic material with associated Mohr-Coulomb failure criterion, and in the behavior of the GFRP composite which was defined using a fourth order polynomial function derived from experimental fitting. Since the investigated hybrid beams featured combined connections, complete shear interaction was assumed in the analyses. The research showed that the predicted bending

responses were slightly more flexible and that the material axial strains were marginally higher compared to the experimental data. Apart from that, the fracture of the CFRP strips and the concrete crushing loads were determined with accuracy by the FE model.

In contrast to the previous investigation, the subsequent finite element analyses found in literature, in chronological order, were more limited in scope and were based on far simpler models. To exemplify, Sekijima *et al.* [44] compared just the experimental load-midspan deflection curve of a single hybrid GFRP-concrete beam with the numerical results from a linear elastic three-dimensional FE model, and with analytical estimations. The validation indicated that the flexural response was accurate but stiffer than in the actual test for higher loads, and demonstrated the importance of angular deformations in calculating deflections. Correia *et al.* [89,117] used also a linear elastic computational model to analyze the in-plane shear stress distribution across the web of the composite profiles, and concluded by carrying a simplified damage simulation series (with manual slab FE deletion) that the maximum shear stress occurred near the midspan for the investigated hybrid beam subjected to three-point bending. Even though the previously mentioned hybrid GFRP-concrete models had mechanical shear connectors and exhibited noticeable interface slip, the connection system and the partial shear interaction were not modeled. In a related study [48], the normal and shear stresses present at the interface of a hybrid beam with bonded epoxy connection were analyzed numerically once again on a linear elastic model made of solid finite elements. The research concluded that the experimental debonding failure occurred a few millimeters inside the concrete slab due to high stress levels developed at the extremities of the beam, and suggested that mechanical shear connectors should be installed in those sensitive areas.

More recently, numerical analyses have focused on evaluating the structural behavior of prototype footbridge superstructures with hybrid FRP-concrete girders or deck systems. A short example was found in a study by Santos Neto and La Rovere [88], where the computed flexural response of a GFRP I-shaped profile glued to a normal strength concrete slab was determined to be significantly more rigid if concrete cracking is ignored. Mendes *et al.* [52] conducted more elaborate simulations for a pedestrian bridge made of a steel fiber-reinforced self-compacting concrete (SFRSCC) deck and two GFRP girders. First of all, a parametric study of the proposed cross-section was used to identify the optimum dimensions of the members from a numerical analysis using nonlinear constitutive curves for the top concrete slab. In a second stage, the benefits of applying pretensioned CFRP strips on the bottom flange of the profiles were explored by updating a linear elastic finite element model of the entire footbridge superstructure. Regarding the connection system which comprised a continuous epoxy layer and two rows of bonded steel bolts, the numerical results showed that the differences in midspan deflections and axial stresses between the model with perfect bond and the model with interface finite elements was smaller than 2% for the discussed application. Gonilha *et al.* [53] investigated a similar structural solution of a hybrid GFRP-SFRSCC footbridge but with pretensioned steel rebars instead of CFRP strips. Nonlinearities in geometry, materials and connections were ignored in the finite element model.

The analysis offered higher deflection values for the prototype bridge and similar axial and shear stress distributions along the height of the web compared to the experimental results. The plane stress Tsai-Hill criterion was adopted to determine the failure load of the model. Subsequently, the predicted maximum load was about 13% lower than the one determined in the laboratory, as the interaction criterion actually indicates the failure initiation load and does not account for progressive damage in the composite. In the end, the calculations revealed that the shear stress contributed to almost 100% of the failure index, proving that a simpler maximum shear stress criterion could have been used in place.

One of the latest studies found in literature about simulating hybrid beams with partial shear interaction was performed by Nguyen *et al.* [54] for a girder composed of a hybrid GFRP-CFRP I-shaped profile and a ultra-high-performance fiber-reinforced concrete (UHPFRC) slab. The mechanical shear connectors were modeled discretely using a bilinear elasto-plastic constitutive law, as in the case of the reinforced concrete slab. The pretension forces in the steel bolts were reproduced within the analysis, however, the connector hole clearance was neglected which led to a stiffer numerical flexural response in comparison with the experiment. In-plane web shear stresses were underestimated because the linear elastic FRP model did not capture the progressive damage that had developed in the composite material. Slip distributions at the interface were correlated well with the analytical estimations.

The main characteristics of the referenced simulations are compiled in Table 2.2. It was noted that all the numerical models were constructed from three-dimensional finite elements that took into account shear deformations in deflection computation and that only simply supported members were analyzed. Most of the models included linear elastic material properties and had a complete shear interaction behavior although they featured mechanical connectors and interlayer slip had been observed. Regarding the geometry, in many situations only half or a quarter of the physical specimens was built in the simulations given the available symmetry conditions, so as to reduce computational times.

2.3.5.2. Conventional composite beam models

In contrast to the reduced number of published numerical studies for hybrid beams, which may be attributed to the novelty of the structural elements, conventional composite beams made of steel profiles or timber members connected to concrete slabs have seen a greater amount of investigations owing to their widespread use and longer history. Hence, in the following paragraphs, several of the relevant researches published especially in the last decade are discussed with emphasis on the modeling techniques and outcomes. These studies constitute a reliable source for developing more advanced FE simulation of hybrid FRP-concrete beams.

The referenced composite beam numerical models were all validated against experimental data and in several cases also against analytical results. All of the models took into account geometry nonlinearities, material plasticity and connection flexibility. In addition, they featured various loading

schemes, supporting conditions, reinforcement layers and profiled sheeting. Only composite beams with mechanical shear connectors are included in the analysis, where the partial interaction effects over structural behavior were considered. Thus, numerical models with bonded or combined shear connections were omitted.

Table 2.2: Summary of FRP-concrete hybrid beam finite element models.

Source	Model and software	Combined materials ^a	Connection	P.I. ^b	Finite element types and material laws
1995 Deskovic et al. [59,116]	3D nonlinear, MARC MENTAT	GFRP CFRP HSC	Epoxy adhesive layer and two rows of pretensioned steel bolts	No	<i>Slab:</i> solids; isotropic, hypoelastic with work hardening. <i>Profile:</i> thick shells; orthotropic, 4 th order polynomial function, elastic. <i>Bottom laminate:</i> thick shells; orthotropic, linear elastic.
2001 Sekijima et al. [44]	3D linear	GFRP NSC	Two rows of headed steel bolts in a cross- stitch pattern	No	<i>Slab:</i> solids; isotropic, linear elastic. <i>Profile:</i> solids; orthotropic, linear elastic.
2007 Correia et al. [89,117]	3D linear, SAP2000	GFRP NSC	Two rows of headed steel bolts	No	<i>Slab:</i> solids; isotropic, linear elastic. <i>Profile:</i> shells; orthotropic, linear elastic.
2009 Correia et al. [48]	3D linear, ANSYS	GFRP NSC	Epoxy adhesive layer	No	<i>Slab, adhesive:</i> solids; isotropic, linear elastic. <i>Profile:</i> solids; orthotropic, linear elastic.
2010 Santos Neto and La Rovere [88]	3D linear, SAP2000	GFRP NSC	Epoxy adhesive layer	No	<i>Slab:</i> solids; isotropic, linear elastic. <i>Profile:</i> shells; orthotropic, linear elastic.
2011 Mendes et al. [52]	3D linear, FEMIX	GFRP CFRP SFRSCC	Epoxy adhesive layer and two rows of redundant bonded steel bolts	Yes	<i>Slab:</i> solids; isotropic, linear elastic. <i>Profiles, bottom strips:</i> thick shells; orthotropic, linear elastic. <i>Bolts:</i> Timoshenko beams <i>Adhesive:</i> 3D interface elements
2014 Gonilha et al. [53]	3D linear, SAP2000	GFRP SFRSCC	Epoxy adhesive layer and two rows of redundant bonded steel bolts	No	<i>Slab, adhesive:</i> solids; isotropic, linear elastic. <i>Profile:</i> solids; orthotropic, linear elastic. <i>Pretensioned bars:</i> frames; isotropic, linear elastic.
2015 Nguyen et al. [54]	3D nonlinear, ABAQUS	HFRP UHPFRC	Two rows of headed steel bolts	Yes	<i>Slab:</i> solids; isotropic, bilinear elastic. <i>Profile:</i> solids; orthotropic, linear elastic. <i>Bolts:</i> connector elements; bilinear elastic load-slip curves.

^a GFRP – glass fiber-reinforced polymer; CFRP – carbon fiber-reinforced polymer; HFRP – hybrid GFRP-CFRP fiber-reinforced polymer; HSC – high-strength concrete; NSC – normal strength concrete; SFRSCC – steel fiber-reinforced self-compacting concrete; UHPFRC – ultra-high-performance fiber-reinforced concrete.

^b P.I. – partial interaction (modeled or not).

There have been several approaches in modeling conventional composite beams in function of the geometry idealization, ranging from simple to more complex simulations. One of these, proposed in a study of Liang *et al.* [118] considered the concrete slab to be discretized with thick shell elements, the steel profile with thin shell elements, and the welded steel studs with beam elements defined by a bilinear

stress-strain material law. The study investigated the strength of steel-concrete composite beams subjected to combined bending and shear, and proposed a design model for estimating the contributions of the concrete slab to shear capacity. The finite element model displayed, however, a higher yielding capacity than the experimental test. In a similar approach, Ban and Bradford [109] analyzed the flexural behavior of composite beams with high-strength steel profiles, by constructing a finite element model with shell elements. In exchange, the shear studs were idealized as connector elements with a defined load-slip behavior using Ollgaard's nonlinear empirical relation [119]. It was observed that the predicted load-deflection curves fitted well with the overall experimental responses, with higher discrepancies noticed after yielding. The relative end slip between the profile and the slab was predicted accurately for a couple of beams; however, the initial complete interaction due to friction or adhesion was not captured. Experimental slip distributions along the span of the beams were proven to be more difficult to reproduce.

Other authors have preferred to model the slabs with solid finite elements in order to depict better the nonlinear concrete behavior. Thus, Nie *et al.* [104] analyzed the stiffness and deflection of steel-concrete beams under negative bending and obtained a satisfactory agreement with experimental load-displacement curves, up to the maximum load. After that point, the stiffness degradation due to crushing was not captured by the model. Furthermore, the simulations supported that interlayer slips should be accounted for, while relative displacements between steel reinforcement bars and concrete slabs can be neglected. Queiroz *et al.* [120] advocated toward using spring elements for shear connector modeling instead of beam elements due to their definition simplicity, and explored the influence of partial interaction effects. The numerical results highlighted a good fit of the bending response and of the slip and connector force distributions along the span of the beams.

More recently, due to advances in computational power, researchers have started to model the profiles and shear connectors with three-dimensional finite elements. This approach eliminates the need for a defined load-slip behavior, replacing it with a material characteristic law that is well suited especially for situations in which push-out tests are not performed on shear connectors. Nevertheless, since a load-displacement curve may encompass supplementary interface contact effects, these would have to be defined separately for the 3D model. Tahmasebinia and Ranzi [121] validated a proposed numerical model with 3D connectors with the experimental results of various simply supported and continuous steel-concrete composite beams with or without steel profiled sheeting. The predicted load-midspan deflection charts demonstrated a good correlation with the tests, confirming the reliability of the method. Prakash *et al.* [122] built a similar fully three-dimensional model of a steel-concrete composite beam, and validated its results against experimental data. The flexural capacity of the beam was underestimated by about 10%, while the slip distributions along the span were within good error margins at initial and high loads. As a last example, Liu *et al.* [123] investigated the numerical response of steel-concrete beams with removable high-strength friction-grip bolts that were modeled with

prestressed 3D solid finite elements. The nonlinear analysis which was carried using a dynamic explicit procedure showed a good correlation with reported experimental results, in terms of load-deflection curves and interface slip variations. An additional parametric study concluded that the spacing of the bolts and the diameter of the holes have a high impact over flexural behavior, while the pretension connector force and the longitudinal rebar arrangement in the concrete slab have a minimal influence.

As an alternative method to studying the bending behavior of composite beams on three-dimensional geometries, planar finite element models were created. To illustrate, Wang and Chung [124,125] developed an advanced nonlinear model with plane stress elements, capable of simulating steel-concrete beams with flexible shear connectors and with perforated or non-perforated profile webs, subjected to hogging or sagging bending moments. The welded headed studs embedded into the concrete slab were modeled with pairs of spring elements corresponding to the horizontal and vertical directions, where the vertical springs had the same stiffness but half of the strength of the horizontal springs. Various load-slip laws for the shear connectors were trialed as enumerated: rigid, rigid-plastic, elastic, bilinear and nonlinear. The numerical results revealed little difference between the bilinear and nonlinear connector models, so the former one was recommended for further use. The outcomes of the bidimensional computer analyses compared well with the experimental load-deflection results. In a later study authored by Titoum *et al.* [126], a planar model was built for the analysis of semi-continuous composite beams with partial shear connection, where the deformational behavior of the steel studs was characterized by an idealized trilinear load-slip curve. The predicted load-deflection results and the slip distributions along the span were validated successfully against the experimental data.

To conclude the steel-concrete modeling techniques, a last example is given from a study of Chiorean [127] in which an advanced computer method is introduced for the nonlinear inelastic analysis of three-dimensional composite frame structures, where only one element is used per physical member to simulate its complex behavior under bending and axial loads. The in-house developed code accounts for shear deformations, residual stresses, second order effects, and distributed plasticity. Out-of-plane deformations (warping of cross-sections) are not considered. The partial shear connection effects were added later to the model in a study by Buru *et al.* [128], which used a fictitious degree of shear connection to replicate slip effects. The proposed numerical model was validated successfully against previously reported laboratory data and the corresponding results of other numerical models constructed using commercially available finite element analysis programs.

Regarding timber-concrete composite beams, Persaud and Symons [111] designed and tested a floor deck system comprised of a concrete slab casted on profiled steel decking joined with coach screws to glue-laminated timber beams. Two finite element models were considered in simulating the flexural behavior of the system, one consisting of bidimensional beam elements for the top slab and bottom beams, and the other of three-dimensional shells and beams. The mechanical connectors were idealized as vertical rigid links with horizontal springs defined by experimental load-slip behavior from push-out

tests. The numerical results were very close for the two models and in generally good agreement with the experimentally registered data. The simulated load-deflection responses were appropriate up to half of the sustained load, and more unconservative after by neglecting concrete cracking effects. Ultimate loads were predicted well in function of the calculated tensile stresses, while the relative interface slips were overestimated at initial loads due to adhesion, and undervalued at higher loads. In preference to the spring representation, Oudjene *et al.* [129] used beam elements with elasto-plastic definition for modeling screwed timber-to-concrete composite connections. The predicted responses matched closely the laboratory tests.

To add, following the discussed numerical models of conventional composite beams, it was noticed that several conditions emerged for establishing the ultimate sustainable load: maximum compressive strains in concrete slabs; maximum tensile or flexural strains in profiles; connector failure criteria (shear capacity or maximum slip); and excessive deformation limits. It was also observed that establishing an exact load associated with concrete crushing is challenging from a numerical point of view. All in all, each modeling technique brings with it certain advantages and disadvantages, in the sense that there is no preferable established approach.

2.3.5.3. *Material constitutive laws*

With respect to the material modeling of the hybrid beams, several constitutive laws were extracted from the literature review.

For instance, the composite profiles were assigned a linear elastic orthotropic definition in almost all situations, to account for the specific behavior of the material in the principal directions. All the analyzed studies considered homogenous properties for the whole cross-section, or separately, for the flanges and webs.

The largest differentiation in material modeling appeared to be related to the complex, nonlinear behavior of concrete. To detail, the compressive inelastic behavior was simulated using experimental curves from uniaxial tests or empirical relations adopted from design codes and published extensive investigations. Generally, the mathematical curves were divided in two segments, the first being associated with a linear elastic response, up to a designated limit of proportionality, and the second with a nonlinear plasticity curve. Various formulations were used by authors in their numerical models, ranging from the quadratic expression of Eurocode 2 [130] implemented in [109,126] and exemplified in Figure 2.17, to Hognestad's curve [131] found in [127,128,132] and Rüsçh's parabola-rectangle law [133] utilized in [134] and illustrated in Figure 2.18. Other studies have used the proposed stress-strain relation of Carreira and Chu [135] for plain concrete, as seen in [118,122,129], or the nonlinear relation introduced by Hsu and Hsu [136] for high-strength concrete.

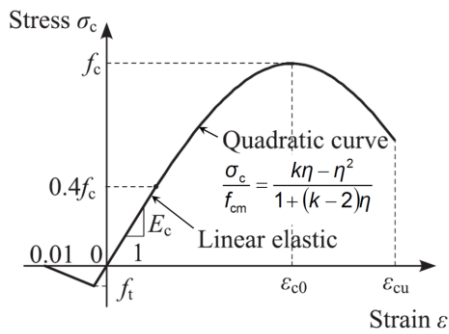


Figure 2.17: Uniaxial stress-strain curve of concrete, adapted from [109]. Compressive curve model from Eurocode 2.

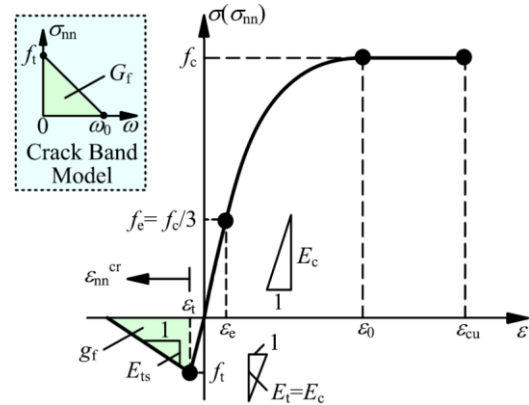


Figure 2.18: Uniaxial stress-strain curve of concrete, adapted from [134]. Rüsçh's compressive parabola-rectangle curve.

It was observed that a significant number of finite element analyses were carried out using the *concrete damage plasticity* (CDP) model available in *Abaqus FEA* software [137], which combines concepts of isotropic damage elasticity with isotropic tensile and compressive plasticity, and assumes two failure mechanisms in the concrete: tensile cracking and compressive crushing. The built-in model adopts the yield function proposed by Lubliner *et al.* [138] with the adjustments made by Lee and Fenves [139] for taking into account the different strength development under tension and compression, and assumes a Drucker–Prager hyperbolic function as non-associated flow rule. The main advantages of the CDP model are the fact that is based on parameters having an explicit physical interpretation and that it provides a general capability for the analysis of concrete structures under monotonic, cyclic, and/or dynamic loading. Furthermore, the model can reflect the stiffness degradation mechanisms related with the permanent damage that takes place during the fracturing process. The parameters and application considerations for the CDP model in simulating reinforced concrete or composite steel-concrete beams were studied in more detail in [140–142].

An alternative method for modeling the behavior of the reinforced concrete slabs was represented by the *concrete smeared cracking* model [137] which is designed for applications in which the material is subjected mainly to monotonic straining at low confining pressures and where cracking is assumed to be the most important aspect of the flexural response. The discussed model consists of an isotropic hardening yield surface that is active when the stress is dominantly compressive and an independent crack detection surface that determines if a point fails by cracking. Due to the tensile loss of capacity, the shear stiffness reduction may be simulated by altering the concrete's shear modulus in function of the opening strain across the crack. The smeared cracking method was found implemented in [109,118,134,143,144] for steel-concrete composite beams.

Both in the damaged plasticity model and in the smeared cracking model, the concrete behavior is considered independently from the reinforcement behavior, and thus, the effects associated with the

reinforcement-concrete interface, such as the bond or slip, can be modeled approximately by introducing tension stiffening in the constitutive curve to simulate the load transfer mechanism between cracks through the reinforcement bars. If these effects are ignored, the stiffness of the structural element may be underestimated.

Regarding the numerical definition of tensile behavior for concrete, although the post-cracking response can be defined by a stress-crack width relationship in order to reduce the mesh sensitivity of the calculations [134], the majority of the finite element analyses have employed stress-strain curves. The basic tensile models, such as the ones previously seen in Figure 2.17 and Figure 2.18, have featured a triangular relation where after the tensile failure, the strain softening reduces the stress linearly to zero. Wang and Hsu [145] have assumed that the total strain reached is 10 times larger than the failure strain for reinforced concrete beams, while other studies have suggested a total value of 0.1 [118,123] or 0.01 [109,146] for steel-concrete composite beams.

More advanced nonlinear tension stiffening formulas were proposed by Gilbert and Warner [147], Vecchio and Collins [148], or Belarbi and Hsu [149], following extensive investigations. The strains used for the stress-strain relationships described are average strains, in the sense that they combine the effects of local strains at cracks, strains between cracks, bond-slip behavior, and crack slip. Correspondingly, the stresses are also average stresses as they implicitly include stresses between cracks, stresses at cracks, interface shear on cracks, and dowel action [150]. One such example of a nonlinear tensile response model for concrete, as implemented by Chiorean [127], is illustrated in Figure 2.19. Adjacently, in Figure 2.20, the tensile stress-strain relationship proposed by Wahalathantri *et al.* [151] is included, as derived from the research performed by Nayal and Rasheed [152] which have deducted through an inverse numerical-experimental approach a tension stiffening model for concrete beams reinforced with steel and fiber-reinforced polymer (FRP) bars.

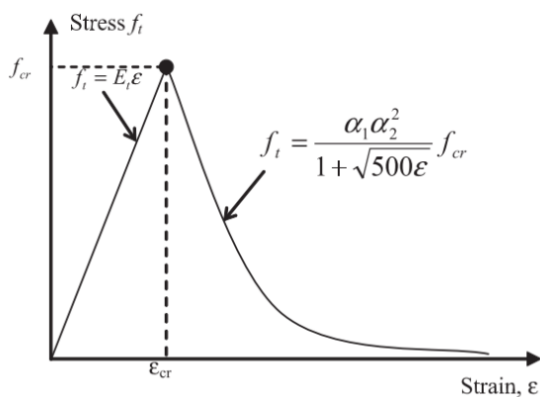


Figure 2.19: Tensile stress-strain relationship of concrete simulated in [127].

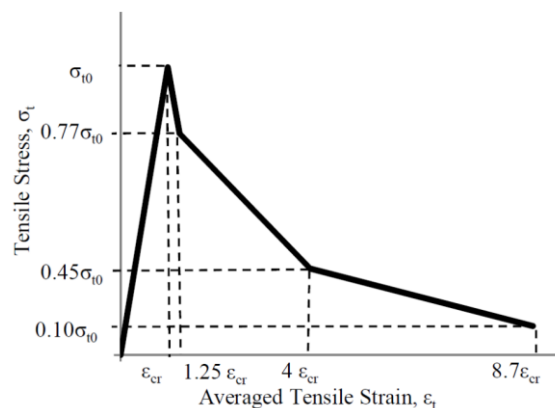


Figure 2.20: Tensile stress-strain relationship of concrete introduced in [151].

From the reviewed bibliography, the reinforcement bars acting in the concrete slabs were mainly modeled as smeared layers or individually embedded finite elements with axial stiffness. The rebars were associated with metal plasticity models that had a generally bilinear behavior.

Finally, the shear connectors in the hybrid/composite beams were modeled with experimental or mathematical force-slip or stress-strain relationships. The latter method was used predominantly for three-dimensional representations, while the former was more common and more preferred from a computational point of view. Force-slip variations ranged from simple linear elastic models [52,125] to bilinear [54,118,121], trilinear [123,126,153] or completely nonlinear representations [104,109,120,128]. Figure 2.21 and Figure 2.22 exemplify the trilinear, respectively the nonlinear definition of interlayer shear transfer behavior.

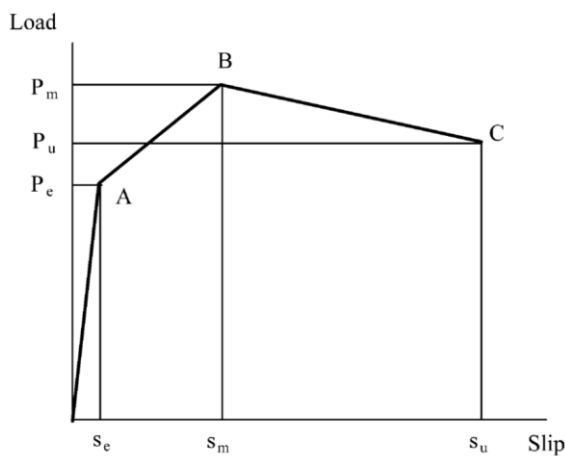


Figure 2.21: Idealized trilinear shear connector force-slip relationship from [153].

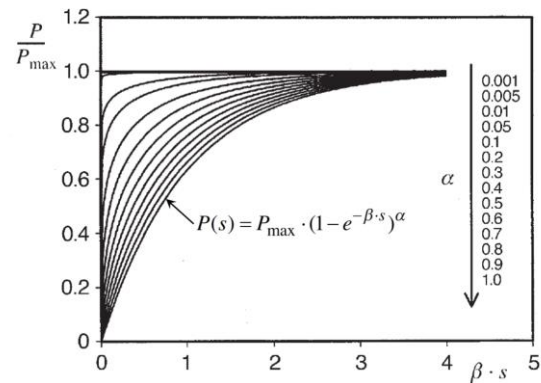


Figure 2.22: Exponential force-slip relationship for steel studs, adopted from Model Code 2010 [77].

2.4. Summary and research needs

Modern composites made of fiber-reinforced polymers (FRPs) have been successfully employed in the last decades in an increasing number of rehabilitation projects and new civil engineering applications owing to their exceptional mechanical and physical properties. FRP profiles have been used especially in infrastructure works, however, their expansion is still impeded by the high deformability, secondary failure modes and brittle behavior that they possess. Thus, a recent tendency was distinguished of designing and using this type of composites in conjunction with traditional materials, such as concrete, to form hybrid structural members with superior characteristics that alleviate some of the problems of using FRP profiles alone. The novel FRP-concrete members exhibit high structural efficiency, great durability, better stiffness and damping, increased stability, and a more rational cost-performance ratio.

A review of the past and existing hybrid beam designs has revealed that the large majority of the solutions have been implemented in prototype or pilot projects, and therefore, there is still a great need for additional experimental results. Although there have been numerous designs proposed and investigated, the most common type of cross-section encountered resembles conventional composite beams with open section profiles and top concrete slabs given their lower cost, design familiarity and ease of connection. Moreover, in most cases the composite shapes were fabricated from pultruded glass FRP (GFRP), for the same economic reasons.

From the bibliographic research on several of the most representative experimental investigations published in this field, the following main observations were extracted:

- Hybrid beams made of normal strength concrete or fiber-reinforced concrete displayed better ductility than the ones made of high strength concrete which showed mostly a linear elastic response and fragile failure modes. Metallic connectors were also preferred over composite connectors for the same engineering logic.
- The shear connection system plays a key role in the structural performance of FRP-concrete beams as joints in this type of combined elements are found to be substantially more flexible. Because of this, interface slip was detected experimentally in many situations, however, its impact on the flexural response was generally overlooked. Slippage was found to be more substantial for hybrid beams with mechanical shear connectors.
- Specimens with bonded joints demonstrated higher flexural stiffness than hybrid beams with mechanical joints but lower ultimate capacity as they suffered from premature failures caused by shear debonding at the interface. Furthermore, because adhesive joints require special application conditions and have a more limited durability, supplementary shear anchorages are indicated to be installed, increasing thus the cost of the hybrid solution.
- Often times the ultimate capacity of the members was limited by the characteristics of the FRP profiles and connection systems.

Secondly, from an overview of the related available design codes and guides, and of the published analytical relations for hybrid beams and conventional composite beams, the subsequent remarks were made:

- There are currently no authoritative codes on the design of structures built with pultruded FRP profiles or hybrid FRP-concrete members. There is also a lack of proper standardization regarding the dimensioning and properties of pultruded composite shapes.
- The majority of the reported analytical models for FRP-concrete beams have neglected the effects of interface slip in evaluating thoroughly the complete flexural behavior by considering a state of full shear interaction which proved to be severely unconservative in certain situations.

Only recently the problem has begun to be studied, although in a more superficial manner than for steel-concrete composite beams, for instance.

- Design codes for conventional composite beams state that slip effects over flexural performance and stress distributions at the serviceability limit states should be accounted for. On this subject, most of the codes and guides offer empirical or approximate relations for calculating deflections or effective beam stiffness values, which are either based on the degree of shear connection or on the connection's shear modulus.
- An appropriate analytical procedure for the design of hybrid beams would have to be based on Timoshenko's composite beam theory and on Newmark's hypotheses for two-layer composite beams in partial interaction.
- Since precise analytical formulations are too complex for day-to-day office use, simple, approximate formulations are needed as an alternative to account for partial interaction effects, which have to be validated against existing code relations and available experimental data.

Lastly, from a comparison of published numerical finite element models used for simulating the flexural response of hybrid beams and conventional composite beams, several conclusions ensued:

- Reported numerical simulations of FRP-concrete beams have been extremely limited and have frequently relied on simplified assumptions. To detail, most of the models were based on linear elastic material stress-strain relations, have considered the concrete and composite parts to be perfectly bonded and have ignored geometry nonlinearities, leading in consequence to inaccurate results. Meanwhile, conventional composite beams have received a greater amount of attention, where more complex simulations and various modelling techniques were trialed.
- Nonlinear analyses are especially needed for hybrid beams with pseudo-ductile failure modes and mechanical shear connectors. The computer predictions should be capable of capturing the influence of partial interaction effects over flexural behavior, and should be validated against experimental data and analytical estimations.
- It is preferable to model shear connectors with nonlinear springs defined by a force-slip relation instead of three-dimensional finite elements based on stress-strain curves, as the interface behavior in hybrid beams depends on a large number of factors apart from the materials' constitutive properties.
- There have been numerous constitutive laws proposed and employed for modelling concrete, nevertheless, the majority of them rely on a damage plasticity model that accounts for crushing and cracking phenomena. Furthermore, the effects of the reinforcement-concrete interface were predominantly replicated with tension stiffening models.

To summarize, the observations derived from the preceding state of the art highlighted the need for supplementary experimental tests carried on hybrid FRP-concrete beams with mechanical shear connectors, with special emphasis on the flexibility of the connection system and its effects. Corresponding advanced analytical and numerical models are also required for estimating thoughtfully the structural performance of these novel members.

3

Experimental campaign

3.1. Introduction

Current research indicates that there is still a great need to investigate experimentally the flexural behavior of pultruded FRP-concrete hybrid beams and to find structural solutions with lower costs. Furthermore, to this point, many studies have limited their analyses by considering a state of complete shear interaction although slip phenomena had been previously observed during testing.

The investigation discussed in this chapter focuses on the analysis of the experimental structural performance of hybrid beams made of pultruded glass fiber-reinforced polymer (GFRP) profiles mechanically connected to reinforced concrete (RC) slabs, suitable for building floors as well as footbridge and marine pier superstructures. The proposed hybrid system is designed to exploit the main advantages of its composing materials whilst overcoming some of the issues that characterize their individual behavior. Thus, the GFRP members are expected to carry mainly the tensile and shear forces in the composite beam, with the concrete layer acting as a compressive and stabilizing top element. Commercially available profiles were used in order to reduce costs and normal strength concrete was chosen so as to improve the ductility of the beams. Due to the hybrid nature of the constructive system, special attention was also paid to the influence of the mechanical joint between the two constitutive parts, by considering a low degree of shear connection. Thus, the effects of partial interaction over flexural behavior, failure modes, internal normal and shear stress states, and composite action could be evaluated.

Following the results and observations of an initial experimental campaign carried out on small-scale hybrid beams with various cross-section configurations [154], a hybrid system similar to standard steel-concrete composite beams was selected as design basis for a second and more comprehensive experimental campaign performed on real-scale specimens. A number of eight hybrid beams were fabricated and their flexural behavior was assessed against that of equivalent reinforced concrete beams and single GFRP structural profiles. The variables of the research were the type of hybrid cross-section and the concrete strength class. The experimental campaign was divided in two phases depending on the specific test setup configuration, and observations were made regarding the

short term behavior of the novel elements under positive bending moments. However, before the main flexural tests were performed, the materials used throughout the investigation were analyzed in a succession of destructive and nondestructive characterization tests. The results obtained are accompanied in advance by the description of the procedures and methodologies employed.

All the experiments discussed in the following sections were executed by the author at the Laboratory for the Technological Innovation of Structures and Materials (LITEM) from Universitat Politècnica de Catalunya – BarcelonaTech, under room temperature and normal relative humidity conditions.

3.2. Materials

3.2.1. Composite profile

Since one of the purposes of the experimental campaign was to develop a better cost-effective hybrid FRP-concrete structural solution, design began with choosing an off-the-shelf glass fiber-reinforced polymer (GFRP) pultruded profile with high performance characteristics and qualities. The composite beams selected were manufactured by GDP S.A. in France and supplied by Composites ate S.L. from Spain.

During a previous small-scale comparative experimental study it was found that a hybrid beam design with features similar to common steel-concrete beams, made of an I-shaped profile and a reinforced concrete slab, displayed the best results among the hybrid designs trialed. Therefore, the composite shape chosen for the real-scale experimental campaign was an IPE 120 profile classified as structural and with the following nominal dimensions: 120 mm in height, 60 mm in flange widths and a thickness of the web and flanges of 8 mm, as seen in Figure 3.1. It is noted that the FRP profile is stockier than its steel IPE 120 counterpart, especially in the web. The transition between the flanges and the web had a 5 mm fillet radius. Profiles came in batches of 3 meters (Figure 3.2), and were later adjusted to the desired testing length.

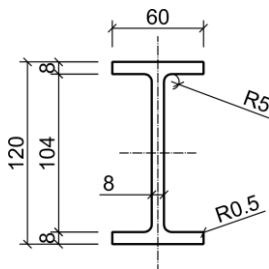


Figure 3.1: Cross-section geometry of the GFRP IPE 120 pultruded profile.



Figure 3.2: GFRP profiles used in the experimental campaign.

The composite profiles were made from a PR500 grade thermosetting unsaturated polyester matrix with basic formulation, reinforced with E-glass fibers. A visual inspection of the transverse section shown in Figure 3.3 reveals a well-structured, highly inhomogeneous symmetrical assembly of unidirectional fibers which act as longitudinal reinforcement, and non-woven continuous strand mats (CSM) disposed on the contour of the shape and at the center plane of the web which perform the role of shear, transverse reinforcement. The mats were made of the same type of fibers but arranged in a multidirectional pattern. The exterior CSM was covered with a thin polymeric, transparent surface veil that provides mechanical and chemical protection.

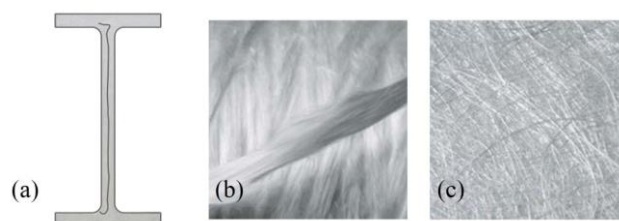


Figure 3.3: Internal macrostructure of the GFRP profile: (a) cross-section layers (emphasized colors); (b) fiber rovings; (c) non-woven continuous strand mats (CSM).

The anisotropic nature of the composite material was further analyzed with help from the Electron Microscopy Service of UPC, under a JEOL scanning electron microscope (model JSM-5610). A sample of the profile's flange was extracted manually, peeled of its veil and examined. The pictures revealing the composite's microstructure are shown in Figure 3.4. Both unidirectional and multidirectional fibers were visible as well as fragments of the polyester resin. The diameter of a single glass fiber appeared to be around 30 μm .

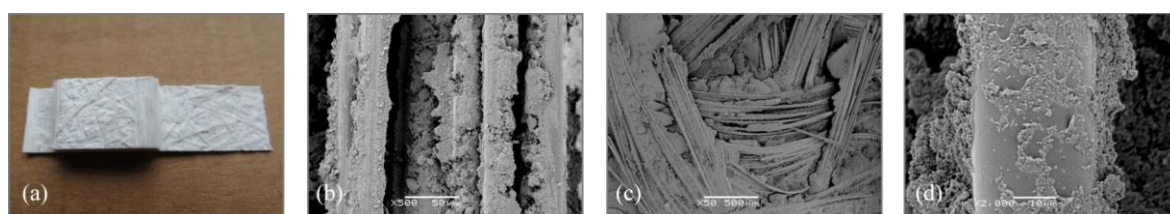


Figure 3.4: Internal microstructure of the GFRP profile: (a) flange sample; (b) unidirectional fibers; (c) multidirectional fibers (CSM); (d) a single glass fiber covered in resin.

A sample of the web-flange junction of the pultruded profile was also analyzed under the microscope. The images presented in Figure 3.5 highlight the dichotomy of the structure at the mid-plane level, where the white continuous multidirectional fibers are positioned alongside the grey unidirectional fiber rovings. The cross-section of the longitudinal fibers, although transparent, appears grey due to the way light is reflected inside of them. The deepest transverse scan also exposed the existence of microscopic structural pores that arise during fabrication and curing that may possibly weaken the profile. Under all these circumstances, the web-flange junction transition area appears to be a region susceptible to failure, as it was confirmed by the full-scale experimental tests.

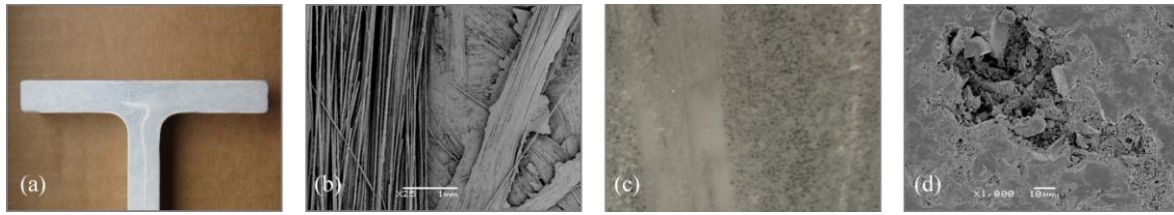


Figure 3.5: Internal microstructure of the GFRP web-flange region: (a) junction sample; (b) lengthwise view; (c) transverse view; (d) structural pores.

The main physical, mechanical and electrical properties of the pultruded GFRP bars and profiles given by the manufacturer are summarized in Table 3.1. The reported values are suggested to be taken only as a guide.

Table 3.1: Declared properties of the GFRP PR500 pultruded shapes.

Property	Bars	Profiles	Units	Testing method
<i>Physical</i>				
Reinforcement rattling in weight	70-80	50-65	%	EN ISO 1172
Apparent density	2.0	1.8	kg/dm ³	EN ISO 1183-1
Barcol hardness	45/50	45/50		EN 59
Water absorption	1.50	1.50	% in weight	EN ISO 62
Coefficient of linear thermal expansion	5.4·10 ⁻⁶	9·10 ⁻⁶	/°C	ISO 11359-2
Thermal conductivity	0.3	0.15	W/K·m	ASTM C117
<i>Mechanical</i>				
Tensile strength	690	207	MPa	EN ISO 527-4
Modulus of elasticity	41.4	17.2	GPa	EN ISO 527-4
Flexural strength	690	207	MPa	EN ISO 14125
Shear strength	35	35	MPa	EN ISO 14130
Compressive strength	414	276	MPa	EN ISO 14126
<i>Electrical</i>				
Dielectric strength	2360	984	kV/m	ASTM D149
Resistivity	10 ¹²	10 ¹²	Ω·m	CEI 60093
Arc resistance	120	120	s	ASTM D495

Due to the lay-up configuration of the profile in webs and flanges, results differ between coupon tests and full-section tests. In addition, it is not possible to predict any of the values from data obtained from a different test mode or test direction. According to the spreadsheet, the glass fiber-reinforced profiles meet the minimum structural requirements of grade E17 indicated by EN 13706-3:2002 [16].

Regarding the thermal properties, the manufacturer states that the pultruded shapes can be used without any restriction between -20 °C and +80 °C. For harsher conditions, below -20 °C and between +80 °C / +200 °C, special formulations are required. The coefficient of thermal expansion of the GFRP profiles lies between 8-10·10⁻⁶/K, which is ideally similar to the coefficient of reinforced concrete structures.

The PR500 grade profiles utilized in the investigation have a thermal endurance class “B” (130 °C) and a limited oxygen index in the axial direction of 30-35%, and in the transverse direction of 25 to 30% (NFT 51-071). Their flame resistance to an incandescent filament during 30 seconds at 960 °C (NFT 20 455 20 455) suggests an extinction time of less than 5 seconds. In what concerns the chemical resistance of the GFRP profiles, the details provided are given in Table 3.2. Higher environmental protection could be achieved by using a vinyl ester matrix in the composition.

Table 3.2: Declared chemical resistance of the GFRP PR500 pultruded shapes.

Chemical resistance	Grade
Resistance to acids	Very resistant
Resistance to bases	Resistant
Organic solvents	Not recommended
Chlorinated solvents	Not recommended
Sea water	Very resistant
Petrol/Diesel oil	Very resistant
Industrial detergents	Excellent resistance
Weathering	Excellent resistance

The composite profiles selected for the tests exhibit a linearly-elastic behavior and are especially recommended for applications that involve either cyclical mechanical stresses or vibrations, or repeated impacts. Bending tests performed by the producer indicate a 10% slight decrease in the elastic modulus after 500.000 cycles under imposed elongation at 80% ultimate stress, with a frequency of 10 Hz.

Given the fact that the mechanical properties declared by the manufacturer were incomplete, have an informative nature and could have been adjusted with safety coefficients, in the first stage of the research the pultruded FRP product was subjected to an extensive campaign of characterization tests. Some of the mechanical properties were evaluated in both axial and transverse directions of the composite shape due to the transverse isotropy (*i.e.*, a particular case of orthotropic materials which possess a plane of symmetry).

Before the mechanical characterization tests, the density of the profiles was reevaluated by weighing and measuring five specimens. The determined apparent density was found to be 1.93 kg/dm³, higher than the corresponding value prescribed in Table 3.1.

The flexural, tensile, compressive, shear and full section properties were obtained by the author, from the experimental tests illustrated in Figure 3.6, following relevant standardized principles and methods specified in CEN, ISO and ASTM International standards. Appendix A of the current document contains the detailed reports of the characterization tests – including scope, principles, testing procedures, results and observations – of over 40 specimens.



Figure 3.6: GFRP profile material characterization tests: (a) flexure; (b) tension; (c) in-plane compression; (d) interlaminar shear; (e) in-plane shear; (f) full section effective moduli.

Flexural properties were obtained by deflecting simply-supported coupons in a three-point bending configuration setup, at a constant rate until they fractured. During the procedure, the force applied to the specimens and the bottom longitudinal strains were measured. In the tensile tests, a specimen was extended along its major longitudinal axis at a constant speed until it ruptured. The load sustained by the coupon and the lengthwise and crosswise elongations were measured. For the compressive trials, an axial force was applied to the unsupported length of a rectangular specimen held in a loading fixture while the applied load and axial strain were recorded. The loading fixture was designed by the author based on the recommendations presented in the informative Annex C of ISO 14126:1999, and served further for the in-plane shear tests. The standard's informative annex references similar compressive fixtures from ISO 8515:1991 and ASD-STAN prEN 2850.

The interlaminar shear strength was determined straightforward using the short-beam method, in which a bar of rectangular cross-section is loaded over a small test span as a simple beam in flexure so that interlaminar failure occurs in the matrix layer. In exchange, determining the in-plane shear strength proved to be more contentious, requiring an adaptation of the ASTM D 3846 method suggested in [10]. Basically, in this case, the strength is defined as the shear stress at rupture in which the plane of fracture is located along the longitudinal axis of a specimen, between two centrally positioned notches machined halfway through its thickness on opposing faces.

Lastly, in order to determine the flexural moduli, pultruded profile specimens were repeatedly loaded in an elastic manner as simple beams in three-point flexure, over a number of different decreasing span lengths. Because the bending and shear contributions to the overall beam deflection vary with each test span, the elastic moduli can be obtained using a linear regression analysis of the bending equation.

In the course of the iterative procedure, the force applied to the specimen and the resulting deflection were measured. Table 3.3 summarizes the main results of the mechanical properties post-processed in Appendix A, together with their corresponding standards for determination.

Table 3.3: Experimentally determined mechanical properties of the GFRP profile (average \pm standard deviation values).

Mechanical property	Value	Units	Testing method
<i>Flexural</i>			
Ultimate strain	2.10 \pm 0.05	%	EN ISO 14125:1998 [155]
Strength	734 \pm 39	MPa	
Modulus of elasticity	35.0 \pm 2.1	GPa	
<i>Tensile</i>			
Ultimate strain	1.37 \pm 0.11	%	EN ISO 527-1:2012 [156] EN ISO 527-4:1997 [157]
Strength	520 \pm 27	MPa	
Poisson's ratio ^a	0.27 \pm 0.02		
Modulus of elasticity	38.0 \pm 1.4	GPa	
<i>Compressive - lengthwise</i>			
Ultimate strain	1.02 \pm 0.11	%	EN ISO 14126:1999 [158]
Strength	406 \pm 30	MPa	
Modulus of elasticity	40.6 \pm 1.8	GPa	
<i>Compressive - crosswise</i>			
Ultimate strain	1.60 \pm 0.13	%	
Strength	115 \pm 3	MPa	
Modulus of elasticity	10.8 \pm 0.5	GPa	
<i>Shear</i>			
Apparent interlaminar strength	31.1 \pm 0.7	MPa	EN ISO 14130:1997 [159]
In-plane strength ^b	49.0 \pm 4.7	MPa	ASTM D 3846-08 [160]
<i>Full-section moduli</i>			
Effective flexural modulus	39.1 \pm 0.14	GPa	EN 13706-2:2002 [15]
Effective shear modulus	3.98 \pm 0.26	GPa	

^a determined for the axial-transversal case.

^b coupons rotated 90°.

A few observations are important to be made regarding the experimental characterization. The method for determining the flexural properties and interlaminar shear strength are not appropriate for the determination of design parameters although they may be used instead for screening materials or quality-control tests. As such, the evaluation of the flexural modulus of elasticity does not account for the shear contribution to deformation and thus the resulting value is less than in reality. Nevertheless, the standard suggests various test span/specimen dimension ratios that minimize this effect and inhibit the development of an interlaminar shear failure. Secondly, the interlaminar shear strength is not an absolute value due to the fact that the shear stress distribution in this case is notably different than the parabolic distribution described by the elasticity theory in cross-sections sufficiently distanced from the supports and the load-application areas. For this reason the term “apparent interlaminar shear strength”

is used. Although manufacturers usually report the interlaminar shear strength of composite shapes, the in-plane shear strength is generally not included due to the difficulty of its evaluation. Considering that the in-plane shear strength can be much greater than the interlaminar shear strength [161], evaluating the shear capacity of a fiber-reinforced pultruded profile solely on the latter property will yield very conservative results. There is currently no European standard that deals with this matter for composites made from multidirectional fibers or combinations of continuous and multidirectional fiber systems. Opposed to using the method specified in ASTM D 3846, other authors have evaluated the in-plane shear strength using tensile tests on double-lap joints [48,162] or the 10° off-axis test [163–165]. The specimen preparation in both cases is fairly complex and the latter method is only suitable for continuous aligned fibers. The 10° off-axis method tends to underestimate the ultimate shear strength and strain due to the combination of transverse tensile and shear stresses [166]. Consequently, there is an important need that has to be addressed, to develop a standardized European testing method to effectively evaluate the in-plane shear strength of FRP pultruded profiles.

3.2.2. Reinforced concrete section

The pultruded GFRP profiles previously described were to be used in conjunction with reinforced concrete sections for the design of the hybrid beams. Normal strength concrete was preferred so as to alleviate the costs of the hybrid solution and more importantly to improve its flexural ductility.

In particular, the type of concrete indicated to the manufacturer, Paver Prefabricados S.A., was according to the EHE-2008 Spanish Code [167] HA-25/F12/I. This type of concrete has a characteristic compressive strength of 25 MPa, a fluid consistency, a maximum aggregate size of 12 mm and is suited for structural members to be tested in non-aggressive environments, as in this case an indoor laboratory facility. After casting took place, the producer provided a detailed inform regarding the determination of the compressive strength on concrete specimens, shape dimensions, curing and other requirements that were followed. In this matter, UNE standards EN 12350-1:2006, EN 12390-2:2006 and EN 12390-3:2003 were abided by the builder.

The concrete was prepared in two different batches due to the number of special molds required. Plasticizer additives were added and a rapid hardening cement type CEM II/A was incorporated, class 42.5 R. The water-cement ratio was 0.53 and the measured average consistency of the samples was 8.0. Concrete compressive strength tests were performed by the producer 28 days after fabrication, for both batches, on 150 mm cubic specimens. Table 3.4 reports the average compressive strength of the two concrete mixes. The average values obtained were higher than the characteristic value indicated by the type of concrete.

Table 3.4: Concrete compressive strength characterization results.

Specimen	Concrete mix (batch)	Compressive strength (MPa)	Average compressive strength (MPa)
1	C1	30.59	30.05
2		29.43	
3		29.16	
4		31.01	
1	C2	35.21	34.98
2		35.21	
3		34.50	
4		34.99	

Since the theoretical assessment of the hybrid beams' flexural performance necessitates knowing additional mechanical properties of the concrete sections, the elastic modulus and average tensile strength of the two concrete mixes were evaluated using the empirical relations provided in Eurocode 2 [130]. The calculated values are given in Table 3.5.

Table 3.5: Mechanical properties of concrete mixes.

Concrete mix	Average compressive strength cube / cylindrical (MPa)	Elastic modulus (GPa)	Average tensile strength (MPa)
C1	30.05 / 24.04	28.6	1.90
C2	34.98 / 27.98	30.0	2.21

Steel reinforcement bars were used only with constructive role in building the full-scale beams. The rebars were made of steel class B500S which has a nominal yielding strength of 500 MPa, modulus of elasticity of 200 GPa, and tensile strength of 550 MPa.

3.2.3. Shear connectors

The hybrid beam design required a mechanical connection system between the GFRP pultruded profile and reinforced concrete section. The shear transfer mechanism had to be flexible enough that shear partial interaction would be visibly noticeable to be studied. Therefore, the selected connectors were M6 steel bolts with a class resistance of 8.8, and a total length of 38 mm ($> 4 \cdot \text{diameter}$). The nominal shear strength of the bolts was 480 MPa.

3.3. Hybrid beam models and fabrication

For the main experimental campaign, two hybrid GFRP-concrete beam models were designed to be investigated. Entitled M1 and M2, the models differed in the type of concrete cross-section geometry.

In addition to these two, an equivalent reinforced concrete model designated M0 was included to serve as reference in the analysis. All members had 2000 mm in length and 170 mm in height, with a top concrete slab of 400x50 mm. Figure 3.7 illustrates the constructive details of the specimens.

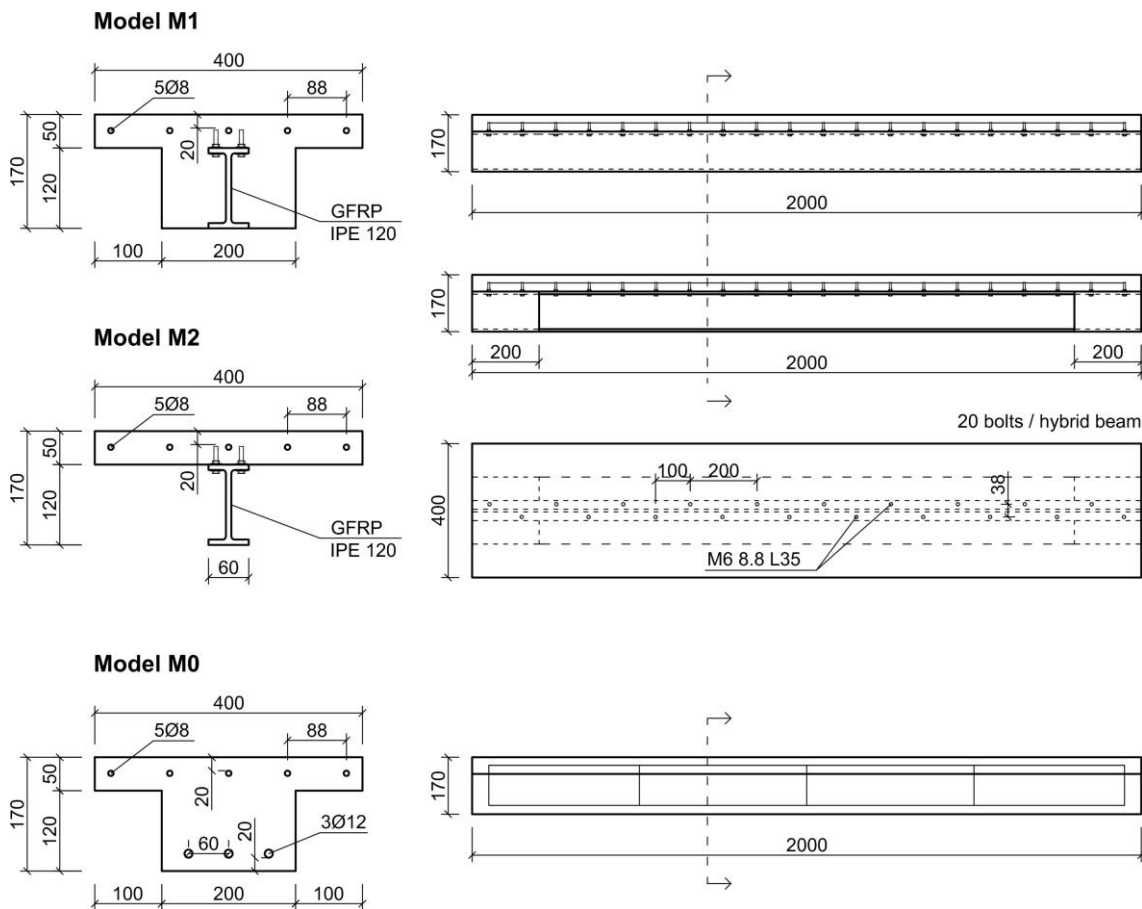


Figure 3.7: Constructive details of the proposed models: cross-sections, lateral views and combined top view of M1 and M2 hybrid beams (mm) – not to scale.

All hybrid beams were made of a GFRP profile attached to the bottom side of a concrete slab by means of steel shear connectors. In contrast to model M2, model M1 had the profile also laterally encased in concrete, forming a T-shaped composite member. The reason behind this was the interest to study the restrictive influence of embedding concrete over flexural behavior and more notably over interlayer slip. Reinforced concrete model M0 featured a similar cross-section to M1 but instead of the GFRP profile the beam had an equivalent area of steel rebars capable of producing a theoretically similar tensile force as the profile working under partial interaction conditions.

Shear connectors were installed before concreting of the hybrid beams, in pre-drilled holes located alternatively at 100 mm along the profile's upper flange, as seen in Figure 3.8. Type M6 steel bolts with a class resistance of 8.8 were manually fastened into position with a torque of 10 N·m. Steel washers were placed on both sides of the flange to prevent the head and nut of the bolts from damaging severely the fiber-reinforced composite. The small diameter of the shanks coupled with the longitudinal alternate distribution allowed for the desired development of partial shear interaction.

To clarify, for beams model M1 there was no supplementary lateral connection provided between the GFRP profile and the concrete (the friction between the two materials is mostly negligible), and for beams model M2, the profile's support regions were encased in 200 mm wide concrete blocks to prevent a premature local crushing failure, as recommended by initial small-scale bending tests.



Figure 3.8: Fabrication process of the hybrid beams: (a) installment of steel bolts; (b) completed formwork; (c) concrete casting; (d) specimens prior to instrumentation and testing.

In order to maintain the integrity of the concrete slab during transportation and testing, 5Ø8 mm steel bars were placed at its center as constructive longitudinal reinforcement. Transverse steel reinforcement was provided only at the midspan and at the ends of the slab. Because the investigation focused on the flexural behavior of the beams, reference model M0 had a minimum amount of constructive transverse reinforcement in addition to the 3Ø12 bottom longitudinal bars. Reinforcement concrete cover was in all cases 20 mm.

Ten beams were fabricated using the three model designs: two units of model M0, four of model M1 and four of model M2. Their designations are found in Table 3.6 together with information about their type, linear distributed weight and concrete mix.

Table 3.6: Beam designation and description.

Specimen (Model-ID)	Type	Weight (kN/m)	Concrete mix
M0-RCB1	Reinforced concrete	1.03	C1
M0-RCB2			C2
M1-HB1	Hybrid FRP-concrete	1.02	C1
M1-HB2			C2
M1-HB3			C1
M1-HB4			C2
M2-HB1	Hybrid FRP-concrete	0.61	C1
M2-HB2			C2
M2-HB3			C1
M2-HB4			C2

The data reveals the fact that hybrid beams model M2 were the lightest, having approximately 40% less mass than the equivalent reinforced concrete beams and M1 hybrid members. Also, for each hybrid model there were two specimens made with the same concrete strength.

3.4. Nondestructive hybrid beam characterization

3.4.1. Introduction

Before investigating the structural performance of the hybrid specimens by means of destructive testing, the elastic mechanical properties of their main constitutive materials were evaluated using a proposed nondestructive method based on the free vibration response.

Commonly, the elastic behavior of a structural element is evaluated experimentally by static test methods like flexural, tensile, compressive and shear tests. Nonetheless, these methods require close to ideal conditions, take up a significant amount of time due to the number of specimens needed to be prepared and tested, are costly because of the nature of composite materials, and rely on simplification hypotheses. The static tests may also include uncertainties such as anisotropic coupling effects, boundary conditions and material heterogeneities, among others [168].

In the past two decades a lot of effort has been put into the evaluation of elastic properties of anisotropic materials using nondestructive techniques [169–175]. One of these techniques which mitigates part of the aforementioned drawbacks of the standard destructive methods is based on measuring the dynamic properties of specimens. The dynamic characteristics are determined by the geometry, boundary conditions, elastic constants and densities of the composing materials. Hence, by adopting an inverse approach these properties can be used to estimate the elastic constants if the other parameters are assumed to be known [176–179]. Moreover, by using an iterative procedure the engineering constants can be updated in a finite element model of the test specimens in such a way that the computed dynamic properties match the measured ones. Therefore, the purpose of this study was to compare the mechanical properties determined with the proposed nondestructive method with the values offered by the manufacturer and the ones obtained from the static tests reported in section 3.2 for the GFRP profiles and hybrid beams model M2 used in the experimental campaign. The aim of the investigation was to prove the feasibility of this method in characterizing real-scale hybrid beam specimens.

The employed characterization procedure consisted of an experimental modal analysis and a finite element modal analysis coupled with a parameter identification method based on a multiple objective genetic algorithm. Before dealing with the methodology and results of the study a brief description of the methods is necessary to be made.

3.4.1.1. Experimental modal analysis

Experimental modal analysis is a method used to empirically estimate the dynamic properties of a linear, time-invariant structure, based on the relation between excitation and dynamic response. The procedure is also built on Maxwell's reciprocity theorem and on the fact that the vibrational response of a linear, dynamic system can be expressed as a linear combination of simple, harmonic movements or normal modes [173]. Ideally, a vibrational normal mode of an oscillating structure is a pattern of motion in which all parts of the system move sinusoidally with the same frequency and with a stable phase relation. The free motion described by normal modes takes place at fixed frequencies also known as natural or resonant frequencies. In addition, each normal mode has a modal damping value and a mode shape which defines the spatial deformation of the structure due to the resonance. Results and methodologies of various modal characterization tests performed on FRP beams, light structures and footbridges have been reported in [21,180–183].

In general, during an experimental modal analysis the structure is artificially excited using an instrument capable of registering the input signal while the response obtained is measured with a translational transducer. In the particular case of using a single impact hammer to induce vibrations and a single accelerometer to record the response, the position of the accelerometer may be fixed while the excitation is applied in various points across the discretized surface of the structure (method known as roving exciter test). Secondly, by using a Fast Fourier Transformation (FFT) analysis of the measurements, a response model of the physical structure may be recreated by calculating a spectrum in the form of Frequency Response Functions (FRFs) from the time domain signal. Subsequently, the experimental modal parameters (natural frequencies, modal damping and modal shapes) can be estimated by curve fitting a set of the registered FRFs. In this process, a mode indicator function is commonly adopted to help identify how many modes are contained in a frequency band of FRF data.

After the evaluation of the modal properties, a quality control check of the data is usually required. In this sense, the Modal Assurance Criterion (MAC) is useful for numerically comparing two different shape estimates. Hence, the criterion can be used to validate experimental modal models and to map a correlation matrix between analytical, experimental or numerical modal models. The criterion is defined as a scalar constant relating the degree of consistency (linearity) between one modal and another reference modal vector [184]. The MAC values vary between 0 and 1, where the minimum value expresses a null consistency and the maximum value a complete consistency (*i.e.*, similar mode shapes). Normally, MAC values superior to 0.8 are found to be acceptable to establish a certain correspondence between two shapes [185]. It is worth mentioning that its reliability is highly dependent on the number of elements (*i.e.*, measured degrees of freedom) in the modal vectors.

3.4.1.2. Finite element modal analysis

The second stage of the nondestructive hybrid beam characterization tests consists in performing a finite element (FE) modal analysis in order to determine the vibrational characteristics of the specimens. The assumptions and restrictions accounted are that the structure is time-invariant and linear – the mass and stiffness matrices are constant – and that there is no external force applied to the mass (*i.e.*, free vibration).

Initial material input, in the form of elastic constants and densities is needed to carry out the FE modal analysis. Thus, the concrete slab is considered to be made entirely of a linearly-elastic isotropic material with a defined elastic modulus and Poisson’s ratio while the GFRP profile is regarded in a simplified manner as a homogenous orthotropic linearly-elastic material with transverse isotropy. A composite member having transverse isotropy, such as the one illustrated in Figure 3.9, has five independent elastic constants: longitudinal and transverse elastic modulus; in-plane longitudinal shear modulus; and two Poisson’s ratios, as exemplified in Table 3.7. The other material constants can be determined from the independent constants.

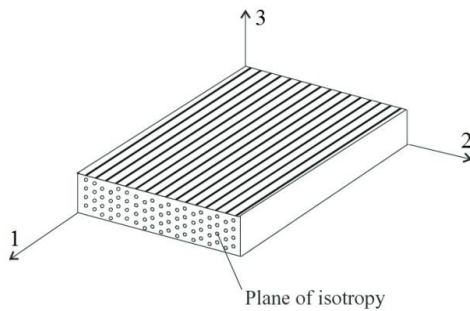


Figure 3.9: Composite material with transverse isotropy.

Material	Elastic constants	
	Independent	Dependent
Orthotropic	E_1, E_2, E_3 G_{12}, G_{13}, G_{23} $\nu_{12}, \nu_{13}, \nu_{23}$	
Transverse isotropic	E_1, E_2 G_{12} ν_{12}, ν_{23}	$E_3 = E_2$ $G_{13} = G_{12}$ $G_{23} = E_2/2(1 + \nu_{23})$ $\nu_{13} = \nu_{12}$

Table 3.7: Elastic constants of orthotropic and transverse isotropic materials.

Besides material information, the FE modal analysis demands geometry and boundary conditions data that reflect the physical structural model. To obtain satisfactory results, easy to simulate conditions should be considered.

The results of the finite element analysis are in the form of eigenfrequencies and corresponding eigenvectors specific to each specimen investigated. To study the relation between the input and output values of the FE model, a parameter correlation study may be performed that can determine which material properties have the most or the least impact on a specific set of dynamic characteristics. In this way, minor input parameters can be disabled to generate a more accurate and less expensive simulation while the highest impact parameters can later be used in conjunction with the results of the experimental modal analysis to set the objectives and constraints of a parameter identification method that can lead to the numerical estimation of material properties.

3.4.1.3. Parameter identification method

The parameter identification method that was found suitable for evaluating the material properties of the pultruded GFRP profiles and hybrid beams, is contained within the *ANSYS Mechanical™ CAE* software solution [186,187]. The technique employs the Direct Optimization single-component system which utilizes real solvers instead of standard response surface evaluations. The optimization method preferred for this scenario was the Adaptive Multiple-Objective Genetic Algorithm (Adaptive MOGA), in which the “best” possible designs candidates are obtained from a sample set, given a list of specified objectives and constraints. It represents a hybrid optimization method that combines a Latin Hypercube Sampling (LHS) method, a Kriging error predictor to reduce the number of evaluations needed to locate the global optimum, and the MOGA algorithm where objectives can be weighted in terms of importance.

In particular, the influence of an input to an output parameter is determined from their correlation. The samples used for the parameter correlation study and optimization method were obtained using the Latin Hypercube Sampling, a statistical method for generating a set of plausible collections of parameter values from a multidimensional distribution. The LHS tries to locate the sampling points such that the space of random input parameters is explored in the most efficient way or acquire the necessary information with a number of minimum sampling points. The presence of points in efficient locations reduces the number of sample points required and increases the accuracy of the results. This is the reason why computed correlations among the input parameters of LHS samples are less than or equal to 5%. Furthermore, Latin Hypercube samples are generated in a random way, with no two points sharing input parameters of identical value.

The Adaptive MOGA in *ANSYS* uses a Kriging response surface that allows for a more rapid optimization process because it does not evaluate all design points, except when necessary, and because part of the sample population is simulated by evaluations. That is to say, Kriging is a meta-modeling algorithm that provides an improved response quality and fits higher order variations of the output parameters. It is an accurate multidimensional interpolation combining a polynomial model which provides a global model of the design space and local deviations so that the model interpolates the design points.

To conclude, in the parameter identification method the objectives are set so that the dynamic properties evaluated in the experimental modal analysis match the dynamic properties of the finite element model. In completion, constraints are added to define the variation boundaries for the material elastic constants so as to simplify the optimization process and improve its accuracy. The material input data is then generated and the resulting modal properties of the specimens are updated in an iterative procedure until the best solution is found for the problem.

The whole proposed process that allows the evaluation of a profile's or hybrid beam's elastic properties through the use of a nondestructive method based on vibrational response is illustrated in the following flowchart in Figure 3.10.

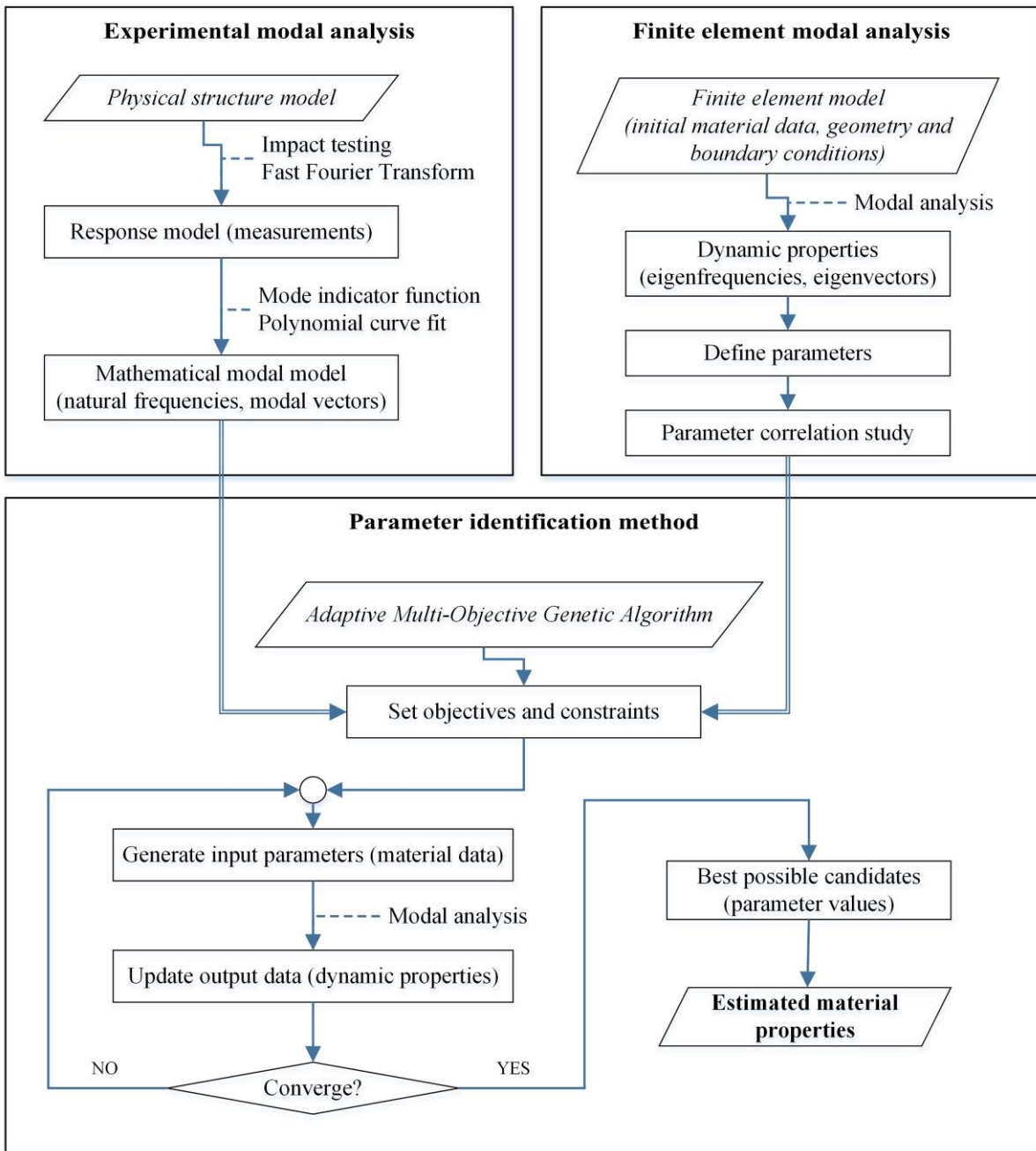


Figure 3.10: Flowchart of the experimental and numerical procedure used in evaluating the elastic properties of the GFRP profiles and corresponding hybrid beams.

3.4.2. Methodology

Three test specimens were chosen for the nondestructive characterization tests: a two meters long GFRP profile and a couple of M2 hybrid beams with distinct concrete compositions (C1 and C2).

Initially, the elastic properties of the profile were evaluated and then introduced as input values for the hybrid beam evaluations.

The experimental modal analysis of the composite profile was performed in both vertical and horizontal directions, on a number of three surfaces: top flange, bottom flange, and web. Due to the inherent low mass, the specimen was investigated under free boundary conditions. Therefore, to allow the free movement of the specimen, two elastic rubber bands were placed around it and connected with nylon threads to a fixed ceiling structure as seen in Figure 3.11.

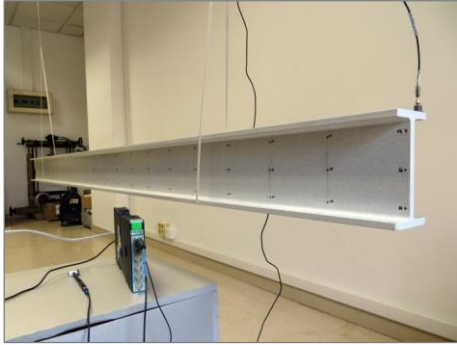


Figure 3.11: Experimental modal analysis test setup for the GFRP profile.

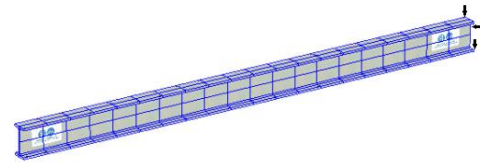


Figure 3.12: GFRP profile model used to visualize the experimental modal results.

Before the impact testing could commence, the surfaces of the profile which had to be studied were meshed. The element size of the mesh usually depends on the geometry of the specimen and the required spatial resolution of the modal vector. Thus, a fine mesh will provide better results but will increase the complexity of the experiment and resulting modal model. On the contrary, a less refined mesh may generate insufficient or poor data. The investigated profile had a mesh with a total number of 168 roving points split into three parts: 63 points arranged in 3 rows on the upper side of the top flange, 63 points arranged in 3 rows on the lateral side of the web and 42 points arranged in 2 rows, one on each side of the upper part of the bottom flange. The rows were placed at 5 mm from the extremities and at the center line of the surfaces. Maximum longitudinal spacing between points was 100 mm (5% of total length). The GFRP model displayed in Figure 3.12 that was used to visualize the experimental modal results had a similar mesh.

Elastic vibrations were induced in the profile with the help of a small impact hammer with a metal tip, model 8204 from Brüel & Kjær, capable of registering signals in a frequency range up to 10 kHz. Two measurements were done for each mesh point to assert the reading coherence, and the average transient response was recorded by a uniaxial accelerometer model 4518-003 from Brüel & Kjær. One of the key aspects in capturing as many vibrational modes as possible is fixing the accelerometer in a proper position and setting an appropriate frequency range for the analysis. Thus, for the GFRP profile the transducer was placed on a point near one of the corners of each subsequent surface and the frequency range was established as 0-800 Hz.

For the two GFRP-concrete hybrid beams, the experimental modal analysis was performed only on the meshed top surface, in vertical direction. This time around, due to the significant mass the specimens were arranged in a simply supported configuration on two 50 mm wide metal cylinders placed on the fixed floor structure of the laboratory. There were a total of 105 impact points disposed in 5 equally-spaced rows drawn along the element, with a spacing distance of 100 mm and an edge retreat of 10 mm. The two hybrid beams were excited two times in each mesh node with a heavier impact hammer with a plastic tip, Brüel & Kjær model 8206 with a frequency range up to 5 kHz. The increased mass and stiffness of the specimens also required a larger accelerometer, model 4370 from the same company, and an augmentation of the analysis frequency band to 1000 Hz. The accelerometer was placed on a point near the edge, in the vicinity of the central cross-line, as seen in Figure 3.13.

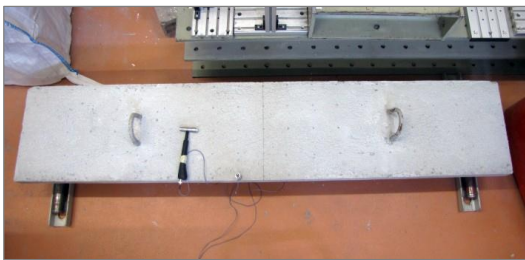


Figure 3.13: Experimental modal analysis test setup for the GFRP-concrete hybrid beams.

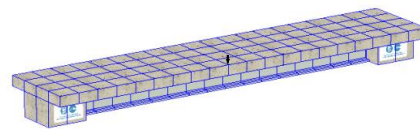


Figure 3.14: GFRP-concrete hybrid beam model used to visualize the experimental modal results.

For all the experimental modal analyses, the time domain signals coming from the impact exciter and accelerometer were recorded using two data channels of a Brüel & Kjær LAN-XI 3050-B-6/0 data acquisition system and converted to frequency spectrums (FRFs) within the accompanying *PULSE LabShop* analyzer.

The last phase of the modal analysis consisted in determining the experimental dynamic properties of the specimens. To accomplish this objective, the data recorded during the tests was post-processed within the *ME'scopeVEST™* software package from Vibrant Technology [188]. Three-dimensional models of the tested specimens were recreated, as seen in Figure 3.14, and meshed. The FRFs were then imported and assigned to each corresponding mesh point from the experiment. Modal parameters were estimated by curve fitting the responses using the Complex Mode Indicator Function (CMIF) and the Alias-Free polynomial method (Figure 3.15 and Figure 3.16). The CMIF was used to determine how many modes are contained in a frequency band of data by counting the resonance peaks above a threshold level. It is useful for finding closely coupled modes – two or more modes represented by a single resonance peak – and repeated roots – two or more modes at the same frequency but with different mode shapes, but also for estimating parameters more accurately from each reference measurement. To exemplify, three references were used during the GFRP profile test, each one corresponding to a roving impact surface. Response noise was more evident for lower frequencies; however, resonance peaks were clearly distinguishable.

The dynamic parameters of the tested specimens estimated in the experimental modal analysis served as seek targets for the objectives of the numerical material parameter identification method.

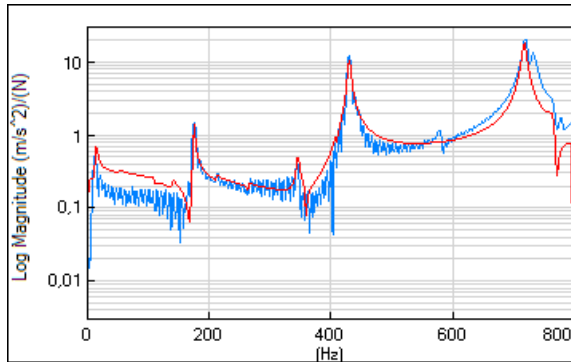


Figure 3.15: Curve fitting for a single magnitude experimental FRF of the GFRP profile.

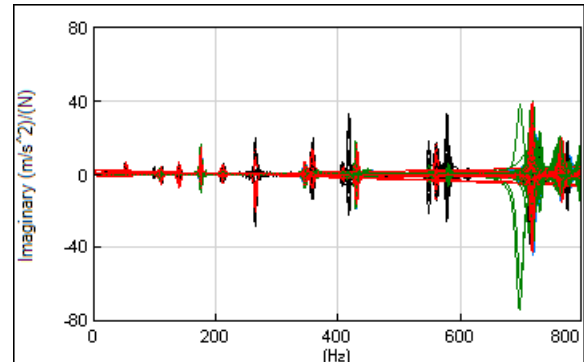


Figure 3.16: Imaginary shapes of all the experimental FRFs of the GFRP profile (three accelerometer references, colored in red, black and green).

Finite element models made of solid elements were built for the GFRP profile and the pair of M2 hybrid beams following the nominal fabrication dimensions. To mimic the modal tests, the GFRP model seen in Figure 3.17 had simulated free boundary conditions while the hybrid model shown in Figure 3.18 was simply supported on translationally restrained edges. For the composite profile, the five independent elastic properties of the orthotropic material described in Table 3.7 were assigned as input parameters with initial values while the remaining four dependent elastic constants were expressed as parameters which derive from the former ones. In the case of the hybrid beams, the properties of the profile obtained from the optimization procedure executed before were considered as known input data and the only input parameter was the elastic modulus of the concrete (E_{c1} or E_{c2}). The interaction between the slab and the profile was considered to be complete for the modal analysis and the steel reinforcement bars were not included in the model to reduce its complexity. Nonetheless, a trial simulation proved that the influence of the rebars over eigenfrequencies for the two beams causes an increase of 1-2% in bending modes and 5-6% in torsional modes.

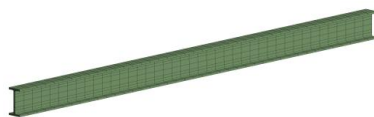


Figure 3.17: GFRP profile finite element model.

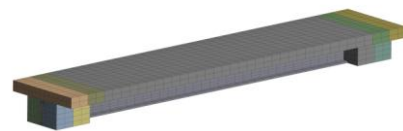


Figure 3.18: GFRP-concrete hybrid beam finite element model.

The output parameters defined for the profile's finite element model were the first three modal frequencies attributed to the longitudinal bending modes, transverse (longitudinal horizontal) bending modes and torsional modes. A parameter correlation study made between the input and output

parameters of the composite shape evaluated which elastic constants have the most or the least impact on eigenfrequencies, and in this way the minor contributing factors could be eliminated when building the optimization method, by treating them as deterministic parameters. The variation limits of the mechanical properties were set to the same values as for the optimization procedure. The resulting correlation matrices displayed in Figure 3.19 were computed for the first three occurring normal modes of the three types of accelerometer references discussed before. The numbers reflect the sensitivity of frequencies to material properties, where a positive sensitivity occurs when increasing the input leads to an increased output and where a negative sensitivity is computed when increasing the input decreases the output. The statistical sensitivities are based on Spearman’s rank order correlation coefficients [189] that simultaneously take into account the amount by which an output parameter varies across the variation range of an input parameter and the variation range of an input parameter (the wider the range, the larger the impact). A perfect correlation of +1 or −1 takes place when each of the variables is a perfect monotone function of the other.

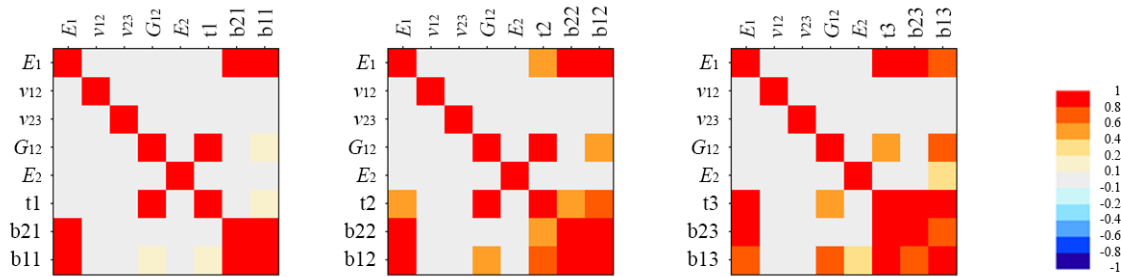


Figure 3.19: Correlation matrices for the three first vibrational modes of the GFRP profile in longitudinal and transverse bending and in torsion.

The first symmetric correlation matrix reflects the fact that the first longitudinal and transverse bending modes (b11 and b21) are dominated by the influence of the longitudinal modulus of elasticity of the profile, and that the first torsional mode (t1) is heavily influenced by the in-plane shear modulus. The remaining correlation analyses indicate that for higher order vibrational modes (b12, b13, b22, b23, t2, t3), the modal frequencies start to be sensitive to multiple elastic properties. The color-coded cells also suggest that the Poisson’s ratios and transverse elastic moduli have a negligible impact and that all relations are positive, where higher elastic constants are the cause of higher natural frequencies.

Once the input parameters were established, the characterization procedure continued with the hybrid optimization method, based on the Adaptive Multiple-Objective Algorithm.

For the pultruded composite profile, the objectives set were that the eigenfrequencies of the first three bending longitudinal and transversal modes as well as torsional modes, determined with the Finite Element Analysis (FEA), seek the corresponding natural frequencies of the empirical modes estimated in the experimental modal analysis. Figure 3.20 depicts three of the aforementioned matching modes (b21, b12 and t2) for the specimen studied.

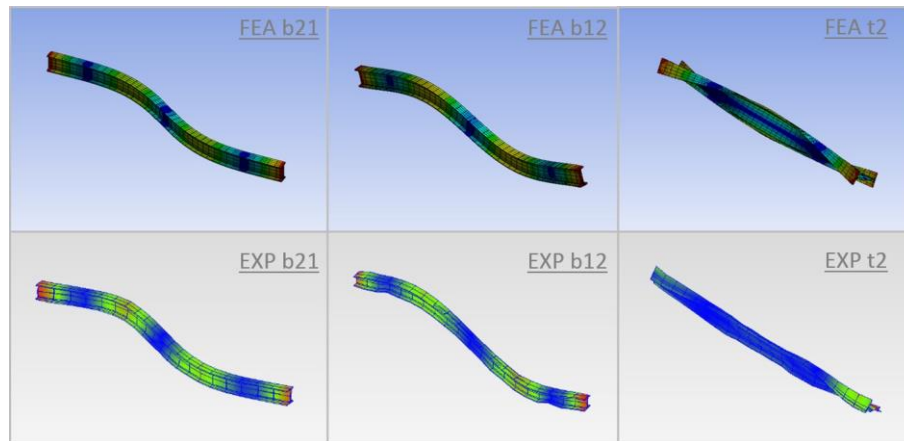


Figure 3.20: Numerical (FEA) and experimental (EXP) matching mode shapes of the profile.

In accordance with the parameter correlation study, the matching objectives covering the first mode frequencies had a higher importance set in the optimization process. Lower and upper bounds were set for the variation of the elastic properties of the glass fiber-reinforced plastic material by gathering possible interval values from literature and design guide manuals [1,9–12,75]. The intervals are reflected in Table 3.8 together with the constraints that were set to a strict handling status for the dependent properties.

Table 3.8: Optimization domain and constraints for the GFRP profile.

Elastic property	Optimization domain	
	Lower bound	Upper bound
E_1 (MPa)	35000	45000
E_2 (MPa)	7000	15000
G_{12} (MPa)	3000	4500
ν_{12}	0.25	0.35
ν_{23}	0.25	0.35
Constraints		
G_{23} (MPa)	3000	5000
ν_{21}	0.06	0.15

For the M2 hybrid specimens, the objectives set were that the eigenfrequencies of the first four bending modes and of the third and fourth torsional modes determined with the Finite Element Analysis seek to match the corresponding natural frequencies of the empirical modes estimated in the experimental modal analysis. The first two experimental torsional modes were unable to be identified in the FE modal analysis and there were no transverse bending modes registered since the experimental modal analysis was carried with a single vertical reference transducer. Figure 3.21 shows two of the matching modes (b12 and t3) for the specimen studied.

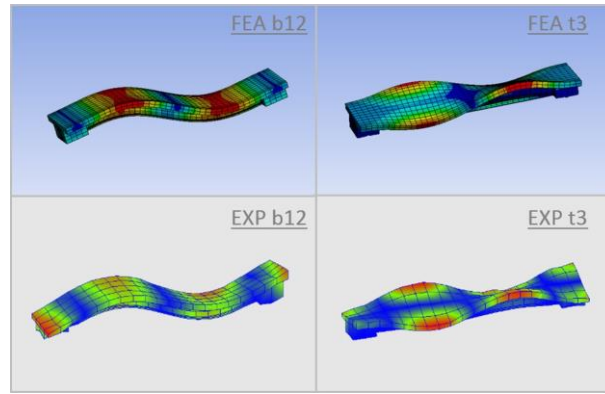


Figure 3.21: Numerical (FEA) and experimental (EXP) matching mode shapes of the M2 hybrid beams.

Lower and upper bound values were assigned for the elastic modulus of the two concrete mixes based on strength class estimations. After the first optimization process was carried out for the beam having a lower concrete strength, the variation interval for the second modulus was narrowed. The values employed are summarized in Table 3.9. There were no constraints set for the hybrid beam simulations.

Table 3.9: Optimization domain for the M2 GFRP-concrete hybrid beams.

Elastic property	Optimization domain	
	Lower bound	Upper bound
E_{c1} (MPa)	25000	35000
E_{c2} (MPa)	30000	35000

As mentioned during the introduction of the current section, the modal vectors to be matched during the parameter identification method were checked using the Modal Assurance Criterion (MAC). With the formulation in cause, a correlation matrix between the experimental and numerical vectors was built for each specimen. The MAC matrices of the profile and hybrid beams are illustrated in Figure 3.22 (for the profile only the first 6 modes are displayed). The bottom values of the experimental mode and eigenvector/numerical mode axis indicate the frequency order number of the mode being compared, and the vertical axis points to the MAC value obtained.

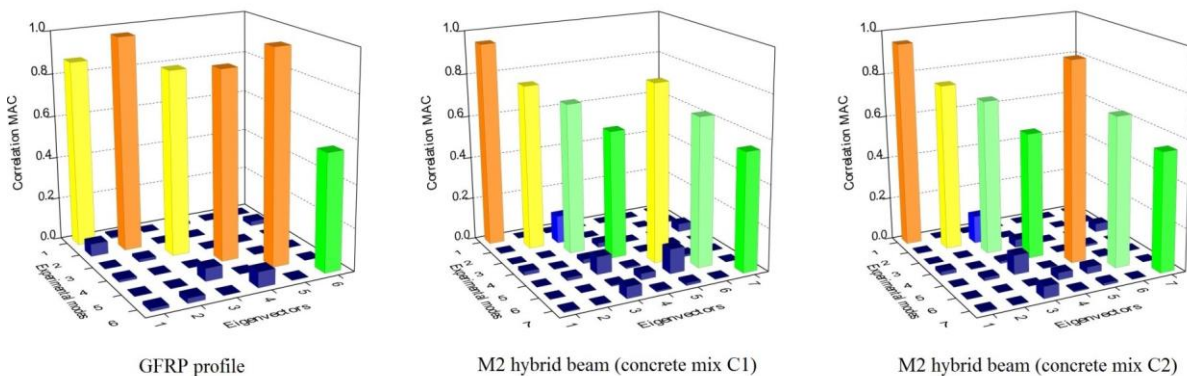


Figure 3.22: MAC values of the first normal modes of the tested specimens.

All three diagrams have a major diagonal distribution demonstrating that the compared modal shapes were similar and correctly identified. The chart bars show high coherence levels (> 0.8) for the GFRP profile and satisfactory values for the hybrid beams.

As a final note to the methodology commentaries, the following relevant settings were specified for the direct optimization method: 100 initial samples to be generated; 50 samples per iteration to find the best 3 candidates in a maximum of 20 iterations; and a maximum allowable Pareto percentage of 70%.

3.4.3. Results and discussion

After running the optimization procedure, the best material data candidates were found in a number of 2 iterations by evaluating over 150 samples (design points) for each one of the specimens. The three design candidates are illustrated for the GFRP profile in Figure 3.23 with green lines over the rest of the generated sample lines. The chart shows the variation of 10 elastic properties and 9 modal frequencies between set and computed optimization boundaries. Therefore, the best candidate for evaluating the material's properties in a nondestructive manner was the one which satisfied the most objectives and constraints set.

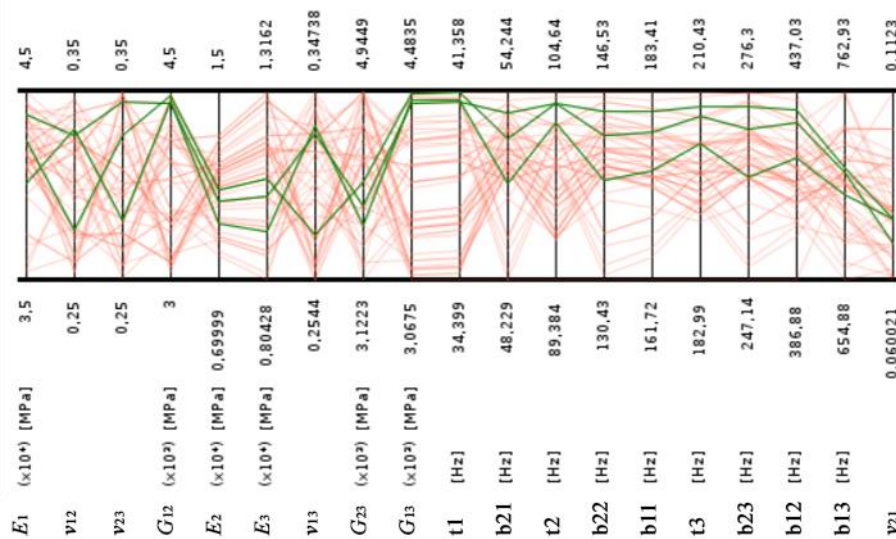











Figure 3.23: GFRP profile design candidates and evaluation samples.




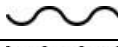


The modal frequencies obtained from the experimental modal analysis and numerical optimization problem are summarized for the GFRP profile in Table 3.10, and for the two hybrid beams in combined Table 3.11. The percentile differences computed for the results of the profile show that for the longitudinal and transverse bending modes, the natural frequencies were very close within a 2% limit. On the other hand, the error between the numerical and experimental values for torsional vibrational modes was negative, with the FE model exhibiting less torsional stiffness. In the case of the hybrid beams, the percentile differences showed similar values for the bending direction modes and torsional modes, but nevertheless higher than for the single profile.

Table 3.10: Experimental (EXP) and numerical (FEA) modal frequency results for the GFRP profile.

Mode ID ^a	Mode shape	f_{EXP}	f_{FEA}	diff.
		(Hz)	(Hz)	(%)
b11		176	179	+1.6
b12		430	429	-0.3
b13		720	717	-0.4
b21		53	53	-0.5
b22		140	143	+2.0
b23		265	270	+2.1
t1		48	41	-13.9
t2		110	104	-5.8
t3		212	207	-2.4

^a b1x – longitudinal bending mode; b2x – transversal bending mode; tx – torsional mode.

Table 3.11: Experimental (EXP) and numerical (FEA) modal frequency results for the GFRP-concrete hybrid beams.

Mode ID	Mode shape	M2 concrete mix C1			M2 concrete mix C2		
		f_{EXP}	f_{FEA}	diff.	f_{EXP}	f_{FEA}	diff.
		(Hz)	(Hz)	(%)	(Hz)	(Hz)	(%)
b11		50	55	+10.0	52	56	+7.7
b12		201	186	-7.5	198	189	-4.5
b13		344	347	+0.9	368	352	-4.3
b14		479	526	+9.8	474	534	+12.7
t3		400	348	-13.0	405	351	-13.3
t4		555	525	-5.4	570	532	-6.7

Comparative charts of the experimentally and numerically estimated frequencies, depicted in Figure 3.24, reveal that the optimization FE method does not prefer stiffer or more flexible designs, as the data markers are dispersed evenly along the spectrum’s diagonal. More so, concerning the GFRP profile, the optimization procedure is able to generate a material data candidate that can satisfy also less important objectives such as seeking to match higher order mode properties. In exchange, it is more difficult to generate suitable design candidates that can match the empirical natural frequencies of high order normal modes of hybrid specimens.

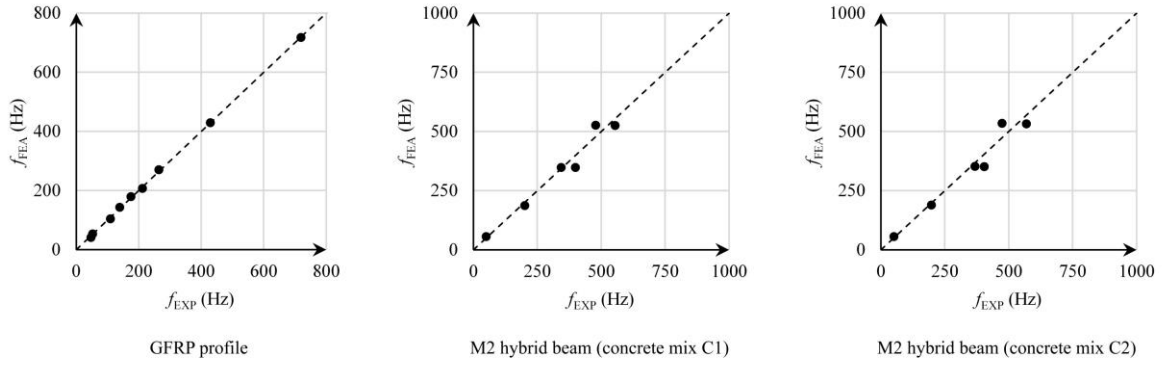


Figure 3.24: Comparative charts of the experimentally and numerically estimated natural frequencies.

Lastly, as the aim of the proposed method was to characterize in a nondestructive manner the elastic properties of the hybrid beams designed for the experimental campaign, a comparison is made between the properties estimated following the numerical parameter identification method and the analogous values offered by the manufacturer and laboratory static tests. Table 3.12 includes in the last couple of columns the percentile differences between the results of the numerical analyses and the other two sources. The computed differences are mostly positive.

Table 3.12: Comparison between the estimated elastic properties using the proposed nondestructive method and the properties offered by the manufacturer or obtained from the destructive static tests.

Elastic property	Data obtained from			diff.manuf. (%)	diff.static (%)
	Manufacturer	Static tests	Nondestructive tests		
E_1 (GPa)	41.40	39.11	42.45	+2.5	+8.5
E_2 (GPa)	n/a	10.77	10.80		+0.3
G_{12} (GPa)	n/a	3.98	4.47		+12.3
ν_{12}	n/a	0.27	0.28		+2.5
ν_{23}	n/a	n/a	0.33		
G_{23} (GPa)	n/a	n/a	4.07		
ν_{21}	n/a	0.07	0.07		-0.1
E_{c1} (GPa)	28.61	n/a	30.55	+6.7	
E_{c2} (GPa)	29.96	n/a	33.61	+12.2	

n/a – not available.

The proposed method is thus able to estimate the complete set of elastic constants of the materials within satisfactory error and time limits. As observed, the elastic properties of the GFRP profile stipulated by the manufacturer are clearly insufficient for analytic or numeric calculations, whereas the data gathered from the static tests, though sufficient, requires a great deal of preparation tasks and experimental trials.

3.5. Bending test setups and procedure

After the nondestructive characterization tests, the specimens were prepared and instrumented for the main experimental campaign that served to analyze their short-term structural behavior under positive bending moments. The campaign was divided in two parts depending on the test setup configuration that was used. In both cases, the beams were simply supported over a span distance of 1800 mm and loaded with a single midspan concentrated force or two symmetrically placed concentrated forces positioned at approximately a third of the test length.

The two test setup configurations were designated I and II depending on the number of forces applied. In test setup I, all the fabricated specimens were supported on a pair of Isolgamma elastomeric pads with a density of 0.7 kg/dm^3 so as to avoid any local failure of the composite profiles at the reaction points. The consequent measurements and observations suggested that the thickness and elasticity of the material were sufficient and allowed the beams to rotate freely until final failure. The axis of rotation was in fact in the proximity of the support's central line, thus keeping a constant test span distance (Appendix B). After the initial tests, the pads were discarded for the second test configuration because observations proved that this measure was too conservative taking into account that the ends of the profiles were encased in concrete. Therefore, in test setup II the beams were simply supported on 50 mm wide steel cylinders.

It must be stated that in addition to the fabricated specimens, a couple of GFRP profiles were also tested during the experimental campaign and served as references beside the M0 reinforced concrete beams. The profiles were deflected in a three-point bending configuration similar to test setup I, although on cylindrical supports, and only the second specimen was instrumented with strain gauges and had wood block stiffeners glued at the critical sections (reaction points). Table 3.13 groups all the tested members depending on the loading scheme that was applied.

Table 3.13: Overview of flexural tests carried out.

Specimen	Test setup and load arrangement	Support type
M0-RCB1	I – one midspan load	Elastomeric pads
M1-HB1		
M1-HB2		
M2-HB1		
M2-HB2		
Profile 1	II – two loads $\sim 1/3$ test length	Steel cylinders
Profile 2		
M0-RCB2		
M1-HB3		
M1-HB4		
M2-HB3		
M2-HB4		

In the first test configuration, the hybrid beams were loaded on the top center crossline using a 250 kN capable MTS hydraulic actuator. A small plywood plate was used to spread the concentrated load from the actuator's head to the irregular top surface of the specimen. In contrast, in test setup II the applied load was produced by a 500 kN capable actuator and distributed in two segments situated 735 mm apart, by a steel frame with semi-cylindrical supports. The M0 specimens were tested in a comparable manner but without the extra instrumentation required by the hybrid beams, as seen in Appendix B. Loading was applied in a quasi-static mode under a constant displacement rate of 2 mm/min, and was measured by the actuator's force transducer. Details of both test setups are illustrated below in Figure 3.25.

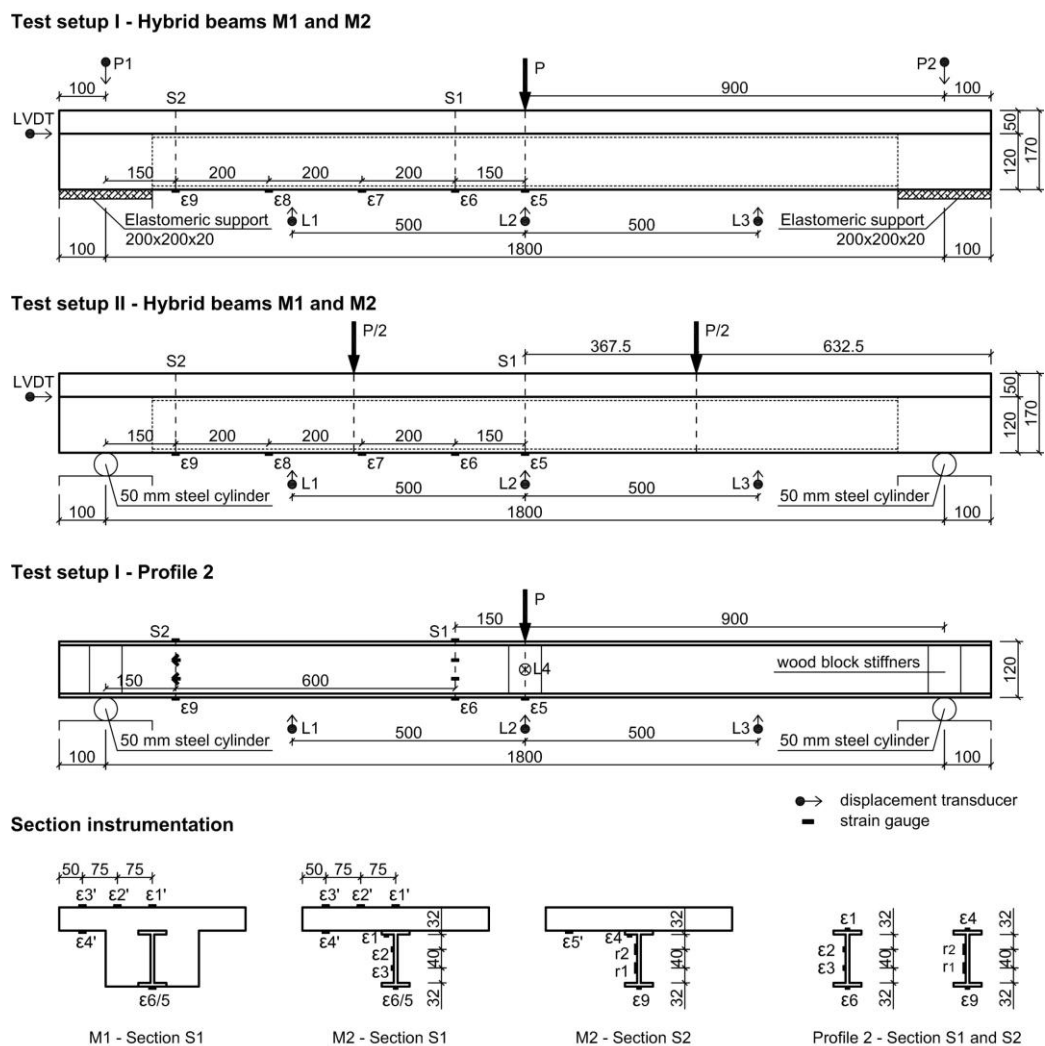


Figure 3.25: Schematic of load arrangements and instrumentation of tested specimens (mm).

The instrumentation of the beams was similar for both configurations so as to record and compare similar parameters of the flexural behavior. Deflections were measured at the midspan and at 500 mm toward each support by RIFTEK RF603.2-125/500 laser triangulation sensors with a range of 500 mm (L1, L2 and L3). Profile 2 had an additional midspan laser, called L4, which monitored the lateral

displacement of the profile. In the case of the beams placed on rubber pads, the vertical displacements of the supports were registered by two Waycon LRW-M-100-S linear potentiometers with a measurement range of 100 mm and a repeatability of 0.01 mm (named P1 and P2). The hybrid specimens were additionally instrumented at one end with an HBM WA20 displacement transducer (LVDT) in order to capture the relative slip between the top flange of the GFRP profile and concrete slab.

Strain gauges were attached on the left part of the specimens considering the symmetric static schemes, in key sections near or at the center span, in S1, and at 150 mm from one of the supports, in S2. HBM linear gauges 1-LY41-6/350 were installed on the composite material and larger HBM 1-LY41-50/120 models were applied on polished concrete surfaces. For beams type M2, axial strains were measured across the concrete slab and the GFRP profile in both sections. In this way the slip strain between the two constitutive materials could also be determined. In section S2, a couple of strain gauge rosettes HBM 1-RY81-6/350 were placed on the profile's web to determine the angular strains in the composite material. Hybrid beams model M1 were instrumented just in section S1 and along the bottom flange of the profile. The control or reference specimens represented by the M0 reinforced concrete beams and the single GFRP profiles were tested in similar configurations to the rest, as illustrated in the compiled images of Figure 3.26 and Appendix B.



Figure 3.26: Laboratory setups and instrumentation: (a) M1 or M0 beams in test setup I; (b) M1 or M0 beams in test setup II; (c) Profile 1 in test setup I; (d) M2 beams in test setup I; (e) M2 beams in test setup II; (f) Profile 2 in test setup I.

Data measured by the sensors were gathered by an HBM MGCplus data acquisition system at a rate of 50 Hz. The flexural behavior of the structural members was also captured with the help of a standard definition camera while in the case of the model M2 hybrid beams a MotionBLITZ® Cube4 high-speed recording camera was also employed to observe the development of the brittle failure at a speed of 1000 fps.

3.6. Bending test results and discussion

The results and observations of the bending tests are discussed in the following section with special emphasis on the flexural behavior and failure modes, internal strain and stress distributions, along with interlayer slip development. The interpretation of the results is corroborated with the information adjoined in Appendix B and is performed in a generally comparative manner.

3.6.1. Flexural behavior and failure modes

3.6.1.1. Reference specimens

First of all, the structural behavior of the reference/control specimens is discussed in order to have a comparison basis. Reinforced concrete beam M0-RCB1 had a typical ductile flexural response where failure was initiated by yielding of the bottom steel reinforcement bars. During the yielding phase, the concrete slab began to crush as a result of the significant deformations induced at the loading area, and final collapse occurred later after a flexural crack extended along the bottom reinforcement. In the case of the second reinforced concrete beam M0-RCB2, tested under four-point bending, the sudden failure was provoked by a diagonal tensile shear crack that formed between the left support and the nearest loading point. Thus, M0-RCB2 lacked a yielding plateau since both reference specimens were primarily reinforced in longitudinal direction so as to focus specifically on the flexural behavior. The crack patterns of the reinforced concrete beams are illustrated in Figure 3.27a,b. No slab crushing was observed for M0-RCB2.

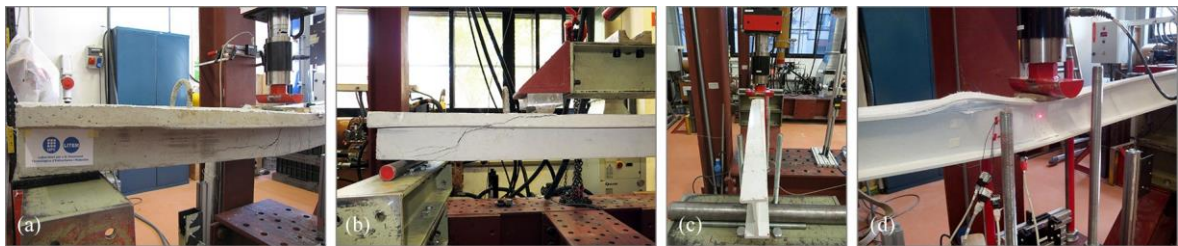


Figure 3.27: Failure characteristics of reference specimens: (a) M0-RCB1; (b) M0-RCB2; (c) Profile 1; (d) Profile 2.

GFRP reference specimens, Profile 1 and 2, exhibited a complete linear elastic behavior until failure. Slight deviations were however visible toward the end for Profile 2. The collapse was caused in both cases by global instability, and more precisely by lateral torsional buckling as illustrated in Figure 3.27c,d. Buckling initiation was captured with the help of the laterally placed laser triangulation sensor. As Profile 2 had web stiffeners bonded on both sides of the web at the reaction points, its achieved capacity was approximately twice as that of the first profile. Consequently, after the initial failure of the second profile, the high uneven axial compressive stress near the load provoked a local buckling of the top flange observable in the same image. The flexural stiffness demonstrated by the single composite

profiles was significantly smaller in comparison with the reinforced concrete specimens. Nevertheless, the ultimate capacity of Profile 2 laid closely due to the presence of web stiffeners.

3.6.1.2. Hybrid beams – test setup I

Hybrid beams M1-HB1 and M1-HB2, which were made of a GFRP structural profile encased in a T-shaped concrete beam, displayed a generally bilinear response up to ~90% of the ultimate load, a superior strength in comparison to M0-RCB1 and double the flexural rigidity of the single profiles. Furthermore, the maximum load sustained by M1-HB2 represented a fourfold increase over the value recorded for Profile 1. The bilinear shape of the responses was attributed mainly to the change in the stress transfer mechanism at the connection level. Thus, the initial slope reflects a complete interaction between the two layers while the second a partial interaction (*i.e.*, flexible connection). The experimental load-midspan deflection curves of the specimens tested under three-point bending are plotted in Figure 3.28, adjacent to the final deflection profiles depicted in Figure 3.29. The latter figure suggests a fairly symmetrical distribution of deformation in the hybrid beams before collapse and similar deflection values for the second, third and fourth specimen. Deflection values were interpolated between the measuring points using a smooth polynomial curve.

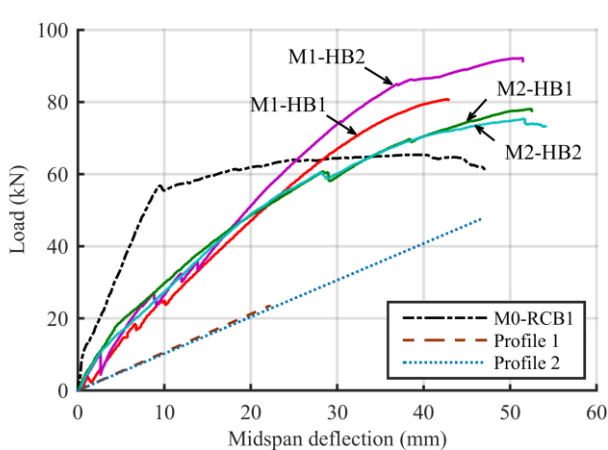


Figure 3.28: Experimental bending results under test setup I: load-midspan deflection curves until failure.

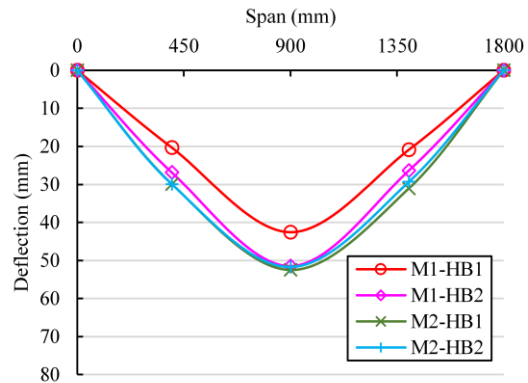


Figure 3.29: Deflection profiles of hybrid beams at maximum load in test setup I.

The flexural responses of hybrid beams M2-HB1 and M2-HB2, which were made of a GFRP structural profile attached with steel bolts to a reinforced concrete slab, were similar to those of the previous M1 hybrid beams. Slight differences are visible in the increased deformability explained by the fact that the composite web was not laterally encased in concrete and in the higher nonlinear response toward collapse, justified by the concrete’s constitutive behavior under high compressive strains. Once more, the generally bilinear behavior was governed by the change in the flexibility of the connection which caused a reduction of the flexural stiffness from the initial complete interaction value that was seemingly close to the flexural stiffness of M0-RCB1.

The comparative load-deflection chart also reflects the change in the slab's compressive strength, whereas beams fabricated using concrete mix C2 have a slightly higher flexural stiffness and capacity, as it will be analyzed later. In spite of this, the ultimate load of the hybrid beams seems to be limited by the amount of bending deformation supported and more precisely by the amount of shear force that the GFRP profile can carry.

At the beginning of the tests three large flexural cracks appeared in the concrete web of the M1 hybrid beams due to the material's loss of tensile strength, as revealed by the jumps in the load-displacement responses. As the loading continued, the cracks progressed toward the inferior central part of the top slab where they dispersed. The cross section views point out that the profile was deforming independently from the slab, causing longitudinal cracks to develop in the concrete top. Failure of M1-HB1 and M1-HB2 began with crushing of the concrete slab at the midspan and ended a few moments later when the profile's bottom flange suddenly detached from the web. The cause of the brittle collapse was determined to be the increased shear stress which had developed at the web-flange junctions, at the ends of the pultruded composite members. Even though the maximum shear stress normally occurs at the top junction, the bottom flange was probably detached by the concrete section which encased the rest of the profile, by inducing important normal tensile strains at the aforementioned junction. After failure, the two M1 hybrid beams continued to work in flexure, displaying a brief recovery capacity of up to 75% of the maximum sustained load.

Photographs of the failures modes experienced by the M1 GFRP-concrete hybrid beams in the three-point bending test setup are illustrated in Figure 3.30. Concrete cracks and fiber delaminations were colored in bright red on the cross-section area.



Figure 3.30: Failure characteristics of hybrid beams model M1 in test setup I: (a) concrete crushing and flexural cracks; (b) inward slip and flange delaminations; (c) bottom flange separation.

In the case of the M2 hybrid beams the flexural cracks were less wide and more spread across the slab, starting especially from the connectors' positions and reaching toward the edges and central line. Horizontal fissures were also noticed between the concrete support blocks and slab. For M2-HB1 failure began with crushing of the concrete top followed by a brittle shear delamination at one of its ends, at the junction between the GFRP profile's top flange and web. The shear failure dispersed instantly toward the midspan of the beam causing an additional vertical displacement of the steel bolts and a local buckling of the compressed web (post-failure mechanism). In contrast, M2-HB2 which displayed a

significantly more damaged slab failed suddenly at the midspan without concrete crushing, in the zone directly placed under the applied load. The failure was probably induced by a fracture of the wood load spreading piece, and thus, a high compressive stress present at the center of the slab and GFRP profile determined a crushing type of collapse to take place in the profile's web. The failure was closely followed by longitudinal delaminations of the composite material, concrete crushing and top flange rupturing or buckling between pairs of central bolts. Apart from this, it was observed that at 75% of the ultimate load of the M2 beams, a longitudinal crack partially split the slab along its midline and produced a jump in the load-deflection response. The split was possibly caused by an insufficient degree of transverse steel reinforcement in the slab and by the narrow flange width of the profile. Finally, no significant recovery capacity was displayed by the M2 hybrid beams during the three-point bending tests. Photographic evidence of the failure characteristics of the M2 GFRP-concrete members are shown in Figure 3.31.



Figure 3.31: Failure characteristics of hybrid beams model M2 in test setup I: (a) profile web-flange shear delamination preceded by concrete slab crushing; (b) post-failure local buckling of the web; (c) transverse crushing of the profile's web.

The visible crack patterns of the hybrid beams marked at the completion of the tests are illustrated in Figure 3.32. Special attention should be paid to the cross section drawings as the web-flange failure cracks are rather short.

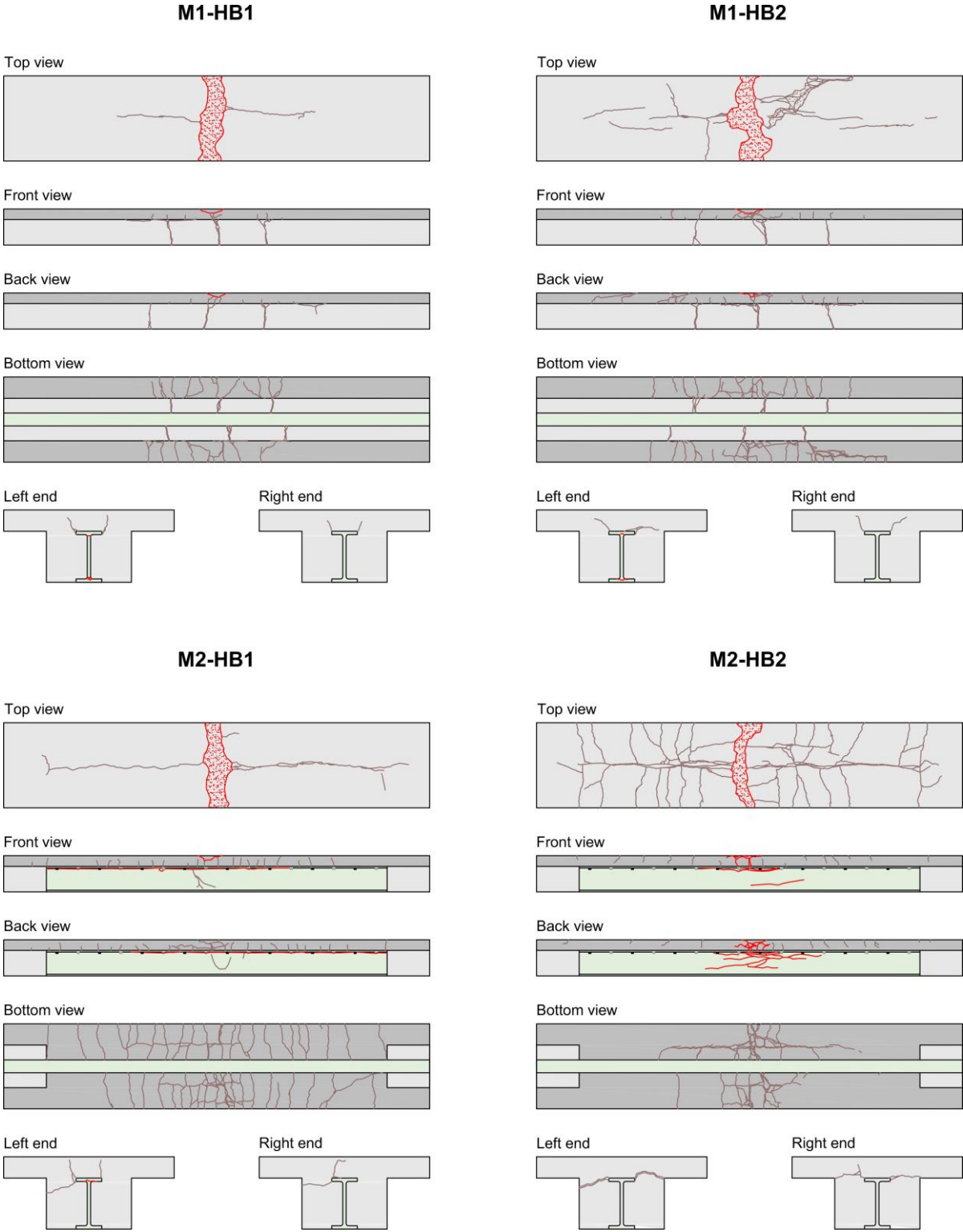


Figure 3.32: Visible crack patterns of hybrid beams in test setup I. Failure cracks and crushing areas are indicated in bright red.

3.6.1.3. Hybrid beams – test setup II

In the second part of the experimental campaign the hybrid specimens tested under four-point bending exhibited a generally bilinear structural response with no concrete crushing and a higher capacity than control beam M0-RCB2. Nonetheless, their flexural stiffness was lower, with M2-HB3 and M2-HB4 experiencing the greatest deformability. The occurrence of flexural cracks is reflected again in the load-midspan deflection curves plotted in Figure 3.33 by the sudden drops in load-bearing capacity especially in the initial stage for the M1 hybrid beams. The change from complete shear interaction to partial shear interaction behavior is visible as well from the initial slope inflection.

Although the M2 members had less flexural stiffness, they exhibited higher ultimate capacities compared to the rest of the specimens. Results also pointed out that the increase in concrete strength led to stiffer responses and higher flexural capacities; however, as in the case of the three-point bending tests, this capacity seems to be limited to a degree by the deformation supported by the composite member.

Next to the load-midspan deflection chart, in Figure 3.34, the final deflection profiles portray a slightly asymmetric distribution of deformations in the hybrid beams, as ideal homogenous materials and boundary conditions are impossible to recreate in practice. Hence, these small imperfections explain why the right side deformed more than the other. The deflection variations also indicate that similar values were attained by similar hybrid beam models, with M1-HB3 and M1-HB4 having a more rigid response due to the additional concrete web.

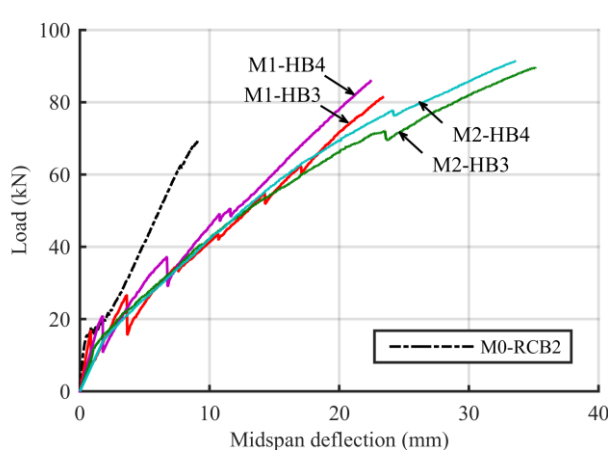


Figure 3.33. Experimental bending results under test setup II: load-midspan deflection curves until failure.

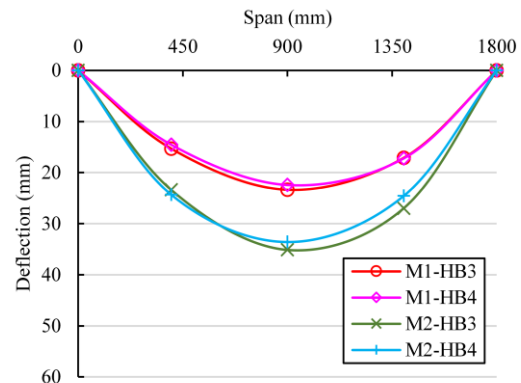


Figure 3.34: Deflection profiles of hybrid beams at maximum load in test setup II.

During the loading of the M1 beams, four large vertical flexural cracks developed in the concrete webs due to the material’s loss of tensile strength. The cracks spread increasingly to the bottom side of the slab and dispersed toward the edges. Longitudinal fissures also appeared in the concrete slabs when the GFRP profiles started to slip, as seen from the cross-section views. M1-HB3 and M1-HB4 failed in

the same manner by longitudinal shear delamination of the top web-flange junction, without any prior crushing of the reinforced concrete slab. They retained after failure a capacity of 50-60% of the maximum load.

In opposition, hybrid beams M2 had significantly more formed but less opened cracks than their M1 relatives. The cross-wise tensile flexural cracks in the slab were concentrated in the proximity of the two loading points and originated mainly from the shear connection positions. Longitudinal slip fissures were likewise visible at the ends of the hybrid beams. Around 80% of the ultimate load, the slab fractured along its midline and produced a jolt in the flexural load-deflection response. Failure occurred suddenly for both M2-HB3 and M2-HB4 due to a longitudinal shear of the top web-flange junction of the composite profile, as in the case of the previous M1 specimens, and was followed soon by global buckling of the web. Beams model M2 provided inconclusive recovery results during the four-point bending experiments.

Photographs of the main failure problems experienced by the M1 and M2 hybrid members in test setup II are illustrated together in Figure 3.35. Concrete cracks, inward slip and fiber delaminations were colored in bright red on the cross-section area.

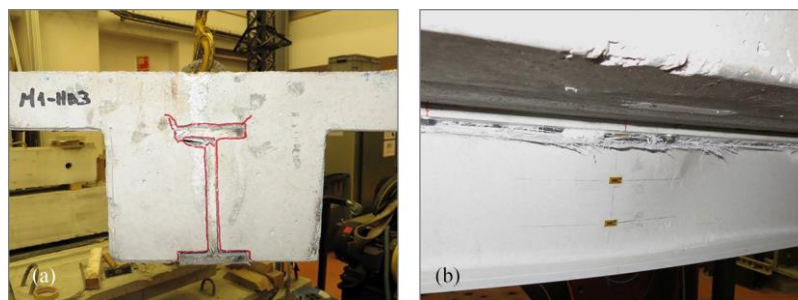


Figure 3.35: Failure characteristics of hybrid beams model M1 and M2 in test setup II: (a) M1 – profile top web-flange shear delamination; (b) M2 – profile top web-flange shear failure followed by global web buckling.

After the tests were completed, the visible cracks which remained on the hybrid beams were marked and the sketches grouped in Figure 3.36. Special attention should be paid to the cross section drawings as the web-flange failure cracks are rather short.

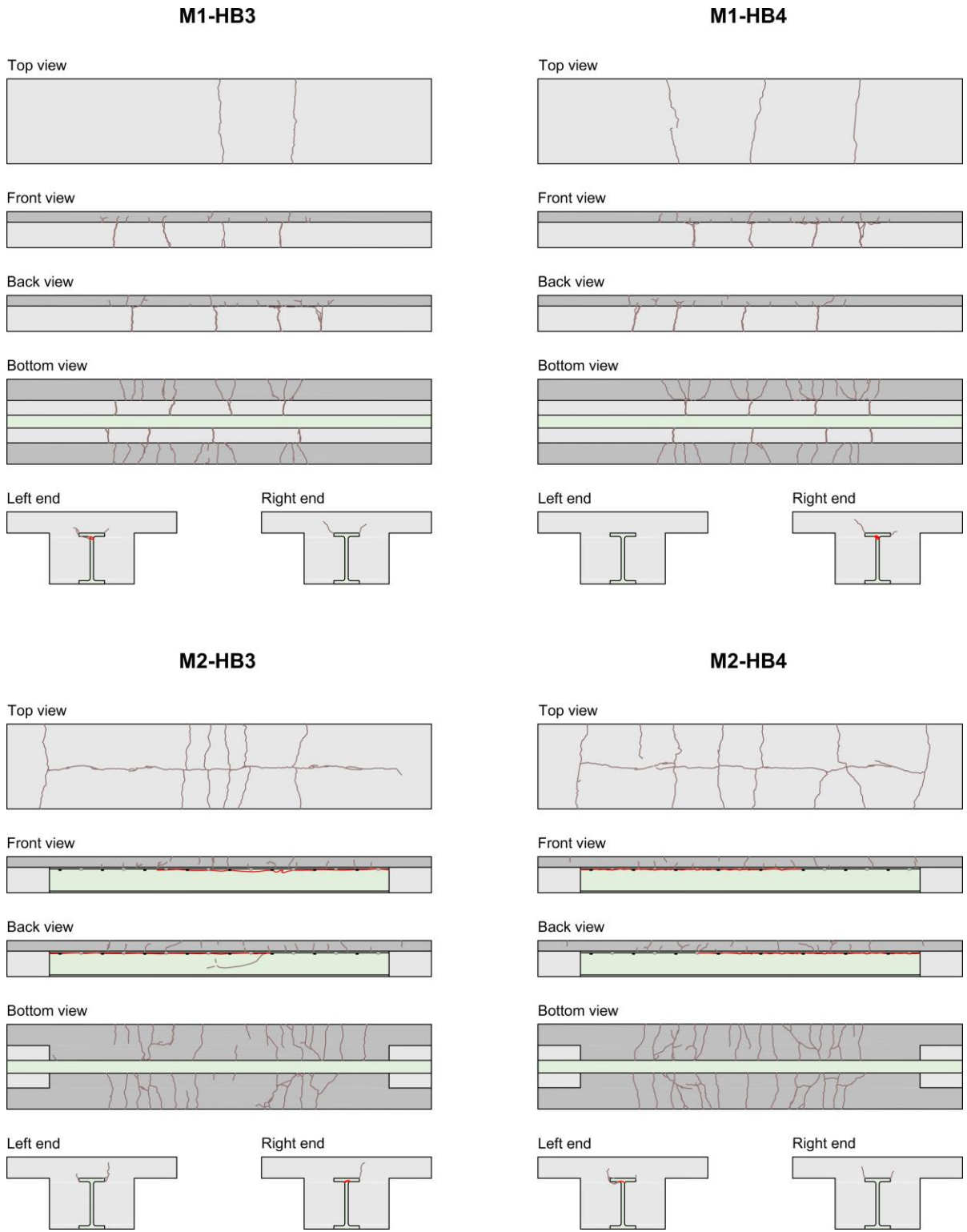


Figure 3.36: Visible crack patterns of hybrid beams in test setup II. Failure cracks are indicated in bright red.

3.6.2. Composite action and interlayer slip

Strain gauge readings were used to interpret the normal and angular strain distributions in the tested specimens, on both the concrete and glass FRP sections. In this way, a view of the developing composite action and interlayer slip strain was possible to be obtained. The complete set of experimental strain variation plots is to be found in Appendix B for the reference members and hybrid beams.

First of all, regarding the control specimens, the axial strain data variation on the concrete slab of reinforced concrete beams M0-RCB1 and M0-RCB2 captured the three stages of the typical flexural behavior of such structural members. There is a linear initial stage, where the concrete section was uncracked, a second, short irregular stage where cracks formed, and a third, longer linear stage where the existing fissures continued to open. Maximum compressive strains under 0.15% indicate that the concrete top at section S1 was still in the linear domain at the collapse of the two beams. The strain gauges placed transversely on the top surface of M0-RCB2 registered similar values across the experiment, proving that the whole slab width was effective.

Bottom flange longitudinal strain distributions and sectional axial strain variations measured in S1 and S2 for Profile 2 denote that the composite shape should have had a linearly-elastic flexural behavior up to failure. In exchange, the angular deformations of the web recorded by the pair of strain gauge rosettes exhibited an increasingly nonlinear variation toward higher shear loads, and thus presumably explaining why Profile 2 had slightly lower flexural stiffness approaching the end of the test. The nonlinear shear behavior could be related to the inhomogeneous nature of the composite profile built from unidirectional and multi-directional fiber arrangements.

Gauge readings at sections S1 and S2 were used to plot the variation of the axial strains in function of the applied load for the eight hybrid beams. Figure 3.37 illustrates the variation in S1 for the particular case of M2-HB4. Similar strains across the top slab suggest that the whole width of the concrete section was effective. This result is in agreement with the design code recommendations of Eurocode 4 for simply supported steel-concrete composite beams [80]. Negative strain values registered on the top flange of the GFRP profile indicate that the pultruded element started to work in compression at higher load levels. For the specimens which failed primarily due to slab crushing, concrete strain curves displayed maximum negative values in the vicinity of 0.3%. Maximum GFRP axial deformations in section S1 were in the range of 0.9% for the beams tested under three-point bending, respectively 0.6% for the specimens under four-point bending. Further observations reveal a linear tensile behavior coupled with a nonlinear compressive response for the composite profiles, significant jolts in the strain variations of beams model M1 due to the incidence of flexural cracks, and an increase in tensile strain nonlinearity near failure for the specimens loaded with a single concentrated force (signifying concrete slab crushing). Under test setup II the concrete slab of beam M1-HB3 and M1-HB4 displayed rather insignificant compressive and tensile strains until ~50% of the ultimate load.

The same data were used to plot the axial strains as a function of the beam's depth for different load levels, using a linear variation between strain measuring points. Hence, a better view of the composite action developing in the hybrid beams was obtained, exemplified here in Figure 3.38 for hybrid beam M2-HB4. As noticed, after 20 kN of load there was an increased slip strain between the concrete slab and the profile that led to the appearance of two neutral axes in the cross-section of the element. The first neutral axis of the T-shaped beam laid in the top concrete slab close to the steel reinforcement level, while the position of the second neutral axis moved from the connection toward the center of the composite member. The reduced composite action formed in the hybrid members allowed for the desired impact analysis of the connection's flexibility over bending behavior to be performed. Due to the relatively low elastic modulus of GFRP, shear has an important role in the behavior of short elements (height/span < 1/20) in the sense that at high stress levels the section does not remain plane after bending. This warping effect of the profiles is slightly visible in the axial strain distribution figures.

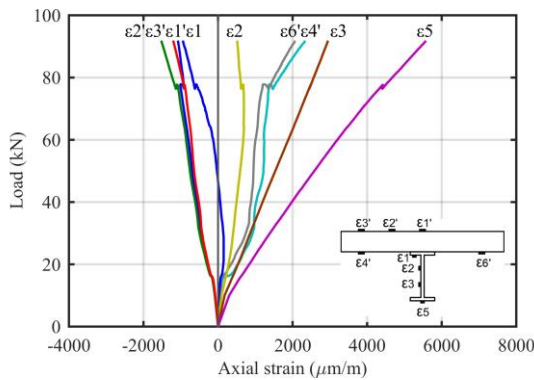


Figure 3.37: Hybrid beam M2-HB4, section S1: variation of axial strains in function of the applied load.

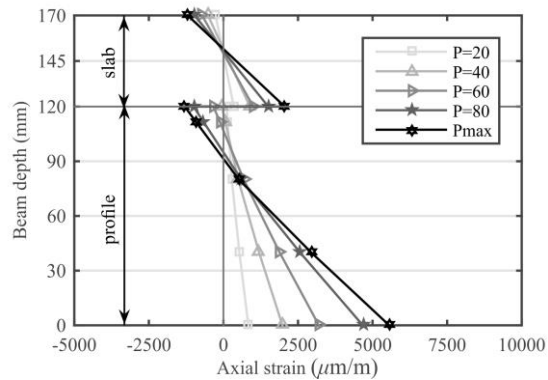


Figure 3.38: Hybrid beam M2-HB4, section S1: normal strain distribution at different load levels (kN).

Comparable strain variation and distribution plots were created for the deformation measurements acquired at section S2. Figure 3.39 and Figure 3.40 illustrate the two plots for the particular case of hybrid beam M2-HB4. Some of the previous observations made for the results in section S1 are still valid, where at higher loads the strain variations steered away from a linear behavior. One interesting remark is that as the top of the web got increasingly compressed, the top flange of the profile worked more and more in tension, and thus presumably contributed to the shear delamination failure mechanism. It is believed that the tensile stress in the top flange was heavily influenced by the presence of the shear connection bolts. Considering the small number of strain gauges and the linear interpolation, the transverse distributions did not capture accurately enough the results at the superior web-flange junction; however, a certain tendency could be discerned.

Normal transverse deformations in the profile's web computed from the pair of rosettes on the M2 beams were insignificant, with values around 0.1%. Strain variation differences between the two hybrid beam models and specimens with different concrete strengths proved also to be modest. Still, under the

same test setup configuration, the deformations in the M1 beams were slightly larger than in the M2 and the hybrid beams fabricated with superior concrete strengths (C2) had lower axial strains.

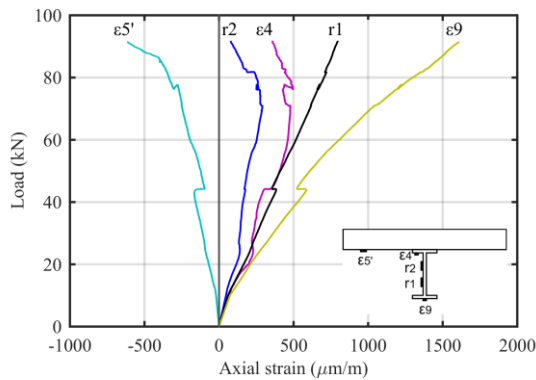


Figure 3.39: Hybrid beam M2-HB4, section S2: variation of axial strains in function of the applied load.

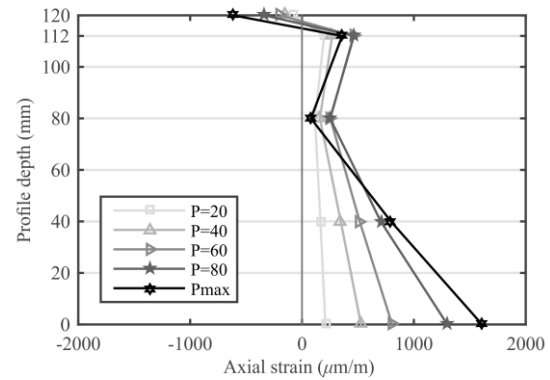


Figure 3.40: Hybrid beam M2-HB4, section S2: normal strain distribution at different load levels (kN).

Finally, data collected from the bottom flange of the profiles were used to chart the variation of the axial strains in longitudinal direction, from the left support to the center, in function of the applied load. As relevant cases, the charts of M2-HB2 and M2-HB4 are reported here in Figure 3.41 and Figure 3.42.

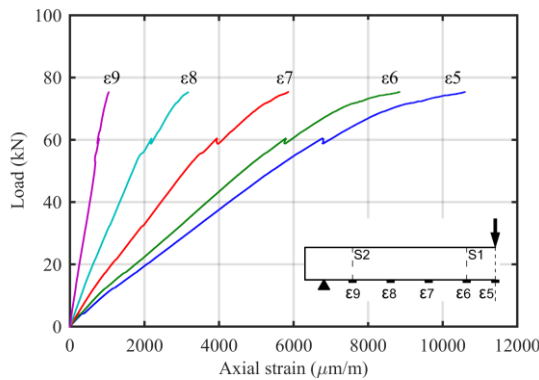


Figure 3.41: Hybrid beam M2-HB2: bottom flange axial strain variations.

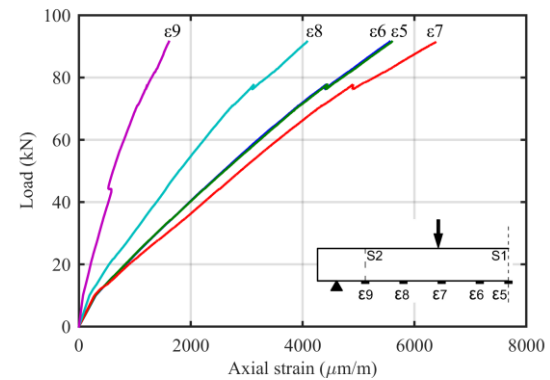


Figure 3.42: Hybrid beam M2-HB4: bottom flange axial strain variations.

Overall, maximum GFRP axial deformations were in the range of 1.2% for the beams tested under three-point bending, respectively 0.6% for the specimens under four-point bending. In contrast to the later specimens, the hybrid beams tested in the first test configuration exhibited nonlinear responses closer to failure and especially toward the midspan, as a sign of the concrete crushing in the slab and important local deformations being induced by the concentrated load. As anticipated, the largest nonlinearity occurred for M2-HB2 which failed from transverse web crushing as commented before. In test setup II, the largest axial strains were recorded under the applied loads with the rest of the midspan deformations following close by. The results of hybrid beams model M1 reflect again the appearance of flexural cracks, within their plots.

It must be said that obtaining reliable tensile deformation data from the bottom side of the concrete slabs proved to be challenging, often resulting in erroneous readings particularly at higher load levels where the cracks were not evenly spread or opened across the section. In those few cases, the data were corrected considering that the concrete section and composite profile deform with the same curvature.

Besides axial strains, angular deformations were evaluated close to the support regions in section S2, for hybrid beams M2 which had no concrete surrounding the web. Considering a uniform distribution of the shear stress in the profile's web and neglecting the contribution of the flanges, Figure 3.43 plots the in-plane shear stress variation in function of the applied shear force for M2-HB4. In all four cases, the variation observed was highly nonlinear in a pattern similar to the response of the second single pultruded profile (Profile 2). The inhomogeneous structure of the composite shape may have led to this kind of experimental shear behavior. Shear results were nearly identical for the four M2 hybrid beams regardless of the concrete strength.

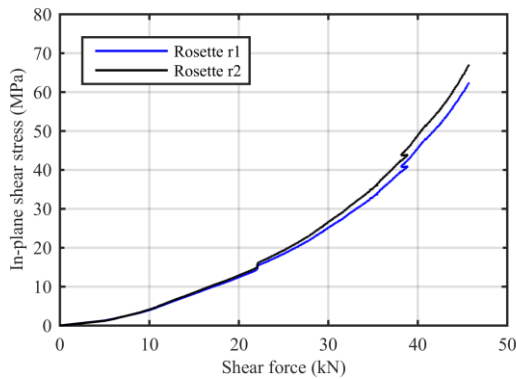


Figure 3.43: Hybrid beam M2-HB4, section S2: in-plane shear stress variation in function of the applied shear load.

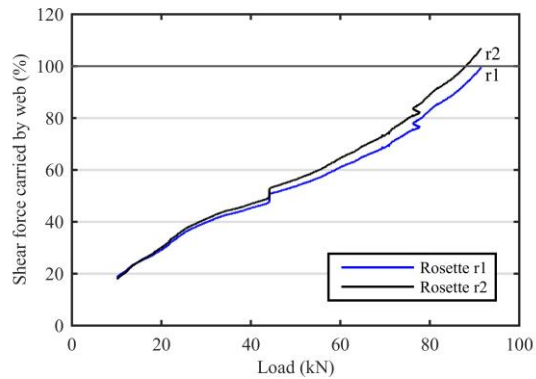


Figure 3.44: Hybrid beam M2-HB4, section S2: shear percentile carried by the profile in function of the applied total load.

Moreover, by plotting the variation of the shear force percentage carried by the composite profile against the total applied load, one could deduce the shear transfer mechanism between the concrete slab and GFRP section. Illustrated in Figure 3.44 for hybrid beam M2-HB4, the percentile variation suggests that the shear load was entirely transferred to the web of the profile before collapse. This type of analysis of the results tends however to overestimate the carried shear force due to the simplifying assumptions made.

Figure 3.45 exposes the appearance of the shear delamination failure for M2-HB1, as captured by the high-speed camera during testing. Noticeable are the cracks along the superior web-flange junction, the instantaneous uplift of the slab and the post-buckling of the web.

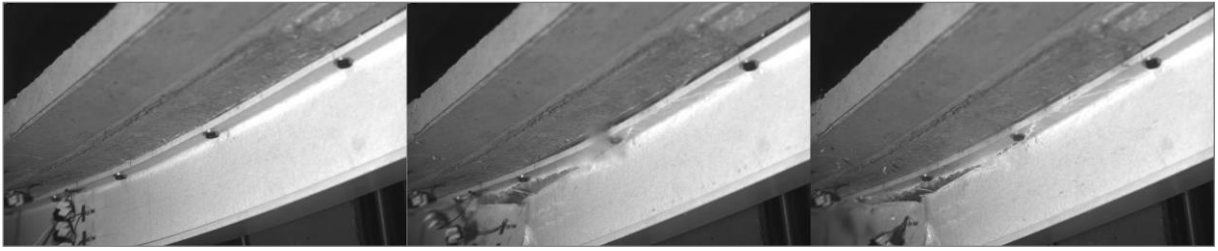


Figure 3.45: High-speed camera images taken during the shear delamination failure of M2-HB1.

The experimental slip strain-bending moment curves of the M2 hybrid beams were derived from the corresponding sectional axial strain distributions. The curves plotted in Figure 3.46 illustrate similar nonlinear responses with an exception residing in the fact that during the first testing phase the deformations attained were double in comparison with the results from the four-point bending tests.

The relative slip between the profile and the slab at the end of the hybrid beams is plotted in Figure 3.47 against the applied load ratio. Hybrid beams model M1 presented a complete shear interaction up to 40% of their ultimate flexural capacity whereas beams model M2 had a weaker shear interaction starting from about 25%. The average maximum interlayer slip was 1.7 mm for specimens type M1 and an almost double amount of 3.5 mm for type M2. Overall, hybrid beams model M1 displayed a higher composite action due to the concrete web which hindered the sliding of the steel bolts and the deformation of the GFRP profile. The concrete strength class had a similar influence, with higher strengths limiting the slip to a greater degree. What is noticeable about the two graphics is that although the beams were designed with a low degree of shear connection, slip strain and slip data reveal that there was an initial bond at the connection level, supposedly in the form of tangential friction and adhesion.

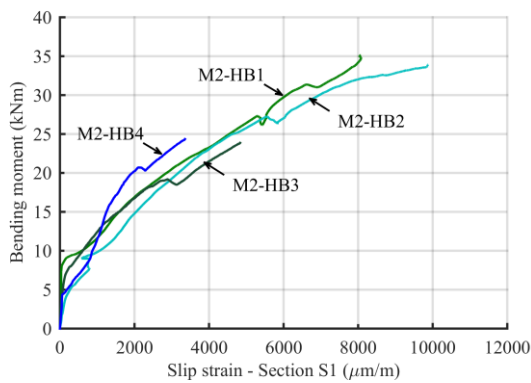


Figure 3.46: M2 hybrid beams: slip strain variation in function of the applied bending moment.

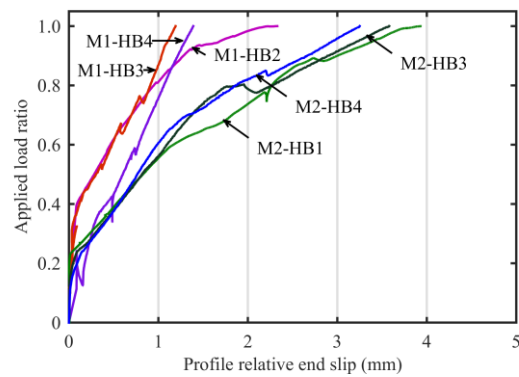


Figure 3.47: Relative end slip of the profiles versus load ratio.

The partial interaction effects attributed to the flexibility of the steel bolts and the shear delamination failures were not only noticed from numerical data but also during a visual inspection of the tested members, as illustrated in the images collated in Figure 3.48. Evidences show multiple signs of slip at the interface level and serious deformations of the connector shanks and drilled holes away from the center line, in the opposite direction of the compressive slab forces. Moreover, a visual examination of

the web-flange rupture areas found that the shear delamination surfaces formed between the central continuous strand mat of the web and the adjacent unidirectional fibers in the flange.



Figure 3.48: Visual evidence of partial shear interaction and shear failure: (a) occurrence of slip and junction shear; (b) deformation of bolts; (c) distortion of connector holes; (d) web-flange rupture; (e) top and bottom flange delaminations of M1-HB2; (f) radial inclination of bolts in M2-HB2 (concrete slab removed).

3.6.3. Comparative analysis

As final evaluation, a comparative analysis is made between the main outcomes of the experimental campaign. Table 3.14 summarizes the main results of the flexural tests involving the reference specimens and hybrid beams, at the moment of failure. The results are grouped depending on the loading configuration that was applied. In addition, several results are also included for the prior concrete crushing failure of M1-HB1, M1-HB2 and M2-HB1 (shown with ‘*cr*’ superscript).

Table 3.14: Experimental results of tested specimens at failure (*u* subscript): bending moment (*M*), midspan deflection (*w*), sustained load (*P*), shear load (*V*), bottom flange maximum axial stress (*σ*), average in-plane web shear stress (*τ*), and relative end slip (*s*).

Beam	Failure mode	M_u^{cr} (kN·m)	w_u^{cr} (mm)	$\frac{M_u^{cr}}{M_u}$	P_u (kN)	M_u (kN·m)	V_u (kN)	w_u (mm)	σ_u (MPa)	τ_u (MPa)	s_u (mm)
M0-RCB1	steel yielding ^a				56.8	25.6	28.4	16.5			
M1-HB1	web-flange shear ^b	34.2	36.5	0.94	80.7	36.3	40.4	42.6	420		n/a
M1-HB2	web-flange shear ^b	38.8	38.6	0.93	92.2	41.5	46.1	51.5	474		2.33
M2-HB1	web-flange shear ^b	34.9	50.2	0.99	78.1	35.1	39.1	52.5	406	64.4	3.94
M2-HB2	web crushing ^a				75.4	33.9	37.7	51.7	415	59.1	n/a
Profile 1	torsional buckling				23.5	10.6	11.7	22.2			
Profile 2	torsional buckling				47.4	21.3	23.7	46.5	360	37.5	
M0-RCB2	inclined shear crack				69.0	18.3	34.5	9.1			
M1-HB3	web-flange shear				81.4	21.6	40.7	23.4	210		1.19
M1-HB4	web-flange shear				85.9	22.8	43.0	22.4	218		1.39
M2-HB3	web-flange shear				89.7	23.9	44.9	35.2	256	59.9	3.58
M2-HB4	web-flange shear				91.5	24.3	45.8	33.6	250	64.7	3.25

^a Followed by concrete slab crushing.

^b Preceded by concrete slab crushing.

n/a – not available.

First off, it is noted that all hybrid members had superior flexural capacities compared to the equivalent reinforced concrete beams and single GFRP profiles. For the three test cases where concrete crushing occurred before the GFRP web had sheared, the associated bending moments were within 7% close to the ultimate shear capacity. In that small increasing load interval the midspan deflections grew considerably up to 33% for M1-HB2. All but one of the hybrid beams failed due to web-flange shear delamination. The ultimate deflections at shear failure were up to 23% higher for the model M2 specimens over M1 under three-point bending, and up to 50% under four-point bending. Aside from the model differences, the 16% gain in concrete strength led to marginal reductions of deflections and increases in bending moments. Figure 3.49 and Figure 3.50 illustrate the flexural capacity ratios computed for the hybrid beams against the equivalent reinforced concrete beams.

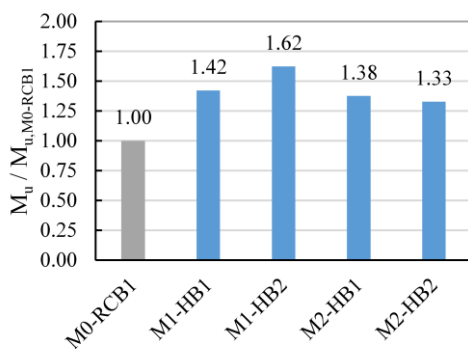


Figure 3.49: Bending capacity increase in hybrid beams vs. equivalent RC beam M0-RCB1, in test setup I.

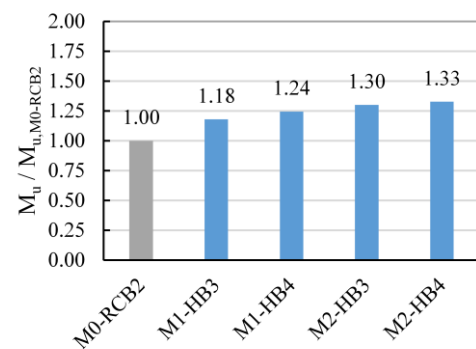


Figure 3.50: Bending capacity increase in hybrid beams vs. equivalent RC beam M0-RCB2, in test setup II.

Ultimate capacities were slightly lower for the M2 beams in the first bending configuration and a bit higher for the second load setup, when compared to the M1 beams. Nevertheless, the flexural capacities of the hybrid structural members were between 18-62% greater than those of the M0 classic beams. Opposed to the single GFRP pultruded profiles, the hybrid beams performed exceptionally well, with no instability type of failure and with triple or quadruple capacity ratios, as displayed in Figure 3.51. Apart from this, the tests have shown that a simple constructive measure such as installing web stiffeners can significantly improve the ultimate bending moment of the profiles.

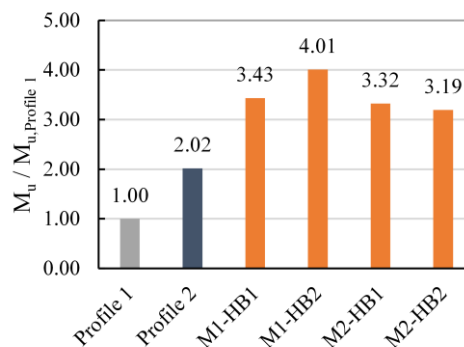


Figure 3.51: Bending capacity increase in hybrid beams vs. single GFRP profiles, under test setup I.

Maximum tensile stress results gathered from the bottom flange of the hybrid beam profiles indicate that the composite shape worked up to 78-91% of its tensile strength under a concentrated midspan load but as low as 40-50% under four-point bending. Web in-plane shear stress measurements were in the vicinity of 60 MPa for beams model M2 and results suggest that the entire shear load was carried only by the profiles before failure. The maximum shear stress values were higher than the material’s measured strength during the characterization tests, raising uncertainties about the nonlinear angular deformation behavior of the composite and the accuracy of the method used to determine this mechanical property.

The low degree of shear connection present at the interface between the concrete slab and the GFRP shape led to the formation of interlayer slip strains that reduced the flexural stiffness of the beams by an average of 47% and increased the midspan deflections by 53% or 58% depending on the test setup, when compared to the corresponding values of equivalent fully composite hybrid beam. The partial interaction behavior also increased the normal stresses in the sections and the internal bending moments.

One of the key aspects which defines the viability of these new hybrid GFRP-concrete solutions is represented by the ratio between the maximum flexural capacity of the members and the self-weight. Figure 3.52 and Figure 3.53 illustrate the calculated structural efficiency of the three investigate models – M0, M1 and M2 – under the two bending test setups.

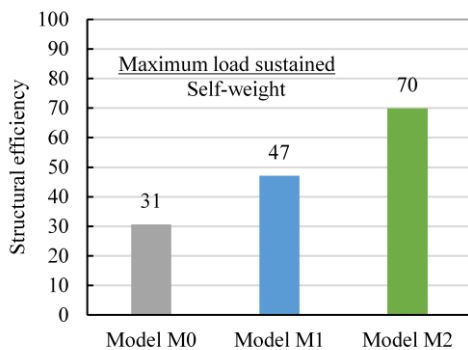


Figure 3.52: Structural efficiency of investigated beam models under test setup I.

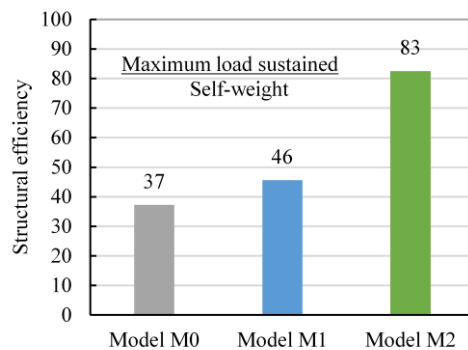


Figure 3.53: Structural efficiency of investigated beam models under test setup II.

Even if the concrete surrounding the composite profiles in hybrid beams model M1 limited the growth of the interlayer slip and general deflections, due to the added mass the structural efficiency of the first model is significantly decreased. On the other hand, the structural efficiency of hybrid beams model M2 was much higher, more than double in comparison to the equivalent reinforced concrete specimens.

3.7. Conclusions

The present chapter analyzed the experimental structural performance of hybrid beams made of pultruded fiber-reinforced polymer (FRP) profiles mechanically connected with steel bolts to reinforced concrete slabs, suitable for building floors and footbridge or marine pier superstructures. Because the flexural behavior of a hybrid element relies greatly on the connection system, a low degree of shear interaction was considered in this work to study its effects.

In the first part of the chapter, the physical and mechanical properties of the constitutive materials of the hybrid members to be designed were analyzed. Henceforth, the following main observations were made:

- A microscopic analysis of the internal structure of the pultruded profiles used in the investigation revealed the existence of additional multi-directional fiber reinforcements at the central vertical plane of the profile's web and highlighted the presence of minuscule pores in the cross-section of the element. More importantly, it was observed that the web-flange junction constitutes a sensitive-to-failure transition region.
- The mechanical properties reported by the manufacturer were incomplete for appropriate analytical calculations or numerical simulations, and might have been altered by safety coefficients. Consequently, an extensive set of in-house characterization tests was performed in order to determine the flexural, tensile, compressive, shear, and full section properties of the composite shapes, for which CEN, ISO and ASTM International standards were followed. The GFRP IPE shape was found to exceed the minimum standard requirements of EN 13706-3:2002 for structural profiles.
- The obtained mechanical properties displayed reduced statistical scattering, with coefficients of variation under 11%, and were greater than the values specified by the producer. Similar results were obtained for both the web and flange extracted coupons. The registered experimental responses of the specimens were linearly-elastic with the exception of the in-plane transverse compressive stress and in-plane shear stress behaviors. The aforementioned nonlinear responses were attributed to the inhomogeneity of the composite profile and to the intrinsic behavior of the polyester matrix.
- The in-plane shear strength experiments revealed certain difficulties in obtaining a reliable property value. Research shows that even the other methods applied so far, the tensile tests on double-lap joints or the 10° off-axis tests, have some limitations. Furthermore, to this point there is no European standard in this sense for anisotropic materials made up of unidirectional and multidirectional fiber reinforced polymers.

With the materials analyzed, eight hybrid beams were fabricated having two different cross-section models – M1 and M2 – and two concrete strength classes. The beams resembled current steel-concrete composite members with the special mention that specimens model M1 had the profiles also laterally encased in concrete. The interlayer shear connection was provided by a flexible mechanical joint of manually-installed steel bolts.

In the second part of the chapter, a nondestructive hybrid beam characterization method was developed to obtain in a fast and reliable manner the mechanical elastic properties of the constitutive materials of the system. The subsequent remarks are reported regarding the procedure's methodology and results:

- The proposed nondestructive method is based on the analysis of the free vibration response of profiles and hybrid specimens, and combines the results of an experimental and numerical modal analysis within an adaptive parameter identification method. In the procedure, the elastic constants were estimated by matching the dynamic properties of the tested beams from the results of a roving impact modal analysis with the dynamic properties of a finite element model of the physical structure that had variable generated material data.
- The adaptive parameter identification method consisted of an iterative procedure during which the elastic constants of the materials were sampled between set intervals and the dynamic properties of the specimens were updated so that the multiple objectives and constraints established could be satisfied with the use of the genetic algorithm. After a prior parameter correlation study, the objectives that sought to equal the first dominant mode shape frequencies were ranked as more important within the algorithm.
- For the single GFRP profile and the two hybrid beams, the first bending and torsional mode frequencies were fit with very good precision. Computed frequency errors for the profile were in the range of 2% for the bending mode shapes and slightly higher for the torsional modes. In the case of the M2 hybrid beams, the maximum calculated errors were about 13%. In all the simulations, the finite element model matched uniformly both lower and higher natural frequencies in the measured spectrum.
- The method proved to be a viable alternative to characterizing the elastic constants of hybrid beams by means of static tests. The mechanical properties obtained resembled the previously determined laboratory values, with a maximum difference of 12% for the in-plane shear modulus. It was also noted that the method has a minor tendency of overestimating results.
- For the nondestructive method to succeed, the experimental modal analysis has to be performed under well-known boundary conditions, and a parameter correlation study should be carried to determine the factors which have the largest impact so as to reduce the complexity of the computational model.

In the last part of the chapter, the results of the main experimental campaign were analyzed and discussed. The flexural behavior of the designed GFRP-concrete hybrid beams with flexible shear connection was assessed from multiple perspectives and in a comparative manner. The following conclusions were drawn from the study:

- To begin with, all the hybrid specimens exhibited a generally bilinear load-midspan deflection response composed of an initial segment of complete shear interaction and a larger segment where interlayer slip developed between the composite profile and the concrete slab.
- Normal strength concrete allowed for a pseudo-ductile type of failure, where crushing of the concrete slab constituted a warning sign of the imminent collapse for three of the eight hybrid beams. Crushing was associated with significant degradation in the measured flexural response and was observed only under three-point bending (test setup I).
- The hybrid designs had around 47% less flexural stiffness than the same models under virtual complete shear interaction assumptions. This led to a 53% average increase in midspan deflections in test setup I, and a 58% average increase under four-point bending (test setup II).
- Brittle delamination of the GFRP profile's web-flange junctions constituted the primary type of failure for seven of the eight hybrid members and was caused mainly by high shear stress concentrations. The remaining hybrid beam collapsed due to a transverse crushing of the profile's web under severe local loading. Concrete jacketing of the web was found to be a viable solution in mitigating premature breaks at the reaction points. At higher load levels, warping of the open section of the profiles became noticeable in the sectional strain distributions.
- Compared to the single pultruded GFRP profiles, the hybrid beams had superior ultimate capacities, double flexural stiffness and no instability type of failure. The capacities were double in comparison to the profile which had web stiffeners installed and almost four times as big as the maximum moment displayed by the simple GFRP profile.
- Compared to the equivalent reinforced concrete beams, the most effective hybrid member supported 62% higher loads in three-point bending and 33% in four-point bending. Nevertheless, the flexural stiffness was lower due to the elastic modulus of the GFRP and especially to the low degree of composite action.
- Maximum axial strains registered on the bottom flange of the profiles were in the range of 1.2% in test setup I and 0.6% in test setup II. This translates to an exceptional use of the composite's tensile properties of 78-90% in the first batch of tests and 40-50% in the second part of the experimental campaign.
- Shear stresses computed from the angular deformations of the profile webs exceeded the material's determined strength by 20%. Furthermore, the shear response proved to be highly

nonlinear. These issues raised certain doubts about the current methods used to characterize the in-plane shear strength of inhomogeneous FRP composite materials.

- Two types of cross-section hybrid models – M1 and M2 – were considered in the experimental campaign, the difference residing in the lateral confinement of the profile for the first model. Overall, similar responses were registered for both types; however, beams M1 had a more rigid mechanical connection with slip values at half of those of M2, a stiffer and more linear load-midspan deflection response and at least a 50% recovery capacity after collapse. Axial strains were slightly higher in the M1 specimens and partial interaction occurred at about 40% of the maximum capacity as opposed to 25% for the second model.
- The increase in concrete strength improved marginally the ultimate bending capacity and stiffness, and decreased the midspan deflections, axial strains and interlayer slips. There were inconclusive slip strain changes and the experimental in-plane shear stress differences were negligible.
- Overall, hybrid beams model M2 had the highest structural efficiency as their weight was about half of the rest. A stiffer mechanical joint could compensate for the effects of concrete lateral confinement over connection slip and profile deformations.

In the end, the experimental data that resulted from the real-scale flexural tests was also used to validate the analytical and numerical models presented in Chapter 4 and Chapter 5.

4

Analytical procedure

4.1. Introduction

The following chapter addresses the need for a robust analytical design procedure for hybrid FRP-concrete beams that takes into consideration the effects of shear interaction behavior. The main reason for this stems from the bibliographic research which has suggested that authors so far have often estimated the flexural performance of these novel elements without accounting for the connection's flexibility, even though interlayer slip had been observed experimentally. Moreover, the main codes that regulate the design of steel-concrete composite members deal with the slip effects only from the perspective of the degree of shear connection (*i.e.*, shear capacity of connectors) or simply ignore them altogether through the use of appropriate detailing measures. However, it must be noted that due to the nature of mechanical connections in hybrid beams, the same assumptions may not be justified.

Since hybrid beams with bonded or combined joints exhibit limited slippage and hybrid beams with mechanical joints display a lower degree of composite action, relations for both complete and partial interaction assumptions are provided in the current study for the majority of the discussed aspects. Besides, for achieving full shear interaction, high performance materials require more shear connectors, but because of the limited number that a top flange can accommodate for an optimal design and due to the stiffness of the connection system, a partial composite design may be selected.

In the proposed analytical procedure, the flexural behavior of the hybrid members is modeled using the Timoshenko beam theory and the elastic interlayer slip principles extended from steel-concrete and timber-concrete composite beams. The interaction effects are included only in the bending component of the Timoshenko composite beam model, after being evaluated for an equivalent shear-rigid composite member.

Partial interaction effects are quantified by using a dimensionless parameter that relies mainly on the connection's shear modulus. Additional expressions of it are derived from other analytical models found in literature and from past or current design codes. With the help of a parametric study, a proper simplified solution is identified to be feasible for practice use, in the sense that is sufficiently close to

the exact formulation. In direct correspondence, exact and approximate relations are presented for estimating deflections, flexural stiffness, interlayer slip, bending capacities, and normal and shear stress distributions under different interaction conditions.

The procedure starts with the serviceability analysis of hybrid beams, where formulas for deflections and flexural stiffness are indicated. Regarding the structural restrictions, admissible midspan deflection rules and excessive vibration limitations are reported. Further along, expressions for estimating the internal actions, stress and interlayer distributions under linear-elastic presumptions are obtained and commented. In the second part of the analytical procedure, that relates to the ultimate limit state considerations, special attention is given to determining the flexural capacity of hybrid beams and to the additional failure criteria that may be applied.

The analytical procedure was validated successfully against available experimental data for hybrid beams with mechanical shear connections and against the results obtained during the experimental campaign performed by the author and reported in Chapter 3. In this way, the viability of using approximate solutions for partial interaction effects was also assessed. The validation process incorporates serviceability and failure analysis coupled with flexural behavior predictions. Normal and shear stress distribution evaluations are likewise included.

4.2. Scope

The most common way found to model analytically the flexural behavior of composite beams is by using the Euler-Bernoulli composite beam theory with no interlayer relative displacement considerations. However, in FRP-concrete members, a notable degree of slip can develop at the interface between the two sections that can cause a reduction of the beam's stiffness and thus an increase in bending flexibility. In addition, there's a significant contribution to deflections from angular deformations produced in the web of the profiles. Therefore, the flexural behavior of a hybrid beam is better characterized by the Timoshenko composite beam theory with partial shear interaction, as shown in Figure 4.1.

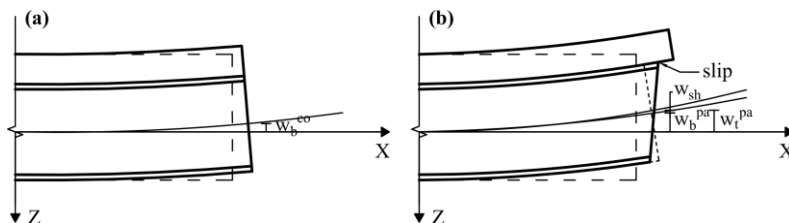


Figure 4.1: Analytical models for the flexural behavior of a hybrid beam: (a) Euler-Bernoulli composite beam with complete shear interaction; (b) Timoshenko composite beam with partial shear interaction.

Consequently, the following sections present analytical formulations suited for characterizing the short-term flexural behavior of Timoshenko hybrid beams under both complete and partial interaction

situations. Mathematical expressions for evaluating deflections, slippage, flexural capacities and stress distributions are discussed for a member composed of an I-shaped pultruded FRP profile connected to a rectangular reinforced concrete slab, as illustrated in Figure 4.2. The formulations can be extended to other prismatic, vertically symmetric cross-sections.

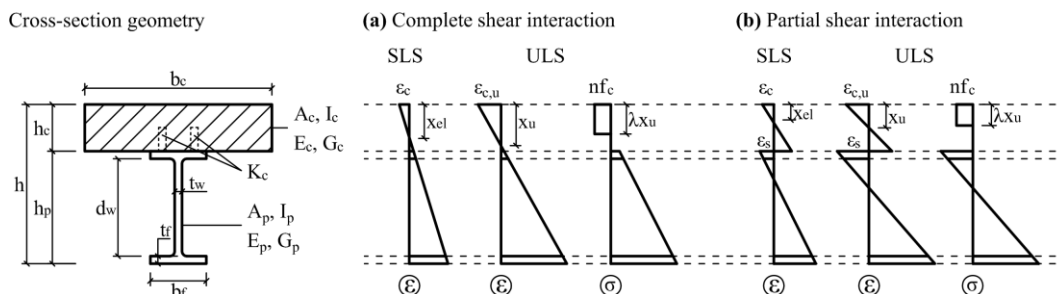


Figure 4.2: Generic hybrid cross-section geometry with corresponding strain (ϵ) and stress (σ) distributions, at SLS and ULS, considering: (a) complete or (b) partial shear interaction.

The composite profile is expected to behave elastically up to failure while the concrete has a typical nonlinear constitutive law as described in Eurocode 2 [130]. The orthotropic mechanical properties of the composite material are the same in the web and flanges, thus the profile’s section is regarded as transversely isotropic. At the Serviceability Limit States (SLS) the neutral axis is defined by x_{el} and the concrete’s compressive strain by ϵ_c . At the Ultimate Limit States (ULS), the concrete’s compressive stress distribution is simplified as a rectangle characterized by parameters λ and n , which are equal to 0.8 and 1.0 for concrete strength classes $\leq C50/60$. The depth of the neutral axis is designated x_u , the ultimate compressive strain $\epsilon_{c,u} = 3.5\%$, the compressive strength of concrete f_c , and the slip strain developing at the interface is denoted ϵ_s . Material and design safety coefficients are not included in the formulas.

The scope of the analysis is restricted to beams subjected to positive bending, so serviceability aspects (SLS) and failure criteria (ULS) are discussed for this specific condition. In order to obtain closed-form solutions to the upcoming differential equations, three statically determinate beam cases are considered and depicted in Figure 4.3. The loads Q , $2Q$ and q_0 are applied over a span L and the displacements (deflections) registered in the Z direction are denoted with $w(x)$ for the corresponding coordinate along the X axis. Other static cases can be solved in a similar manner by applying the appropriate boundary conditions.

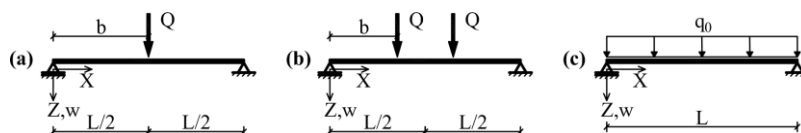


Figure 4.3: Static cases analyzed. Simply-supported hybrid beams subjected to: (a) a midspan point load; (b) two symmetrically applied point loads; (c) a uniformly distributed load.

4.3. Serviceability limit states (SLS)

Due to the high strength-to-weight ratio of composites and superior compressive properties of concrete, hybrid structures can be designed to span greater lengths than equivalent structures built with traditional materials. The downside of these novel elements is that their design tends to be governed by serviceability criteria rather than strength due to the reduced stiffness of pultruded FRP structural shapes. Hence, the following section presents the formulas needed to calculate the deflection and flexural stiffness under complete or partial shear interaction conditions.

4.3.1. Deflection and flexural stiffness

4.3.1.1. Complete shear interaction

The analytical model of an FRP-concrete hybrid beam with complete shear interaction is based on the following assumptions:

- plane sections remain plane after deformation;
- there is no vertical separation or longitudinal slippage between the pultruded FRP profile and the reinforced concrete slab;
- the top steel reinforcement contribution is neglected;
- the whole width of the concrete slab is effective.

In addition, the evaluation of deflections is performed under the elastic range of the beam's constitutive materials because hybrid members possess an inherent generally linear behavior until failure.

Due to the high ratio between the longitudinal elastic modulus and the shear modulus of pultruded orthotropic composite materials, it is necessary to consider also the shear deformation contributions in computing deflections. Thus, the elastic curve that describes the deflected shape of a hybrid FRP-concrete element is a function of its flexural rigidity EI and transverse shear rigidity κGA . Consequently, the total deflection at a certain point, $w_t^{co}(x)$, is expressed as the sum of the deflection due to bending deformation $w_b^{co}(x)$ and the deflection due to shear deformation $w_{sh}(x)$:

$$w_t^{co}(x) = w_b^{co}(x) + w_{sh}(x) = \frac{f_i(x)}{EI_{co}} + \frac{g_i(x)}{\kappa GA} \quad (4.1)$$

where $f_i(x)$ and $g_i(x)$ are functions given by the elasticity theory which depend on the load and supporting conditions. The functions are provided in Table 4.1 for the three common load arrangements illustrated in Figure 4.3.

Table 4.1: Deflection functions for simply supported beams.

Load type	Coordinate domain	$f_i(x)$	$g_i(x)$
Point load at midspan	$x \in [0, L/2]$	$f_1(x) = \frac{Qx}{48}(3L^2 - 4x^2)$	$g_1(x) = \frac{Qx}{2}$
Two point loads at a distance b from the supports	$x \in [0, b]$	$f_2(x) = \frac{Qx}{6}(3Lb - 3b^2 - x^2)$	$g_2(x) = Qx$
	$x \in [b, L/2]$	$f_2(x) = \frac{Qb}{6}(3Lx - 3x^2 - b^2)$	$g_2(x) = Qb$
Uniformly distributed load	$x \in [0, L/2]$	$f_3(x) = \frac{q_0x}{24}(L^3 - 2Lx^2 + x^3)$	$g_3(x) = \frac{q_0x}{2}(L - x)$

The bending function represented by $f_i(x)$ has the same expression in both shear deformation theory and Euler-Bernoulli classic beam theory. In the discussed example of a simply supported (statically determined) member, if Timoshenko beam theory is used, the internal forces are not a function of the deflections as opposed to the case of statically indeterminate beams.

The flexural rigidity under complete interaction conditions can be obtained from the following relation:

$$EI_{co} = EI_0 + \overline{EA} \cdot d_c^2 \quad (4.2)$$

where:

$$EI_0 = E_c I_c + E_p I_p \quad (4.3)$$

$$\overline{EA} = \frac{E_c A_c \cdot E_p A_p}{E_c A_c + E_p A_p} \quad (4.4)$$

where EI_0 represents the flexural rigidity when there is no shear interaction, \overline{EA} the axial stiffness ratio and d_c the distance between the centroids of areas A_c and A_p , equal to $(h_c + h_p)/2$. Variables E_c and E_p represent the longitudinal elastic moduli of the concrete and the profile, with effective value for the latter, while I_c and I_p are the principal moments of inertia of the two. If the slab cracks under tension, only the compressed concrete area should be considered for calculating I_c .

Alternatively, the equivalent stiffness of the transformed section, EI_{co} , can be obtained by calculating the depth of the neutral axis, x_{el} :

$$x_{el} = \frac{E_p A_p (h_c + h_p/2) + E_c A_c h_c/2}{E_p A_p + E_c A_c} \quad (4.5)$$

$$EI_{co} = \frac{E_c A_c h_c^2}{12} + E_c A_c \left(x_{el} - \frac{h_c}{2}\right)^2 + E_p I_p + E_p A_p \left(h_c + \frac{h_p}{2} - x_{el}\right)^2 \quad (4.6)$$

After cracking occurs in the concrete slab, the neutral axis and flexural stiffness can be obtained from the following equations:

$$E_c b_c x_{cr}^2 + 2E_p A_p x_{cr} - 2E_p A_p \left(h_c + \frac{h_p}{2} \right) = 0 \quad (4.7)$$

$$EI_{cr} = \frac{E_c b_c x_{cr}^3}{3} + E_p I_p + E_p A_p \left(h_c + \frac{h_p}{2} - x_{cr} \right)^2 \quad (4.8)$$

When it comes to the shear rigidity of a hybrid beam, based on the fact that the majority of the shear stress in a composite member develops in the web of the profile, it can be assumed in a conventional approach that its effective value can be approximated as:

$$\kappa GA \approx G_p A_w \quad (4.9)$$

where κ is the Timoshenko shear coefficient, GA transverse shear rigidity of the beam, G_p the effective in-plane shear modulus of the FRP profile, and A_w is the profile's web area. Several studies [190–197] have proposed various expressions for computing the shear coefficient for thin-walled composite profiles but nevertheless they prove to be too complex for current use. In the end, the differences between the exact and approximate methods of determining the transverse shear rigidity for an I-shaped profile have been reported in [1] to be between 10 and 20%, with the approximate method giving a lower value which translates into a higher predicted shear deflection that is safer from a design perspective.

While some design codes recommend including all the time shear deformations in the analysis of flexural members, others specify that for span-to-depth ratios greater than 20, the shear influence can be neglected with errors in deflection computation below 5%. However, in certain scenarios, ignoring the concrete's contribution is not satisfactory so the shear coefficient for the whole section can be obtained from the following expression developed by Timoshenko [198]:

$$\kappa^{-1} = \frac{A}{I^2} \int_A \frac{S^2(z)}{b(z)} dA \quad (4.10)$$

where A represents the total area of the beam, I its corresponding principal moment of inertia, S first moment of area at vertical coordinate z (measured from the neutral axis), and $b(z)$ the measured width at the same coordinate z .

For the serviceability limit state, the calculated maximum deflections must be less than the maximum admissible deflections specified in building codes. Eurocode 4 [80] defines a limit of $L/250$ for the quasi-permanent load combination, for composite members that do not support fragile elements, and $L/500$ otherwise. The ASCE Structural Plastics Design Manual [73] limits deflections to $L/180$ for visual appearance and $L/400$ for vibration sensitivity. The Eurocomp Design Code and Handbook [12] recommends limiting instantaneous deflections to $L/300$ and long-term deflection to $L/250$ for frame structures. The Italian Guide for Structures made of FRP Pultruded Elements [74] recommends limiting the deflection to $L/250$ for the quasi-permanent load combination for floors and to $L/100$ for pedestrian bridges, for the rare load combinations. All in all, a general limitation of $L/250$ for the maximum

deflection of hybrid FRP-concrete beams in buildings is thought to be suffice for the quasi-permanent load combination.

4.3.1.2. Partial shear interaction

If a partial interaction model is considered in the design, relative deformations are allowed at the interface between the FRP profile and concrete slab. It is therefore necessary to know how the behavior of a hybrid beam is modified by the presence of slip. The shear-slip behavior between the FRP and concrete is problematic, presenting similar characteristics to the steel-concrete slip behavior. Nevertheless, studies [97] have shown that the shear-slip relation can be simplified as linear elastic under service load, in situations in which forces on connectors do not exceed about half their ultimate strength.

The current analytical model of an FRP-concrete hybrid beam with partial shear interaction is based on the following assumptions:

- shear connection stiffness is uniform and continuous along the interface;
- there is no vertical separation between the composite profile and the reinforced concrete slab;
- Bernoulli's hypotheses are applicable to both materials independently;
- the top steel reinforcement contribution is neglected;
- the whole width of the concrete slab is effective.

As before, the evaluation of deflections is performed under the elastic range of the beam's constitutive materials.

In the discussed partial interaction models, the connected sections are considered to be shear-rigid, *i.e.*, the shear deformability is neglected for both connected layers, when quantifying the effects of the interlayer slip from the perspective of shear deflection contributions (w_{sh} is thus not affected by slip).

The study extends the method presented in [103] of using a dimensionless parameter ξ that takes into account the influence of the reduced flexural stiffness due to connection flexibility, by affecting only the bending deflection under complete interaction assumptions:

$$w_b^{pa}(x) = (1 + \xi) \cdot w_b^{co}(x) \quad (4.11)$$

where the corresponding effective flexural rigidity is:

$$EI_{eff} = \frac{EI_{co}}{1 + \xi} \quad (4.12)$$

Hence, the total deflection in the partial interaction model is obtained from:

$$w_t^{pa}(x) = w_b^{pa}(x) + w_{sh}(x) \quad (4.13)$$

By using an inverse approach, it is possible to obtain ξ from the deflection formula suggested in an earlier version of Eurocode 4 [81], for steel-concrete composite beams:

$$\xi_{EC4} = c(1 - \eta) \left(\frac{EI_{co}}{E_p I_p} - 1 \right) \quad (4.14)$$

where c is 0.5 for propped and 0.3 for unpropped construction, and η represents the degree of shear connection based on the total capacity of the studs over the minimum internal axial force needed to be transferred.

Similarly, a second expression for ξ can be obtained from the equivalent flexural rigidity of composite beams discussed in Commentary part I3 of the American Specifications for Structural Steel Buildings ANSI/AISC 360-05 [199]:

$$\xi_{AISC-05} = \frac{EI_{co}}{E_p I_p} \left[1 + \sqrt{\eta} \left(\frac{EI_{co}}{E_p I_p} - 1 \right) \right]^{-1} - 1 \quad (4.15)$$

In the updated version of the specifications, ANSI/AISC 360-10 [84], an effective moment of inertia is introduced to account for the amplification effects of the inelastic behavior. Thus, the partial interaction parameter becomes:

$$\xi_{AISC-10} = \frac{1}{0.75} \cdot \frac{EI_{co}}{E_p I_p} \left[1 + \sqrt{\eta} \left(\frac{EI_{co}}{E_p I_p} - 1 \right) \right]^{-1} - 1 \quad (4.16)$$

For steel-concrete composite beams with partial shear connection at the cross-section, the Australian Standard AS 2327.1-2003 [85] indicates in Appendix B the use of an effective second moment of area in the evaluation of deflections. From the expression provided, the following formula of the dimensionless parameter is obtained:

$$\xi_{AS} = \left[1 + 0.6(1 - \eta) \left(\frac{E_p I_p}{EI_{co}} - 1 \right) \right]^{-1} - 1 \quad (4.17)$$

According to Eqs. (4.14-4.17), if a sufficient number of connectors is installed in a composite beam, *i.e.* $\eta = 1$, then $\xi = 0$ and the deflection is the same as under complete interaction assumptions. Nevertheless, research [200] has shown that even in these cases deflections larger than predicted may occur, and hence it is necessary to include the connection's stiffness in evaluating the partial interaction parameter ξ .

From push-out tests performed on shear connectors, a typical load ratio-slip response is registered similar to the one plotted in Figure 4.4. The secant slope of the initial linear elastic response is known as the connection stiffness K_c . Deriving a reliable design formulation for calculating K_c presents difficulties and where experimental data is unavailable empirical formulations obtained from previous research may be used. In the case of steel-concrete composite beams with conventional steel studs, after

performing a large number of push-out test, Oehlers and Coughlan [201] deduced the following expression from statistical interpretation:

$$K_c = \frac{P_{max}}{d(0.16 - 0.0017f_c)} \quad (4.18)$$

where P_{max} is the maximum capacity of a connector, d its diameter, and f_c represents the concrete slab's compressive strength.

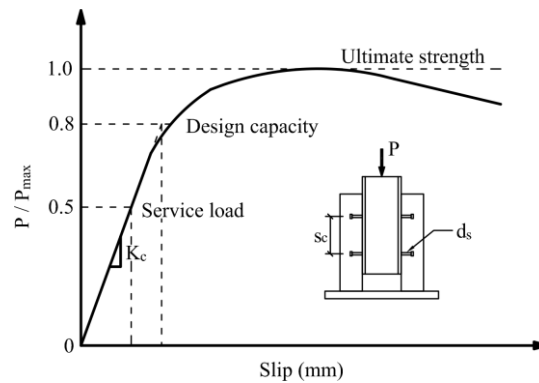


Figure 4.4: Typical load ratio-slip curve for a steel shear stud.

The shear connector capacity specified in Eurocode 4 is found from:

$$P_{max} = \min\left[0.8f_u(\pi d_s^2/4); 0.29d_s^2\sqrt{f_{ck}E_{cm}}\right] \quad (4.19)$$

where, f_u is the ultimate tensile strength of the stud and E_{cm} is the mean secant modulus of concrete.

Since hybrid FRP-concrete beams have a similar configuration to steel-concrete composite beams it is possible to use the same kind of tests or analytical expressions in the evaluation of connection strength and stiffness. For timber composite beams, Eurocode 5 [86] suggests an empirical formula for the connector's stiffness based on the density of the connected materials; however, during the validation procedure this second expression was found to be inappropriate for hybrid beams, so Eq. (4.18) was used consequently throughout this study.

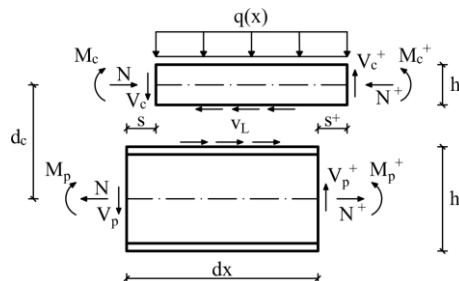


Figure 4.5: Differential element for a hybrid pultruded FRP-concrete beam with partial interaction.

Starting from a differential element of an FRP-concrete hybrid beam with partial shear interaction, as depicted in Figure 4.5, and by writing the appropriate equilibrium and compatibility equations

[100,110,202] based on the hypotheses mentioned before, one could arrive at the following two differential equations needed for determining the exact bending deflection $w_b^{pa}(x)$:

$$\frac{\partial^6}{\partial x^6} w_b^{pa}(x) - \alpha^2 \frac{\partial^4}{\partial x^4} w_b^{pa}(x) = \frac{1}{EI_0} \frac{\partial^2}{\partial x^2} q(x) - \alpha^2 \frac{1}{EI_{co}} q(x) \quad (4.20)$$

$$\frac{\partial^2}{\partial x^2} N(x) - \alpha^2 N(x) = -\frac{K_c d_c}{s_c EI_0} M(x) \quad (4.21)$$

where $M(x)$ is the total bending moment acting on the element, $N(x)$ the axial force, s_c the longitudinal spacing of the connectors, and α is given by:

$$\alpha = \sqrt{\frac{K_c EI_{co}}{s_c EI_0 \bar{E}A}} \quad (4.22)$$

Solutions to differential Eqs. (4.20) and (4.21) can be found by applying suitable boundary conditions, where at specific coordinates along the beam the deflection or its derivatives (slope and curvature), internal axial forces or bending moments have a known value. As a result, the exact closed-form solutions to the bending deflection contributions of hybrid beams with partial shear interaction were obtained using a computational software program, *Mathematica*, for the three static cases illustrated in Figure 4.3.

For Figure 4.3(a), $x \in [0, L/2]$, the exact bending deflection expression and maximum bending deflection solution are as follows:

$$w_{b,1}^{pa}(x) = w_{b,1}^{co}(x) + \frac{Q}{2\alpha^3 EI_{co}} \varphi \left[\alpha x - \operatorname{sech}\left(\frac{\alpha L}{2}\right) \sinh(\alpha x) \right] \quad (4.23)$$

$$w_{b,1,max}^{pa} = \frac{QL^3}{48EI_{co}} + \frac{Q}{2\alpha^3 EI_{co}} \varphi \left[\frac{\alpha L}{2} - \tanh\left(\frac{\alpha L}{2}\right) \right] \quad (4.24)$$

for Figure 4.3(b), $x \in [0, b]$ and $x \in [b, L/2]$:

$$w_{b,2}^{pa}(x) = w_{b,2}^{co}(x) + \frac{Q}{\alpha^3 EI_{co}} \varphi \left\{ \alpha x + \sinh(\alpha x) \left[\sinh(\alpha b) \tanh\left(\frac{\alpha L}{2}\right) - \cosh(\alpha b) \right] \right\} \quad (4.25)$$

$$w_{b,2}^{pa}(x) = w_{b,2}^{co}(x) + \frac{Q}{\alpha^3 EI_{co}} \varphi \left\{ \alpha b + \sinh(\alpha b) \left[\sinh(\alpha x) \tanh\left(\frac{\alpha L}{2}\right) - \cosh(\alpha x) \right] \right\} \quad (4.26)$$

$$w_{b,2,max}^{pa} = \frac{Qb}{24EI_{co}} (3L^2 - 4b^2) + \frac{Q}{\alpha^3 EI_{co}} \varphi \left[\alpha b - \sinh(\alpha b) \operatorname{sech}\left(\frac{\alpha L}{2}\right) \right] \quad (4.27)$$

and for Figure 4.3(c), $x \in [0, L/2]$:

$$w_{b,3}^{pa}(x) = w_{b,3}^{co}(x) + \frac{q_0}{\alpha^4 EI_{co}} \varphi \left\{ \cosh \left[\alpha \left(x - \frac{L}{2} \right) \right] \operatorname{sech}\left(\frac{\alpha L}{2}\right) - \frac{(\alpha x)^2}{2} + \frac{\alpha^2 Lx}{2} - 1 \right\} \quad (4.28)$$

$$w_{b,3,max}^{pa} = \frac{5q_0L^4}{384EI_{co}} + \frac{q_0}{\alpha^4EI_{co}} \varphi \left[\operatorname{sech}\left(\frac{\alpha L}{2}\right) + \frac{(\alpha L)^2}{8} - 1 \right] \quad (4.29)$$

where $\varphi = EI_{co}/EI_0 - 1$.

Using Eq. (4.11) and the deflection relations provided before, Table 4.2 summarizes the corresponding exact analytical expressions of the dimensionless partial interaction parameter ξ and its maximum values in function of the relative coordinates denoted with $x_r = x/L$.

Table 4.2: Exact analytical expressions for the partial interaction parameter ξ and corresponding midspan values.

Static case/ var. domain	Exact analytical expressions ^a
Figure 4.3(a) $x_r \in (0,0.5]$	$\xi_1(x_r) = \frac{24}{(\alpha L)^3(3 - 4x_r^2)x_r} \varphi \left[\alpha L x_r - \operatorname{sech}\left(\frac{\alpha L}{2}\right) \sinh(\alpha L x_r) \right]$ $\xi_{1,mid} = \frac{24}{(\alpha L)^3} \varphi \left[\frac{\alpha L}{2} - \tanh\left(\frac{\alpha L}{2}\right) \right]$
Figure 4.3(b) $x_r \in (0, b_r]$	$\xi_2(x_r) = \frac{6}{(\alpha L)^3(3b_r - 3b_r^2 - x_r^2)x_r} \varphi \left\{ \alpha L x_r + \sinh(\alpha L x_r) \left[\sinh(\alpha L b_r) \tanh\left(\frac{\alpha L}{2}\right) - \cosh(\alpha L b_r) \right] \right\}$
$x_r \in [b_r, 0.5]$	$\xi_2(x_r) = \frac{6}{(\alpha L)^3(3x_r - 3x_r^2 - b_r^2)b_r} \varphi \left\{ \alpha L b_r + \sinh(\alpha L b_r) \left[\sinh(\alpha L x_r) \tanh\left(\frac{\alpha L}{2}\right) - \cosh(\alpha L x_r) \right] \right\}$ $\xi_{2,mid} = \frac{6}{(\alpha L)^3(0.75 - b_r^2)b_r} \varphi \left[\alpha L b_r - \sinh(\alpha L b_r) \operatorname{sech}\left(\frac{\alpha L}{2}\right) \right]$
Figure 4.3(c) $x_r \in (0,0.5]$	$\xi_3(x_r) = \frac{24}{(\alpha L)^4(1 - 2x_r^2 + x_r^3)x_r} \varphi \left\{ \cosh \left[\alpha L \left(x_r - \frac{1}{2} \right) \right] \operatorname{sech}\left(\frac{\alpha L}{2}\right) + \frac{(\alpha L)^2}{2} (x_r - x_r^2) - 1 \right\}$ $\xi_{3,mid} = \frac{76.8}{(\alpha L)^4} \varphi \left[\operatorname{sech}\left(\frac{\alpha L}{2}\right) + \frac{(\alpha L)^2}{8} - 1 \right]$

^a Here $b_r = b/L$ is the relative coordinate of the application point of the concentrated loads.

Due to the complexity of the expressions for bending deflections considering partial interaction effects, various authors have suggested approximate solutions to the problem. By applying the proposed method from the current study, their formulas for effective flexural stiffness or effective maximum deflection were converted into the dimensionless parameter ξ .

A research study presented in [91] recommended using in all situations the exact solution of the maximum deflection of a uniformly loaded, simply supported steel-concrete composite beam with interlayer slip, irrespective of the boundary conditions. The following ξ expression was determined from it:

$$\xi_w = \frac{76.8}{(\alpha L)^4} \varphi \left[\operatorname{sech}\left(\frac{\alpha L}{2}\right) + \frac{(\alpha L)^2}{8} - 1 \right] = \xi_{3,mid} \quad (4.30)$$

Similar investigations have been carried out on composite beams made of mechanically joined timber layers or timber members connected to reinforced concrete sections that possess incomplete shear interaction. Annex B of Eurocode 5 offers an analytical model for calculating the effective flexural stiffness for this type of elements, where the equation provided represents the exact solution for a simply

supported beam with an applied load generating a parabolically or sinusoidally varying bending moment. From its expression, the subsequent ξ value was deduced:

$$\xi_{EC5} = \varphi \left[1 + \left(\frac{\alpha L}{\pi} \right)^2 \right]^{-1} \quad (4.31)$$

Several studies [99,100,102] have adjusted the formula for the effective flexural stiffness from Eurocode 5 by taking into account the effective length of the analyzed composite member as in the Euler buckling model. The same studies proved that differences between the effective μ_{eff} and complete interaction μ_{co} Euler buckling coefficients are minimal, with a small exception for the pinned-clamped static case. Using Eq. (4.12), the dimensionless parameter obtained is:

$$\xi_G = \left(\frac{\mu_{eff}}{\mu_{co}} \right)^2 \varphi \left[1 + (\mu_{eff})^2 \left(\frac{\alpha L}{\pi} \right)^2 \right]^{-1} \quad (4.32)$$

For a simply supported composite beam $\mu_{eff} = \mu_{co} = 1.0$ and the formula reverts to Eq. (4.31).

In a study of steel-concrete composite beams considering shear slip effects [103], the authors suggest after a number of approximations the following formula adapted here, which was determined from the uniformly loaded beam example:

$$\xi_{NC} = \frac{12}{(\alpha L)^2} (\varphi + 1) \left[0.4 - \frac{3}{(\alpha L)^2} \right]; \alpha L \geq 4 \quad (4.33)$$

The Chinese code for the design of steel structures, GB 50017-2003 [87], specifies that the bending stiffness should be taken with reduced value considering the effects of the connection's flexibility, for composite beams subjected to positive bending moments. From the expression of the reduced stiffness, the next corresponding partial interaction parameter was computed:

$$\xi_{CH} = 1.5 \frac{12}{(\alpha L)^2} (\varphi + 1) \left[0.4 - \frac{3}{(0.9^2 \alpha L)^2} \right]; \xi_{CH} \geq 0 \quad (4.34)$$

As seen, the equation is comparable with the previous expression, with the amendment of applying a couple of new coefficients.

One of the advantages of using the approximate formulations for ξ as opposed to the exact ones is, besides their simplicity, the fact that the results are not sensitive to the load type and supporting conditions and thus the expressions can be regarded as generally valid.

4.3.1.3. Parametric study

In the following comparison charts, key parameters of the expressions presented before were varied in order to identify a single suitable approximate formulation for ξ to be used in current design, which produces values sufficiently close to the exact formulations presented in Table 4.2.

The dimensionless parameter ξ which quantifies the effects of the connection's flexibility in a hybrid beam's equation of deflection is mostly dependent on three dimensionless factors: the composite action parameter αL , the relative coordinate along the beam $x_r = x/L$, and the relative bending stiffness parameter represented by the ratio EI_{co}/EI_0 .

First off, the variation of the composite action parameter αL in function of the connection's shear stiffness K_c is analyzed in Figure 4.6 for the specific case of hybrid beam M2-HB4. The plotted curve indicates a parabolic correlation, where lower values of the modulus produce increasingly lower results for αL . In an analogous manner, after a certain initial stiffness rise, the composite action gains are not so substantial as before.

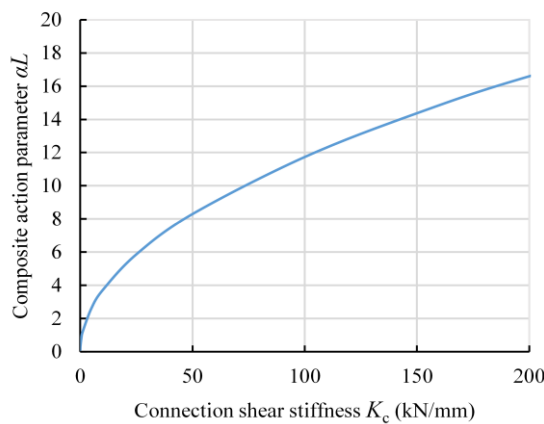


Figure 4.6: Variation of composite action parameter αL in function of connection shear stiffness K_c .

Because ξ displays a linear variation in function of EI_{co}/EI_0 , a constant value of 2.5 was set for the ratio for the rest of the parametric study, as averaged from the values in the second column of Table 4.5 of the reported FRP-concrete beams with mechanical connections.

The variation of the exact and approximate formulations of ξ for the three static cases illustrated in Figure 4.3, in function of the relative longitudinal coordinates, is plotted in Figure 4.7. Furthermore, the analysis is considered for three distinct values of αL (5, 10 and 20) which imply that the connection has a lower or greater shear interaction degree, and for three distinct load application points for the second static case, where $b_r = (0.25; 0.333; 0.40)$ and αL is kept at a constant halfway value of 10.

It is observed from the graphics that as the connection's stiffness increases, the greater the αL , the plotted curves of the equations tend to merge. Even for low interaction cases, errors in the increased bending deflection versus the exact formulations are smaller than 4%, and for the maximum deflection are even less with the notable exception of ξ_{NC} and ξ_{CH} . As expected, ξ_W and ξ_3 coincide at the midspan ($x_r = 0.5$), and as the two point loads approach the center in the second static case ($b_r \rightarrow 0.5$) the variation of ξ_2 in function of x_r becomes more similar to that of ξ_1 . The midspan concentrated load case appears to produce the largest variation (hence, increase in midspan deflection due to slip) in comparison

with the other two static cases and the general approximate formulations. The constant values of ξ_W , ξ_{EC5} and ξ_G appear to fit the best the three exact distributions given by ξ_1 , ξ_2 and ξ_3 .

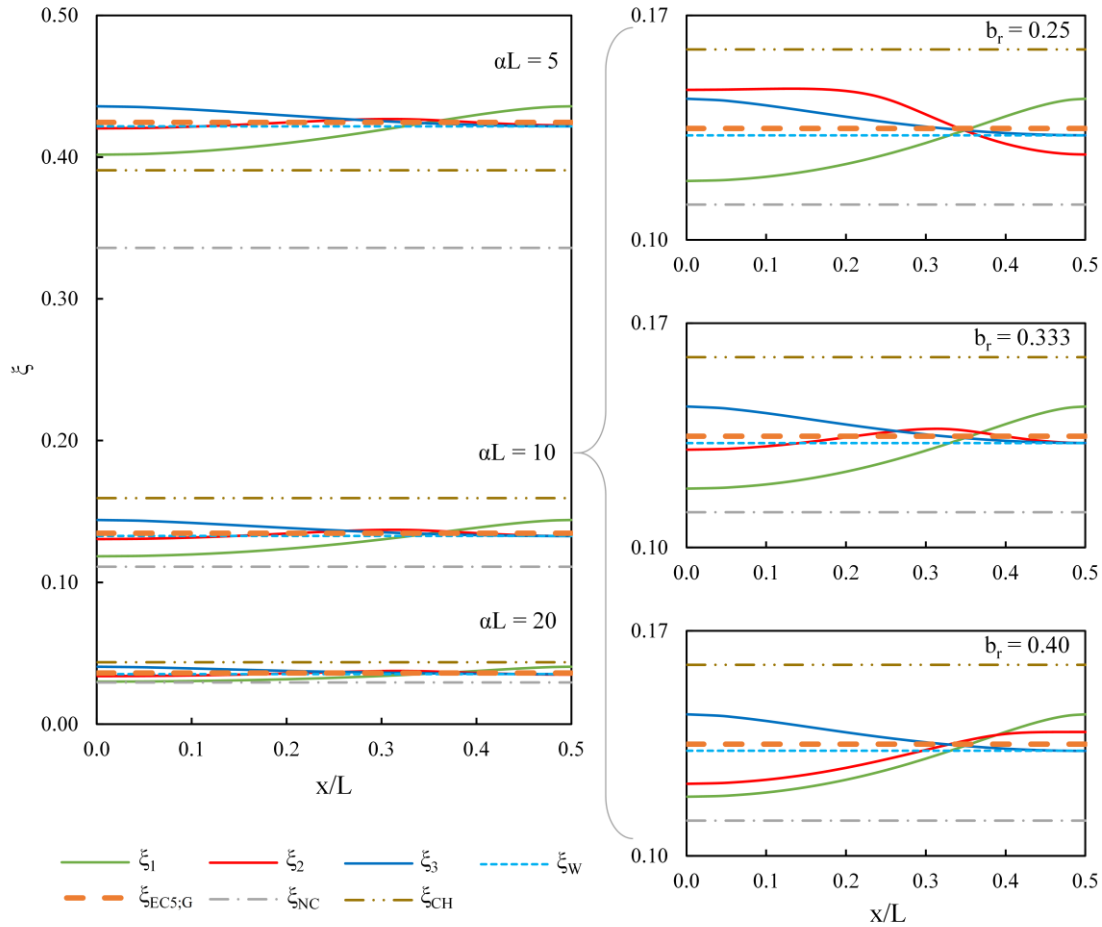


Figure 4.7: Variation of partial interaction parameter ξ to relative coordinates $x_r = x/L$ and $b_r = b/L$.

A second comparison is made in Figure 4.8 concerning the influence of the composite action parameter αL over ξ , at midspan ($x_r = 0.5$). The range of αL values is chosen to cover most of the practical scenarios and midspan values for ξ are presented for the static cases depicted in Figure 4.3. As mentioned before, ξ_3 and ξ_W coincide at the center and ξ_{EC5} and ξ_G are ubiquitously similar for simply supported beams. For the second static case, the forces are considered to be applied at a third of the span's distance ($b_r = 0.333$).

The relation presented in the chart is highly nonlinear, where a direct increase in the composite action parameter significantly reduces the value of ξ . Results obtained using the approximate formulation from Eq. (4.33) and (4.34) are either on the inferior part of the exact distributions or on the superior side, respectively. Parameters ξ_{NC} and ξ_{CH} depart increasingly from the rest of the expressions as the connection provided in the hybrid member becomes more flexible. For low interaction situations ($\alpha L \leq 5$) there are important discrepancies noticed in the variation of the two parameters. On the other

hand, the approximate equation derived from Eurocode 5 fits very well the exact values given by the relations in Table 4.2 for the three distinct static cases.

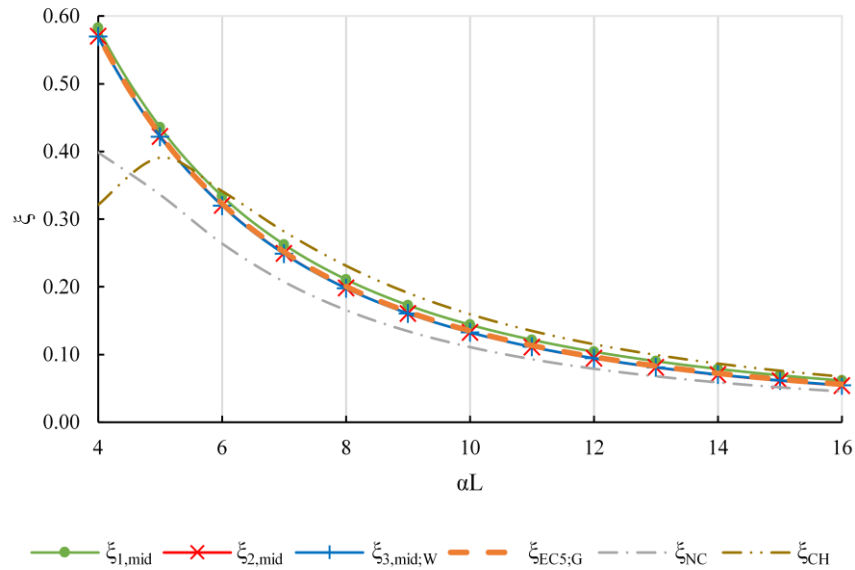


Figure 4.8: Influence of composite action parameter αL over partial interaction parameter ξ , at beam midspan.

Opting for the simplicity and accuracy of Eq. (4.31), the normalized effective bending deflection contribution is computed with Eq. (4.11) and plotted in Figure 4.9 against relative longitudinal coordinates, together with the normalized exact bending deflection formulas for the previously mentioned cases, considering complete and partial shear interaction behavior. Normalization was performed by dividing the local expression with the maximum deflection under complete interaction presumptions. Composite action parameter αL was fixed to 5 so as to highlight the fact that a weak connection between the FRP profile and concrete slab may cause an almost 50% increase in bending deflection.

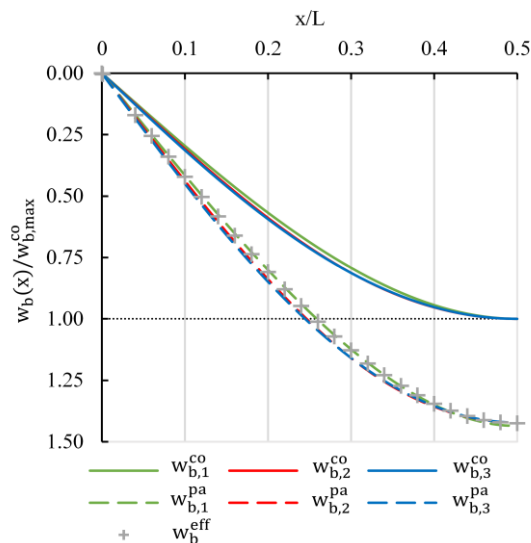


Figure 4.9: Variation of complete and partial normalized deflections to relative coordinates $x_r = x/L$.

The previous chart also points out that the global approximate solution gives proper values regardless of the applied load arrangement, especially at the midspan where admissible deflection criteria are usually checked.

Finally, for the situations in which the partial interaction parameter ξ depends on the degree of shear connection η and not on the stiffness K_c , Figure 4.10 plots the correlation between the first two indicatives using the previous Eqs. (4.14-4.17) deducted from several of the main composite design codes. The ratio between the flexural stiffness of the whole hybrid beam under complete interaction and the flexural stiffness of the composite profile – EI_{co}/E_pI_p – was fixed to 1.4, as determined from the average of ratios of the hybrid beams used in the validation process. An additional expression for ξ is calculated from the effective moment of inertia proposed recently by Nguyen et al. [92] for hybrid beams made of combined glass-carbon FRP pultruded profiles and ultra-high performance fiber-reinforced concrete slabs.

$$\xi_{HN} = \frac{EI_{co}}{E_pI_p} \left[1 + \eta^2 \left(\frac{EI_{co}}{E_pI_p} - 1 \right) \right]^{-1} - 1 \quad (4.35)$$

The minimum applicable limits for the formulas are plotted in the same figure for the three design codes. All $\xi - \eta$ variations are generally linear, down to a limit of 50% for the degree of shear connection. With the exception of AISC 360-10 which considers amplification effects from inelastic behavior, the rest of the curves start from the origin position where, according to the expressions, a full composite beam produces a null partial interaction parameter. Furthermore, Eurocode 4 (DD ENV 1994-1-1:1994), AISC 360-05 and AS 2327.1-2003 relations produce closely-positioned ξ distributions, whereas $\xi_{AISC-10}$ and ξ_{HN} values are at least twice as high for the same degree of shear connection.

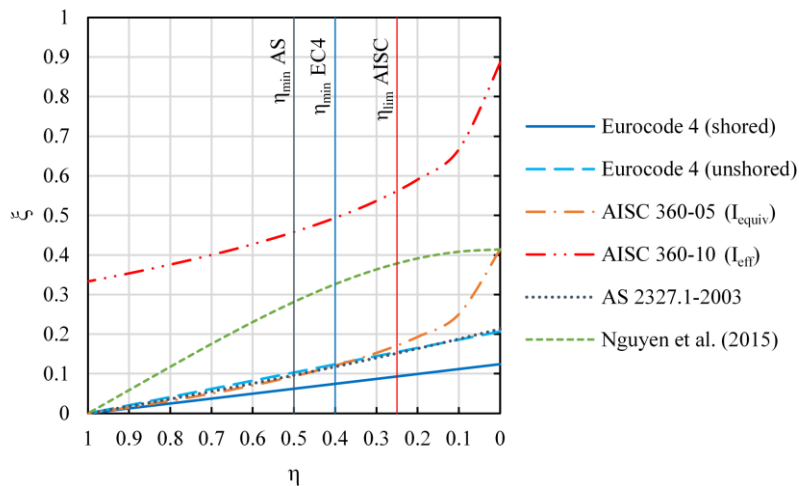


Figure 4.10: Variation of partial interaction parameter ξ in function of the degree of shear connection η , according to several design code formulations for composite beams. Corresponding inferior limits for η are also plotted.

In the end, the bending deflection of a hybrid beam is much more sensitive to the connection's stiffness and mechanical properties of the connected materials than to the approximations considered in evaluating the partial interaction parameter, as it will be proved in the validation of the analytical model.

4.3.2. Vibrations

Due to the lightness of hybrid elements, structural vibration issues could arise that should be considered at the serviceability limit state. Usually, for typical floor spans in light-frame constructions such as office buildings, the likelihood of objectionable vibration is minimized if the fundamental frequency of the floor is greater than about 8 Hz [17,86,203–205]. These vibrations can be mitigated effectively by tuning the frequency of the floor system away from the dominant frequencies or by limiting the maximum induced accelerations to 0.05 m/s². In case of frequency tuning for composite structures in office buildings, the natural frequency normally should exceed 7.5 Hz if the first, second and third harmonic of the dynamic load-time function can cause significant acceleration [206].

A simple method for identifying vibration problems of floors with excessive springiness is to determine the static deflection of the floor under a concentrated load applied at the midspan [207]. For a simply supported system with a 1 kN load, the static deflection w should not exceed:

$$w \leq 7.5/L_f^{1.2} < 2 \text{ mm} \quad (4.36)$$

where L_f is the floor span.

4.4. Internal actions and stress distributions

4.4.1. Complete shear interaction

For hybrid beams with full composite action, the normal stress in a section can be computed using Navier's formula:

$$\sigma_{j,co}(x, z) = \mp \frac{M(x)E_j}{EI_{co}} z \quad (4.37)$$

where subscript j defines the material layer (c for concrete and p for the FRP profile), x the longitudinal coordinate and z the distance in the Z direction from the section's neutral axis to the point of interest. The minus sign corresponds to the top layer whereas the plus sign refers to the bottom layer. Maximum axial deformations are found at the extremities and even though the distribution is considered to be linear, warping of the composite profile may occur especially in short, stocky members.

The shear stress in an FRP-concrete beam can be obtained from the Jourawski-Collignon formula:

$$\tau_{j,co}(x, z) = \frac{V(x)E_j S(z)}{EI_{co}b_j(z)} \quad (4.38)$$

where the shear force $V(x)$ is considered positive, $S(z)$ represents the first moment of area calculated at coordinate z , and $b_j(z)$ is the width of material layer j measured at z . Maximum shear stresses usually occur at the position of the hybrid beam's neutral axis or towards the interface between the connected elements.

Equally, expressions for computing the internal bending moments M_j , interface longitudinal shear force per unit length v_L and internal shear forces V_j , can be obtained:

$$M_{j,co}(x) = \frac{E_j I_j}{EI_{co}} M(x) \quad (4.39)$$

$$v_{L,co}(x) = \left(1 - \frac{EI_0}{EI_{co}}\right) \frac{V(x)}{d_c} \quad (4.40)$$

$$V_{j,co}(x) = v_{L,co}(x) \frac{h_j}{2} + \frac{E_j I_j}{EI_{co}} V(x) \quad (4.41)$$

4.4.2. Partial shear interaction

In the case of hybrid beams with partial shear connection, where the flexibility of the connectors affects the stress distributions in the structural member, Eqs. (4.37) and (4.38) can be adapted in an approximate analysis [99] by substituting the flexural stiffness under full connection assumptions with an effective flexural stiffness determined from Eq. (4.12).

Thus, the expression for normal stress becomes:

$$\sigma_{j,eff}(x, z_j) = \left[\mp \left(1 - \frac{1 + \xi}{1 + \varphi}\right) \frac{1}{A_j d_c} + (1 + \xi) \frac{E_j z_j}{EI_{co}} \right] M(x) \quad (4.42)$$

where z_j represents the coordinate measured from the centroid of layer j towards the calculation point (in the Z direction), and A_j is the transverse area of part j . The minus and plus signs are once more applied as specified for Eq. (4.37).

The shear stress distribution is calculated from:

$$\tau_{j,eff}(x, z_j) = \left[\left(1 - \frac{1 + \xi}{1 + \varphi}\right) \frac{A_{sh,j}(z_j)}{A_j d_c b(z_j)} + (1 + \xi) \frac{E_j S(z_j)}{EI_{co} b(z_j)} \right] V(x) \quad (4.43)$$

where the sheared area of layer j , denoted $A_{sh,j}(z_j)$, the first moment of area $S(z_j)$ and the width $b(z_j)$ are all determined using local coordinates z_j .

Similarly, expressions for computing the internal bending moments M_j , interface longitudinal shear force per unit length v_L and internal shear forces V_j can be found:

$$M_{j,eff}(x) = (1 + \xi) \frac{E_j I_j}{EI_{co}} M(x) \quad (4.44)$$

$$v_{L,eff}(x) = \left(1 - \frac{1 + \xi}{1 + \varphi}\right) \frac{V(x)}{d_c} \quad (4.45)$$

$$V_{j,eff}(x) = V_{s,eff}(x) \frac{h_j}{2} + (1 + \xi) \frac{E_j I_j}{EI_{co}} V(x) \quad (4.46)$$

In comparison with the complete interaction hypothesis, for a hybrid beam with interlayer slip the normal stresses and internal bending moments are always higher and the in-plane shear stresses and internal normal actions are always lower than their counterparts.

If the shear capacity of the concrete slab in the composite beam is insufficient, the FRP profile is assumed to carry entirely the shear force applied. For an Euler-Bernoulli I-shaped profile, the in-plane shear stress in the web can be expressed as:

$$\tau_p(x, z_p) = \frac{V(x)}{8 \cdot I_p} [4(h_p - t_f)(b_f - t_f) + h_p^2 - 4z_p^2] \quad (4.47)$$

where z_p is the vertical coordinate measured from the central axis of the profile.

For homogenous I-shaped composite profiles with isotropic phases, Gay and Hoa [3] proposed the following adapted relation which includes the effects of the longitudinal warping function:

$$\tau_p(x, z_p) = \frac{V(x)}{8 \cdot I_p} [4h_p b_f + h_p^2 - 4z_p^2] \quad (4.48)$$

4.5. Interlayer slip

Besides deflections, stress distributions in FRP-concrete beams are important to be determined especially for failure analysis. For a hybrid composite member with incomplete shear interaction, the first step in this process is to evaluate the slip and consequently the slip strain which develops at the interface of the connected materials, as seen in Figure 4.2.

By writing the appropriate equilibrium and curvature compatibility equations based on the hybrid differential element illustrated in Figure 4.5 and on the hypotheses introduced in section 4.3.1.2, the quadratic differential equation for the interlayer slip $s(x)$ can be written as:

$$\frac{\partial^2}{\partial x^2} s(x) - \alpha^2 s(x) = -\beta \alpha^2 V(x) \quad (4.49)$$

where $V(x)$ represents the total shear force acting on the element and

$$\beta = \frac{d_c}{\alpha^2 EI_0} \quad (4.50)$$

The key assumption which leads to this differential equation is that the connection system is a uniform and elastic medium where the longitudinal shear force per unit length v_L is directly proportional to the developing slip s , in function of the connectors' stiffness K_c and longitudinal spacing s_c :

$$v_L = K_c/s_c \cdot s \quad (4.51)$$

For the three static cases illustrated in Figure 4.3, the general expressions for interlayer slip $s(x)$ were obtained by considering that no relative displacements occurs at the midspan and slip strain is zero at the ends of the hybrid beams (*i.e.*, $s(L/2) = 0$ and $\varepsilon_s(0) = 0$). Slip strain $\varepsilon_s(x)$ equations were then computed by differentiating the appropriate slip equations.

For the static case illustrated in Figure 4.3(a) where $x \in [0, b]$, the expressions are:

$$s_1(x) = \beta \frac{Q}{2} \left[1 - \frac{\cosh(\alpha x)}{\cosh(\alpha b)} \right] \quad (4.52)$$

$$\varepsilon_{s,1}(x) = \alpha \beta \frac{Q}{2} \frac{\sinh(\alpha x)}{\cosh(\alpha b)} \quad (4.53)$$

for Figure 4.3(b) where $x \in [0, b]$:

$$s_2(x) = \beta Q \left\{ 1 - \operatorname{sech} \left(\frac{\alpha L}{2} \right) \cosh \left[\alpha \left(\frac{L}{2} - b \right) \right] \cosh(\alpha x) \right\} \quad (4.54)$$

$$\varepsilon_{s,2}(x) = \alpha \beta Q \left\{ \operatorname{sech} \left(\frac{\alpha L}{2} \right) \cosh \left[\alpha \left(\frac{L}{2} - b \right) \right] \sinh(\alpha x) \right\} \quad (4.55)$$

and where $x \in [b, L/2]$:

$$s_2(x) = \beta Q \left\{ \operatorname{sech} \left(\frac{\alpha L}{2} \right) \sinh \left[\alpha \left(\frac{L}{2} - x \right) \right] \sinh(\alpha b) \right\} \quad (4.56)$$

$$\varepsilon_{s,2}(x) = \alpha \beta Q \left\{ \operatorname{sech} \left(\frac{\alpha L}{2} \right) \cosh \left[\alpha \left(\frac{L}{2} - x \right) \right] \sinh(\alpha b) \right\} \quad (4.57)$$

respectively, for Figure 4.3(c) where $x \in [0, L/2]$:

$$s_3(x) = \beta q_0 \left\{ \left(\frac{L}{2} - x \right) - \frac{1}{\alpha} \operatorname{sech} \left(\frac{\alpha L}{2} \right) \sinh \left[\alpha \left(\frac{L}{2} - x \right) \right] \right\} \quad (4.58)$$

$$\varepsilon_{s,3}(x) = \beta q_0 \left\{ 1 - \operatorname{sech} \left(\frac{\alpha L}{2} \right) \cosh \left[\alpha \left(\frac{L}{2} - x \right) \right] \right\} \quad (4.59)$$

Since the maximum values for slip and slip strain are important in estimating the flexural capacity of hybrid beams with partial interaction, Table 4.3 summarizes their expressions. If the position of the

two point loads b is equal to $L/2$ then the equations for slip and slip strain revert to those of the first case.

Table 4.3: Exact analytical solutions for the maximum slip and slip strain in a hybrid beam with partial shear interaction.

Static case	Analytical expressions
Figure 4.3(a)	$s_{1,max} = \beta \frac{Q}{2} \left[1 - \operatorname{sech} \left(\frac{\alpha L}{2} \right) \right]$ $\varepsilon_{s,1,max} = \alpha \beta \frac{Q}{2} \tanh \left(\frac{\alpha L}{2} \right)$
Figure 4.3(b)	$s_{2,max} = \beta Q \left\{ 1 - \operatorname{sech} \left(\frac{\alpha L}{2} \right) \cosh \left[\alpha \left(\frac{L}{2} - b \right) \right] \right\}$ $\varepsilon_{s,2,max} = \alpha \beta Q \left\{ \operatorname{sech} \left(\frac{\alpha L}{2} \right) \cosh \left[\alpha \left(\frac{L}{2} - b \right) \right] \sinh(\alpha b) \right\}$
Figure 4.3(c)	$s_{3,max} = \beta q_0 \left[\frac{L}{2} - \frac{1}{\alpha} \tanh \left(\frac{\alpha L}{2} \right) \right]$ $\varepsilon_{s,3,max} = \beta q_0 \left[1 - \operatorname{sech} \left(\frac{\alpha L}{2} \right) \right]$

The main parameters on which slip and slip strain rely are the position along the beam x/L , the dimensionless composite action parameter αL , parameter β , and the applied load. The normalized longitudinal distributions of slip and slip strain for the three static cases analyzed are plotted in Figure 4.11 considering a low degree of composite action $\alpha L = 5$ and $b_r = 0.333$ for the two point loads case. The distribution profiles are highly nonlinear, with maximum slip values occurring at the supports and maximum slip strains showing up at critical, maximum bending moment sections.

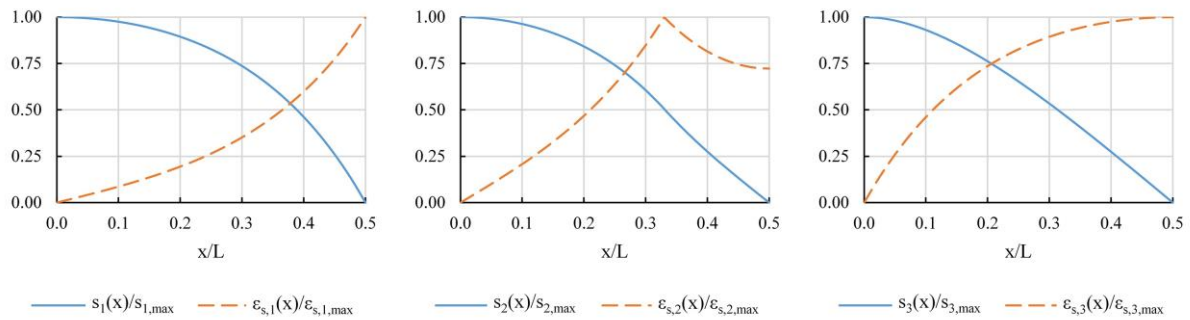


Figure 4.11: Normalized longitudinal distributions of slip and slip strain for the three static cases discussed.

Finally, relevant design measures may be found if the influence of the connection's shear stiffness over the development of slip strains is studied. Figure 4.12 plots for hybrid beam M2-HB4 the variation of ε_s in function of K_c , for the three virtual load arrangements examined. The stiffness takes values from 0 kN/mm, when the two materials deform independently, to 200 kN/mm.

A couple of effects are noticeable from the chart. First, the maximum slip strain is higher when the beam is subjected to concentrated loads, especially at the midspan where the results are double in comparison with the uniformly distributed load case. Secondly, after an initial increase in connection

stiffness up to about 50 kN/mm, the benefits of adding more connectors or installing stiffer systems diminish in return, so an optimal cost-effective design should be selected.

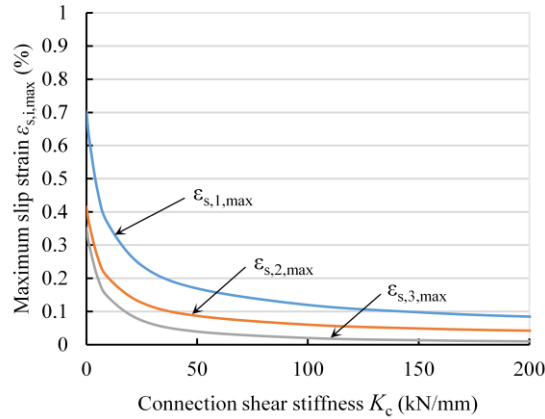


Figure 4.12: Variation of maximum slip strain in function of the connection’s shear stiffness for hybrid beam M2-HB4.

4.6. Ultimate limit states (ULS)

4.6.1. Flexural capacity

Using the constitutive models of the hybrid beam’s materials, as described in section 4.2 and depicted in Figure 4.2, coupled with the hypotheses enumerated in sections 4.3.1.1 and 4.3.1.2, the analytical expressions for the flexural capacity of hybrid beams with full and partial shear connection are presented. The calculations refer to the situations in which the neutral axis crosses the concrete top slab or the profile’s web for specimens subjected to positive bending moments. It is noteworthy however that a composite profile acting both in compression and tension would be undesired from a stability point of view. The preferred failure mechanism to be obtained is by concrete slab crushing.

4.6.1.1. Complete shear interaction

If the connection is capable of transmitting entirely the axial force developed in the reinforced concrete slab to the FRP profile and if the neutral axis lays inside the concrete layer as seen in Figure 4.2(a), the depth of the neutral axis x_u found from the equilibrium of the cross-section is extracted from:

$$0.8b_c \frac{f_c}{\epsilon_{c,u}} x_u^2 + A_p E_p x_u - A_p E_p \left(\frac{h_p}{2} + h_c \right) = 0 \quad (4.60)$$

Therefore, the maximum bending moment that the hybrid beam can sustain considering a crushing failure of the concrete slab and a full shear connection is computed as:

$$M_{u,co} = 0.6x_u F_c + F_{ft} \left(h_c - x_u + \frac{t_f}{2} \right) + F_w \left(h_c - x_u + \frac{h_p}{2} \right) + F_{fb} \left(h - x_u - \frac{t_f}{2} \right) \quad (4.61)$$

where the internal forces acting in the concrete slab F_c , profile's top flange F_{ft} , web F_w , and bottom flange F_{fb} are:

$$F_c = 0.8x_u b_c f_c \quad (4.62)$$

$$F_{ft} = A_f E_p \frac{\varepsilon_{c,u}}{x_u} \left(h_c - x_u + \frac{t_f}{2} \right) \quad (4.63)$$

$$F_w = A_w E_p \frac{\varepsilon_{c,u}}{x_u} \left(h_c - x_u + \frac{h_p}{2} \right) \quad (4.64)$$

$$F_{fb} = A_f E_p \frac{\varepsilon_{c,u}}{x_u} \left(h - x_u - \frac{t_f}{2} \right) \quad (4.65)$$

in which A_f represents the profile's flange area and A_w its web area. The rest of the geometric parameters are shown in Figure 4.2.

If the neutral axis lays in the web of the profile, then the equations become:

$$x_u = \frac{\varepsilon_{c,u} E_p A_p \left(h_c + \frac{h_p}{2} \right)}{\varepsilon_{c,u} E_p A_p + A_c f_c} \quad (4.66)$$

$$\begin{aligned} M_{u,co} = & F_c \left(x_u - \frac{h_c}{2} \right) + F_{ft} \left(x_u - h_c - \frac{t_f}{2} \right) + F_{w1} (x_u - h_c - t_f) + F_{w2} (h - x_u - t_f) \\ & + F_{fb} \left(h - x_u - \frac{t_f}{2} \right) \end{aligned} \quad (4.67)$$

$$F_c = A_c f_c \quad (4.68)$$

$$F_{ft} = A_f E_p \frac{\varepsilon_{c,u}}{x_u} \left(x_u - h_c - \frac{t_f}{2} \right) \quad (4.69)$$

$$F_{w1} = t_w E_p \frac{1}{2} \frac{\varepsilon_{c,u}}{x_u} (x_u - h_c - t_f)^2 \quad (4.70)$$

$$F_{w2} = t_w E_p \frac{1}{2} \frac{\varepsilon_{c,u}}{x_u} (h - x_u - t_f)^2 \quad (4.71)$$

$$F_{fb} = A_f E_p \frac{\varepsilon_{c,u}}{x_u} \left(h - x_u - \frac{t_f}{2} \right) \quad (4.72)$$

4.6.1.2. Partial shear interaction

For hybrid beams with partial shear connection, where a relative slip develops at the interface and the neutral axis is lying in the concrete layer as shown in Figure 4.2(b), the depth of the neutral axis depends in addition on the maximum slip strain $\varepsilon_{s,max}$, and can be determined from the following equilibrium equation adapted from [89]:

$$0.8b_c f_c x_u^2 + A_p E_p (\varepsilon_{c,u} + \varepsilon_{s,max}) x_u - A_p E_p \varepsilon_{c,u} \left(\frac{h_p}{2} + h_c \right) = 0 \quad (4.73)$$

Hence, the maximum bending moment that the hybrid beam can sustain, considering a crushing failure of the concrete slab and an incomplete shear connection, is:

$$M_{u,pa} = 0.6x_u F_c^{pa} + F_{ft}^{pa} \left(h_c - x_u + \frac{t_f}{2} \right) + F_w^{pa} \left(h_c - x_u + \frac{h_p}{2} \right) + F_{fb}^{pa} \left(h - x_u - \frac{t_f}{2} \right) \quad (4.74)$$

where the forces acting in the concrete slab F_c^{pa} , profile's top flange F_{ft}^{pa} , web F_w^{pa} , and bottom flange F_{fb}^{pa} are:

$$F_c^{pa} = 0.8x_u b_c f_c \quad (4.75)$$

$$F_{ft}^{pa} = F_{ft} - A_f E_p \varepsilon_{s,max} \quad (4.76)$$

$$F_w^{pa} = F_w - A_w E_p \varepsilon_{s,max} \quad (4.77)$$

$$F_{fb}^{pa} = F_{fb} - A_f E_p \varepsilon_{s,max} \quad (4.78)$$

If the neutral axis lays in the web of the profile then the relations needed to determine the bending capacity under partial interaction assumptions are:

$$x_u = \frac{(\varepsilon_{c,u} + \varepsilon_{s,max}) E_p A_p \left(h_c + \frac{h_p}{2} \right)}{(\varepsilon_{c,u} + \varepsilon_{s,max}) E_p A_p + A_c f_c} \quad (4.79)$$

$$M_{u,pa} = F_c^{pa} \left(x_u - \frac{h_c}{2} \right) + F_{ft}^{pa} \left(x_u - h_c - \frac{t_f}{2} \right) + F_{w1}^{pa} (x_u - h_c - t_f) + F_{w2}^{pa} (h - x_u - t_f) + F_{fb}^{pa} \left(h - x_u - \frac{t_f}{2} \right) \quad (4.80)$$

$$F_c^{pa} = A_c f_c \quad (4.81)$$

$$F_{ft}^{pa} = A_f E_p \frac{(\varepsilon_{c,u} + \varepsilon_{s,max})}{x_u} \left(x_u - h_c - \frac{t_f}{2} \right) \quad (4.82)$$

$$F_{w1}^{pa} = t_w E_p \frac{1}{2} \frac{(\varepsilon_{c,u} + \varepsilon_{s,max})}{x_u} (x_u - h_c - t_f)^2 \quad (4.83)$$

$$F_{w2}^{pa} = t_w E_p \frac{1}{2} \frac{(\varepsilon_{c,u} + \varepsilon_{s,max})}{x_u} (h - x_u - t_f)^2 \quad (4.84)$$

$$F_{fb}^{pa} = A_f E_p \frac{(\varepsilon_{c,u} + \varepsilon_{s,max})}{x_u} \left(h - x_u - \frac{t_f}{2} \right) \quad (4.85)$$

Using a different approach [103], by considering that the flexural moment is the sum between the flexural moment for the same hybrid beam but with full connection and the negative moment produced

by the couple between the axial forces developed from partial interaction, the decrease in flexural capacity due to the flexibility of the shear connection system is:

$$\Delta M(x) = \frac{h_p}{6h} E_p (2h_c A_f + h A_w) \varepsilon_s(x) \quad (4.86)$$

Because the slip strain equation has to be solved afresh for each force increment and different boundary conditions, the formulation is cumbersome for routine design. In exchange, by expressing the curvature increase of the beam through the proposed dimensionless partial interaction parameter ξ as below:

$$\Delta \phi(x) = \frac{\varepsilon_s(x)}{h} = \frac{M_{co}(x)}{EI_{co}} \xi(x) \quad (4.87)$$

a simple, yet reliable formula may be obtained for the effective flexural capacity of hybrid beams with partial shear connection:

$$M_{u,eff} = M_{u,co} - \Delta M = M_{u,co} \left[1 - \xi \frac{h_p E_p}{6EI_{co}} (2h_c A_f + h A_w) \right] \quad (4.88)$$

In situations in which the hybrid beams are subjected to negative bending moments, relations can be found in [104] and [49].

4.6.2. Additional failure criteria

For design purposes, accompanying checks should be made regarding other possible failure modes of hybrid beams that may cause a premature fragile collapse instead of the previously commented pseudo-ductile crushing mode.

4.6.2.1. Profile tensile failure

In both complete and partial interaction cases, the maximum tensile strain or stress on the bottom flange of the profile should be verified against the allowable values specified by the manufacturer, or better yet, determined from static tests.

4.6.2.2. Transverse web crushing

Due to the anisotropy of the composite material, pultruded profiles are susceptible to crushing failure at the reaction points and under concentrated loads, as seen from experimental testing. Its compressive strength in transverse direction $\sigma_{cM,T}$ could be five times lower than in longitudinal direction and thus, the critical crushing force should be calculated using the following expression:

$$Q_{crush} = \sigma_{cM,T} A_{eff} \quad (4.89)$$

where A_{eff} is the effective web area over which the force is distributed.

This is the motive why web stiffeners should be placed at the critical reaction points, by connecting additional FRP shapes, more rigid materials, or simply by local concrete jacketing the feeble sections.

4.6.2.1. In-plane web shear

As observed during the experimental campaign, web-flange delamination constituted the primary failure mode of the hybrid beams. Therefore, the maximum in-plane shear stress determined with Eq. (4.38) or (4.43) should be lower than the strength of the composite material. When the concrete slab is thin, severely cracked or has an insufficient capacity to carry shear loads, a conservative hypothesis can be established that the shear stress in the member is entirely carried by the profile's web and its distribution is relatively uniform along the depth. Hence, the critical shear force for a homogeneous profile due to web material failure can be approximated as:

$$V_u \approx \tau_{max,LT} A_{sh} \quad (4.90)$$

where $\tau_{max,LT}$ is the in-plane shear strength of the FRP profile and A_{sh} is the sheared area estimated as:

$$A_{sh} \approx t_w (d_w + t_f) \quad (4.91)$$

Often times, the in-plane shear strength of FRP profiles is not reported by manufacturers due to the complexity involved by the experimental determination of this property. Nevertheless, the interlaminar shear strength is usually reported and can be used instead. Being smaller than the in-plane shear strength, the calculation will lead to overly conservative designs for conventional pultruded profiles.

4.6.2.2. Shear connection failure

In simply supported hybrid beams the longitudinal spacing s_c between shear connectors should be lower than:

$$s_c \leq \frac{n_c P_{max} L}{F_c} \frac{1}{2} \quad (4.92)$$

where n_c is the number of rows of installed connectors, P_{max} the shear capacity of a connector, F_c the compressive force developed in the concrete slab, and L the span of the beam.

If an insufficient number of connectors is provided or the total shear capacity is lower than required, hybrid beams may fail suddenly before the concrete slab can reach plastic deformations. Moreover, in the absence of proper constructive detailing, the resistance of the fasteners to uplift forces in the slab should also be checked.

4.6.2.3. Interaction failure criteria

For pultruded profiles subjected to high bending moments and high shear forces at the same time, the Italian guide CNR-DT 205/2007 [74] recommends using the following second-order interaction equation suggested also in [1]:

$$\left(\frac{M_Q}{M_u}\right)^2 + \left(\frac{V_Q}{V_u}\right)^2 \leq 1.0 \quad (4.93)$$

where M_Q and V_Q represent the bending moment and shear force produced by the applied load, and M_u and V_u represent the ultimate bending and shear capacity of the composite member.

A similar quadratic failure criterion for when the profile's web is subjected to combined in-plane axial compressive (flexural) stress and in-plane shear stress is indicated in [73]:

$$\left(\frac{\sigma_{Q,L}}{\sigma_{max,L}}\right)^2 + \left(\frac{\tau_{Q,LT}}{\tau_{max,LT}}\right)^2 \leq 1.0 \quad (4.94)$$

where $\sigma_{Q,L}$ and $\tau_{Q,LT}$ are the in-plane axial and shear stress induced by the load, and $\sigma_{max,L}$ and $\tau_{max,LT}$ are the appropriate strengths of the FRP material. The method is reportedly not as conservative as the previous condition.

One last interaction failure criterion to be satisfied by composite profiles in hybrid beams was suggested in a study performed by Gonilha et al. [53] that investigated the flexural behavior of combined GFRP-concrete beams. The researchers applied the well-known Tsai-Hill failure criterion in order to estimate analytically the ultimate load resisted by the structure. The theory states that the normal and shear stresses in the web should satisfy the following inequality:

$$\left(\frac{\sigma_{Q,L}}{\sigma_{max,L}}\right)^2 + \left(\frac{\sigma_{Q,T}}{\sigma_{max,T}}\right)^2 + \left(\frac{\tau_{Q,LT}}{\tau_{max,LT}}\right)^2 - \frac{\sigma_{Q,L}\sigma_{Q,T}}{\sigma_{max,L}} \leq 1.0 \quad (4.95)$$

where subscripts L and T refer to the longitudinal or transverse direction of the profile. From the reported results, the in-plane shear stress contributed to over 99% of the failure index value so an interaction failure criterion was not really relevant in that given state.

4.7. Validation with previous experimental data

4.7.1. Description of specimens

To assert the validity of the analytical relations presented before, the published characteristics and experimental results of six FRP-concrete hybrid beams were used [43–46,48,89]. The chosen specimens featured only mechanical connections with either steel bolts or GFRP dowels, had different spans, load conditions and cross-section geometries, as illustrated in Figure 4.13.

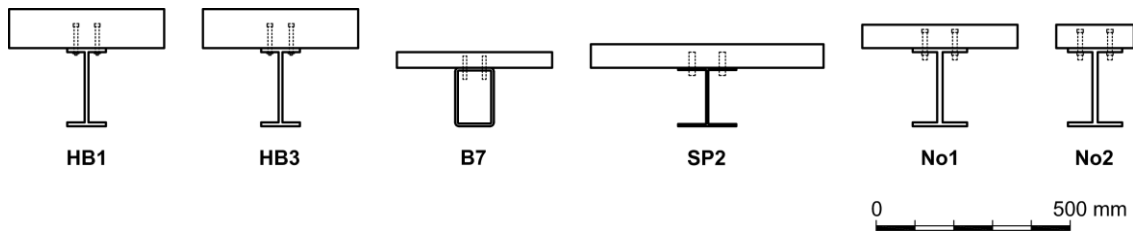


Figure 4.13: Cross-sections of the hybrid beams used in the validation analysis.

Table 4.4 summarizes in addition to the dimension ratios of the specimens, the degree of shear connection according to Eurocode 4, the experimental stiffness of the shear connection K_c^{exp} where push-out tests were performed, and the corresponding analytical values determined from Eq. (4.18). Dimension notations from the table are to be found in Figure 4.2 and Figure 4.3.

Table 4.4: Characteristics of the hybrid beam specimens chosen for validation analysis.

Beam	Profile type	Test method	L/h	b/L	b/h	h_p/b_f	η	K_c^{exp} (kN/mm)	K_c (kN/mm)	diff. (%)
HB1 [48,89]	I-beam	3 point flexure	13.3	0.50	6.7	2.00	1.03	38.1	32.0	-16.0
HB3 [48,89]	I-beam	4 point flexure	6.0	0.32	1.9	2.00	0.31	27.6	28.2	+2.2
B7 [46]	Rectangular tube	4 point flexure	14.7	0.44	6.4	1.50	0.74	12.0	10.4	-13.3
SP2 [45]	Wide flange beam	4 point flexure	9.8	0.33	3.3	1.00	1.00	n/a	32.0	n/a
No1 [43,44]	I-beam	4 point flexure	8.5	0.41	3.5	1.43	1.24	n/a	28.0	n/a
No2 [43,44]	I-beam	4 point flexure	8.5	0.41	3.5	1.43	3.04	n/a	28.0	n/a

n/a – not available.

The geometry ratios reveal that both slender and stocky beams were taken into consideration for the analysis, with specimen HB3 having the smallest shear span-to-depth ratio. The application points of loads varied in the investigations from the midspan toward a third of the test distance. Utilized profiles had a narrow or wide I section, or a rectangular tubular (box) shape.

According to Eurocode 4, the high degree of shear connection η suggests that part of the beams had a full shear connection; however, during the reported tests, larger deflections and slippage at the interface were noticed in all cases. Therefore, the continuing analysis under partial interaction assumptions is based on the connection's flexibility reflected by the modulus K_c . The percentile

difference between the experimental and analytical connection modulus proves to be conservative, on the safe side of design.

With the help of the relations provided in section 4.3.1.2, the main parameters of partial interaction were computed for each hybrid specimen and presented in Table 4.5.

Table 4.5: Computed parameters of partial interaction.

Beam	EI_{co}/EI_0	αL	EI_{eff}/EI_{co}	$\xi_{i,mid}$	ξ_{EC5}	diff. (%)
HB1	2.50	9.7	0.87	0.153	0.144	-5.9
HB3	2.54	3.7	0.61	0.636	0.639	+0.5
B7	2.92	7.7	0.79	0.282	0.272	-3.5
SP2	1.94	6.3	0.84	0.185	0.186	+0.5
No1	2.87	6.0	0.71	0.412	0.405	-1.7
No2	2.70	6.4	0.75	0.341	0.335	-1.8

The results demonstrate that the beams had a low to medium degree of composite action, where the reduction in flexural rigidity varied between 13% and 39%. At the same time, the differences between the exact value of the dimensionless partial interaction parameter $\xi_{i,mid}$ depending on the static case i , as determined with the equations from Table 4.2, and the approximate value ξ_{EC5} obtained from Eq. (4.31) that was derived from Eurocode 5, appear to be negligible.

Participation ratios of the internal moments and forces acting in the hybrid beam sub-systems were computed in Table 4.6 considering a linear elastic behavior of the materials, for both complete and incomplete connection cases. The numbers indicate a significant reduction, up to 26%, in the coupling moment Nd_c between the two layers, for the partial connection model. As a result, the individual moments carried by the profile M_p and concrete slab M_c increase significantly. The percentile differences regarding the shear force in the two layers are by comparison not so important; however, if the reinforced concrete element carries a large part of it, then, instead of using the approximate Eqs. (4.9) and (4.90) in evaluating the deflection and shear capacity, Eqs. (4.10), and (4.38) or (4.43) are recommended.

Table 4.6: Participation percentages of hybrid beam sub-systems.

Beam	Complete interaction		Partial interaction	
	$M_p/M_c/Nd_c$ (%)	V_p/V_c (%)	$M_p/M_c/Nd_c$ (%)	V_p/V_c (%)
HB1	18/22/60	58/42	20/25/55	57/43
HB3	18/21/61	59/41	30/35/35	53/47
B7	25/10/65	77/23	32/12/56	76/24
SP2	19/33/48	53/47	22/39/39	50/50
No1	29/6/65	79/21	41/8/51	80/20
No2	34/3/63	82/18	45/5/50	84/16

For the current analysis, the concrete shear capacity was taken into account for specimens SP2 and HB3 which had higher shear participation ratios of the slabs.

4.7.2. Serviceability analysis

Based on a review of the main codes, guides and manuals for the design of composite beams or structures built from pultruded FRP members, a maximum value for the midspan deflection under serviceability conditions has been suggested in section 4.3.1.1 which is used in the current validation routine, equal to $L/250$ for the quasi-permanent load combination for floors.

Considering analytical models with both complete and partial shear interaction under different hypotheses and given the fixed experimental deflection w_t^{exp} , the maximum total load Q_t acting on each beam is computed and presented in Table 4.7 together with the percentile difference versus the experimental value.

Table 4.7: Computed loads at SLS considering various hypotheses.

Beam	Experimental		Analytical ^a							
			Complete interaction				Partial interaction			
	w_t^{exp} (mm)	Q_t^{exp} (kN)	$\kappa GA, \xi = 0$		$\kappa GA, \xi_{l,mid}$		$\kappa GA, \xi_{EC5}$		$G_p A_w, \xi_{EC5}$	
		Q_t (kN)	diff. (%)	Q_t (kN)	diff. (%)	Q_t (kN)	diff. (%)	Q_t (kN)	diff. (%)	
HB1	16.0	43.7	36.3	-17.0	33.0	-24.5	33.2	-24.1	33.2	-24.1
HB3	7.2	119	162	+36.0	124	+3.6	123	+3.5	89.1	-25.3
B7	11.2	16.6	16.0	-3.8	16.0	-3.8	16.0	-3.8	16.0	-3.8
SP2	8.2	32.2	35.0	+8.5	30.5	-5.4	30.5	-5.5	22.9	-28.9
No1	8.8	93.1	93.1	±0.0	74.8	-19.7	75.0	-19.4	68.4	-26.5
No2	8.8	81.9	85.1	+3.9	70.0	-14.5	70.4	-14.0	64.4	-21.3

^a Here diff. represents the difference in percentage between the analytical and corresponding experimental value.

Four hypotheses are presented in the table, as explained: (i) complete shear interaction with exact shear stiffness; (ii) partial shear interaction with exact shear stiffness and exact partial interaction parameter; (iii) partial interaction with exact shear stiffness and approximate interaction parameter; and finally, (iv) partial interaction with approximate shear stiffness (carried entirely by the web of the profile) and approximate partial interaction parameter.

The numbers suggest a minimal error between the exact and effective (approximate) partial interaction model, and a bigger one versus the experimental data. The differences increase when simplifying the calculations by assuming that the concrete slab possesses no shear capacity. Figure 4.14 plots the loads obtained at SLS versus the corresponding experimentally measured values. Adjoined to the image, in Figure 4.15, the midspan deflections at 50% of the maximum sustained loads are compared.

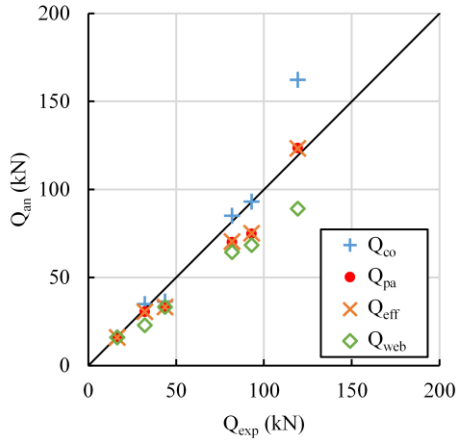


Figure 4.14: Analytically computed load versus experimental load at SLS.

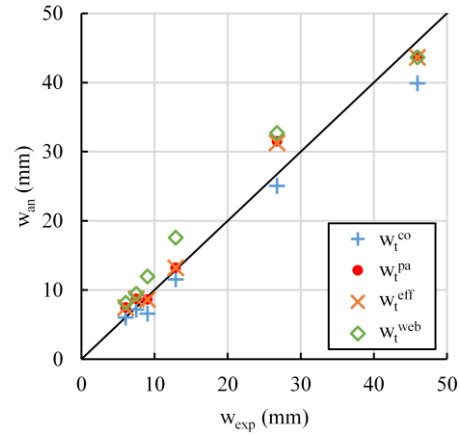


Figure 4.15: Analytically estimated midspan deflection versus experimental deflection at 50% of the maximum sustained load.

To conclude, the analytical partial interaction models produce lower loads than the experiments at the serviceability deflection check and higher deflections for intermediate loads, where the hybrid beams are presumably still behaving in the elastic domain. Thus, the results point out that analytical designs based on the connection’s flexibility yield more conservative data, especially for the fourth hypothesis. At inferior load levels, the predicted deflections may be affected by the presence of initial adhesion or friction at the interface.

4.7.3. Failure analysis

As observed, the main reported failure mode of the investigated hybrid beams was characterized by the loss of shear strength capacity in the web of the FRP profiles. Nevertheless, maximum bending capacities were calculated for each specimen according to Eqs. (4.80) and (4.88), assuming that the concrete slab crushes under compression, and results show a tolerable difference between using the complex formulations including slip estimation and the more simple, approximate expression of using the introduced dimensionless parameter of partial interaction ξ (in this case ξ_{EC5}). By employing Eqs. (4.43) and (4.90) for determining the critical in-plane shear stress, the calculated maximum flexural moments limited by the shear load, $M_{u,pa}^{sh}$, are represented in Table 4.8 as percentages of the bending capacities considering the previously mentioned concrete crushing hypothesis. The capacity ratios reveal that for three of the six FRP-concrete beams the ultimate bending moment determined by a shear failure was almost half of the maximum moment determined from a flexural failure of the slab.

Table 4.8: Experimental failure characteristics and maximum computed moments.

Beam	Failure mode	$M_{u,pa}$ (kNm)	$M_{u,eff}$ (kNm)	diff. (%)	$M_{u,pa}^{sh}/M_{u,eff}$ (%)
HB1	web shear ^a	175	185	+5.7	97
HB3	flange-web shear	154	159	+3.2	58
B7	GFRP dowels shear	46.3	47.0	+1.5	90
SP2	flange-web shear	67.7	70.7	+4.4	47
No1	web shear	131	124	-5.3	43
No2	web shear	81.6	78.8	-3.4	79

^a Narrowly preceded by crushing of the concrete slab.

Once more, after studying models with both complete and partial shear connection under different hypotheses and provided the experimental results, the analytical values for the total acting loads Q_t and midspan deflections w_t were grouped in Table 4.9 together with the difference in percentage versus the experimental values. The same four hypotheses that were used in the serviceability analysis for the partial interaction calculations are repeated for the ultimate limit state.

Results show that partial interaction formulations model better the flexural response of the hybrid beams compared to the complete interaction equations. Deflection values are underestimated due to the fact that concrete has a profound nonlinear response closer to its maximum strength. The analysis also reveals that deflections obtained considering only the shear deformation contributions of the profile's web are more conservative, as expected.

Table 4.9: Maximum loads and total deflections considering various hypotheses at ULS.

Beam	Experimental		Analytical ^a											
			Complete interaction						Partial interaction					
			$\kappa GA, \xi = 0$			$\kappa GA, \xi_{l,mid}$			$\kappa GA, \xi_{EC5}$			$G_p A_w, \xi_{EC5}$		
Q_t^{exp} (kN)	w_t^{exp} (mm)	Q_t (kN)	diff. (%)	w_t^{co} (mm)	diff. (%)	Q_t (kN)	diff. (%)	w_t^{pa} (mm)	diff. (%)	w_t^{eff} (mm)	diff. (%)	w_t^{web} (mm)	diff. (%)	
HB1	181	92.8	179	-1.1	78.9	-15.0	179	-1.1	86.8	-6.5	86.3	-7.0	86.3	-7.0
HB3	296	21.0	253	-14.7	11.2	-46.6	317	+7.0	18.5	-12.0	18.5	-11.9	25.6	+22.1
B7	70.9	70.4	74.7	+5.3	52.8	-24.9	69.0	-2.8	61.3	-12.9	60.8	-13.6	63.6	-9.7
SP2	98.3	33.4	89.2	-9.3	20.9	-37.4	98.4	+0.1	26.5	-20.8	26.5	-20.7	35.2	+5.4
No1	127	12.6	119	-6.3	11.3	-10.7	119	-6.3	14.0	+11.2	14.0	+10.8	15.3	+21.4
No2	139	16.6	130	-6.5	13.4	-19.2	130	-6.5	16.3	-1.9	16.3	-2.2	17.7	+6.6

^a Here diff. represents the difference in percentage between the analytical and corresponding experimental value.

The differences shown in Figure 4.16 between the analytical midspan deflections considering the four hypotheses, and the experimental ultimate midspan deflections in the tests indicate that neglecting the interface slip in the hybrid beams leads to unconservative results. The validation diagram presented in Figure 4.17 confirms that the ultimate bending capacity M_u as well as the corresponding ultimate

midspan deflection w_u obtained with the formulas for the simplified model with partial composite action are more accurate than the analytical model with full/complete shear connection.

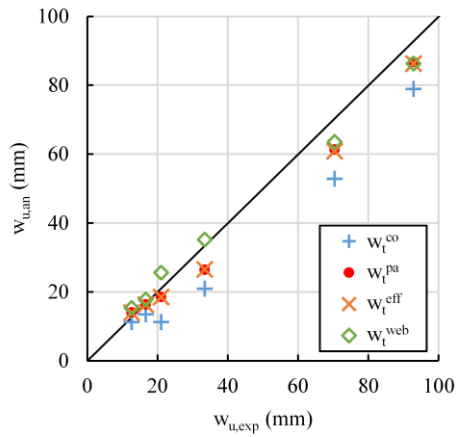


Figure 4.16: Analytically computed midspan deflections versus experimental deflections at ULS.

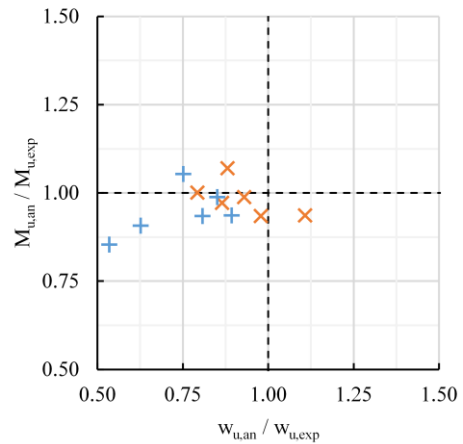


Figure 4.17: Validation diagram for the proposed analytical models in terms of flexural capacity and maximum deflection at ULS.

Finally, if the analytical results at SLS and ULS are divided by the corresponding experimental results, the validation diagrams depicted in Figure 4.18 show that the simplified partial interaction equations capture the test data far more accurately than the analytical model with complete shear interaction. Furthermore, the assumptions that were used are on the safe side of the design.

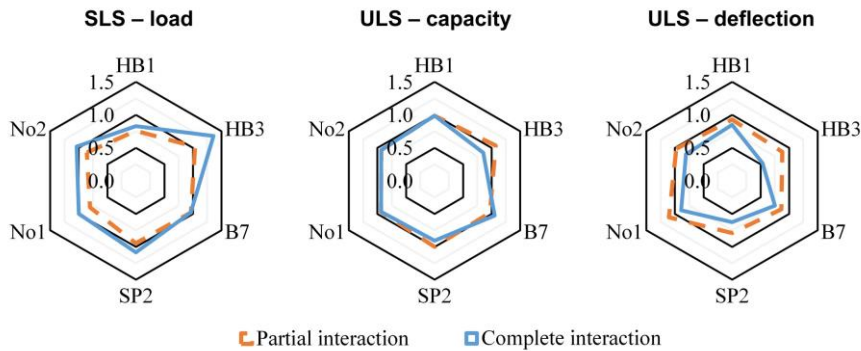


Figure 4.18: Validation diagrams for the proposed analytical models, at SLS and ULS, for the six hybrid beams used in the procedure. Numbers indicate the ratio between the analytical and experimental results.

4.7.4. Flexural behavior

The experimental and analytical load-midspan deflection curves obtained for the six hybrid beam specimens, considering incomplete and full composite action, are plotted in Figure 4.19. For the partial interaction model, approximate values of the dimensionless parameter ξ were used as derived from the Eurocode 5 expression. The uncracked and cracked state of the concrete slab was also simulated.

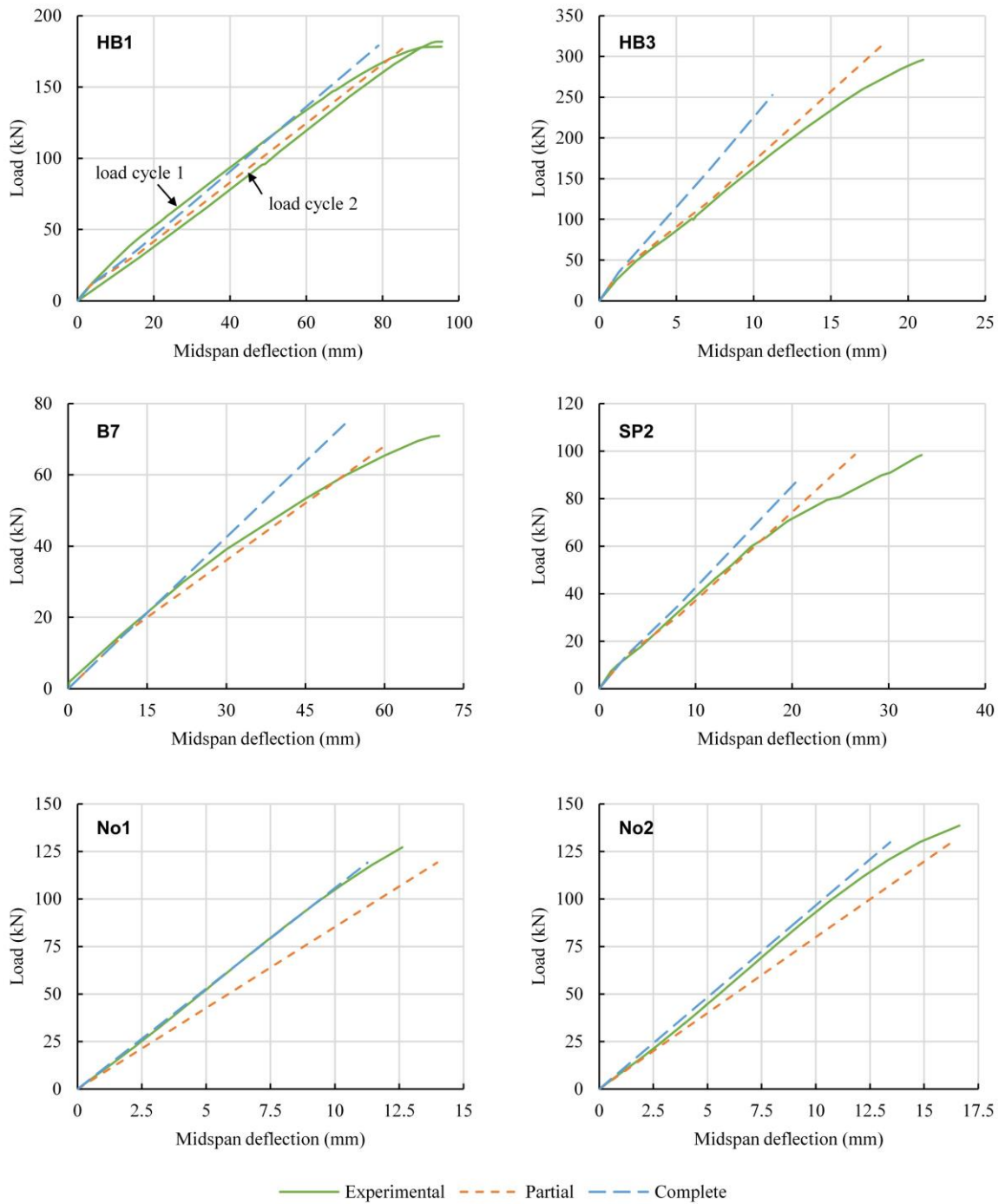


Figure 4.19: Experimental and analytical load-deflection curves of hybrid beam specimens. Partial and complete interaction considered.

Results indicate that by including the slip effects in the design of FRP-concrete beams, better predictions can be made regarding the theoretical flexural behavior, as the displayed effective bending stiffness is closer to the experimentally recorded response. The ultimate capacities and deflections are also more representative of the real performance, as commented earlier. Nevertheless, for specimens No1 and No2 the complete interaction curves are more accurate probably because of the empirical nature of Eq. (4.18) used to determine the stiffness of the connection system. Thus, whenever possible, push-out tests should be performed on equivalent specimens to determine this property. At superior load levels, in all six cases, the theoretical responses deviate slightly as the concrete part develops a nonlinear behavior.

To illustrate in a comparative manner which design codes or proposed formulations give the flexural stiffness the closest to the experimental value, the partial interaction parameter is calculated foremost using the various equations introduced in section 4.3.1.2. The plotted chart in Figure 4.20 confirms several of the observations made in the parametric study in section 4.3.1.3. Thus, the approximate values given by ξ_{EC5} and ξ_W are almost identical to the exact results from evaluating $\xi_{i,mid}$ in function of the beam's load arrangement and support conditions. The equations for ξ_{NC} and ξ_{CH} provide proportionally lower values, with a notable discrepancy for hybrid beam HB3 which had a low degree of shear connection ($\eta = 0.3$). The expressions deduced for the partial interaction parameter from Eurocode 4, ANSI/AISC 360-10, ANSI/AISC 360-05 and AS 2327.1-2003 are null for the four specimens which had a full shear connection (*i.e.*, $\eta \geq 1.0$). Otherwise, for beams HB3 and B7, parameters ξ_{EC4} and $\xi_{AISC-10}$, respectively $\xi_{AISC-05}$ and ξ_{AS} , had close values.

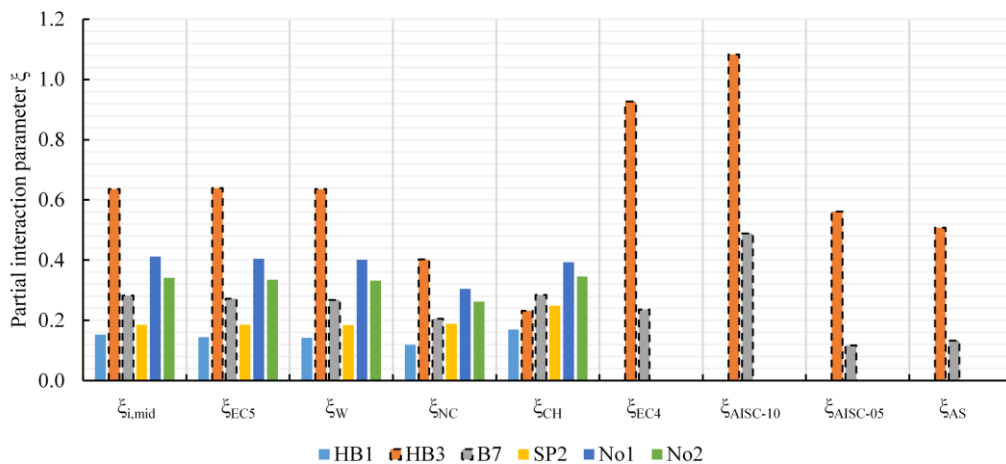


Figure 4.20: Comparative chart of the estimated partial interaction parameters ξ for the six hybrid beams used in the validation procedure.

With the partial interaction parameters computed, the percentile difference between the analytical and experimental flexural stiffness was assessed for the six hybrid beams and plotted in Figure 4.21. A careful examination of the data reveals that the analytical model with complete interaction and with the concrete slab uncracked (pristine) or cracked produces the highest errors in estimating the bending

stiffness. The best overall results are given by Eurocode 5 and the study of Wang. The differences related to the Chinese design code and the study of Nie and Cai are fairly similar to the previous two; however, for hybrid beams with a low degree of shear connection the results are more imprecise.

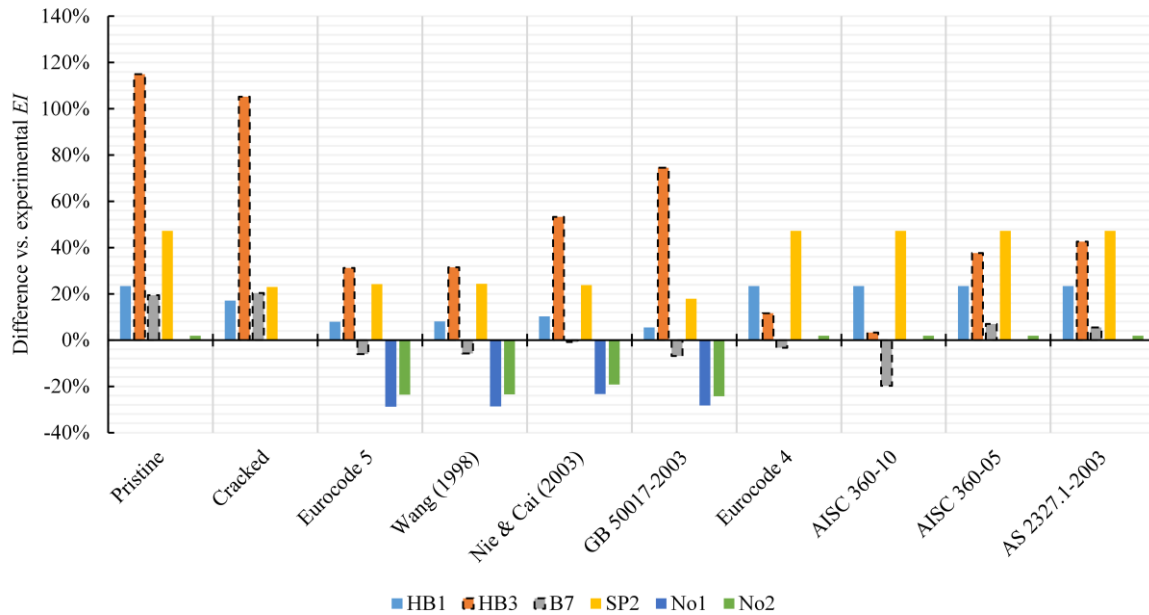


Figure 4.21: Comparative chart of the percentile difference of analytical versus experimental flexural stiffness EI for the six hybrid beams used in the validation procedure.

The errors in the theoretical estimation of flexural stiffness are bigger for the expressions based on the degree of shear connection rather than on the modulus of the connection. The previous version of the American standard for structural steel buildings and the Australian standard for composite structures yield unconservative differences up to 50%. On the other hand, the previous form of the Eurocode 4 and the actual AISC standard return better results, except for one of the six specimens. As commented in advance, the shear modulus of the connectors installed in specimens No1 and No2 was not properly estimated using the empirical relation for steel-concrete composite beams, which explains why the complete interaction analytical model fits better the experimental results.

4.7.5. Strain and stress distributions

A final validation is made by comparing the available experimental strain and stress distributions of the hybrid beams with the results computed from the equations discussed in section 4.4. Firstly, the load-strain curves obtained from cross-sectional strain gauge measurements on the profiles and concrete slabs are compared against the analytical values calculated with Eq. (4.42) under partial interaction premises. The plots depicted in Figure 4.22 prove that the discussed analytical model is adequate.

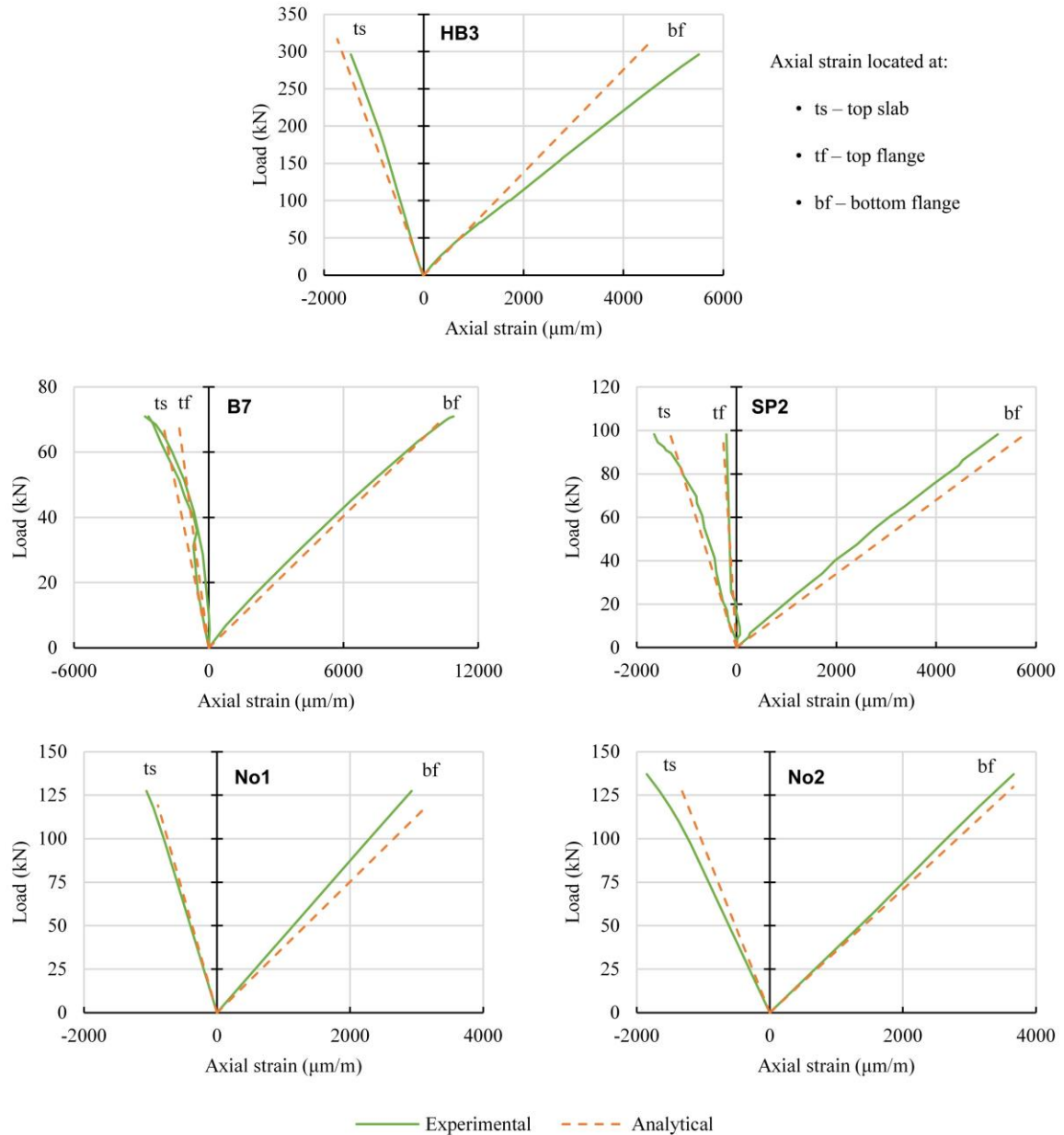


Figure 4.22: Experimental and analytical load-strain curves of hybrid beam specimens. Only partial interaction considered.

Moreover, Eqs. (4.38) and (4.43) which calculate the complete (τ_{co}) and effective (τ_{eff}) in-plane shear stress were used to plot the sectional stress distributions for hybrid beam specimen HB1 in Figure 4.23. The results were validated against the experimental data measured at the instrumented location ($\tau_{exp,max}$) and the strength of the pultruded composite material (τ_{max}).

As indicated in Table 4.8, HB1 ultimately failed due to shearing of the profile’s web, a fact also confirmed accurately by the analytical maximum effective in-plane shear stress distribution. In addition, the figure supports the hypothesis that the majority of the shear force is carried by the hybrid beam’s profile web, as approximated in Eqs. (4.9) and (4.91).

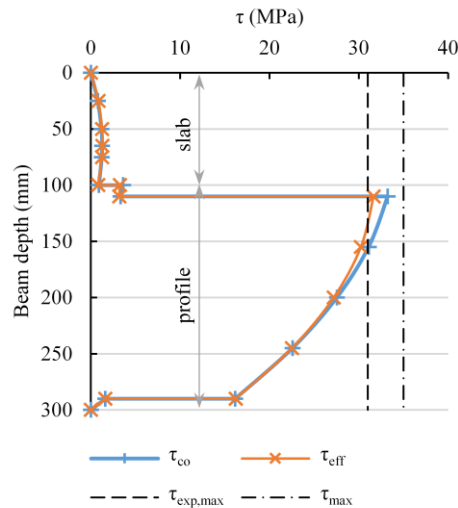


Figure 4.23: Analytical in-plane shear stress distribution over the depth of hybrid beam HB1.

4.8. Validation with experimental campaign results

Based on the analytical formulations detailed in advance, the results obtained during the experimental investigation performed by the author were compared with theoretical predictions. Firstly, the results for the reference specimens are discussed and then those of the hybrid FRP-concrete beams related to serviceability and failure aspects, flexural behavior and strain and stress distributions.

4.8.1. Reference specimens

Reinforced concrete beams model M0 had an ultimate bending capacity of 25.6 kN·m for M0-RCB1 and 18.3 kN·m for M0-RCB2. The results computed in function of the registered failure modes were 24.2 kN·m for the first specimen, in test setup I, and 17.3 kN·m for the second, in test setup II. Hence, the analytical capacities in both cases were about 5% less than the experimental ones.

For the two GFRP profiles that served as reference specimens, the analytical results were calculated for an applied force equal to the maximum sustained load during experiments. Due to the test setup configuration, an ultimate theoretical load attributed to the global lateral torsional buckling failure of the profiles was difficult to be determined as the deformational behavior of the composite's top flange was hindered by the actuator's head. The shear stiffness of the pultruded profiles was estimated using a reduced cross-section area determined by multiplying the total area with Timoshenko's shear coefficient. The results of three possible formulas for the coefficient are shown in Table 4.10. The two cited methods were developed for thin-walled beams constructed of orthotropic laminated composite panels, and include the influence of the elastic properties of the material. The theory presented by Omidvar [192] considers the effect of Poisson's ratio in the transverse direction to the contour, while the

earlier one given by Bank [190] neglects this effect. An average error of just over 2% was calculated between the simplified formulation and the more complex expressions. Thus, for the analytical predictions of Profile 1 and Profile 2, the effective shear area was taken as the profile’s web area.

Table 4.10: Timoshenko shear coefficient of the GFRP pultruded profile.

Shear coefficient	Omidvar [192]	Bank [190]	A_w/A_p	error (%)
κ	0.454	0.453	0.464	+2.3

The comparative experimental-analytical charts for the two reference profiles are illustrated in Appendix C. The load-midspan deflection plots show an accurate fit of the experimental results, with a small exception for the closing behavior of Profile 2 which started to bend laterally at a lower load. The sectional strain variations (S1 and S2) in Profile 2 are very similar, with a slight difference in the compressed top flange. Bottom flange axial strain variations of the same profile are reproduced below in Figure 4.24. Due to the concentrated midspan load, the deformations measured at the center (at ϵ_9) were locally altered, explaining the divergence versus the analytical curve.

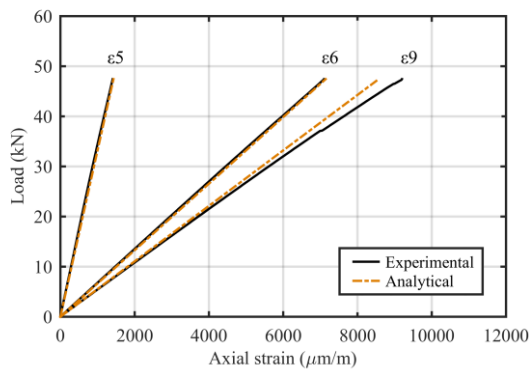


Figure 4.24: Bottom flange axial strain variations of Profile 2: experimental and analytical curves.

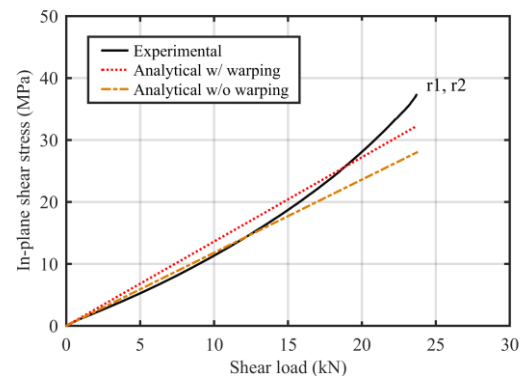


Figure 4.25: In-plane shear stress variation in Profile 2, section S2, in function of the applied shear load: experimental and analytical curves with or without longitudinal warping.

The shear stress distribution in section S2 of Profile 2 is plotted in Figure 4.25 versus the analytical curves computed using Eqs. (4.47) and (4.48). The theoretical model without longitudinal warping predicts fairly well the initial half of the response, while the relation that includes the longitudinal warping function generates superior shear stress values for the same amount of shear load. Nevertheless, both equations produce a linear distribution as opposed to the bending test.

4.8.2. Serviceability and failure analysis

For the eight FRP-concrete hybrid beams tested in the investigation, a comparison is made in Table 4.11 between the experimental and analytical results at the serviceability and ultimate limit states (SLS

and ULS). The serviceability bending moments correspond to a maximum midspan deflection equal to $L/250$, as commented in section 4.3.1. The ultimate bending capacities were determined in function of the registered failure modes, by using Eq. (4.89) or (4.90). The shear load was considered to be carried entirely by the profile's web and the maximum deflections were obtained using the simplified formula for the partial interaction parameter ξ , as derived from Eurocode 5.

Table 4.11: Results for hybrid beams at the serviceability (SLS) and ultimate limit states (ULS/ u): bending moment (M), midspan deflection (w), and bottom flange ultimate axial stress (σ).

Beam	Experimental	Analytical										
	Failure mode	M_{SLS} (kNm)	M_u (kNm)	w_u (mm)	σ_u (MPa)	M_{SLS} (kNm)	diff. (%)	M_u (kNm)	diff. (%)	w_u (mm)	diff. (%)	M_u/M_u^{cr}
M1-HB1	web-flange shear ^a	7.9	36.3	42.6	420	10.5	+33.0	36.7	+1.1	35.2	-17.3	1.04
M1-HB2	web-flange shear ^a	10.4	41.5	51.5	474	10.5	+1.2	39.5	-4.8	36.5	-29.1	1.00
M2-HB1	web-flange shear ^a	10.7	35.1	52.5	406	10.5	-1.8	36.7	+4.5	35.2	-32.9	1.04
M2-HB2	web crushing ^b	9.4	33.9	51.7	415	10.5	+12.4	33.9	+0.1	31.4	-39.4	0.86
M1-HB3	web-flange shear	9.0	21.6	23.4	210	8.8	-1.3	21.7	+0.4	25.5	+9.0	0.62
M1-HB4	web-flange shear	8.7	22.8	22.4	218	8.9	+2.2	23.4	+2.4	26.3	+17.5	0.59
M2-HB3	web-flange shear	8.8	23.9	35.2	256	8.8	+0.2	23.4	-2.3	27.5	-22.0	0.67
M2-HB4	web-flange shear	8.7	24.3	33.6	250	8.9	+1.9	23.4	-3.9	26.3	-21.6	0.59

^a Preceded by concrete slab crushing.

^b Effective crushing area was taken as $t_w(h_c + b_{plate})$, where b_{plate} – width of the load bearing plate.

The tabular numbers reveal a difference under 5% among the ultimate experimental and analytical bending moments and an even smaller difference for the serviceability limit case. There are two larger exceptions for SLS because of the jolts in deflection measurements induced by the occurrence of large flexural cracks. The differences between maximum deflections at failure are underestimated since the concrete behavior is considered linear in the analytical model. Nevertheless, the overall stiffness of the hybrid beams with partial interaction is estimated with good precision as it will be shown and discussed in the next section.

The ratio between the bending moment considering a fragile type of failure and the one based on a compressive failure of the concrete slab, M_u/M_u^{cr} , reveals an important ductility aspect of the hybrid beams. For the four-point bending test configuration the ratios are less than unity while for the three-point setup most of the values are slightly over it. This theoretical evaluation coincides with the experimental observations where three of the eight hybrid beams, M1-HB1, M1-HB2 and M2-HB1, failed in a pseudo-ductile manner, while on the contrary the rest had a predominantly brittle response.

For the three hybrid specimens mentioned before which failed initially due to concrete crushing, Table 4.12 presents an analytical assessment of the results considering three main hypotheses: (i) complete shear interaction – Eqs. (4.61) and (4.1); (ii) partial shear interaction with slip strain evaluation – Eq. (4.74); and (iii) partial shear interaction using the approximate approach and the Eurocode 5 definition of effective flexural stiffness – Eqs. (4.88) and (4.13). Differences expressed in terms of percentages indicate that the values considering complete interaction are on the unsafe side of the design, overestimating the flexural capacity of the hybrid beams by as much as 20%, whereas results

reflecting the third hypothesis are the most accurate, with error levels under 3% for capacities and slightly higher for midspan deflections.

Table 4.12: Flexural responses of hybrid beams considering concrete crushing: bending moment (M) and midspan deflection (w).

Beam	Experimental		Analytical									
			Complete interaction					Partial interaction				
	M_u^{cr} (kNm)	w_u^{cr} (mm)	M_u^{cr} (kNm)	diff. (%)	w_u^{cr} (mm)	diff. (%)	M_u^{cr} ^a (kNm)	diff. (%)	$M_{u,eff}^{cr}$ ^b (kNm)	diff. (%)	w_u^{cr} (mm)	diff. (%)
M1-HB1	34.2	36.5	41.1	+20.1	28.2	-22.7	36.1	+5.5	35.1	+2.6	33.7	-7.5
M1-HB2	38.8	38.6	45.3	+16.7	31.0	-19.7	39.5	+1.7	39.5	+1.8	36.5	-5.3
M2-HB1	34.9	50.2	41.1	+17.8	28.2	-43.8	36.1	+3.4	35.1	+0.6	33.7	-32.9

^a Computed by estimating the maximum interlayer slip strain.

^b Computed using the approximate approach.

4.8.3. Flexural behavior

Figure 4.26 and Figure 4.27 plot the analytical and experimental load-midspan displacement curves for the M1 and M2 type of hybrid beams. The theoretical predictions take into account the initial complete shear interaction behavior and the uncracked state of concrete, as well as the ensuing development of interface slip and slab cracking. Plastic deformations of the concrete slab are not simulated and the steel reinforcement contribution is neglected. The stiffness of the connection present in the M1 beams was evaluated using the same empirical relation that was applied for the M2 specimens since quantifying the influence of the concrete embedding the profile was problematic.

The structural behavior is reproduced with good accuracy by the analytical procedure, and particularly the flexural stiffness which reflects the transition from complete to partial shear interaction. The theoretical responses emulate the effects of a higher concrete strength class but limit the analysis to an elastic domain. Nonlinear behavior was more present in the M2 experiments and reflects the constitutive behavior of the concrete at higher normal strains before the ultimate load.

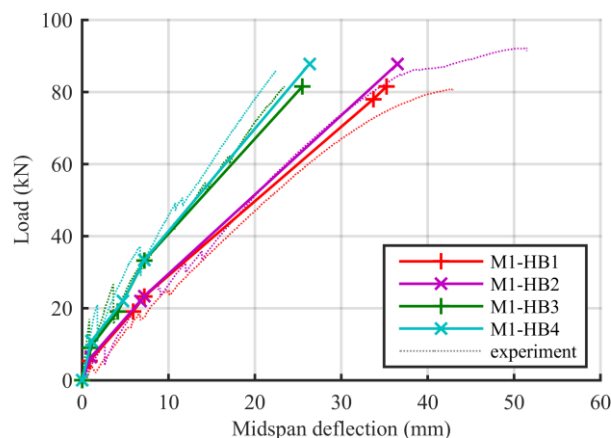


Figure 4.26: Hybrid beams model M1: analytical and experimental load-midspan deflection curves.

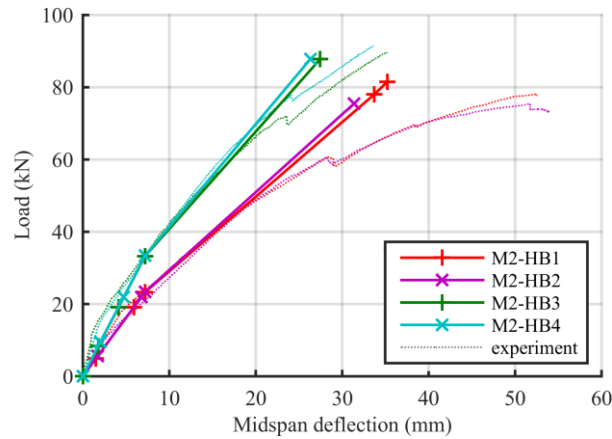


Figure 4.27: Hybrid beams model M2: analytical and experimental load-midspan deflection curves.

The flexural stiffness exhibited in the main part of the tests was estimated by calculating the partial interaction parameter from the various equations introduced in section 4.3.1.2 that were derived from design codes and proposed analytical models. Figure 4.28 and Figure 4.29 illustrate in a comparative way the estimated values for the hybrid beams in function of the employed theories, for the two different specimen batches. The chart columns are color-coded based on the determining factor of the results. Thus, the white columns refer to a hybrid beam with complete shear interaction, the light gray columns relate to the theories based on the connection’s modulus, while the dark gray columns indicate the formulas based on the degree of shear connection. A secondary axis is added to reflect the corresponding partial interaction parameter values and a horizontal line indicates the level of the average experimental stiffness of the specimens having the same concrete strength.

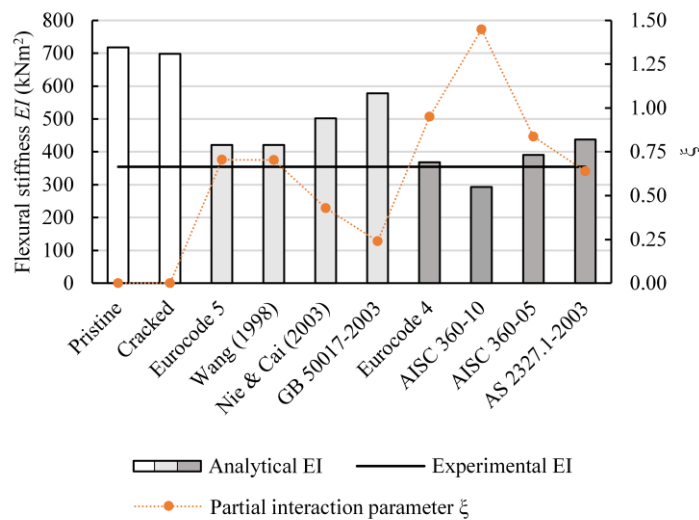


Figure 4.28: Analytical and experimental flexural stiffness of hybrid beams with concrete mix C1. Various design code and proposed formulations are compared.

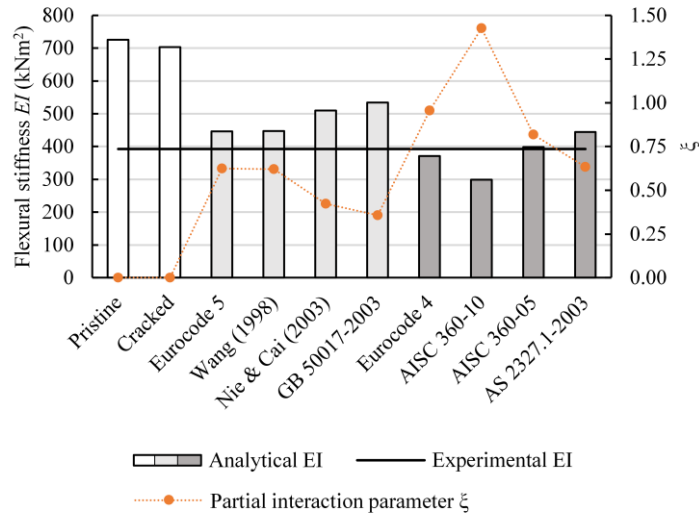


Figure 4.29: Analytical and experimental flexural stiffness of hybrid beams with concrete mix C2. Various design code and proposed formulations are compared.

The graphics demonstrate several similarities between the theories. Firstly, the flexural stiffness determined by neglecting the interface slip, in either a pristine or cracked hybrid beam, is almost double in comparison with the experimental one. The results given by Eurocode 5, Eurocode 4 and AISC 360-05 are the closest to the reference line. On the other hand, the Chinese design code GB 50017-2003 and the Australian Standard AS 2327.1-2003 provide slightly higher effective stiffness values. By accounting for inelastic behavior, the current American specifications, AISC 360-10, offer the most conservative values.

After the analytical flexural stiffness results were estimated, the percentile differences versus the experimental data were plotted in the following pair of clustered column charts, in Figure 4.30 and Figure 4.31, depending on the test setup configuration that was used. There are four color-coded columns attributed to the tested beams in the referenced setup that are grouped in relation to each of the previously commented theories.

The first two analytical models produce discrepant results which require the use of partial interaction theories. Eurocode 4 and AISC-05 percentiles are the smallest from the series, indicating an approximation error of under 15%; however, the codes limit their application range. The effective stiffness estimated with the relations from Eurocode 5, the study of Wang or the Australian standard follow closely, with errors under 25%. The remaining analytical models elicit important deviations from the experimental outcome. The vast majority of the formulations overestimate the flexural stiffness, with the notable exception of AISC 360-10. Somewhat higher flexural stiffness values were calculated for the specimens loaded under four-point bending.

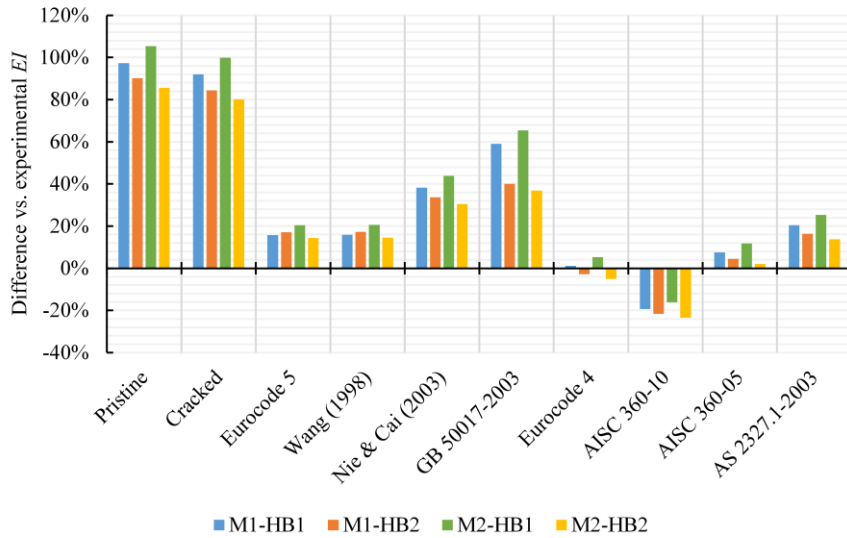


Figure 4.30: Comparative chart of the percentile difference of analytical versus experimental flexural stiffness EI for the four hybrid beams tested under three-point bending (test setup I).

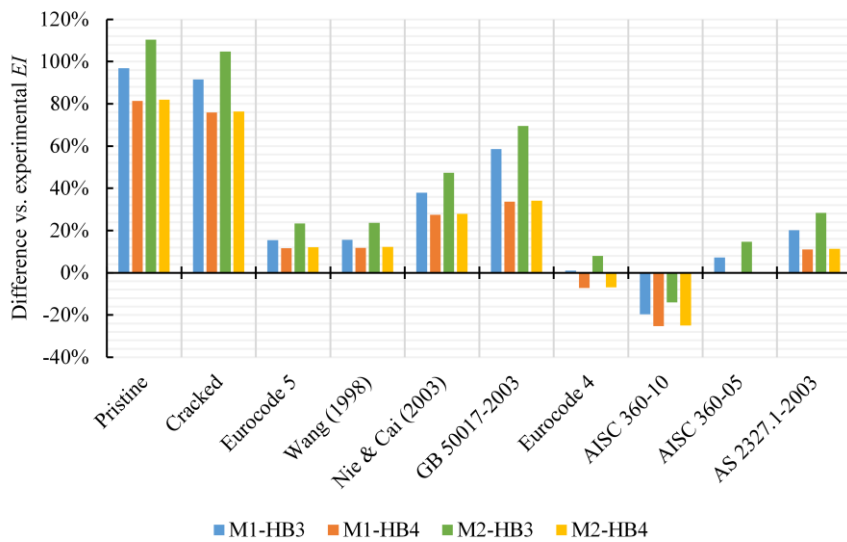


Figure 4.31: Comparative chart of the percentile difference of analytical versus experimental flexural stiffness EI for the four hybrid beams tested under four-point bending (test setup II).

To emphasize, the investigated hybrid beam models had a low degree of shear connection, so for fully composite equivalent specimens the equations based on the stiffness/modulus of the connectors will yield the most accurate results.

4.8.4. Strain and stress distributions

A comparative analysis between the experimental and analytical strain and stress distributions is carried out for the four M2 hybrid beams since they were notably more instrumented. Comparative

charts are shown for all four specimens in the additional Appendix C, and in continuation results are illustrated only for a singular emblematic case.

An analytical estimation is made in Figure 4.32 for the position of the neutral axes across the depth of M2-HB1. The uncracked complete shear interaction model predicts well the initial part of the variation while the cracked model with interlayer slip exhibits slight differences versus the final position of the two neutral axes before collapse. The data reveals that the hybrid beam subsystems were almost working independently at the moment of failure.

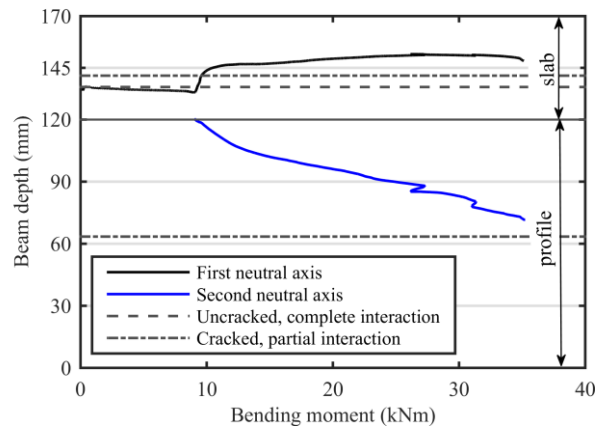


Figure 4.32: Neutral axis depth variation in function of the applied load for hybrid beam M2-HB1 in section S1. Experimental curves and analytical predictions.

The longitudinal strains computed with the equations detailed in sections 4.4 and 4.5 accurately predict the sectional distributions in the hybrid beams at intermediate load levels, where the members still display a mostly linear behavior. The experimental and analytical strain distribution of M2-HB4 is depicted in Figure 4.33 for an applied load of 50 kN.

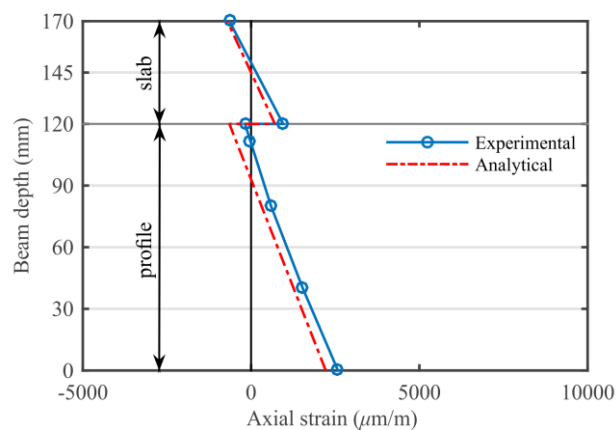


Figure 4.33: Experimental and analytical axial strain distribution in hybrid beam M2-HB4, in section S1, at an intermediate load level of 50 kN.

Experimental and analytical slip strains, maximum midspan strains and corresponding axial stresses are compiled in Table 4.13 for the same intermediate load of 50 kN, above the serviceability limit check, where the concrete’s stress distribution was still plane. The percentile differences for the interlayer slip

strain show that the beams had a more flexible shear connection than assumed. With respect to the maximum axial strain and stress which developed in the GFRP profiles, the average difference was lower, around 15%.

Table 4.13: Strain and stress results at an intermediate load of 50 kN: interlayer slip strain at section S1 (ϵ_s), maximum GFRP axial strain (ϵ_{max}) and corresponding maximum longitudinal tensile stress (σ_{max}).

Beam	Experimental			Analytical				
	ϵ_s (%)	ϵ_{max} (%)	σ_{max} (MPa)	ϵ_s (%)	diff. (%)	ϵ_{max} (%)	σ_{max} (MPa)	diff. (%)
M1-HB1		0.56	219	0.26		0.46	180	-18.1
M1-HB2		0.51	198	0.23		0.45	176	-11.1
M2-HB1	0.37	0.52	203	0.26	-28.5	0.46	180	-11.5
M2-HB2	0.38	0.54	212	0.23	-38.4	0.45	176	-16.8
M1-HB3		0.35	137	0.16		0.27	106	-22.4
M1-HB4		0.32	127	0.14		0.27	104	-17.7
M2-HB3	0.11	0.30	117	0.16	-36.8	0.27	106	-9.6
M2-HB4	0.11	0.29	113	0.14	-18.8	0.27	104	-7.8

The analytical variation of the slip and slip strain in function of the applied action was confirmed to be linear by the plots contained in Appendix C. In the mathematical evaluations, the shear modulus of the connection inside beams model M1 was considered to be the same as for specimens M2, a fact contradicted by the values exposed in the previous table. The longitudinal distribution of the slip at the interface of the two materials is plotted in Figure 4.34 for the specific case of M2-HB4. As observed, the relative end displacement measured in the experiment lays close to the theoretical prediction, on the inferior side of the curve.

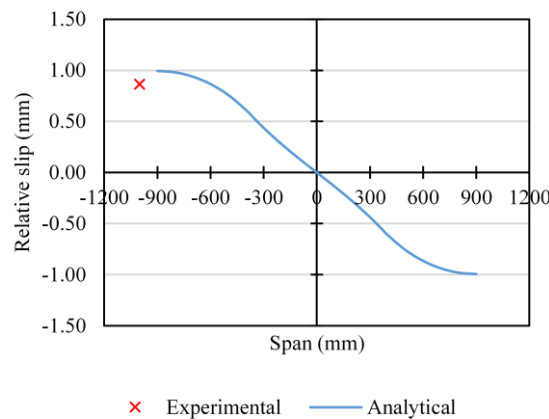


Figure 4.34: Analytical longitudinal slip distribution in hybrid beam M2-HB4 at an intermediate load level of 50 kN, versus the registered experimental data slip point.

Finally, in-plane web shear stress values determined using the two analytical models from Eqs. (4.48) and (4.47) are plotted in Figure 4.35 for M2-HB4 versus the shear force carried by the hybrid beam, and against the experimental curves obtained from the two strain gauge rosettes. The first model

which includes the longitudinal warping of the cross-section produces higher stress results compared to the second, classic formulation of Jourawski-Collignon. A significant discrepancy is noticed between the theoretical linear responses and the measured nonlinear curves, most likely explained by the anisotropic, inhomogeneous nature of the composite profile. Both estimations are also larger than the measured data probably due to the conservative approach in supposing that the entire shear force in the hybrid member is carried just by the profile's web. Ultimate stress values were at least 20% higher than the determined strength of the material, as there is currently no precise established standard method for determining this property for pultruded composite shapes made up of combinations of uniaxial and multiaxial fibers.

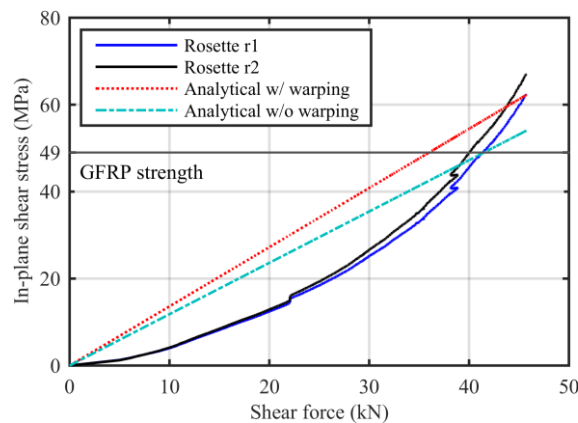


Figure 4.35: In-plane shear stress variation in hybrid beam M2-HB4, section S2, in function of the applied shear load. Experimental and analytical curves with or without warping.

If the shear role of the concrete slab is accounted for, then, by employing Eqs. (4.38) and (4.43), a better assessment of the sectional shear stress distribution in the hybrid beams can be obtained, as exemplified here by Figure 4.36 for M2-HB4.

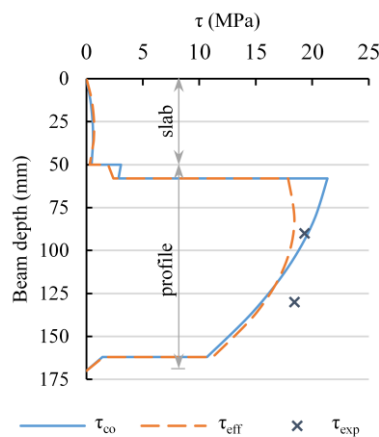


Figure 4.36: In-plane shear stress distribution in M2-HB4, in section S2, at an intermediate load of 50 kN. Analytical curves under complete (τ_{co}) and partial (τ_{eff}) shear interaction assumptions versus experimental data points (τ_{exp}).

This time around, the analytical values are lower but far closer to the experimental data, and the partial interaction model proves once more that is better fitted at simulating the flexural behavior of hybrid beams with mechanical shear connectors. The chart also indicates that the maximum shear stress occurred at the web-flange junction, where the failure was also perceived experimentally.

4.9. Conclusions

Analytical studies performed on hybrid beams so far have rarely acknowledged the influence of interface slip over flexural behavior. Furthermore, there are currently no available construction codes, guides or manuals for the design of such novel composite elements that incorporate pultruded FRP profiles. Hence, the concluded chapter presented a detailed analytical design procedure suitable for hybrid beams with flexible shear connection, made of pultruded FRP shapes attached to reinforced concrete slabs. Serviceability and failure aspects were discussed and then the proposed formulas were validated against available experimental data from several published investigations and from the laboratory campaign carried by the author. Since hybrid beams can exhibit limited slippage when using bonded joints or combined joints, and in exchange, a significant slip on behalf of mechanical connection systems, both complete and partial shear interaction assumptions were considered in deducing the majority of the mathematical expressions.

The following main observations are made regarding the analytical procedure:

- A dimensionless parameter was introduced to quantify the effects of partial shear interaction in estimating flexural capacities, deflections, internal actions and stress distributions of hybrid FRP-concrete beams. From the perspective of the connection's flexibility, exact and simplified expressions were deduced for it from the equations found in Eurocode 5, the Chinese design code GB 50017-2003 and in several published studies. Conversely, from the perspective of the degree of shear connection, parameter formulas were extracted from the relations provided in the main steel-concrete composite design codes – the Eurocode 4 (DD ENV 1994-1-1:1994), the American ANSI/AISC 360 and the Australian AS 2327.1. From the comparison, it was concluded that in order to model effectively both fully and partially composite hybrid beams with mechanical joints, the relations should be based on the stiffness of the connection and not on the capacity.
- The simplified dimensionless expression derived from Eurocode 5, which is independent of the load and supporting conditions, fitted very well the exact analytical parameter distributions even for low values of composite action, with errors under 4% for the midspan location. On the contrary, the solution adapted from GB 50017-2003 produced more discrepant results, especially for weak joint systems. Bending deflection was found, however, to be much more

sensitive to the stiffness of the connection system than to the error in approximating the dimensionless partial interaction parameter.

- Normal stresses and internal bending moments are higher and in-plane shear stresses and internal normal forces are lower in hybrid FRP-concrete beams with partial interaction than in their equivalent variants with complete shear interaction.
- Maximum interface slips occur at the support regions, while maximum slip strains are found at the positions of the applied loads (maximum moment sections). For the same hybrid beam, larger slip strains appear as the load is applied in a more concentrated way. Results also indicated that after an initial increase in connection stiffness, the benefits of adding more shear connectors diminish as the slip strain varies asymptotically, suggesting that even for fully composite members its value is not null.

The analytical procedure was validated first against published experimental data of flexural tests performed on FRP-concrete beams with mechanical connections. The selected hybrid specimens had various cross-section geometries, joint designs and composite materials, were more slender or stockier in dimensions and presented a full or partial shear connection. Several conclusions were drawn from the validation study, as commented below:

- Analytical estimations showed that the effective bending stiffness of the members was between 13-39% lower and the coupling moment of the FRP-concrete sections up to 26% less, when interlayer slip was considered.
- At the Serviceability Limit State (SLS), the calculated midspan deflections according to the complete or partial interaction assumptions framed the experimentally measured values as there was probably still some initial friction or adhesion at the interface. The results obtained by using the simplified parameter deducted from Eurocode 5 predicted fairly well the deflections caused by flexural deformations; however, by limiting the evaluation of angular deformations to the web of the profiles, a more conservative response was achieved at SLS. At half of the ultimate reached load, the results accounting for the connection's stiffness were already more accurate, suiting better the experimental data.
- Maximum bending moments at concrete compressive failure demonstrated that there is little difference between using the simple dimensionless interaction parameter or the more complex expression based on calculating slip strains. Acceptable errors were found for the simplified partial interaction model in predicting the maximum sustained moment and the midspan deflections. In contrast, for the complete interaction model, the calculated bending capacities were around 15% higher and the midspan deflections were about 50% lower in comparison with the experimental results. Since the analysis is based on a linear elastic behavior of the materials,

deflections that are underestimated for higher concrete compressive strains can be adjusted by considering shear deformations only in the web of the profiles.

- The analytical load-displacement curves of the partial interaction model displayed an appropriate fit except for a couple of specimens. This fact was most likely caused by an incorrect estimation of the shear connection stiffness by the empirical formula adopted from steel-concrete composite beams.
- The analytical flexural stiffness of the hybrid beams computed with the parameter deducted from Eurocode 5 offered the best resolution. On the other hand, the Eurocode 4 (initial version), ANSI/AISC 360 and AS 2327.1 overvalued the flexural stiffness by as much as 50%. Lastly, GB 50017-2003 generated higher errors for the specimens with a low degree of shear connection, as anticipated.
- The theoretical model considering the effects of interlayer slip fitted better the sectional experimental strain variations and shear stress distributions. It was pointed out that if the concrete slab takes more than half of the shear load then its contribution must be reflected in the model as the approximate shear stress formula can lead to inefficient design and use of material properties.

In the last part of the chapter, the accuracy of the analytical procedure was checked against the results of the experimental tests performed by the author. The ensuing conclusions of the study are reported beneath:

- The flexural behavior of the single profiles was predicted very well in terms of displacements and axial strains. Slight nonlinearities such as section warping and local load deformation effects were not reproduced. The in-plane shear stress distribution was challenging to match because of the anisotropy of the material and inherent behavior of the polyester matrix.
- Computed sustained moments at SLS (deflection check) and ULS (fragile failure) were determined with high accuracy by the theoretical model, within 5% of the experimental results. Midspan deflections at ULS were underestimated due to the strong nonlinear behavior toward collapse.
- The analytical method allows to establish the order of the causes to which the beams fail. Consequently, in three cases, concrete crushing was evaluated to be the principal mode of failure followed by web-flange shearing. The ultimate bending capacities neglecting interface slip were 20% higher than in the tests. Alternatively, for the partial interaction model, the errors in calculating flexural crushing capacities and midspan deflections were below 3% and 8% respectively, for certain situations.

- Theoretical load-deflection curves displayed a high degree of correlation to the experimental data, where they were able to capture the change from complete to partial shear interaction, the variation in concrete strength class and the reduction in stiffness due to concrete cracking.
- Regarding the evaluation of flexural stiffness, the complete shear interaction model and the formulas deducted from GB 50017-2003 severely overestimated the results, while the Eurocode 4 and AISC 360-05 produced the smallest differences, under 15%. The relations adapted from Eurocode 5 and AS 2327.1 generated slightly higher values, with differences up to 25%. The current version of the American specifications, AISC 360-10, was the only conservative method which undervalued the flexural stiffness by almost 20%.
- Axial strain distributions and position of neutral axes were properly replicated at an elastic stage by the partial interaction model, whereas interface slips and slip strains had larger estimation errors.
- Three methods were discussed for the determination of in-plane shear stresses in the webs of the FRP profiles. The first two which neglected the shear contribution of the concrete slab overpredicted the shear stresses, regardless of the section warping, and thus were deemed to be conservative from a design point of view. The third method, which did not exclude the slab's shear contribution, produced better initial results and indicated the position of the maximum occurring stress across the beam's depth.

Overall, due to the improved accuracy of the expressions accounting for shear connection flexibility, the analytical procedure based on the Timoshenko composite beam theory and the elastic interlayer slip model is capable of capturing in a proper way the flexural behavior and performance of hybrid FRP-concrete beams.

5

Numerical models

5.1. Introduction

Finite element modeling has become in the recent decades an attractive numerical tool for designing, analyzing and predicting the mechanical behavior and performance of novel construction elements or technologies. Thus far, however, in contrast to the research developments in simulating steel-concrete composite beams, hybrid FRP-concrete numerical models have preponderantly relied on simplified material, geometry and contact considerations, limiting in consequence the accuracy required for obtaining reliable engineering data. Furthermore, given the characteristics and influence of the mechanical shear connection systems, finite element analyses capable of reproducing the associated interface interactions are desired. Lastly, as evidenced by the previous analytical validations, a linearly-elastic model based on a constant interface stiffness may not be suited for estimating the flexural behavior outside of the serviceability domain for hybrid beams with low degree of shear connection.

Hence, the current chapter presents the development of an effective finite element model that is capable of capturing the fundamental behavior of hybrid beams with partial shear interaction subjected to combined bending and shear. First of all, a number of preliminary models are introduced and discussed which have increasingly complex definitions and features. They help to identify the governing parameters which influence the structural response, and following the conclusions of these initial trials, a definitive three-dimensional nonlinear finite element model is proposed and its results are verified. The descriptions of the models refer to the material constitutive laws, geometry, mesh, interactions and constraints, boundary and load conditions, as well as to the analysis settings and outputs.

The M2 hybrid specimens from the laboratory campaign were used in the validation procedures along several other referenced hybrid beams found in literature. Of interest for checking were the flexural behavior, normal and shear stress variations, and the interface slip distributions. The numerical data were compared against the experimental results and the estimations offered by the analytical model with partial shear interaction obtained by using the simplified parameter expression deduced from Eurocode 5.

5.2. Initial finite element models

To begin with, a couple of simulations were performed to ascertain that the structural response of single GFRP profiles can be appropriately predicted by using the homogenized effective mechanical properties determined by the author through destructive and nondestructive testing. Afterwards, simple finite element (FE) models with linear elasticity were built for part of the hybrid beam specimens tested in the campaign and for several experimental cases found in the bibliography. The last initial models deal with the inclusion of material and connection nonlinearities in geometrically idealized FE models.

5.2.1. GFRP profile calibration

Three-dimensional models of the glass fiber-reinforced Profile 1 and Profile 2 from the experimental campaign (see Chapter 3) were created and analyzed within *ANSYS Mechanical™ CAE* [186,208]. The finite element representations included the steel loading plates, web-flange fillets and, in the case of Profile 2, the laterally bonded wood web stiffeners as seen in Figure 5.1.

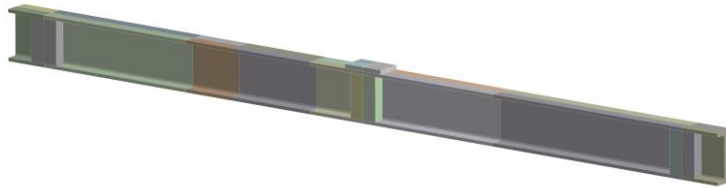


Figure 5.1: Three-dimensional model of GFRP Profile 2 including stiffeners and loading plate.

The composite material assigned to the profile was considered to have orthotropic elasticity with similar properties in the cross-sectional plane. Thus, the longitudinal elastic modulus was taken as 39.11 GPa, the transverse elastic moduli were equal to 10.77 GPa and the three independent shear moduli were assumed identical and equal to 3.98 GPa. The major Poisson ratios in the pair of orthogonal axial planes were taken as 0.27 and in the transverse plane as 0.33. The plates and stiffeners had isotropic elasticity and typical material properties associated. Simply-supported boundary conditions were reproduced and the load applied was equal to the maximum force sustained experimentally. At this initial stage, the mesh was left to be generated automatically with solid elements by the software program.

As commented before, one of the objectives of the simulations was to see how well the numerical results fit with the experimental recordings and with the analytical estimations. The load-midspan deflection responses of Profile 1 and Profile 2 are plotted in Figure 5.2, respectively Figure 5.3. It is noted that the numerical response practically overlaps the mathematical model and the laboratory results for both specimens, with a small exception for the latter where at higher loads the experimental response

was slightly more flexible. Moreover, the finite element model appears to take correctly into account the deflection contributions from angular deformations of the composite material.

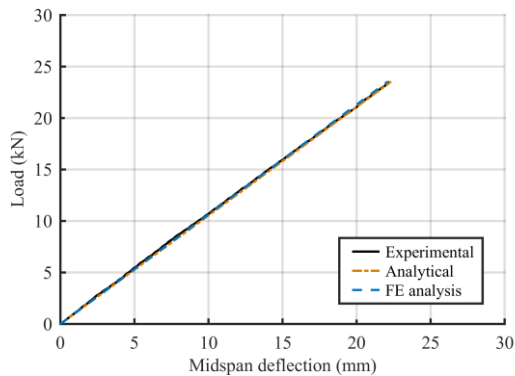


Figure 5.2: Load-midspan deflection response of Profile 1: experimental, analytical and numerical curves.

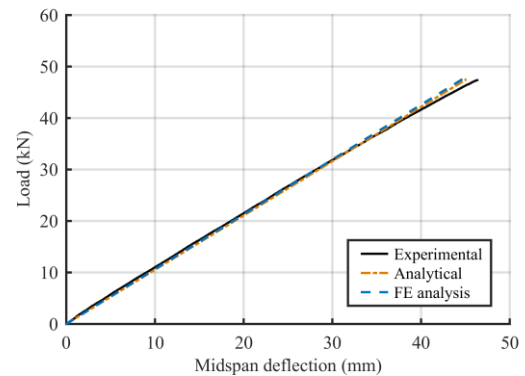


Figure 5.3: Load-midspan deflection response of Profile 2: experimental, analytical and numerical curves.

In terms of axial strain variations, the results obtained at section S1 from the finite element analysis of Profile 2 match the analytical estimations as seen in Figure 5.4, and reside closely to the experimental data. Good agreements were found also at section S2, near the left support, and along the bottom flange of the profile. In contrast, the in-plane shear stress distribution in the profile's web is not suitably captured by the linear elastic model at higher sustained loads. The numerical response is similar to that of the analytical expression without longitudinal warping and yields lower values than the formula considering axial strain contributions from out-of-plane deformations (w/ warping). The nonlinear increase of shear stresses in the GFRP toward higher loads explains the additional flexibility of the late experimental flexural response from Figure 5.3.

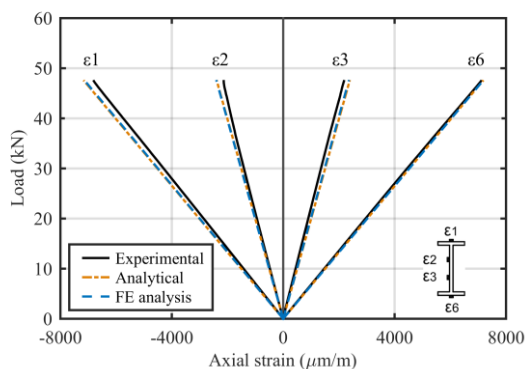


Figure 5.4: Axial strain variations of Profile 2 in section S1: experimental, analytical and numerical values.

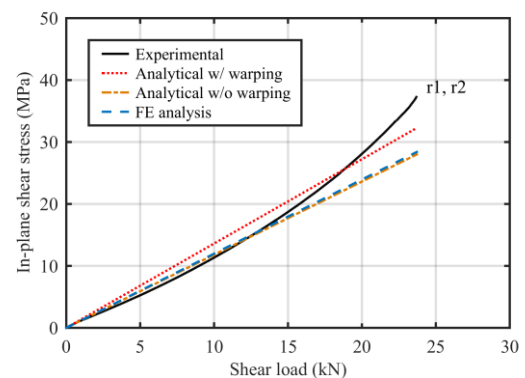


Figure 5.5: In-plane shear stress variation in Profile 2, section S2, in function of the applied shear load: experimental, analytical and numerical curves.

Overall, in the absence of more complex composite material definitions in the finite element model, the fundamental flexural behavior of the GFRP profiles can be reproduced to a great degree with the orthotropic elasticity definition based on the homogenized effective mechanical properties.

5.2.2. Linear elastic model for hybrid beams

The first finite element model for FRP-concrete hybrid beams was conceived as an easy-to-implement numerical solution where the structural components are reduced to their geometrical essence and where the constitutive materials and connectors behave in a linear elastic way. Consequently, the partial interaction at the interface between the concrete slab and composite profile was based on the elastic stiffness of the connectors as determined from push-out tests or empirical formulations (Eq. (4.18)). This approach is different to the analytical model described in the previous chapter, in the sense that the connection is represented by a series of discrete finite elements and not by a continuous interface with uniform stiffness. Therefore, it allows for a more accurate depiction of structural members with mechanical shear connectors and with varying grades of connector spacing.

On these considerations, a three-dimensional finite element model was developed in the structural analysis software *SAP2000* [209] that served as basis for the M2 hybrid beams tested by the author. Similar models were also created for the referenced beams used in the validation of the analytical equations (section 4.7). The concrete slab was modeled as a thick shell which includes transverse shear deformations in the out-of-plane plate-bending behavior, following the thick-plate Mindlin-Reissner formulation. Longitudinal slab reinforcement bars were modeled as smeared layers in the definition of the shell elements; however, the results showed that their inclusion has a minimal influence over the global flexural response of the hybrid beams. The composite profiles were idealized as frame elements based on Timoshenko's beam theory while the shear connectors were modeled as a single condensed row of link elements positioned at the specified physical coordinates, as seen in Figure 5.6.

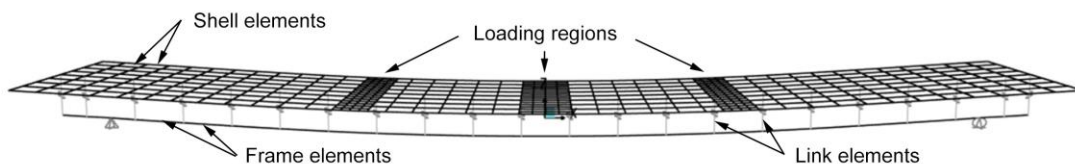


Figure 5.6: Schematic view of the deformed hybrid beam M2 finite element base model.

Since material nonlinearity is accounted by the software only at the location of concentrated plastic hinges and when using layered shell objects, the structural components were assigned elastic material properties according to the available data. Concrete was considered to be homogeneous, isotropic and was defined by its elastic modulus and Poisson's ratio. The composite profiles were designed as homogeneous with orthotropic elasticity and with defined material orientation. In the case of the M2 hybrid beams, the GFRP input values were the same as in the profile calibration tests previously discussed. Shear connectors were characterized just by their elastic stiffness and were allowed to deform only in the principal direction of the beam. For complete shear interaction modeling, the movement of the links was restricted in all directions.

The member's top shell was meshed with quadrilateral elements with a maximum size of 50 mm, and further divided at the load application regions. The bottom frame was meshed automatically at the joints formed by the intersection with the connector links. One of the supporting ends of the beam had all three translations fixed while the other support had all but the axial direction restrained. Several trials of the load application method, either on small areas, element edges or central nodal points, proved that there is little difference amongst them, so the latter method was adopted. As hybrid beams model M2 shared the same geometry, the loading cases and elastic properties were necessary to be changed in-between simulations.

A static linear analysis was performed for each one of the considered specimens using the maximum recorded force from the experiments. Henceforth, geometrical nonlinearities from second order effects such as large displacements and large deformations were not included for these initial models. In addition, to simplify the simulation procedure, the analysis was limited to the main longitudinal plane of bending by restricting the other degrees of freedom available.

Under these conditions, the midspan deflection results of the referenced hybrid beams are presented in Table 5.1 and discussed. The experimental and analytical results at failure act as a validation tool for the FE numerical model. For comparison reasons, both complete and partial shear interaction states were investigated, and the concrete slab was assumed to be uncracked in this first analytical model. Exceptionally, for this calculation, the exact $\xi_{i,mid}$ parameter was used instead of the simplified ξ_{EC5} .

Table 5.1: Comparison between experimental, analytical and finite element analysis midspan deflections (w_t) computed at failure considering a state of complete (w_t^{co}) or partial (w_t^{pa}) shear interaction.

Beam	Experimental	Analytical (uncracked slab section)						FE analysis				
	w_t (mm)	w_b^{co} (mm)	w_{sh} (mm)	$\xi_{i,mid}$	w_t^{co} (mm)	w_t^{pa} (mm)	diff. ^a (%)	w_t^{co} (mm)	diff. ^b (%)	w_t^{pa} (mm)	diff. ^b (%)	diff. ^a (%)
HB1	92.8	49.1	9.1	0.153	58.2	65.7	-29	58.0	-0.2	64.6	-1.6	-30
HB3	21.0	6.2	6.7	0.636	12.8	16.8	-20	12.9	+0.6	16.4	-2.3	-22
B7	70.4	45.3	4.6	0.282	49.8	62.6	-11	49.7	-0.2	61.2	-2.2	-13
SP2	33.4	15.2	4.8	0.185	20.1	22.9	-32	20.0	-0.4	22.4	-2.0	-33
No1	12.6	7.2	4.9	0.412	12.0	15.0	+19	12.0	±0.0	14.7	-2.1	+16
No2	16.6	9.0	5.3	0.341	14.4	17.4	+5	14.3	-0.5	17.1	-2.1	+3

^a Difference versus experimental value.

^b Difference versus analytical value.

During the post-processing of the results, it was observed that the simple computational model failed to capture appropriately the shear deformations of the composite members, although individually (*i.e.*, per component) it evaluated them correctly. In consequence, since the partial interaction effects impact mostly the bending deflection contribution w_b and not the shear deflection component w_{sh} , the analytical value of the latter was added to the bending deflection computed in the FE analysis. The differences between the numerical and analytical predicted deflections prove to be very small – around 2% for the partial interaction scenario and nearly undiscernible for the complete shear interaction case.

Nevertheless, the differences against the experimental values are significant for both theoretical models due to the absence of nonlinear features. Thus, the flexural response of the FE model is substantially more rigid, as seen from the load-deflection charts plotted in Figure 5.7 for the referenced hybrid beams. This time around, the analytical model included for comparison assesses the flexural stiffness of the beams based on the reduced concrete section due to cracking and on the simplified dimensionless parameter ξ_{EC5} . As seen, the linearly-elastic finite element model may be suited only for serviceability analyses or for simple checks at initial load values, when the concrete slab is not severely damaged.

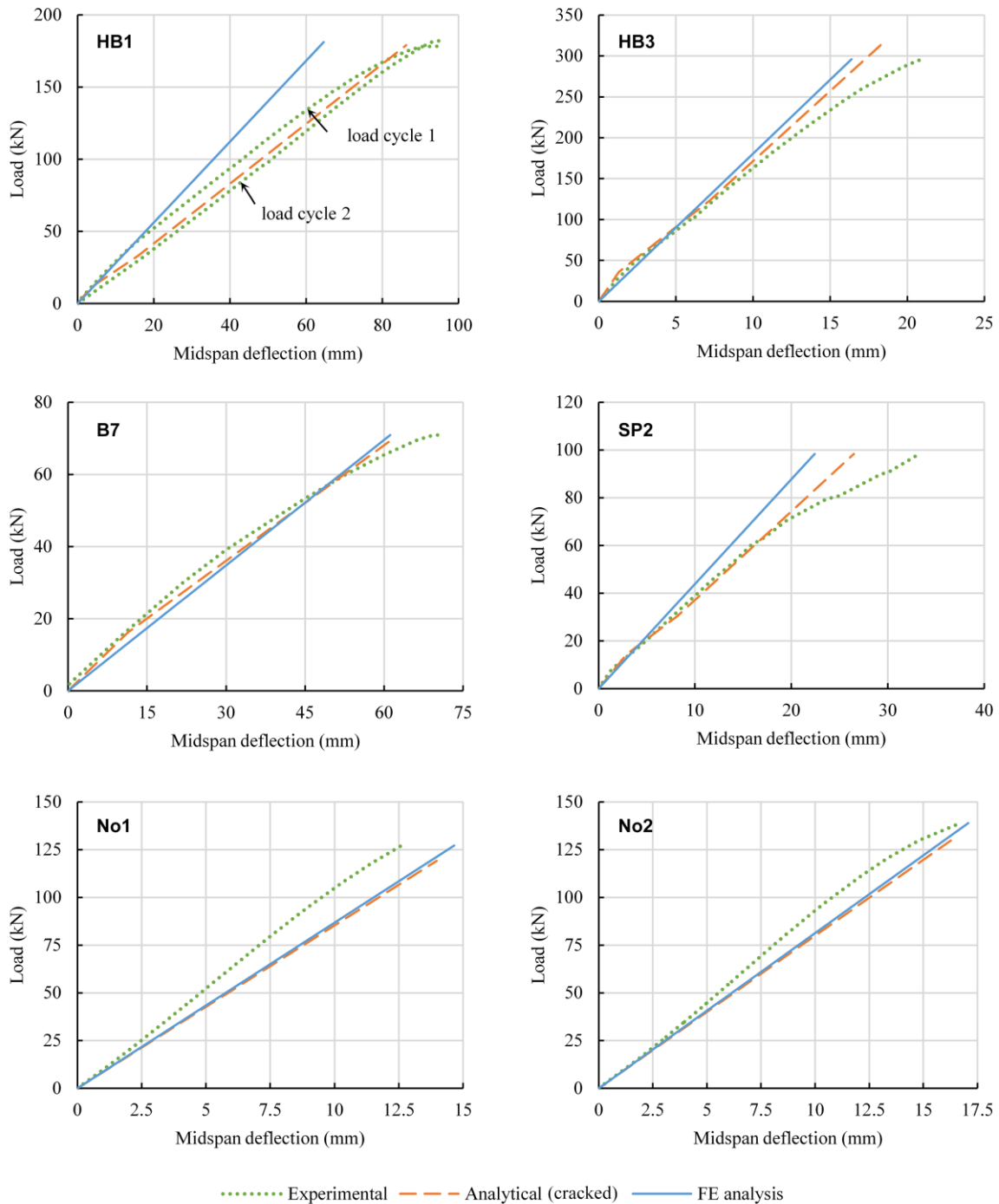


Figure 5.7: Numerically predicted flexural responses of referenced hybrid beams versus experimental curves and analytical estimations. Concrete cracking and partial interaction were accounted for in the analytical model.

In a second comparison, the load-deflection curves of the M2 hybrid beam models tested by the author are plotted in Figure 5.8. Once more, the FE model is able to follow the experimental response only at an initial stage. After the concrete slab starts cracking and the bolts begin yielding, the linearly-elastic model diverges abruptly from the test. Initial interaction effects caused by adhesion, friction or pretension of the bolts were neglected throughout the simulations.

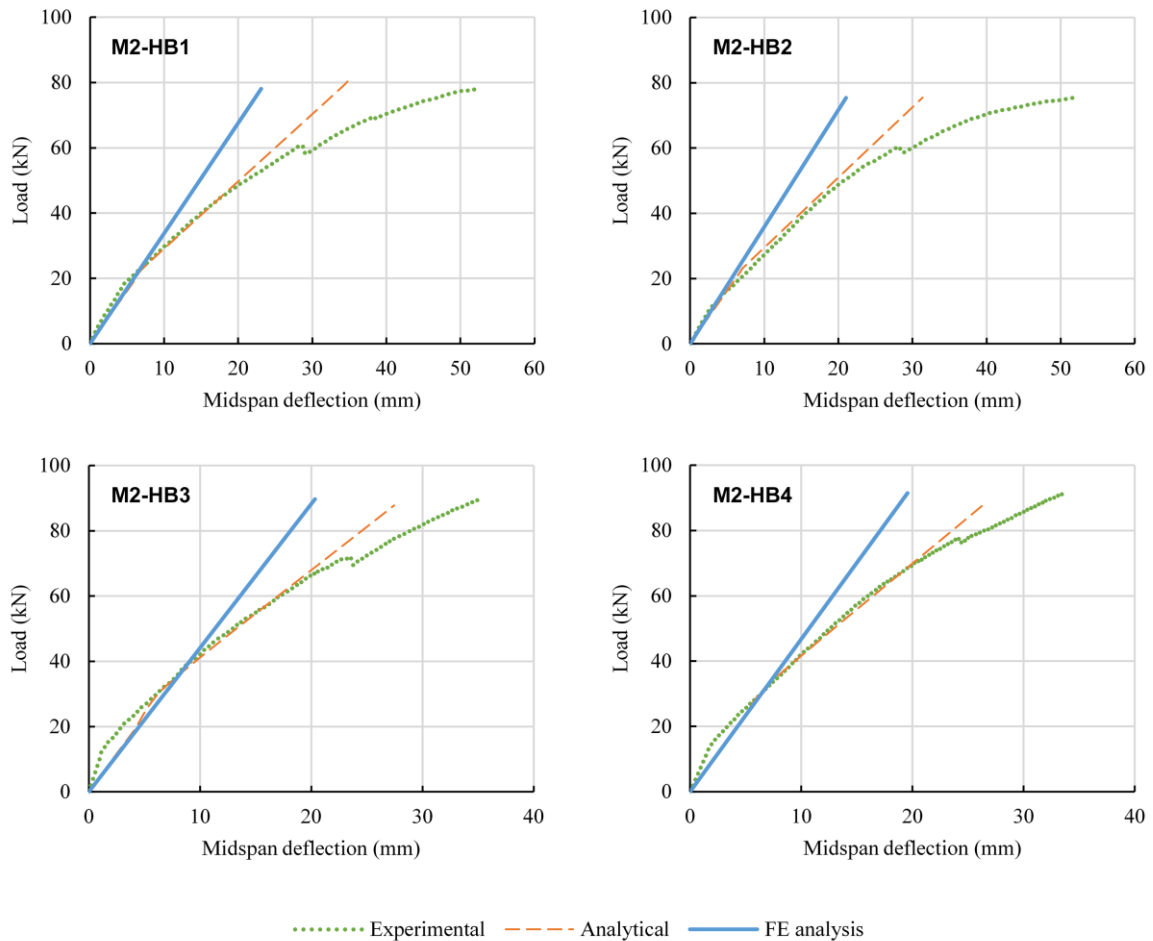


Figure 5.8: Numerically predicted flexural responses of hybrid beams M2 versus experimental curves and analytical estimations. Concrete cracking and partial interaction were accounted for in the analytical model.

A last analogy was made between the numerical, analytical and experimental slip distributions along the interface of the M2 hybrid beams, at an intermediate load value of 50 kN. The charts illustrated in Figure 5.9 demonstrate a good equivalence for the two theoretical models and furthermore indicate that the relative end slip measured during the tests was close to the predicted results. Notwithstanding, there are slight differences toward the supports, where the FE model displays lower slip values than the analytical calculations. Finally, it was observed that regardless of the static scheme applied, three-point bending or four-point bending, the analytical and numerical distributions had a similar degree of correlation.

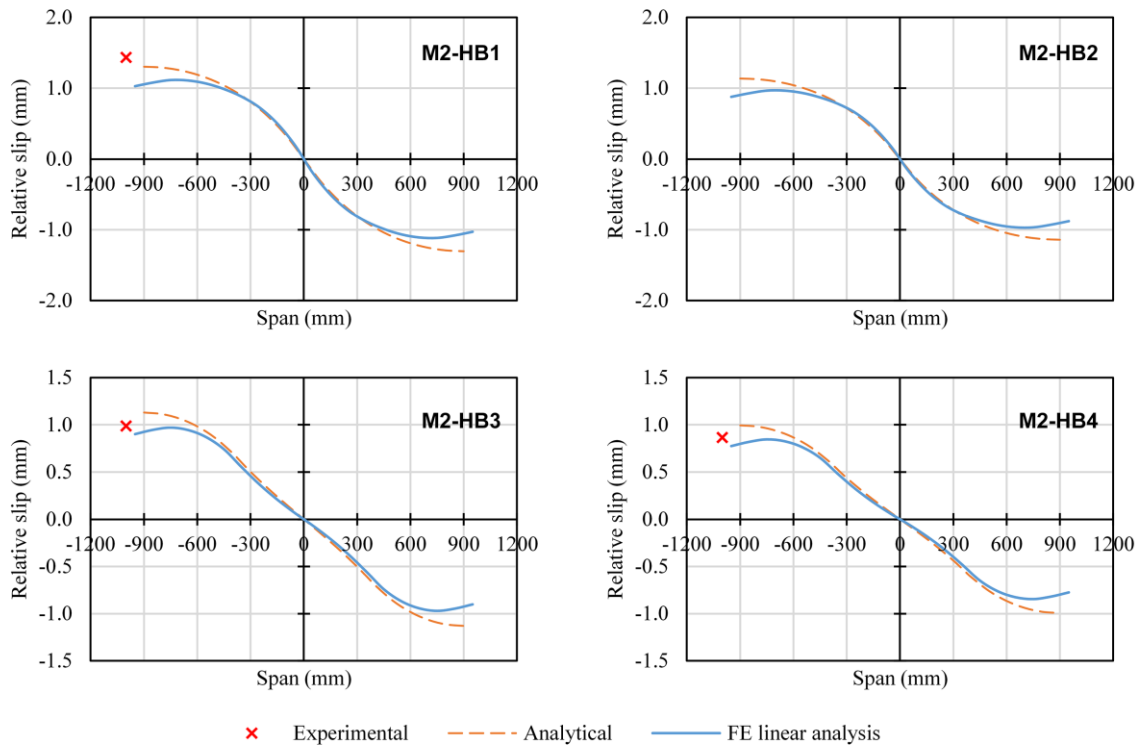


Figure 5.9: Numerically computed longitudinal slip distributions in hybrid beams M2, at an intermediate load level of 50 kN, versus experimental data points and analytical predictions.

5.2.3. Preliminary nonlinear model for hybrid beams

In a following phase to the previously developed linearly-elastic finite element model, a more accurate analysis was built by including material, geometry and connection nonlinearities into a preliminary model design. Much of the discrepant differences observed in the flexural responses before were caused by neglecting the plastic deformations that form in the concrete slab and at the interface level. The geometric representation of the hybrid system was kept, however, mostly simple as before.

The validation of the preliminary nonlinear model was carried out by comparing the numerical bending behavior with the experimental recordings of the referenced specimens which had laboratory push-out tests performed on their connections, and more specifically of hybrid beams HB1, HB3 [48,89] and B7 [46]. From the reported tests conducted by the author, the experimental data of hybrid beam M2-HB1 were used in the validation process.

The current model was constructed with the aid of the *Abaqus* FEA unified software solution [137], given its capability of performing complex simulations of structural nonlinear problems. The composite materials of the profiles were characterized by the orthotropic elasticity values from the linearly-elastic FE models, with the exception of HB1 and HB3 which had the properties changed to the ones employed by the author in [117]. The upper slabs were assigned the concrete damage plasticity model contained within *Abaqus*, with the default plasticity parameters set and without any compression or tension damage

parameters introduced. The concrete's constitutive law for compression was modeled after the nonlinear relation described in Eurocode 2 [130] while the tensile behavior including post-cracking response was defined according to the model suggested by Wahalathantri *et al.* [151]. Longitudinal and transverse steel reinforcement bars were idealized as smeared layers in the concrete slabs and had a bilinear isotropic elasticity behavior associated, with no hardening branch.

With respect to the geometry discretization, the hybrid beams were modeled with homogeneous conventional shells representing the slab defined by its midplane surface and thickness, connected by discrete wires to the bottom profile modeled with beam finite elements, as seen in Figure 5.10 for specimen B7. The shear connectors were placed at the exact locations found in the specimens with the aid of attachment point lines. Profile web-flange fillets and supporting parts were not modeled; however, loading regions were recreated as rigid (undeformable) plates. Material and section orientations were assigned to the profiles accordingly.

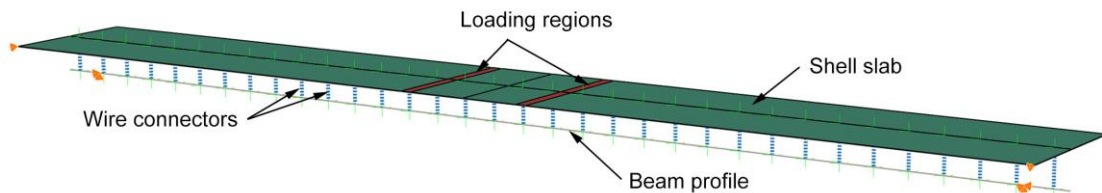


Figure 5.10: Assembly view of the nonlinear finite element model of FRP-concrete hybrid beam B7.

The concrete slab was meshed with linear quadrilateral elements of type S4R, a 4-node general-purpose shell with reduced integration and hourglass control, while the planar loading plates were discretized with 3D rigid linear quadrilateral elements of type R3D4. In function of the cross-section shape, the thin-walled composite profile was meshed with B31 or B31OS Timoshenko (shear flexible) beam elements with linear interpolation formulation. The fundamental assumption used is that the beam section cannot deform in its own plane, except for a constant change in cross-sectional area. *Abaqus* assumes that the transverse shear behavior of Timoshenko beams is linear elastic with a fixed modulus and, thus, independent of the response of the beam section to axial stretch and bending. The method uses Cowper's shear coefficient relations [210] to calculate the transverse shear stiffness of the profile, which yields marginally smaller values than the ones presented in Table 4.10 for the profiles used in the current investigation. In addition, when modeling open section thin-walled beams in space, a further consideration arises from the possible warping (out-of-plane deformations) of the beam's cross-section under torsional loading which modifies the axial and shear strain distribution throughout the section. Therefore, the open section variant of B31 finite element, designated B31OS, was used to adequately represent the torsional behavior of the I-shaped profiles. Closed sections offer greater resistance to torsion and do not warp significantly, hence, the box-shaped profile of specimen B7 was discretized with the standard B31 elements.

Regarding the implementation of the mechanical shear bolts into the finite element model, the wire set connecting the shell slab and the beam profile was constrained by tying its extremities' degrees of freedom to the corresponding nodes on the connected members. The wire elements had a Cartesian + Align type of connector section which constrained the relative rotations in the principal directions. The connector behavior was considered to be rigid elastic in the cross-sectional plane of the hybrid beams and nonlinear elastic in the axial direction, defined by load-displacement tabular data. As mentioned earlier, for the referenced beams analyzed in this section, the force-slip distributions were taken from the reported experimental push-out tests. For the M2-HB1 hybrid beam, there were two connector behaviors considered as portrayed in Figure 5.11, the first being the linearly-elastic model used before in the analytical calculations and in the *SAP2000* FE model, and the second a rigid-perfectly plastic model where the yielding capacity of the connectors was calculated based on the Eurocode 4 expression presented in advance, in Eq. (4.19).

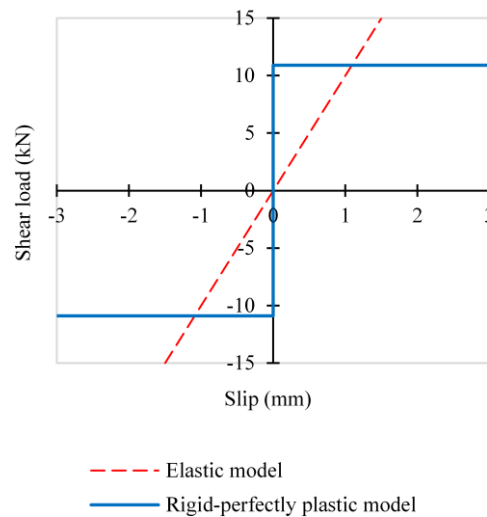


Figure 5.11: Shear connector behavior models for hybrid beam M2-HB1.

The simply-supported conditions were recreated in the FE model by constraining the translational degrees of freedom at the test setup locations and leaving the right ends freely to move in the axial direction. Furthermore, as seen from Figure 5.10, two of the corners of the shell slab were fixed in the lateral direction to prevent the occurrence of global instability problems. The maximum registered experimental loads were applied incrementally as concentrated forces on reference points placed on the rigid loading plates. Geometric nonlinearity was accounted for in all simulations and the nonlinear static Riks procedure was employed to capture the stable and unstable flexural response of the hybrid beams.

The numerical results gathered from the preliminary nonlinear simulations are presented in comparison with the experimental data and previously predicted linear behaviors, in Figure 5.12. It is immediately noticeable that the refined finite element model is able to estimate much better the entire experimental load-deflection response of the hybrid members.

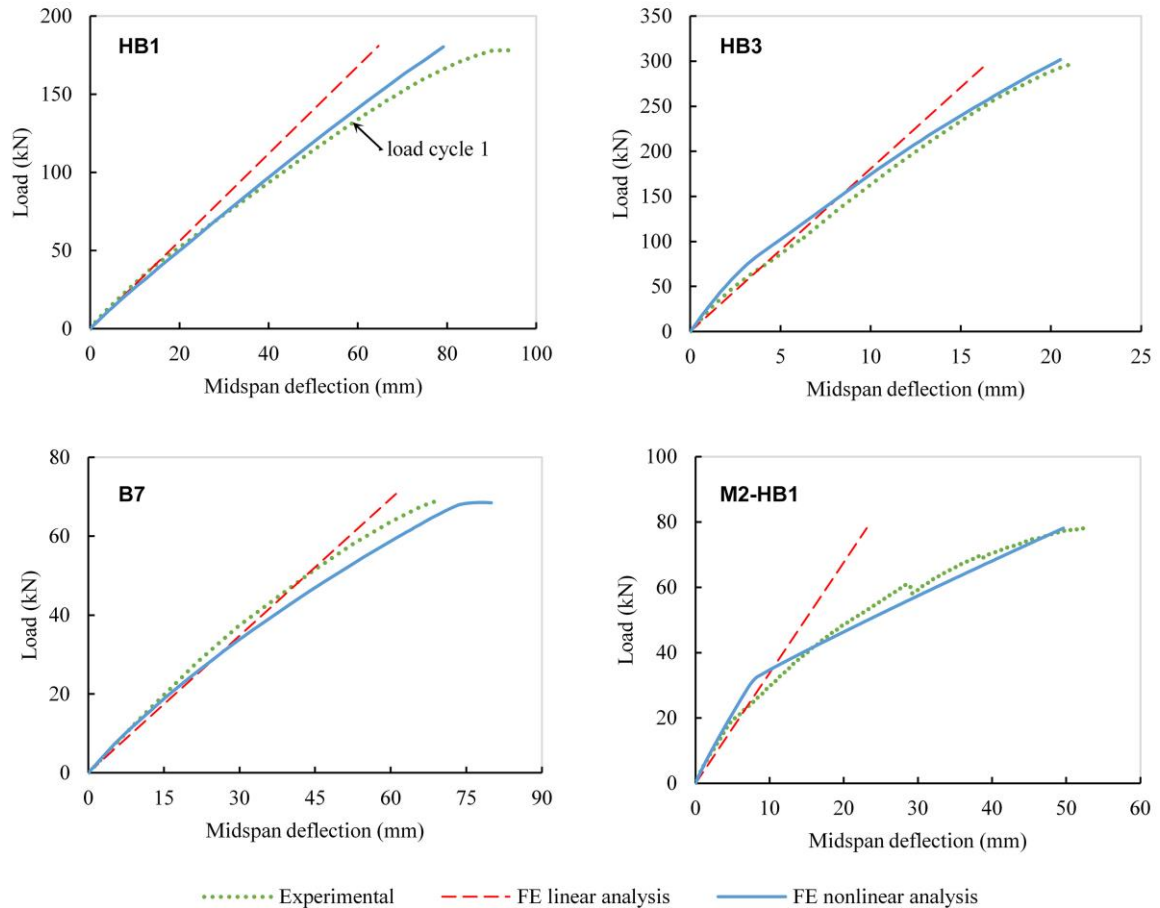


Figure 5.12: Comparison between experimental and numerical flexural responses. Linear and nonlinear finite element models considered.

The charted results demonstrate that concrete crushing and cracking material behavior is essential in modeling effectively the structural performance of hybrid beams. On the same level of importance lays the inclusion of actual connection behavior, as evidenced by the numerical results for specimen B7 which reflect the experimentally-observed shear dowel failure of the GFRP connectors at the ultimate load. Lastly, the numerical results obtained with the preliminary model for the M2-HB1 specimen which had a low degree of shear connection suggested that there was still room for improvements and adjustments of the finite element analysis, and consequently an advanced nonlinear FE model was proposed as a final solution.

5.3. Advanced nonlinear finite element model

The current section presents a definitive finite element model for the M2 hybrid beam specimens tested in the experimental campaign, which brings refinements to the material, geometry and interface modeling and studies the main components of the hybrid system as formed from three-dimensional solid elements. Opposed to the initial FE models, the present discussion goes into more details about the

material constitutive laws, idealized geometry and mesh, interactions and constraints, boundary and load conditions, as well as about the analysis parameters and outputs. The results of the numerical simulations with the advanced model are then compared with the experimentally registered data and with the predictions made by the analytical model with partial shear interaction (with ξ_{EC5}). In the validation procedure, the flexural behavior of hybrid beams is assessed together with the stress and strain distributions and with focus on the developed composite action and interlayer slip.

5.3.1. Material constitutive laws

5.3.1.1. GFRP

The glass fiber-reinforced polymer profiles were designed having orthotropic elasticity properties based on the nine engineering constants shown in Table 5.2. The subscripts of the property notations point to the principal directions of the material, as exposed earlier in Figure 3.9, where “1” represents the path in which the material was pultruded (*i.e.*, the longitudinal axis) and “2” and “3” denote the transverse directions, with “3” indicating the vertical axis in the bending plane.

Table 5.2: Composite profile engineering data for the advanced FE model.

Material	E_1 (GPa)	E_2 (GPa)	E_3 (GPa)	ν_{12}	ν_{13}	ν_{23}	G_{12}^a (GPa)	G_{13} (GPa)	G_{23}^a (GPa)
GFRP	39.11	10.77	10.77	0.27	0.27	0.33	3.98	3.98	3.98

^a Assumed value.

The composite material was, thus, idealized as a linearly-elastic homogeneous material with transverse isotropy and with effective properties as determined from laboratory tests. In fact, the same values were also used in the initial finite element analyses of the M2 specimens. The associated constitutive behavior of the GFRP profiles is plotted below in Figure 5.13.

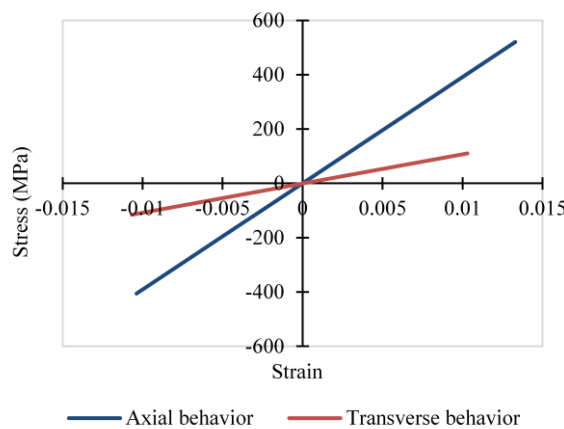


Figure 5.13: GFRP modeled constitutive behavior for the two principal material directions.

Measured strength criteria were considered in restraining the performance of the material in the main directions, for both tensile and compressive stress-strain variations. There were, however, a couple of limitations of the material model in what concerns the representation of the transverse compressive behavior and most importantly the in-plane shear behavior, as the model did not reproduce the nonlinearities associated with these properties within the stress-strain distributions recorded during the experimental characterization tests.

5.3.1.2. Normal strength concrete

Concrete was modeled as a homogeneous isotropic material having a combined elasto-plastic constitutive curve for both the compression and tension behavior. The elastic response was expressed in function of the estimated Young's modulus and the typical Poisson's ratio for concrete. In the meantime, the plastic response was simulated with the *Abaqus* concrete damage plasticity model which was developed specifically for the nonlinear analysis of concrete structures. The average compressive and tensile cylindrical strengths of the two concrete compositions employed in the fabrication of the M2 hybrid beams are found in Table 5.3, next to the input elastic properties.

Table 5.3: Concrete engineering data for the advanced FE model.

Concrete mix	f_{cm} (MPa)	f_{ctm} (MPa)	ν	E_c (GPa)
C1	24.0	1.90	0.2	28.6
C2	28.0	2.21	0.2	30.0

The compressive behavior varied linearly up to a proportionality limit equal to $0.4f_{cm}$ and afterwards continued based on the quadratic nonlinear stress-strain relationship provided in Eurocode 2 [130]. Referring to the tensile behavior, it was defined according to the stress-strain model proposed by Wahalathantri *et al.* [151], which takes into account the post-cracking response of concrete. The two input behavior models are displayed in Figure 5.14 and Figure 5.15, for each concrete mix.

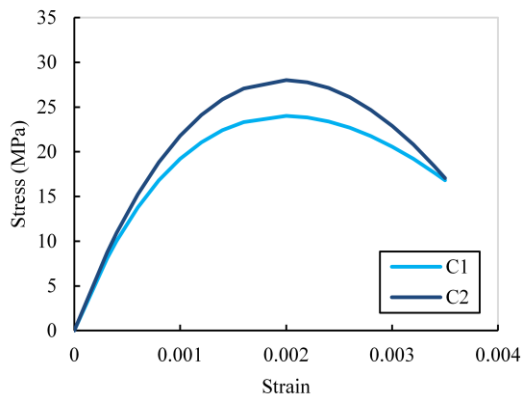


Figure 5.14: Concrete mixtures constitutive behavior model for compression.

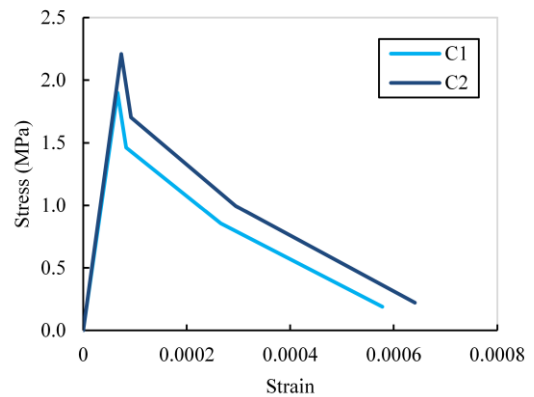


Figure 5.15: Concrete mixtures constitutive behavior model for tension.

To highlight, the implemented concrete model accounts for concrete crushing and cracking, tension stiffening, strain softening and rebar interaction with concrete. The main parameters of the concrete damage plasticity model were set to the following values: the dilation angle was taken as 38° [140]; the flow potential eccentricity was set to 0.1; the ratio of initial equibiaxial compressive yield stress to initial uniaxial compressive yield stress was 1.16; the ratio of the second stress invariant on the tensile meridian to that on the compressive meridian, at initial yield, equaled 0.667; and the viscosity parameter was chosen as 0.01 to deter convergence problems. Apart from the first and last plasticity parameters enumerated, the rest were equal in fact with the default values suggested in the documentation [137].

As the material model takes into consideration the degradation of the elastic stiffness from induced plastic straining in both tension and compression by assuming a scalar isotropic damage, the damage parameters for the two concrete compositions were calculated proportionally following the decrease in maximum compressive or tensile stress. The damage parameter values were tied to the corresponding inelastic strains for compression and with the related cracking strains for tension. There was no tension recovery capacity specified, although in contrast, full compression recovery was enabled.

5.3.1.3. Steel reinforcement

The steel reinforcement bars present at the midplane of the concrete slab were modeled with a bilinear elasto-plastic stress-strain relationship with isotropic hardening. The B500S bars were characterized by the mechanical properties indicated in Table 5.4, where f_y represents the yield strength, f_u the maximum sustainable stress, E_s the modulus of elasticity, and $E_{s,h}$ the elastic modulus of the hardening branch. The second elastic modulus was estimated as $0.005E_s$, as suggested by the study of Nie *et al.* [134]. The constitutive behavior of the steel reinforcement is illustrated in Figure 5.16.

Table 5.4: Steel reinforcement engineering data for the advanced FE model.

Steel	f_y (MPa)	f_u (MPa)	ν	E_s (GPa)	$E_{s,h}$ (GPa)
B500S	500	550	0.3	200	1.0

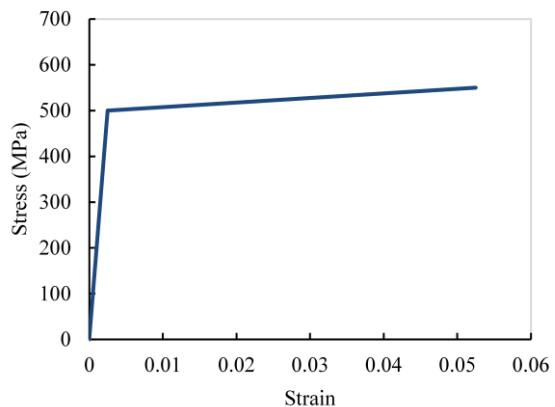


Figure 5.16: Steel reinforcement constitutive behavior model.

5.3.1.4. Steel bolts

Shear connector behavior was modeled with a more refined nonlinear force-slip relationship in comparison to the rigid-perfectly plastic model used in the preliminary FE model (Figure 5.11). The

exponential function proposed by Ollgaard *et al.* [119] after a series of push-out tests performed on concrete embedded steel headed studs was adapted here for the steel bolts used in the hybrid beams, in the absence of experimental data. As a result, the empirical force-slip relationship is expressed by the following equation:

$$P(s) = P_{max} \cdot (1 - e^{-\beta \cdot s})^\alpha \quad (5.1)$$

where $P(s)$ represents the variable shear force on the connector, P_{max} the connector shear resistance taken here as the yielding capacity according to the relation provided in Eurocode 4, s the relative slip at the FRP-concrete interface, and α and β the constants which characterize the curve. In particular, parameter α dictates the initial stiffness, and parameter β influences the shape of the response by a proper scaling of the slip [77]. After a number of calibration simulations, the two constants were adjusted to the following values: $\alpha = 0.5$ and $\beta = 1.5$. Under these presumptions, the force-slip constitutive curve of a steel bolt connector is plotted in Figure 5.17.

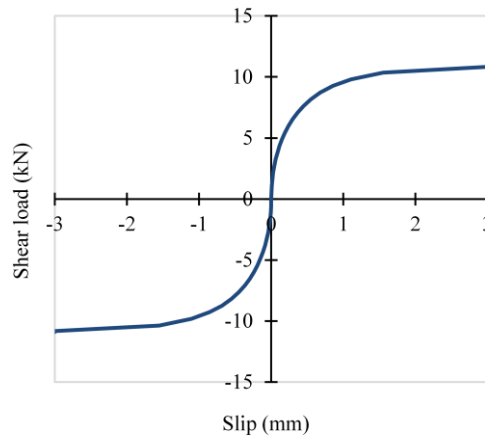


Figure 5.17: Steel bolt constitutive behavior model.

5.3.2. Geometry and mesh

Once the material definitions were established, the study proceeded with the modeling of the hybrid FRP-concrete beams. A primary model was constructed in *Abaqus* which served as basis for the four specimens investigated: M2-HB1, M2-HB2, M2-HB3 and M2-HB4. The model was slightly altered for each simulation to account for the varying experimental test setup conditions and different concrete compositions.

A three-dimensional finite element model was built, where the concrete and GFRP parts were defined as deformable solids and the steel reinforcement bars as deformable elements with wire shape. For an accurate representation, the web-flange fillets of the composite profiles and the concrete support cubes were also incorporated in the analyses. Finally, loading plates were modeled as deformable solids at the locations of the application loads, but with really high elastic stiffness to avoid eventual

convergence issues. Due to the symmetry of the static loading schemes, only half of the physical model was constructed for the simulations in order to spare computational resources, as seen in the material color-coded assembly views presented in Figure 5.18. The GFRP material coordinates 1, 2, 3 were assigned to correspond to the global coordinate axes X, Y, Z displayed in the same figure.

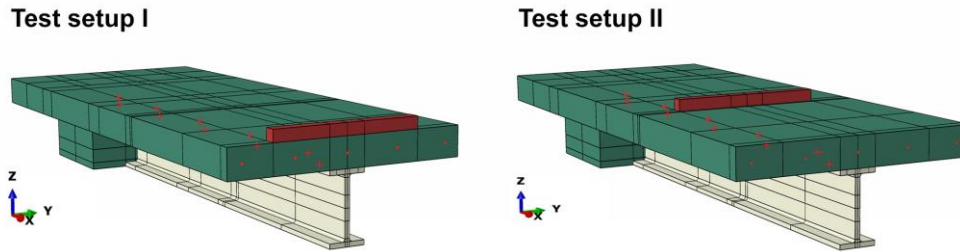


Figure 5.18: Assembly view of the hybrid beam finite element model in function of the applied load setup (three-point bending or four-point bending).

The position of the steel bolts was accurately reproduced by a series of fastener attachment points on the top surface of the profile, while the connectors themselves were idealized as mesh-independent fasteners. Lastly, in preparation of the meshing procedure, the parts were further partitioned at intersecting edges and at points of interest such as instrumentation locations.

All parts were discretized independently with a maximum seed dimension of 10 mm and the general meshing technique was structured so that all the created nodes at the contact regions were coincident. There were a couple of noticeable exceptions for the profile flanges and web-flange fillets which were discretized with a sweep meshing technique built with hex-dominated, respectively wedge element shapes. Additional local seeds were introduced for the profile by subdividing the thickness of the thin walls to improve the accuracy of the solution. A series of mesh nodes were also created at the position of the mesh-independent connector elements. The meshed assembly of the hybrid beam model can be viewed below in Figure 5.19 accompanied by the sectional discretization.

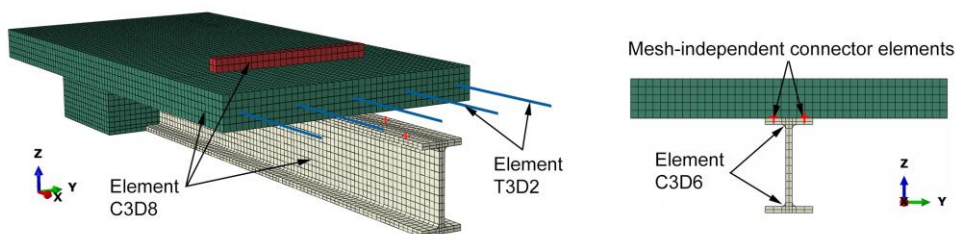


Figure 5.19: Spatial and cross-section view of the meshed finite element model (central part of slab removed for visualization reasons).

Regarding the mesh element library, the concrete parts, the profile (without the fillets) and the loading plate were attributed the C3D8 linear hexahedral element type which is a first-order, fully integrated 8-node linear brick that includes shear deformation and warping formulations. It is part of the

solid (or continuum) elements in *Abaqus* that can be used for linear analysis and for complex nonlinear analyses involving contact, plasticity, and large deformations. It is noted that fully integrated elements that are subjected to bending may suffer from shear and volumetric locking which can give rise to shear strains that do not really exist and, therefore, may appear too stiff in bending, in particular if the element length is of the same order of magnitude as or greater than the wall thickness [137]. This observation justifies the mesh subdivision made in the process. The web-flange fillets were assigned the C3D6 linear wedge element type which is a first-order, fully integrated 6-node linear triangular prism, while the reinforcement bars were modeled with linear line truss elements of type T3D2 which have only axial stiffness and do not support moments or forces perpendicular to the centerline.

5.3.3. Interactions and constraints

Point-based fasteners with a radius of 6 mm were created at the attachment point locations with the face-to-face attachment method, in order to simulate the mechanical shear connection system between the GFRP profile and the concrete slab. At the initial load step, the two nodes of each connector shared the same location, and as the load increased, the nodes were allowed to move relatively. The connector type was Cartesian + Align, restricting the rotations related to the three global coordinate system axes and allowing the definition of behavior options for the translational components. Hence, a rigid behavior was assigned in the vertical Z and lateral Y direction, whereas in the longitudinal X direction, the translational movement was characterized by the nonlinear force-slip relationship defined earlier.

Initial contact nonlinearities from adhesion, connector hole clearance and prestress were not modeled due to their evaluation complexity. The relative slip between the steel reinforcement bars and concrete was also neglected as studies about steel-concrete composite beams have suggested that it has a small impact on the flexural behavior [104,123].

The contact region between the GFRP and the concrete surfaces was defined using the surface-to-surface standard contact method with finite sliding formulation, with the GFRP surface assigned as the master surface due to its higher rigidity. The interaction property had a normal behavior component with “hard” contact pressure-overclosure behavior without separation, and a tangential behavior component with penalty friction formulation with a friction coefficient of 0.20 as estimated from laboratory measurements using the inclined plane method.

An embedded region constraint was set for the reinforcement bars, in which the translational degrees of freedom of the embedded nodes were constrained to the interpolated values of the corresponding degrees of freedom of the host slab elements. Furthermore, surface constraints were applied at the interface between the concrete slab and the loading plate, and between the concrete slab and supporting cube using the master-slave tie constraint to fuse the translational and rotational motion as well as all the other active degrees of freedom of the selected surfaces.

5.3.4. Boundary and load conditions

Simply supported laboratory conditions were replicated in the finite element model by restraining the lateral and vertical displacement of the left supporting edge and by creating a plane of symmetry on the right face of the model. The nodes and faces at the midspan had all translations and rotations fixed except for the movement in the vertical Z direction, permitting the beam to deflect in bending. The lateral midspan restraining served to impede unsuitable numerical global buckling solutions, as there were no such phenomena observed during the experiments.

Half of the measured force was applied on the top surface of the rigid plate as a distributed pressure load, though in the case of specimen M2-HB2 which suffered a transverse crushing type of failure, the pressure load was distributed directly on the top flange of the profile, on a surface of equal width, so as to study the impact of the severe local loading caused by the fractured thin slab. Dead loads were not considered in the model as the recorded data were zeroed at the beginning of the quasi-static experimental tests. The boundary and load conditions for the hybrid beam finite element model are shown in Figure 5.20.

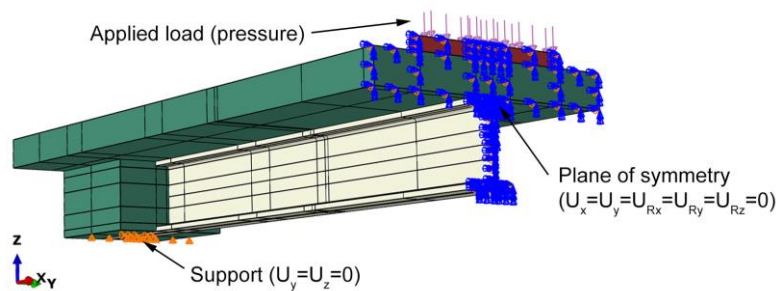


Figure 5.20: Boundary and load conditions for the hybrid beam finite element model.

5.3.5. Analysis procedure and outputs

The analysis was performed using the Static Riks procedure which is suitable for predicting the unstable, nonlinear response of a structure. It is an implicit load control method in which the load is applied proportionally in several steps. In each analysis step, the equilibrium iteration is performed and the equilibrium path is tracked in the load–displacement space employing the arc-length method. The maximum number of increments was set to 200, with an initial arc length increment of 0.01 and a minimum and maximum length of 1E-6, respectively 0.05. The estimated total arc length was set as 1.

Geometric nonlinearities were included in the analysis to account for large displacements and large deformation second-order effects. The maximum load proportionality factor (LPF) was fixed to 1.0 and the unsymmetric matrix storage option was checked for the equation solver to allow for better convergence.

From the nonlinear analysis outputs, of interest were the element and node translations, stress and strain components (both elastic and plastic), reaction forces, as well as the connector relative displacements and sustained forces, at each increment of the applied load factor. No failure criteria were provided since concrete crushing is difficult to isolate to a specific load due to the stress singularities that form near and under the rigid loading plate, and especially since the in-plane shear deformations had been considered to vary linearly. Thus, the numerical results were plotted for the maximum experimental load. The indicated 1, 2 or 3 directions for the results conform with the global coordinate system defined by axes X, Y and Z.

5.3.6. Validation with experimental and analytical results

Once the finite element analyses were completed, the numerical results were compared with the experimental data and analytical estimations presented in Chapter 3, respectively Chapter 4.

5.3.6.1. Flexural behavior

Foremost, the predicted general flexural behavior of the four M2 hybrid beam specimens was validated. The obtained load-midspan deflection curves are presented adjacently, in Figure 5.21.

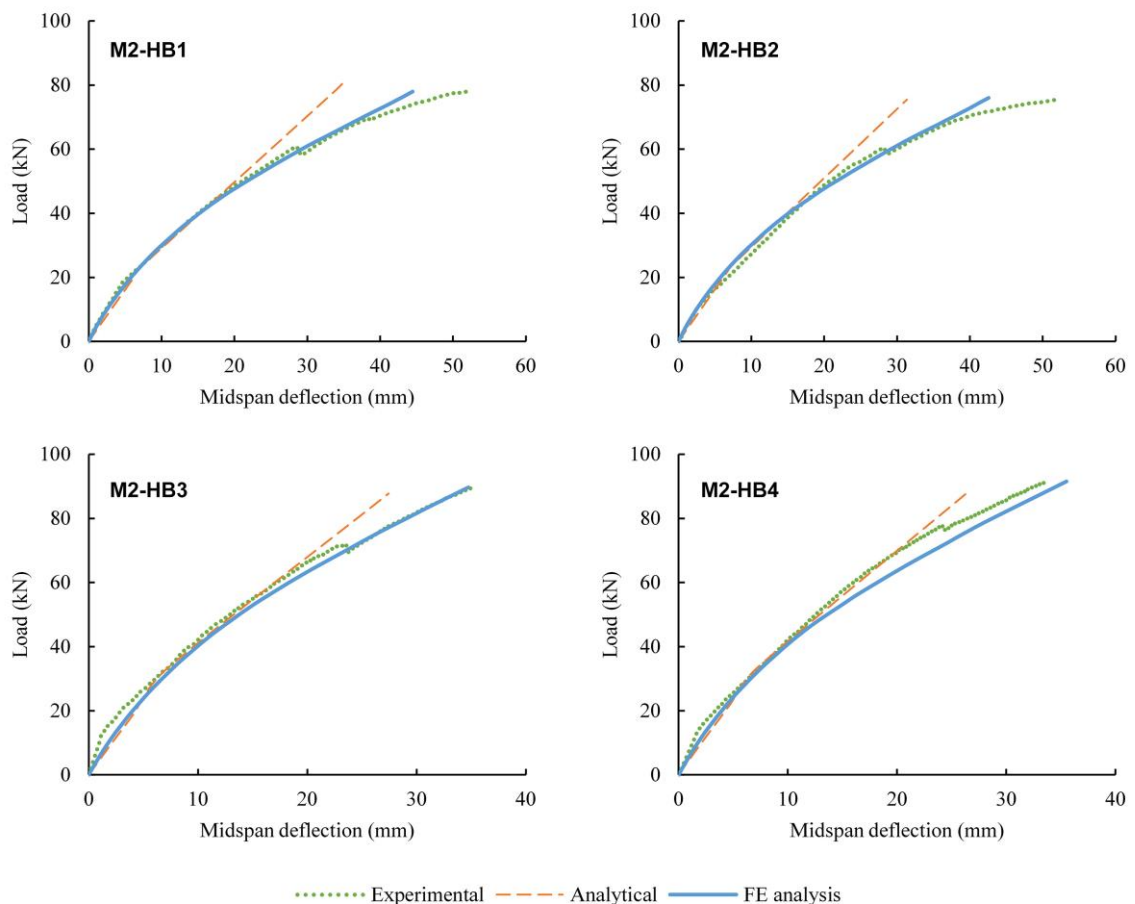


Figure 5.21: Numerically predicted global flexural responses of M2 hybrid beams versus experimental curves and analytical estimations.

As observed, the advanced finite element model is capable of reproducing the main nonlinear features that were associated with the experimental general bending behavior of the GFRP-concrete beams. There are, however, slight dissimilarities for the structural members tested under three-point bending, M2-HB1 and M2-HB2, where the severe stiffness degradation of the concrete slab near the ultimate load was underestimated. Compared to the analytical model with partial shear interaction formulation, the numerical model predicted better the load-deflection response especially after the shear bolt connectors began to yield.

The deflection results along the bottom flange of the beams are plotted in the Figure 5.22 for an intermediate total load of 50 kN. The charts show that the numerical distributions fit well with the experimental deflections regardless of the bending scheme applied.

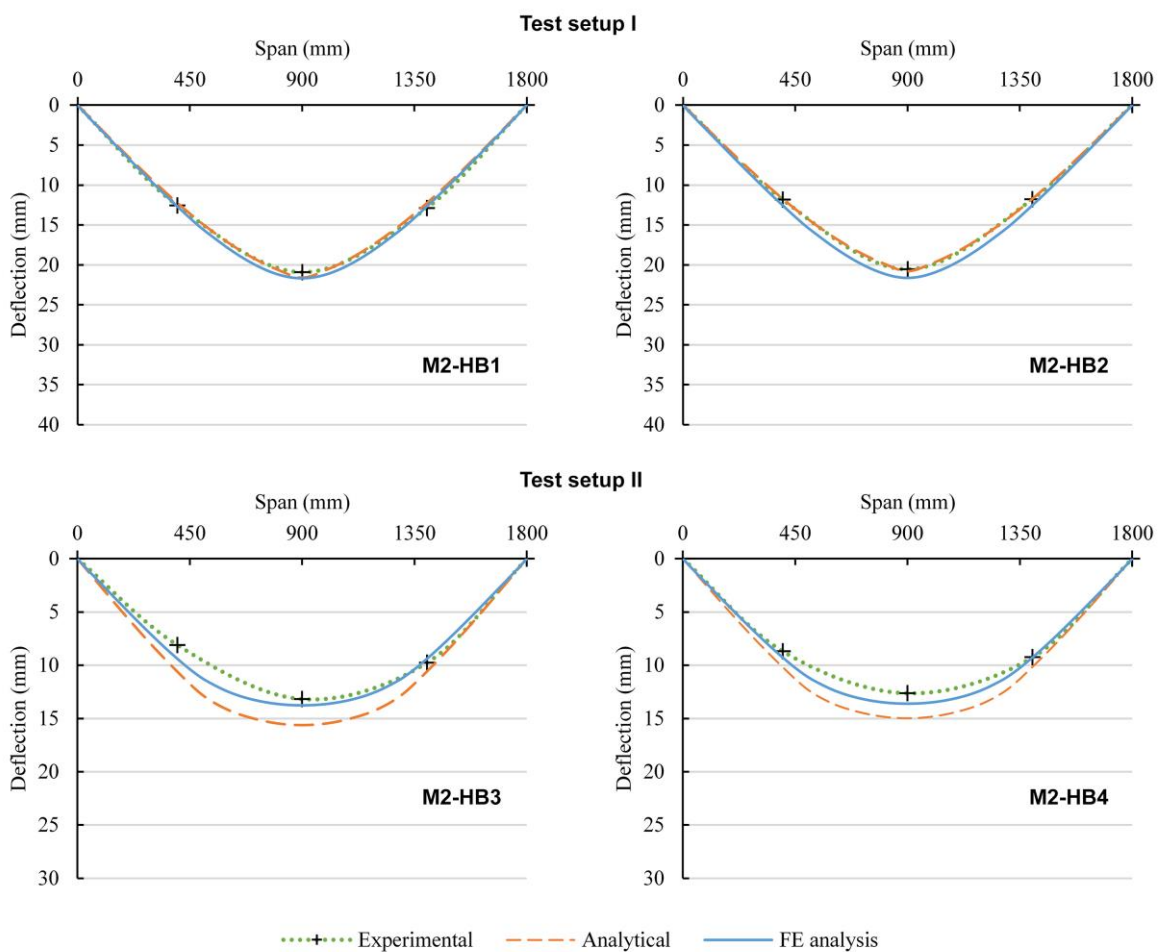


Figure 5.22: Numerically predicted deflection profiles versus experimental curves and analytical estimations, at an intermediate load of 50 kN.

The exact determined midspan deflection values at the intermediate and ultimate load are summarized in Table 5.5 next to the laboratory and analytical results. Computed bending moments at the serviceability limit state are also presented in the table. Percentile differences of the estimated results were computed against the corresponding experimental values.

Table 5.5: Comparison between experimental results and analytical and numerical estimates for serviceability bending moments (M_{SLS}) and midspan deflections (w) measured at an intermediate load of 50 kN and at the ultimate failure load.

Beam	M_{SLS} (kNm)			diff. ^a (%)		w_{50} (mm)			diff. ^a (%)		w_u (mm)			diff. ^a (%)	
	EXP	ANA	FEA			EXP	ANA	FEA			EXP	ANA	FEA		
M2-HB1	10.7	10.5	10.6	-2	-1	21.0	21.6	21.7	+3	+3	52.5	35.2	44.6	-33	-15
M2-HB2	9.4	10.5	10.7	+12	+14	20.7	20.8	21.6	± 0	+4	51.7	31.4	42.1	-39	-19
M2-HB3	8.8	8.8	8.4	± 0	-5	12.8	15.6	13.8	+23	+8	35.2	27.5	34.8	-22	-1
M2-HB4	8.7	8.9	8.5	+2	-2	12.5	15.0	13.6	+20	+9	33.6	26.3	35.5	-22	+6

^a Percentile differences computed between analytical (ANA) or numerical (FEA) predictions and experimental (EXP) results.

The calculated differences reveal the prevalence of the nonlinear finite element model in estimating deflections, notably at higher loads. Nonetheless, the elastic analytical model shares rather similar differences with the FE analyses in terms of predicted serviceability bending moments.

5.3.6.2. Stress and strain distributions

Axial stress and strain distributions produced by the simulations were first analyzed and validated. Figure 5.23 illustrates with banded isolines, on a mirrored complete model, the longitudinal normal stress distributions at failure for a representative specimen of each test setup. Since the stresses and strains are computed at an element level, the displayed results were averaged for viewing reasons.

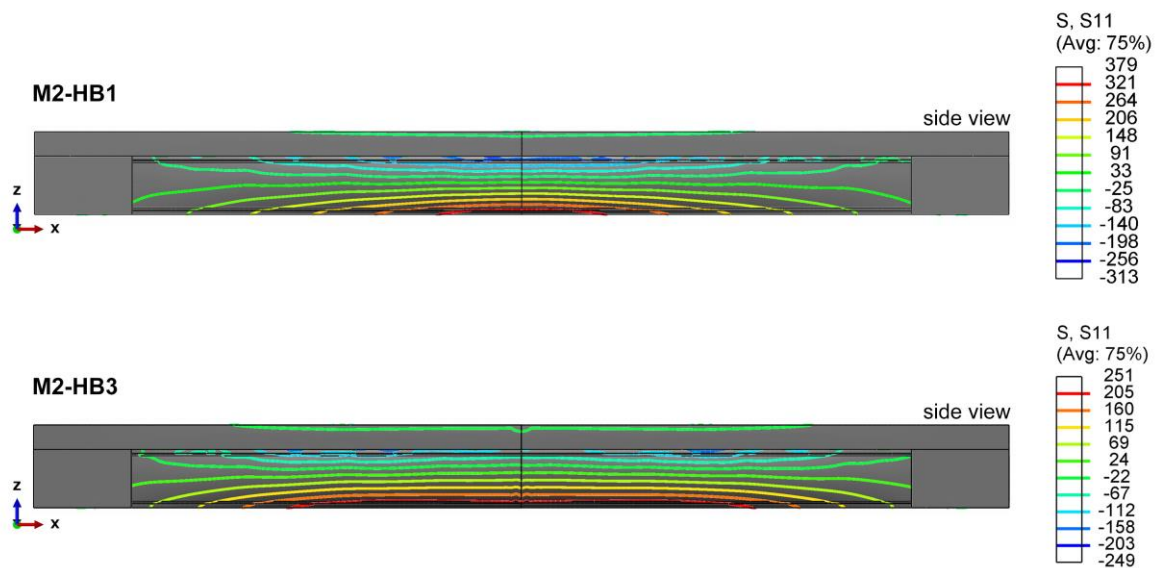


Figure 5.23: Longitudinal normal stress distributions at the ultimate load, for hybrid beams M2-HB1 and M2-HB3 (MPa).

The axial strain variations at section S1 (near or at the midspan) and along the bottom flange of the GFRP profile were validated against the experimental curves, and rendered in Figure 5.24, respectively Figure 5.25. The strain values were probed at unique nodal points matching the installed strain gauge positions, and essentially represent the extrapolated output values from the corresponding element integration points.

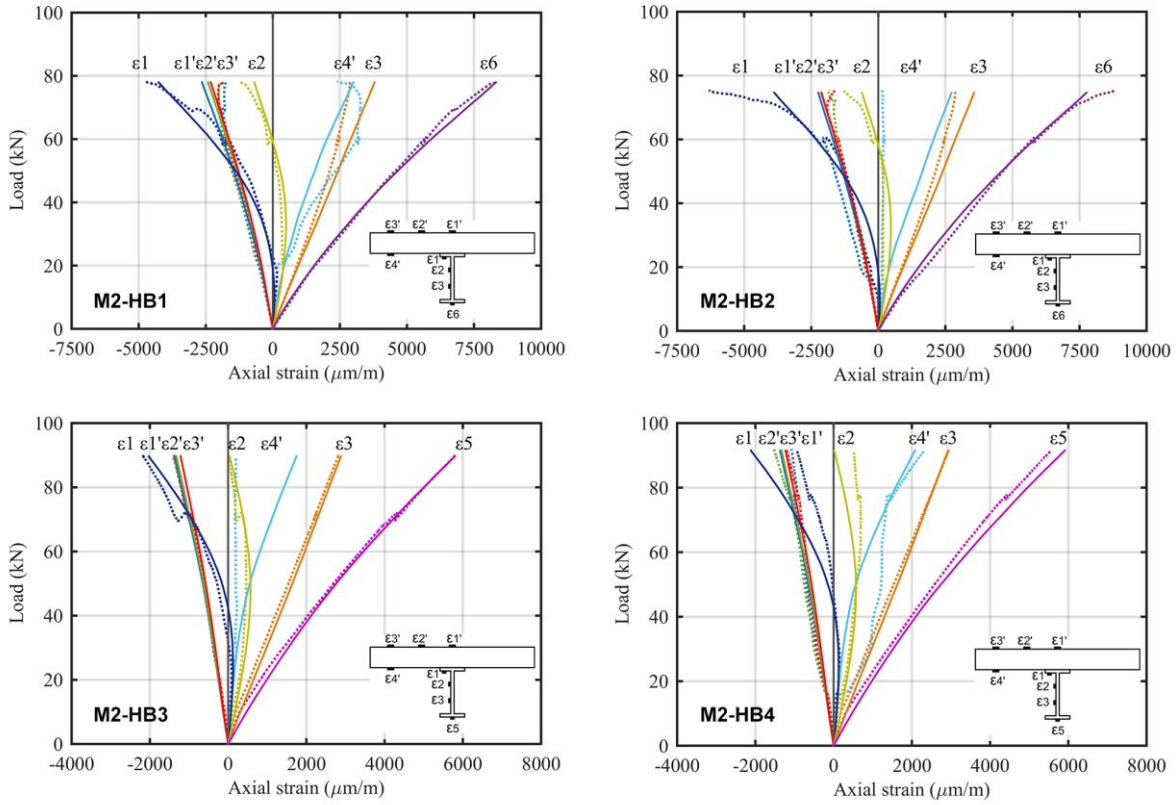


Figure 5.24: Numerical (solid line) versus experimental (dotted line) axial strain variations in section S1.

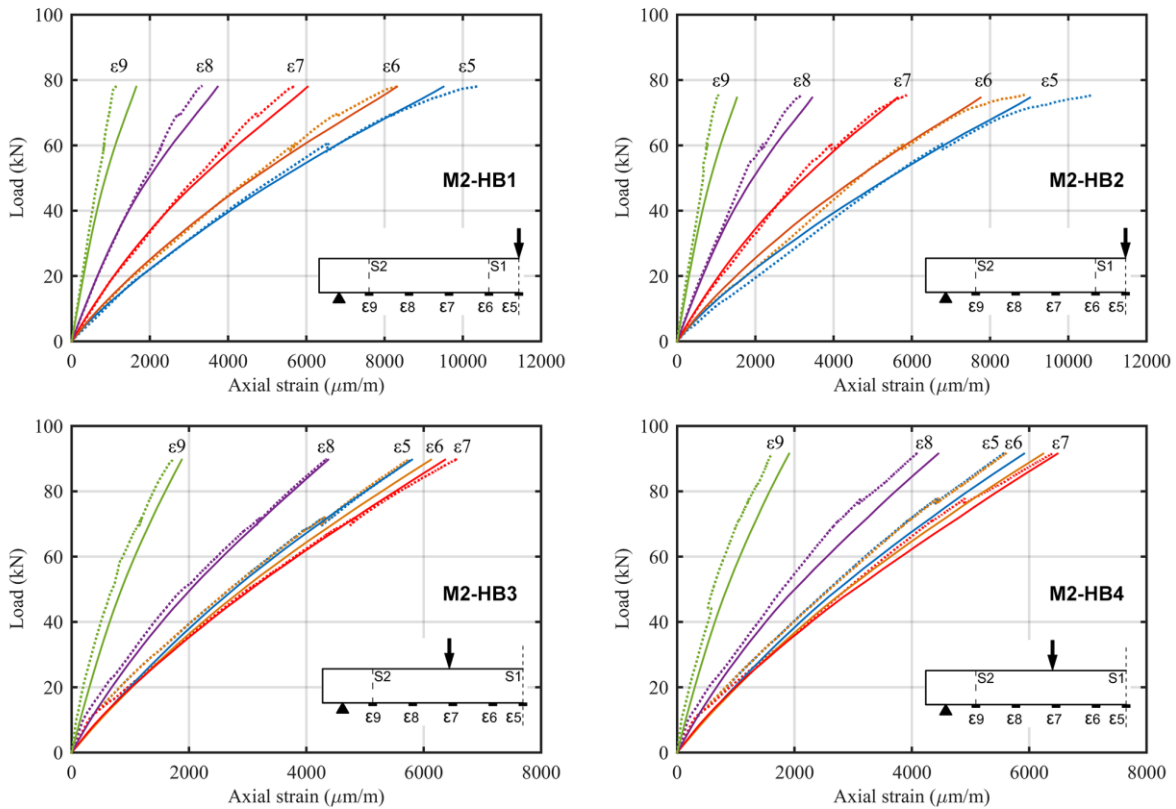


Figure 5.25: Numerical (solid line) versus experimental (dotted line) bottom flange axial strain variations.

As noticed from the previous batches of figures, the numerically predicted axial strains are in good agreement with the experimental values for all four hybrid GFRP-concrete specimens. Furthermore, the finite element model reflects appropriately in the results the change in concrete composition and applied loading scheme, without any preference for a specific configuration. Opposed to the linear elastic analytical model, the nonlinearity of the actual registered responses is replicated well in both tension and compression, particularly for the GFRP members. Concrete compressive strains were predicted properly, but in exchange, the tensile strains on the bottom side of the slab were mismatched due to the localization of cracks in the experiments. Minor divergences were also detected near the ultimate load for M2-HB2 which failed due to web transverse crushing, and along the bottom flange, close to the concrete-jacketed support.

The numerical axial strain distributions at section S1 were plotted in Figure 5.26 for the four specimens, in function of the beam's depth and for an intermediate total load of 50 kN, alongside the experimental and analytical corresponding strain distributions. The finite element analysis estimates with remarkable precision the laboratory data, in both structural components of the hybrid beams. In addition, the output values were closer than the ones obtained from the analytical model with partial shear interaction. Bottom slab axial strains in the M2-HB1 and M2-HB2 beams loaded with a concentrated midspan force were farther from the experimental observations, as explained before.

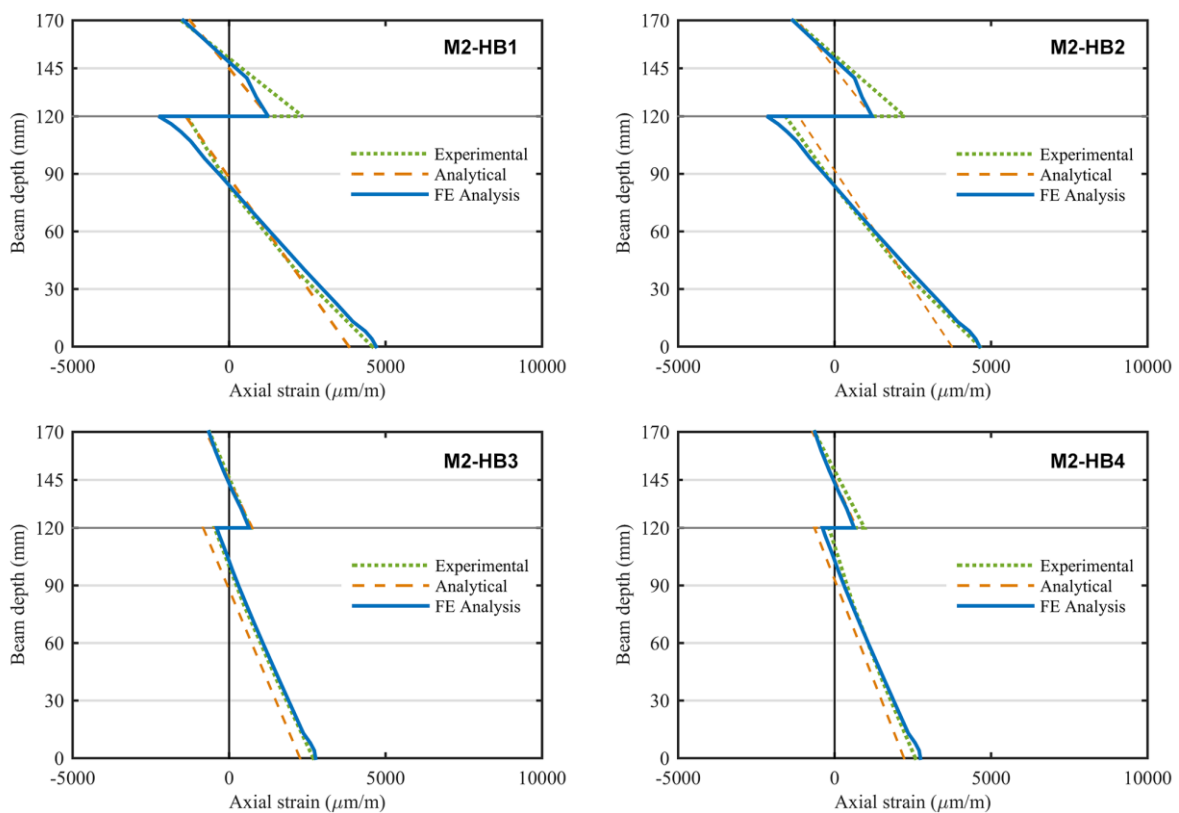


Figure 5.26: Experimental, analytical and numerical axial strain distributions of hybrid beams M2 in section S1, at an intermediate load level of 50 kN.

A comparative analysis between the estimated and registered axial strains and stresses for the hybrid beams are shown in Table 5.6 for an intermediate load of 50 kN, and in Table 5.7 for the ultimate failure load, together with computed percentile differences. The concrete compressive strain at section S1 and the maximum tensile strain and stress in the profile were analyzed.

Table 5.6: Concrete compressive strain ($\epsilon'_{1,u}$ – section S1) and bottom flange maximum axial strain ($\epsilon_{f,max,u}$) and stress ($\sigma_{f,max,u}$) at an intermediate load of 50 kN.

Beam	$\epsilon'_{1,50}$ (%)			diff. ^a (%)		$\epsilon_{f,max,50}$ (%)			diff. ^a (%)		$\sigma_{f,max,50}$ (MPa)			diff. ^a (%)	
	EXP	ANA	FEA			EXP	ANA	FEA			EXP	ANA	FEA		
M2-HB1	-0.15	-0.13	-0.15	-18	-4	0.52	0.46	0.54	-12	+3	203	180	210	-12	+3
M2-HB2	-0.13	-0.12	-0.13	-7	+4	0.54	0.45	0.54	-17	±0	212	176	215	-17	+2
M2-HB3	-0.06	-0.07	-0.06	+18	+3	0.30	0.27	0.28	-10	-8	117	106	110	-10	-6
M2-HB4	-0.06	-0.07	-0.06	+10	-1	0.29	0.27	0.27	-8	-5	113	104	109	-8	-3

Table 5.7: Concrete compressive strain ($\epsilon'_{1,u}$ – section S1) and bottom flange maximum axial strain ($\epsilon_{f,max,u}$) and stress ($\sigma_{f,max,u}$) at failure load.

Beam	$\epsilon'_{1,u}$ (%)			diff. ^a (%)		$\epsilon_{f,max,u}$ (%)			diff. ^a (%)		$\sigma_{f,max,u}$ (MPa)			diff. ^a (%)	
	EXP	ANA	FEA			EXP	ANA	FEA			EXP	ANA	FEA		
M2-HB1	-0.19	-0.20	-0.26	+6	+42	1.04	0.72	0.95	-31	-8	406	281	376	-31	-7
M2-HB2	-0.18	-0.18	-0.23	-1	+25	1.06	0.68	0.91	-36	-14	415	265	364	-36	-12
M2-HB3	-0.14	-0.13	-0.14	-6	-4	0.65	0.49	0.58	-26	-11	256	191	231	-26	-10
M2-HB4	-0.12	-0.13	-0.14	+8	+14	0.64	0.49	0.59	-24	-7	250	191	235	-24	-6

^a Percentile differences computed between analytical (ANA) or numerical (FEA) predictions and experimental (EXP) results.

The tabular data demonstrate that the advanced nonlinear finite element model is a powerful tool in obtaining reliable axial stress and strain results, with errors as small as 4% for the intermediate load and with acceptable differences up to 14% for the ultimate load. The percentile difference at 50 kN did not indicate a tendency of overestimating or underestimating the response; however, the results at failure were slightly undervalued because of the pronounced nonlinear behavior of concrete at high compressive and tensile plastic strain rates. Analytical errors were regarded as acceptable for the initial part of flexural behavior, and on the other hand, firmly unconservative at the failure load by as much as 36% for the GFRP profile. Possibly due to the localized damage in the concretes slab at failure, the total compressive strains were overestimated by the finite element analyses, in particular for the beams subjected to three-point bending.

Numerical distributions of the top concrete strain across the slab, at section S1, are plotted in Figure 5.27 and Figure 5.28, for one specimen from each test setup. The distributions were extracted for an intermediate load level of 50 kN and for the ultimate load (Pmax). The charts show a relatively uniform cross-section variation at the first step, with higher strain concentrations in the proximity of the top

flange at the moment of failure. Moreover, concentrations are more extensive, as expected, in the case of M2-HB1 which was loaded with a midpoint concentrated force.

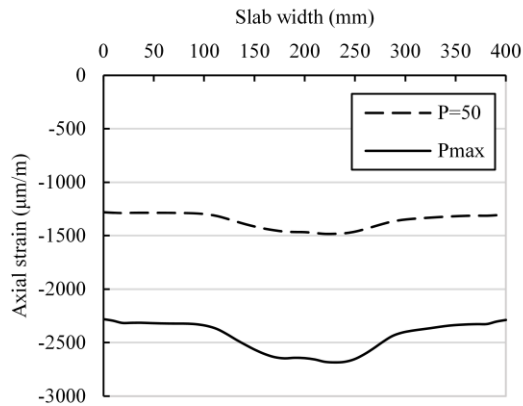


Figure 5.27: Concrete slab axial compressive strain at section S1 for hybrid beam M2-HB1 (load in kN).

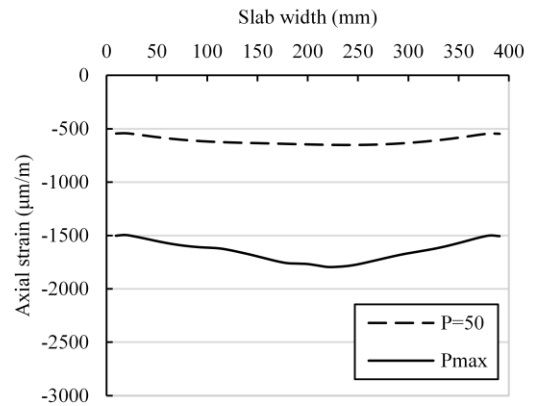


Figure 5.28: Concrete slab axial compressive strain at section S1 for hybrid beam M2-HB3 (load in kN).

For the particular case of hybrid beam M2-HB2 which had a different failure mode than the rest, an analysis was performed regarding the transverse normal stress distribution at the midspan that most probably determined the collapse. Figure 5.29 illustrates with color-coded isolines the aforementioned stress distribution along the entire hybrid beam model, while Figure 5.30 and Figure 5.31 depict the distribution at the central cross-section level.

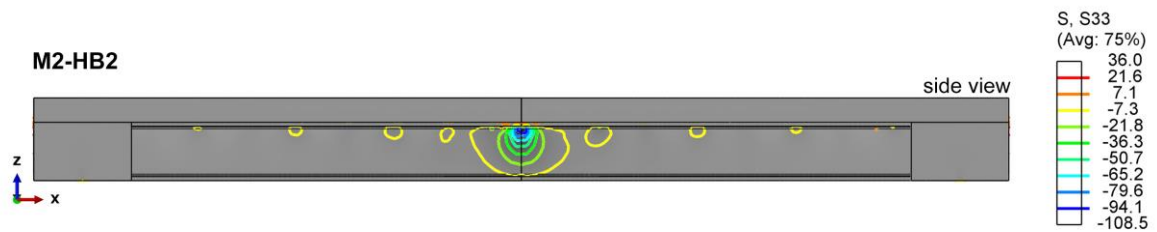


Figure 5.29: Transverse normal stress distribution at the ultimate load, for hybrid beam M2-HB2 (MPa).

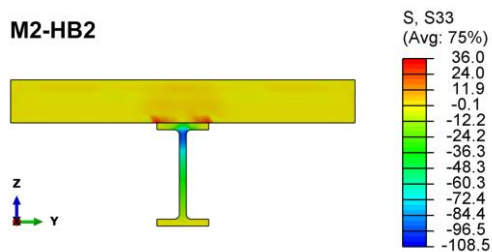


Figure 5.30: Midspan sectional transverse normal stress distribution at failure, for hybrid beam M2-HB2 (MPa).

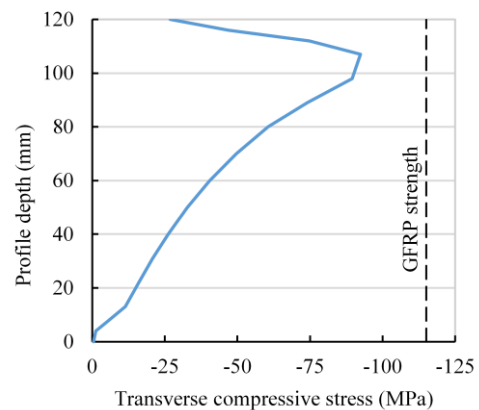


Figure 5.31: Transverse compressive stress in the GFRP profile versus material determined strength.

The finite element analysis proved that the maximum transverse compressive stress occurred right under the position of the concentrated load, in the upper web region of the composite profile. The actual stress distribution at failure shown in Figure 5.31 was certainly higher as the constitutive GFRP elastic model did not capture the nonlinear stress-strain relationship recorded by the characterization tests, which validates the hypothesis that the compressive transverse strength of the material was reached.

Additionally, the finite element analysis is able to anticipate the location of the tensile concrete cracks and potential crushing areas, and to simulate the relative slip of the mechanical connection. The experimentally detected cracks were overlaid in Figure 5.32 on the computed maximum principal plastic strains monitored on the bottom face of the four investigated M2 hybrid beams.

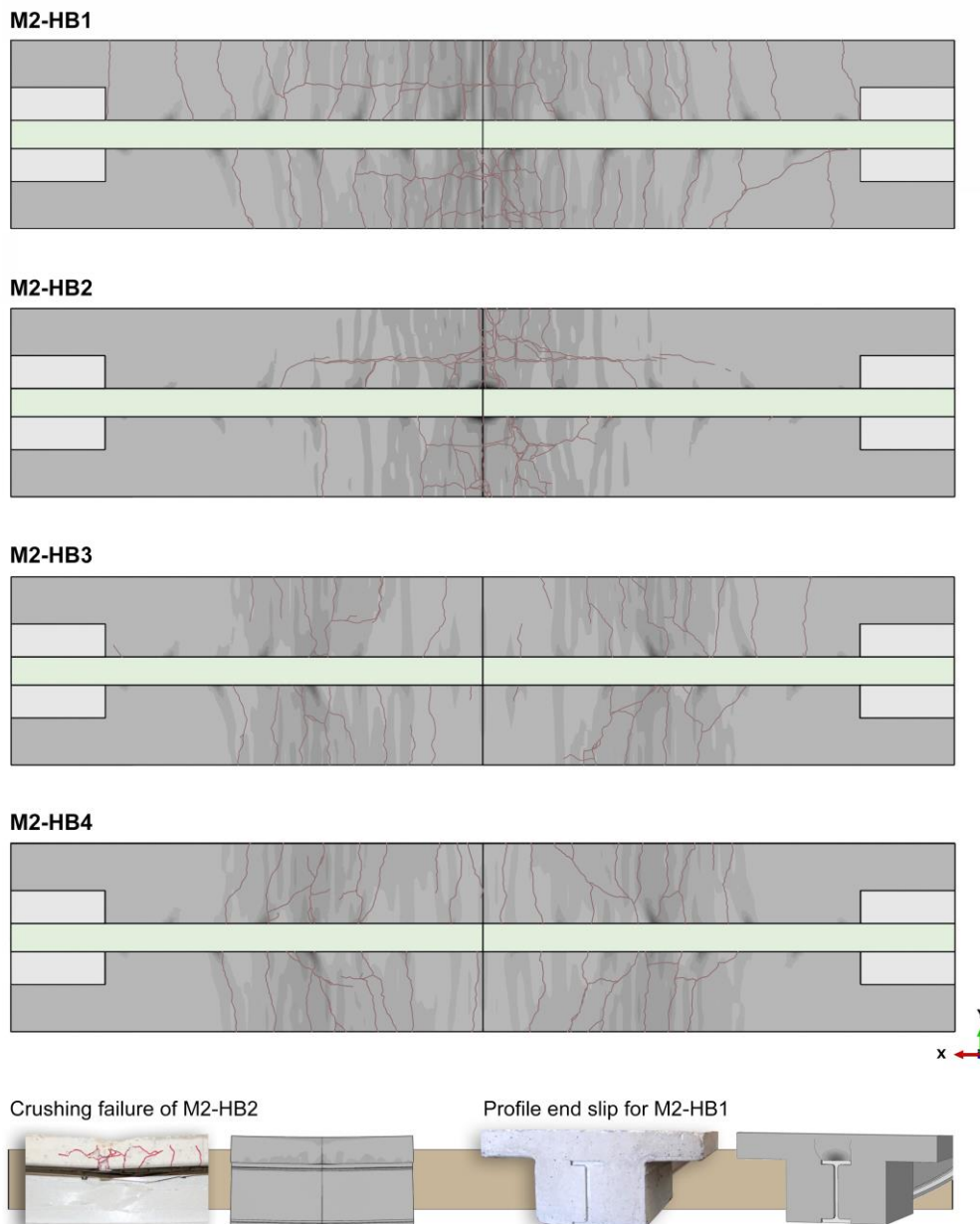


Figure 5.32: Comparison between the experimental and numerical plastic deformations of the concrete slab.

As noted in the simulations and confirmed by the experimental tests, the flexural cracks in the concrete slab originated from the position of the steel bolts and spread toward the edges at an inclined angle away from the supports. The highest density of cracks was concentrated under the direct loading regions and in their immediate vicinity, and at the same time it was more pronounced for the beams tested under three point bending. Important inelastic strains were determined also at the end of the hybrid members, above the upper flange of the profile, around the area where fissures were caused by the connector shear forces.

The predicted axial stress distributions at failure in the concrete slab are plotted for a representative specimen of each test setup in Figure 5.33. Loading plates were removed in the visualization explaining thus the concentrated blue color-coded stress regions, and both the top and bottom surfaces of the slabs were illustrated. The output variations confirm that the compressive stresses were more spread in the second load setup and that the bottom tensile stresses were more significant in the first.

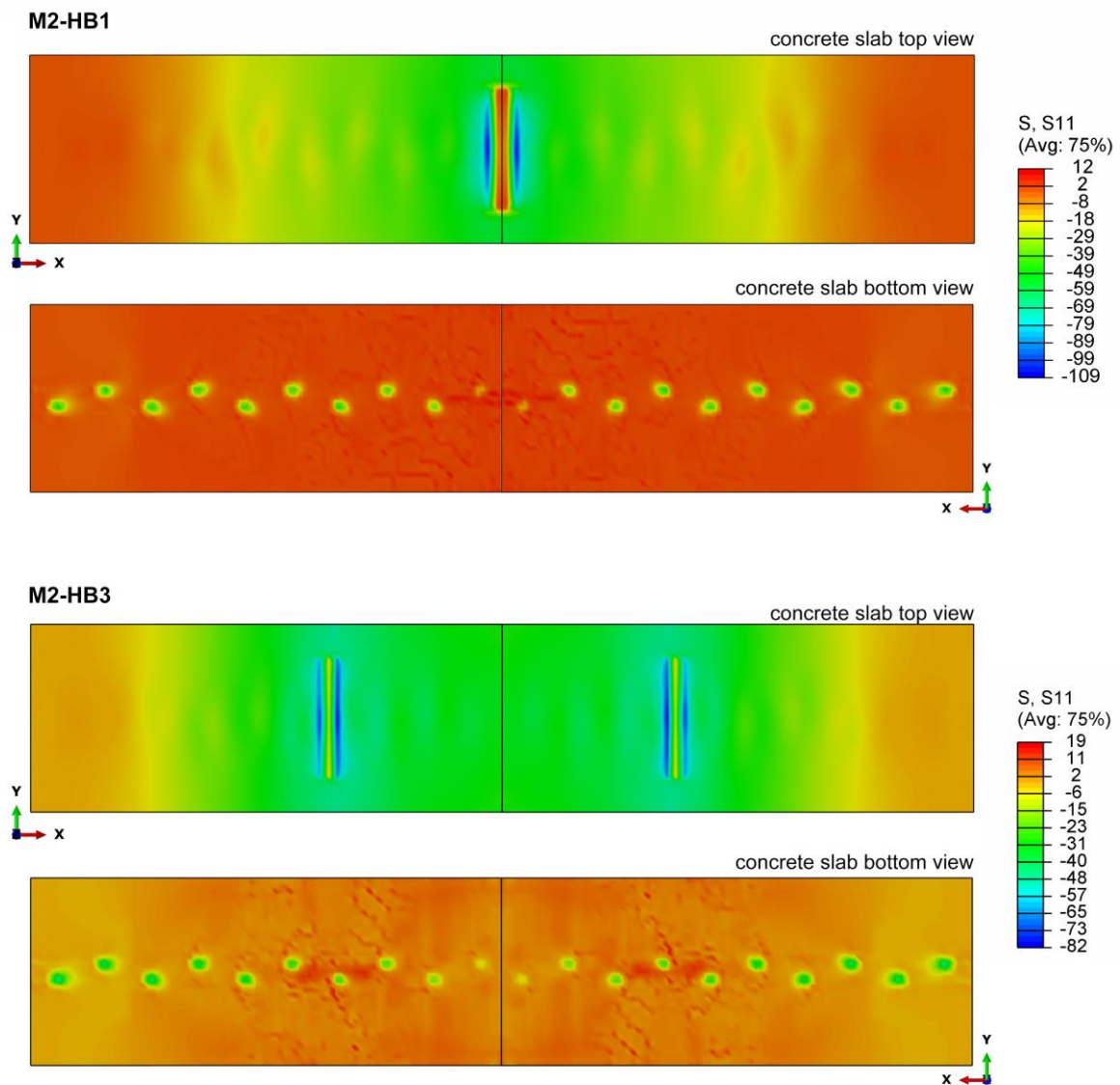


Figure 5.33: Axial stress distributions of the concrete slab at failure, for hybrid beams M2-HB1 and M2-HB3 (MPa).

The bottom face axial stress distributions show also the compressive stress concentrations surrounding the shear connectors. In this regard, the bolts installed closer to the supports transmitted more axial stress into the concrete slab through the shear mechanism behavior, than the bolts placed near the central region.

Figure 5.34 depicts the longitudinal in-plane shear stress distributions in the representative pair of hybrid beams. As expected, the notable shear stresses occurred in the web of the GFRP profiles, in the shear span regions of the loading schemes. Maximum values were registered close to a quarter of the testing span distance.

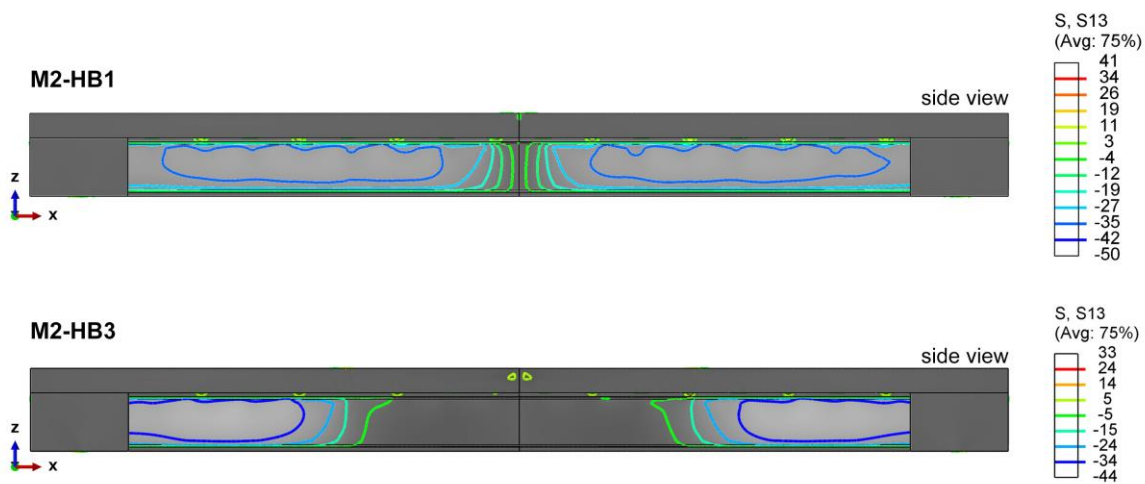


Figure 5.34: Longitudinal in-plane shear stress distributions at the ultimate load, for beams M2-HB1 and M2-HB3 (MPa).

Transverse in-plane shear stress distributions at section S2, near the left support, are presented in Figure 5.35 for M2-HB1 and M2-HB3. The variations reconfirm that the highest shear stresses ensued in the in the upper web region of the profiles, closer to the connected slab. In contrast, the concrete and the composite flanges did not contribute significantly to the shear resistance of the hybrid beam.

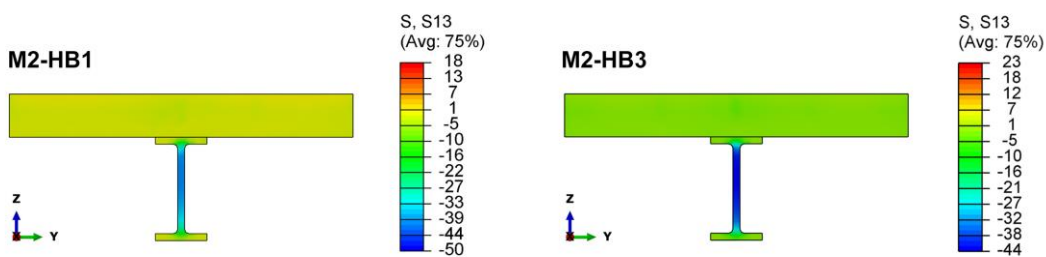


Figure 5.35: Cross-sectional (S2) in-plane shear stress distribution at failure, for beams M2-HB1 and M2-HB3 (MPa).

The numerical in-plane shear stress variations at the position of the strain gauge rosettes (section S2) were compared in Figure 5.36 against the experimental measurements and analytical estimates. For this specific validation, the simplified analytical formulas with or without warping were used, in which

the shear load is considered to be carried entirely by the web of the profile and to be distributed uniformly over the sheared area.

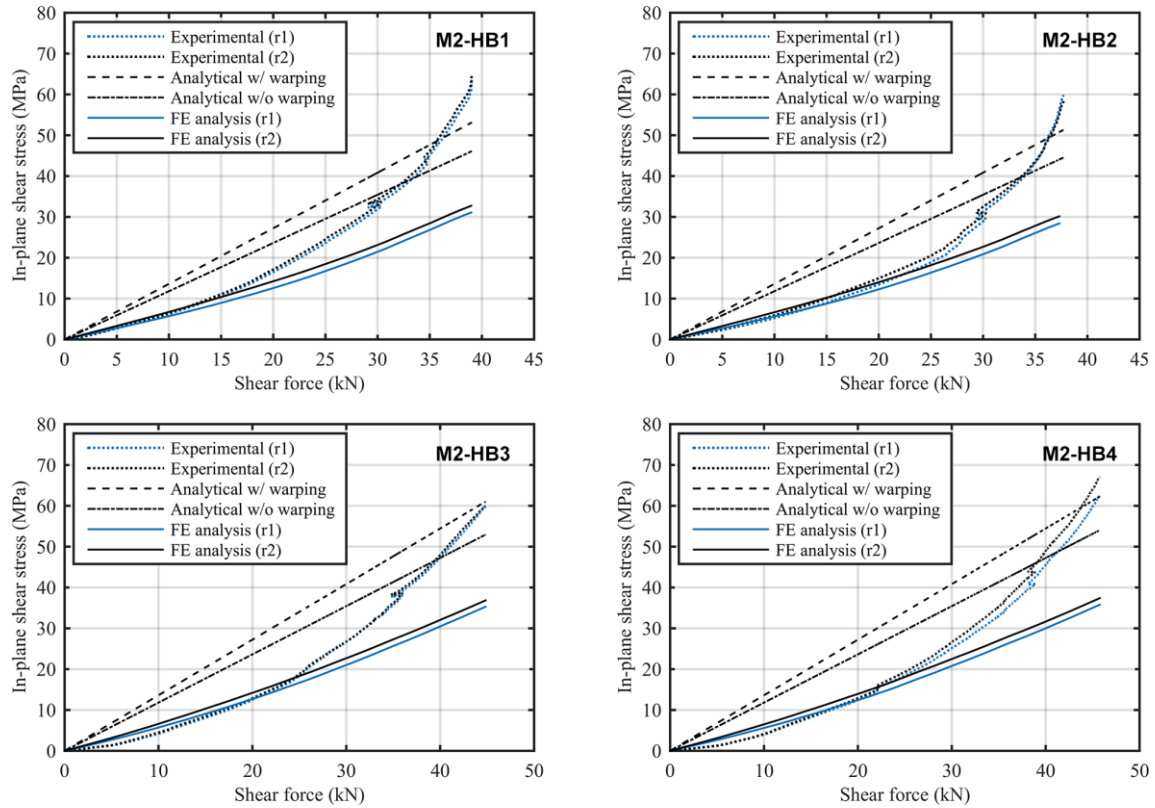


Figure 5.36: Experimental, analytical and numerical curves of the web in-plane shear stress variation in hybrid beams M2, section S2, in function of the applied shear load.

The advanced finite element model is capable of predicting a more realistic shear stress variation as it does not neglect the shear contribution of the slab and flanges. The numerical response fits well with the experiments until approximately half of the applied shear load. After this point, due to the fact that the GFRP composite material had a linearly-elastic constitutive behavior defined, the stress is severely underestimated and it becomes justifiable to use as an alternative solution the simplified analytical approach.

Conversely, if the analytical expression from Eq. (4.43) is used, which accounts for partial shear interaction, slab shear contribution and nonuniform stress variation, closer estimations to the numerical results can be obtained. Hence, the experimental and numerical shear stress values at an intermediate test load of 50 kN are summarized in Table 5.8 along the newly obtained analytical results. The percentile differences calculated between the predicted and the experimental stresses at the strain gauge rosette positions show a good agreement among the theoretical models and a close estimation of the experimental shear stress, especially for the beams tested under four-point bending. The associated intermediate stress distributions across the depths of the four investigated hybrid members are depicted in Figure 5.37.

Table 5.8: Comparative web in-plane shear stresses at rosette positions ($r1$, $r2$), at an applied total load of 50 kN.

Beam	$\tau_{r1,50}$ (MPa)			diff. ^a (%)		$\tau_{r2,50}$ (MPa)			diff. ^a (%)	
	EXP	ANA	FEA			EXP	ANA	FEA		
M2-HB1	23.6	16.0	16.9	-32	-28	24.6	18.4	18.9	-25	-23
M2-HB2	18.8	15.8	16.5	-16	-12	20.5	18.3	18.6	-11	-9
M2-HB3	18.3	16.0	16.8	-13	-8	18.7	18.4	18.7	-2	± 0
M2-HB4	18.4	15.8	16.5	-14	-10	19.3	18.3	18.4	-5	-5

^a Percentile differences computed between analytical (ANA) or numerical (FEA) predictions and experimental (EXP) results.

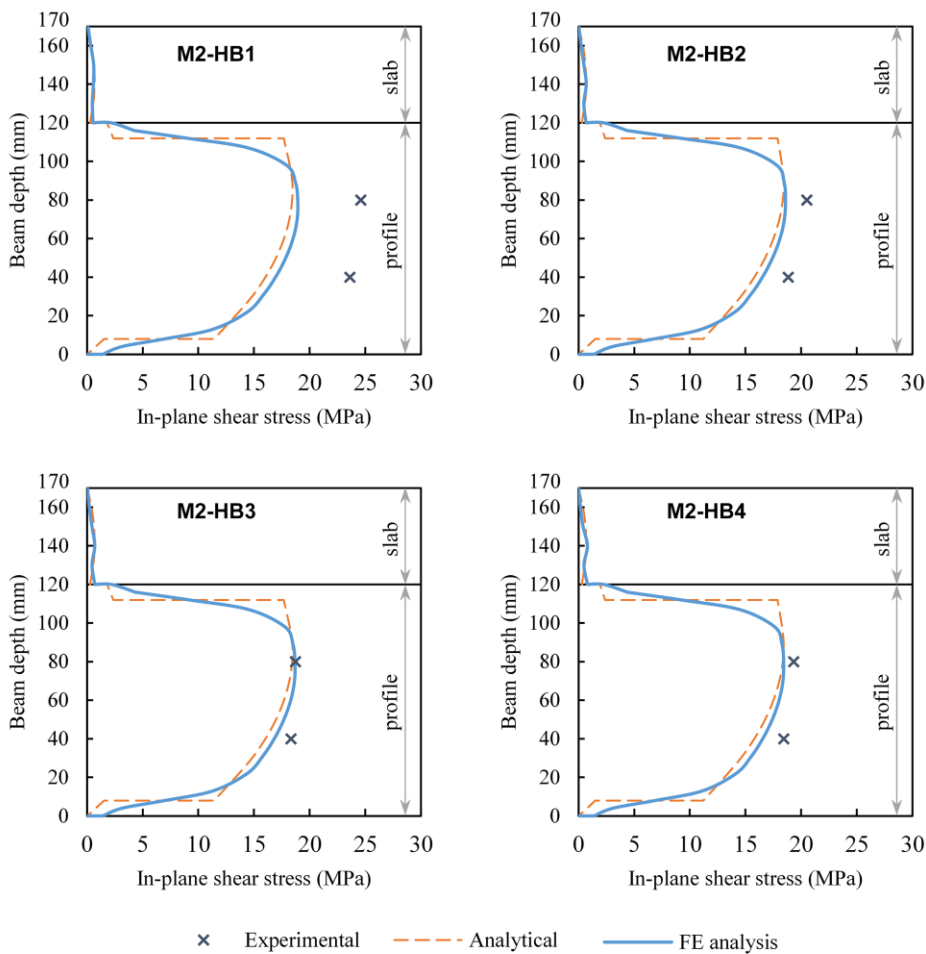


Figure 5.37: In-plane shear stress distributions in hybrid beams M2, in section S2, at an intermediate load of 50 kN. Numerical and analytical estimated distributions versus experimental data points.

The intermediate numerical shear stress distributions across the beams are very similar in magnitude to the analytical estimations, with a couple of minor exceptions at the filleted regions of the web-flange junctions. As formerly commented, in the absence of a nonlinear constitutive shear model of the GFRP composite, the results obtained from the simulations were smaller than the experimental stresses. This fact is further highlighted by the data gathered in Table 5.9 at the maximum load.

Table 5.9: Comparative web in-plane shear stresses at rosette positions ($r1$, $r2$), at failure load.

Beam	$\tau_{r1,u}$ (MPa)			diff. ^a (%)		$\tau_{r2,u}$ (MPa)			diff. ^a (%)	
	EXP	ANA	FEA			EXP	ANA	FEA		
M2-HB1	63.9	25.0	31.5	-61	-51	64.9	28.8	33.4	-56	-49
M2-HB2	59.9	23.8	29.0	-60	-51	58.2	27.7	31.1	-53	-47
M2-HB3	59.9	28.7	35.5	-52	-41	59.8	33.1	37.4	-45	-38
M2-HB4	62.4	28.9	36.0	-54	-42	67.0	33.6	37.9	-50	-43

^a Percentile differences computed between analytical (ANA) or numerical (FEA) predictions and experimental (EXP) results.

For the reason mentioned, the in-plane shear stresses at failure predicted by the finite element model underestimated the laboratory measurements by as much as 50%. Still, the numerical results were closer than the corresponding analytical values. Errors were greater once again for the inferior strain gauge position ($r1$) closer to the reaction edge, where the behavior had been possibly influenced by the concrete support jacket.

Lastly, the longitudinal variations of analyzed shear stress are plotted in Figure 5.38 and Figure 5.39.

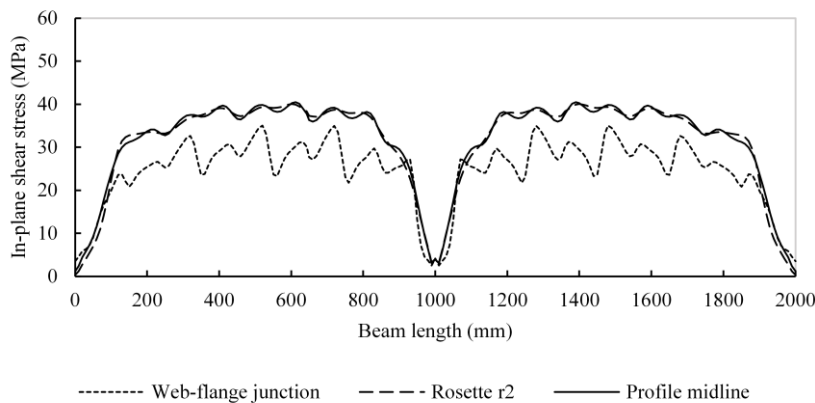


Figure 5.38: Simulated longitudinal in-plane shear stress distributions for M2-HB1 in test setup I, at the maximum load, at different coordinate levels across the profile.

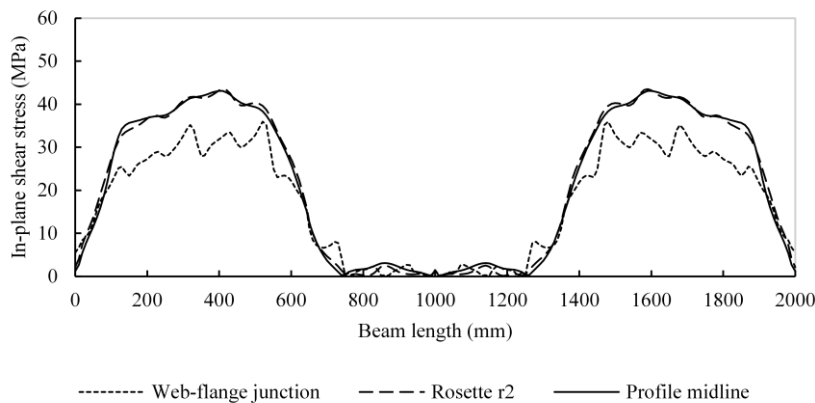


Figure 5.39: Simulated longitudinal in-plane shear stress distributions for M2-HB3 in test setup II, at the maximum load, at different coordinate levels across the profile.

The previous pair of charts are representative for the two static schemes used in the campaign, and reveal that the highest shear stresses have occurred in the upper half of the web of the profiles. The stress variation at the top web-flange junction was smaller due to the radii of the pultruded shape, and more irregular due to the presence of shear connectors. Nonetheless, because of the transitive nature of the composite microstructure, the shear stress at this location proved to be critical in the experienced web-flange shear delamination failure mode.

5.3.6.3. Composite action and interlayer slip

The composite action developed at the interface of the GFRP-concrete beams was analyzed in the final validation process from the perspective of interlayer slip strain, slip, and connector shear load estimations.

Figure 5.40 and Figure 5.41 plot the slip strain variations at section S1 until failure, in function of the applied bending moment. The numerical responses grouped by the static scheme considered show a good correlation with the experimental curves, by demonstrating a high initial composite action followed by a constant slip strain increase after the plasticization of the steel shear connectors. Because the primary contact effects were not modeled due to their complexity, the finite element analysis implied a lower degree of shear interaction than observed for initial bending moments. A comparison between the experimental, analytical and numerical slip strain results is carried out in Table 5.10.

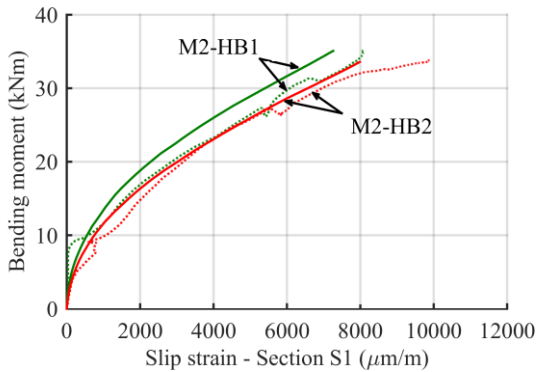


Figure 5.40: Numerical (solid line) versus experimental (dotted line) bending moment-slip strain variations near the midspan for the M2 specimens of test setup I.

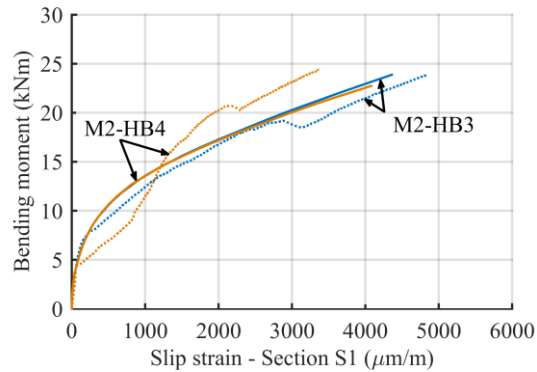


Figure 5.41: Numerical (solid line) versus experimental (dotted line) bending moment-slip strain variations at the midspan for the M2 specimens of test setup II.

Table 5.10: Evaluation of interlayer slip strain at an applied load of 50 kN and at the ultimate load, in section S1.

Beam	$\epsilon_{s,50}$ (%)			diff. ^a (%)		$\epsilon_{s,u}$ (%)			diff. ^a (%)	
	EXP	ANA	FEA			EXP	ANA	FEA		
M2-HB1	0.37	0.26	0.30	-28	-20	0.81	0.40	0.73	-51	-10
M2-HB2	0.38	0.23	0.38	-38	± 0	0.99	0.35	0.81	-64	-18
M2-HB3	0.11	0.16	0.09	+37	-17	0.48	0.52	0.44	+7	-10
M2-HB4	0.11	0.14	0.10	+19	-16	0.34	0.47	0.48	+39	+43

^a Percentile differences computed between analytical (ANA) or numerical (FEA) predictions and experimental (EXP) results.

The percentile differences presented in the previous tabular form indicate that the slip strain was underestimated to some extent by the finite element model; however, the calculated errors had a similar magnitude at the intermediate and maximum sustained load. Contrary, the analytical results were more dispersed since the mathematical formulations were based on a linear elastic interface medium with a linear variation of the slip strain.

Computed slips at the left extremity of the hybrid beams were compared against the experimental data in function of the applied load ratios, in Figure 5.42 and Figure 5.43, respective tot the test setup configuration employed. It must be commented that the end slip in the finite element model was evaluated at the position of the last installed shear bolt.

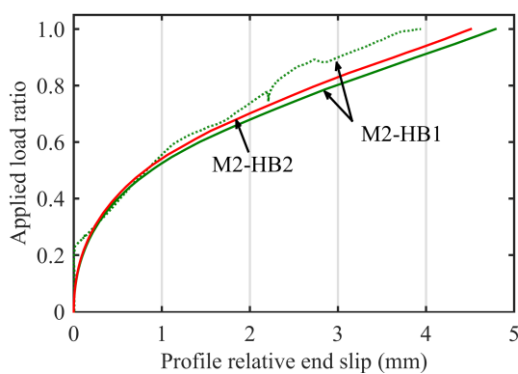


Figure 5.42: Numerical (solid line) versus experimental (dotted line) profile end slip variation in function of the applied load ratio for the M2 specimens of test setup I.

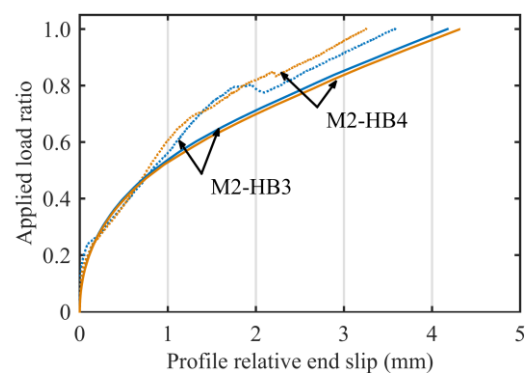


Figure 5.43: Numerical (solid line) versus experimental (dotted line) profile end slip variation in function of the applied load ratio for the M2 specimens of test setup II.

The numerical curves resemble the shape of the registered nonlinear variations of the relative end slip for the four hybrid beams, with a notable divergence for the specimens tested under four-point bending, where the computed slips were greater at higher load ratios. The initial complete shear interaction was not captured due to the modeling criteria discussed in advance.

The predicted slip results at 50 kN of force and at the maximum resisted load were compared in Table 5.11 with the experimentally and analytically determined corresponding values. In contrast to the slip strain, the end slip was slightly overestimated by both theoretical models which offered close percentile errors in the assessment for several specimens.

Table 5.11: Measured and predicted extreme interlayer slip at an applied load of 50 kN and at the ultimate load.

Beam	s_{50} (mm)			diff. ^a (%)		s_u (mm)			diff. ^a (%)	
	EXP	ANA	FEA			EXP	ANA	FEA		
M2-HB1	1.44	1.30	1.71	-9	+19	3.94	2.03	4.79	-48	+22
M2-HB2	n/a	1.14	1.72	n/a	n/a	n/a	1.72	4.51	n/a	n/a
M2-HB3	0.99	1.13	1.09	+15	+11	3.58	4.06	4.18	+13	+17
M2-HB4	0.86	0.99	1.09	+15	+27	3.25	3.63	4.32	+12	+33

^a Percentile differences computed between analytical (ANA) or numerical (FEA) predictions and experimental (EXP) results.
n/a – not available.

Concerning the computed interface slip distribution along the entire length of each specimen, Figure 5.44 illustrates the referred results next to the experimental measurements and analytical curves, at an intermediate sustained load of 50 kN. For the beams tested in three-point bending, the numerical results were higher than the analytical estimations, while for the second setup scheme, the theoretical responses were mostly overlapped. Above all, laboratory monitored slips laid closely in the proximity of the predicted distributions.

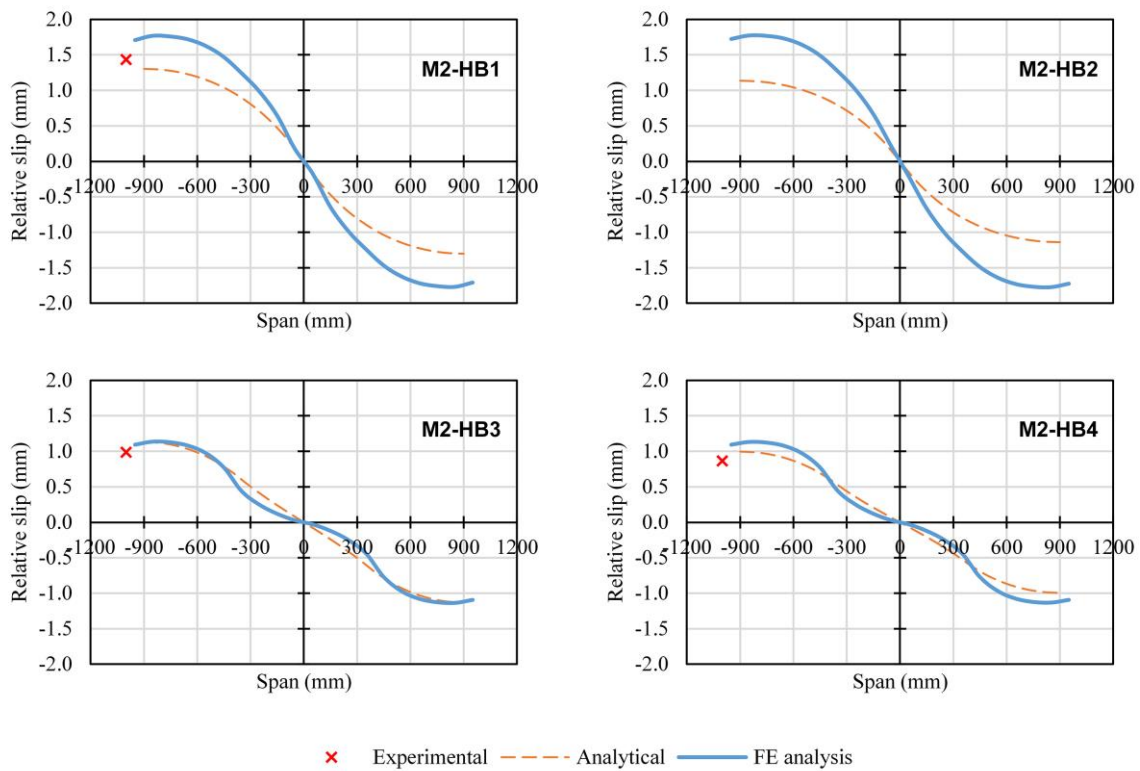


Figure 5.44: Numerical longitudinal slip distributions in hybrid beams M2, at an intermediate load level of 50 kN, versus registered experimental data points and analytical results.

Finally, the bolt shear force distributions from Figure 5.45 and Figure 5.46 confirm that at the ultimate applied bending load, the majority of the connectors had reached the material yielding strength.

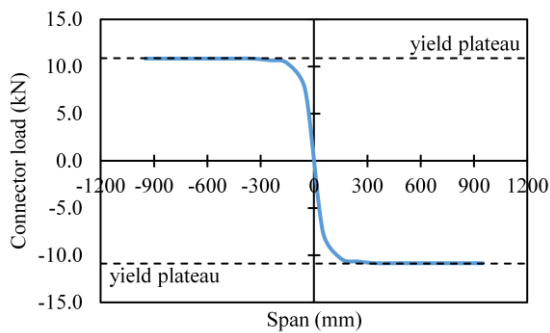


Figure 5.45: Longitudinal shear connector load variation at the maximum load, for specimen M2-HB1.

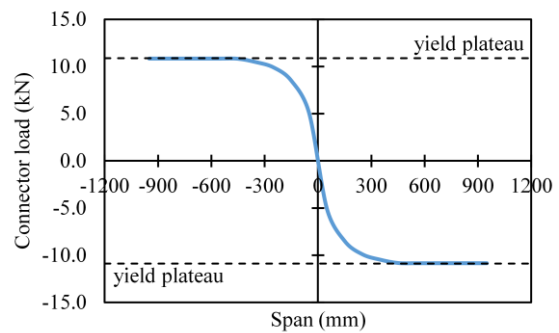


Figure 5.46: Longitudinal shear connector load variation at the maximum load, for specimen M2-HB3.

5.4. Conclusions

A series of finite element models capable of capturing the fundamental short-term behavior of FRP-concrete hybrid beams subjected to combined bending and shear have been proposed, analyzed and verified in the current chapter. Since the majority of the simulations reported so far have been performed mostly on linear elastic models that have disregarded interface characteristics, the proposed finite element models described herein were specifically targeted at hybrid structural elements with mechanical shear connections, which are more sensitive to partial interaction effects. In the presentation of the contrived models, special emphasis was put on the material constitutive laws and interface modeling considerations.

The results of the numerical models were analyzed and discussed in a comparative manner against the experimental results and analytical estimations of the four M2 hybrid beams investigated in the laboratory campaign, and against the available data of several other reported hybrid FRP-concrete beams with mechanical shear connections.

In the first part of the chapter, several initial finite element models were proposed and validated. Thus, the following conclusions were drawn:

- Primarily, a finite element analysis of the single GFRP profiles tested in the investigation demonstrated that the flexural behavior of the composite shapes can be effectively modeled with the homogenous orthotropic elastic properties determined from the static characterization tests. In particular, the experimental and analytical load-displacement responses and the axial strain variations were matched with good accuracy by the numerical data, with a slight exception at high sustained loads where the actual rigidity had decreased. In exchange, the web in-plane shear stresses were predicted well only for about half of the applied shear load, as the experimental variations had increased drastically after this point.
- In the subsequent step, a linear elastic finite element model was built to simulate the flexural behavior of FRP-concrete beams with partial shear interaction. The hybrid specimens were idealized as three-dimensional assemblies formed from a concrete shell and a linear beam profile attached by discrete connector links with a defined constant elastic stiffness. The maximum deflection estimation errors versus the analytical uncracked elastic model with or without partial interaction were minor (about 2%), however, versus the experimental measurements and the analytical model with cracking, the errors were highly pronounced. Lastly, the slip distributions along the interface, at an intermediate load, compared well with the analytical estimates and experimental findings. Overall, the linear elastic numerical model was found to be more suited for serviceability checks.

- The last preliminary FE hybrid beam model kept the same assembly geometry idealization but added initial plasticity characteristics to the materials and shear connectors. Warping of the open section thin-walled profiles, and second order effects were also considered. Subsequently, the validation of the models highlighted the importance of including nonlinear features and inelastic deformations, as the predicted load-deflection bending responses of the referenced members were in better agreement with the experimental curves, and much more precise than the outcome data of the linear elastic FE model. Replicating numerically the plastic behavior of the connectors was confirmed to be essential for modeling hybrid beams with low composite action, which may suffer from premature connection-related types of failure.

In the second part of the chapter, an advanced nonlinear three-dimensional model with solid finite elements was proposed that improved especially upon material definitions and contact interactions. It is emphasized that for the concrete slab, crushing and cracking, tension stiffening, contact friction, and stiffness degradation effects from plastic straining were all taken into consideration. The plastic behavior of the connectors from the M2 specimens was characterized by a calibrated elasto-plastic constitutive curve adapted from an empirical exponential function. From the validation process, the subsequent main observations resulted:

- Flexural load-displacement responses were captured with an increased accuracy over the preliminary finite element models and especially compared to the analytical formulations. The predicted deflections and serviceability bending moments were estimated well; however, the stiffness reduction in the three-point bended beams due to severe concrete slab degradation was not reflected by the charts.
- The sectional and longitudinal axial stress and strain variations were predicted fairly accurately within a 4% difference versus the experimental results at an intermediate load. At the maximum sustained load, the advanced FE model was still superior to the analytical calculations, offering concrete and GFRP compressive strain values within a 14% difference versus the laboratory tests. The FE analysis had a minor tendency to underestimate the strains at failure and to overestimate the slab compressive strains in the specimens loaded with a single concentrated force. There were also small differences versus the experimental data at the position of the strain gauges placed closer to the supports, and on the inferior side of the slab due to cracking.
- Axial strains were determined to be relatively uniform across the concrete slab at initial loads, and more concentrated near the top profile flange region at the ultimate load. The maximum transverse normal stress computed for hybrid beam M2-HB2 which suffered a premature web crushing failure occurred at the midspan, near the top web-flange junction, and was inferior to the associated material strength. Nevertheless, if the actual nonlinear stress-strain behavior had been implemented in the model, the results would have certainly overpassed the material's

strength. The advanced finite element model was also able to replicate the dispersion and direction of the tensile cracks in the concrete slabs that originated from the steel bolts, and the inward slip of the profiles.

- Longitudinal in-plane shear stress distributions indicated that the maximum stresses were situated at approximately a quarter of the beams' length, in the upper part of the web, closer to the top web-flange junction. The computer model predicted a better variation of the shear stresses in function of the applied shear load than the analytical model which considers only the shear capacity of the profile's web and a uniform distribution. Alternatively, versus the analytical model with partial shear interaction and variable sectional shear stress distribution, the numerical results were very close and marginally higher in value. At superior load levels, due to the nonlinear shear behavior of the composite material, the real stresses were underestimated by the FE model by almost 50%, and therefore, it may be justifiable to use the simple analytical approach in the shear capacity design.
- The experimental bending moment-slip strain curves were predicted properly by the nonlinear FE analyses, with similar differences at the intermediate and ultimate loads, but without the initial contact evidences. Slip strains were somewhat underestimated by the model while relative slab-profile displacements were overestimated. Slip distributions along the interface were largely in accordance with the analytical calculations and on the superior side of the experimental measurements, especially for the midspan loaded beams. Lastly, the numerical analyses confirmed that the highest shear forces were resisted by the connectors installed closer to the supports.

To summarize, the finite element model with advanced nonlinear characteristics is capable of predicting the global experimental flexural response of FRP-concrete hybrid beams, and it generally provides more accurate data than the analytical formulations. However, because it is time-consuming and involves a great deal of complexity, it may be impractical for day-to-day office design and more suited for validating prototype hybrid structural solutions.

6

Conclusions and outlook

6.1. Conclusions

The present work aimed to investigate the structural performance of hybrid beams made of fiber-reinforced polymer (FRP) pultruded profiles attached to concrete slabs, with highlight on the effects of the flexibility of the connection system over bending behavior. The analyzed hybrid beams may serve as load bearing members in building floors, platforms, footbridge and marine pier superstructures.

The outcomes of the initial bibliographic study have indicated that there is a great need for additional experimental research and for the development of reliable predictive models and procedures capable of simulating the behavior of such novel constructive solutions. The present research has been also motivated by the current lack of mandatory codes for designing structures with composite profiles and consequently FRP-concrete members. Furthermore, the preceding analytical formulations and numerical models for hybrid beams have been limited both in extent and degree of complexity. Most importantly, in the majority of the previous investigations a state of complete shear interaction was assumed, so the influence of the connection system has not been properly investigated yet.

Therefore, the experimental campaign, analytical procedure and numerical simulations developed and implemented in the present thesis have aided in addressing the abovementioned issues which are essential in lessening the introduction of advanced composite materials in common types of public works and constructions currently built with traditional materials.

Overall, the objectives initially established for the development of the doctoral research were accomplished and the principal conclusions and contributions to the state of the art, related to each of the principal parts of the work, are exposed in the following sections. Because the specific conclusions of each research task were discussed in more detail at the end of each chapter, only the main results are reported here, accompanied by design recommendations.

Finally, because the study highlighted areas where additional research is still needed, the document concludes with several future lines of investigation.

6.1.1. Experimental campaign

The first objective set was to characterize experimentally the structural response of hybrid beams with mechanical shear connection. In this regard, eight GFRP-concrete beams with steel bolt connectors were designed and subjected to combined bending and shear, and their registered behavior was assessed from multiple perspectives and in a comparative manner against single composite profiles and equivalent reinforced concrete beams. The flexural tests were preceded in advance by destructive and nondestructive characterization tests. The acquired data was complete and sufficiently precise to be used in the validation of the analytical formulations and numerical models.

Regarding the characterization tests of the composite material, the following main observations were made:

- Due to the layout of the fiber rovings and continuous strand mats in the glass FRP profiles, the web-flange junctions constituted a sensitive-to-failure region.
- Supplied material properties from the manufacturer were found to be incomplete for appropriate calculations so extensive characterization tests had to be performed. The determined data were greater than the specified properties, on the safe side of design; however, more rigorous minimum material requirements should be implemented for FRP structural shapes.
- The anisotropic behavior of the pultruded profiles was linear elastic with the exception of the transverse compressive stress-strain response and in-plane shear response which displayed a distinct exponential growth. Furthermore, it was quite difficult to obtain a reliable measurement of the in-plane shear strength as there is currently no established method to be used in this sense.

Concerning the methodology and results of the proposed nondestructive characterization procedure for obtaining the elastic properties of the constitutive materials of hybrid members, the subsequent remarks are reported:

- The presented nondestructive method is based on the analysis of the free vibration response of profiles and hybrid specimens, and combines the results of an experimental and numerical modal analysis within an adaptive parameter identification algorithm.
- For the single GFRP profile and the hybrid beams tested, the natural frequencies of the considered bending modes were fit with good precision. On the other hand, torsional modes proved more challenging to be matched. Nevertheless, frequency estimation errors were relatively uniform across the spectrum.
- The resulting elastic constants were close to the material scattering intervals for the pultruded GFRP profiles, however, the method proved to have a minor tendency of overestimation when compared to the static test data, especially for the in-plane shear modulus and concrete moduli.

- Work is still needed on this topic but the initial results have demonstrated that the global elastic behavior of hybrid GFRP-concrete beams and GFRP profiles can be accurately described in a short amount of time using a nondestructive technique. Notwithstanding, precise dynamic measurements are necessary for a correct evaluation and a large number of input parameters demand high computational resources.

From the main flexural tests of the experimental campaign, the following conclusions were drawn regarding the structural performance and response of the hybrid beams:

- The flexural response was characterized by a generally bilinear behavior induced by the occurrence of partial shear interaction after a certain load level. The flexibility of the mechanical joint caused an increase of more than 50% in deflection and a comparable percentile reduction in bending stiffness.
- The use of normal strength concrete allowed for a more ductile response to be obtained, where concrete crushing constituted the first failure mode in several situations. The main collapse of seven of the eight hybrid beams was by web-flange delamination caused by high levels of in-plane shear stress. Reached shear stress values exceeded the material's determined strength by almost 20%, for the reasons mentioned beforehand. The other beam failed due to transverse web crushing under the applied central load. Ultimately, the flexural capacity was limited by the intrinsic properties of the profile, regardless of the concrete strength class augmentation.
- Concrete jacketing of the web was found to be a viable solution in mitigating premature breaks at the reaction points. It is believed that profiles with closed sections could also defer the occurrence of brittle failure modes as well as increase the shear capacity of the members.
- Compared to the single pultruded profiles, the flexural behavior of the GFRP-concrete beams was far superior in terms of ultimate capacity, rigidity and resistance to instability failure modes. The combined beams also demonstrated an exceptional use of the composite's axial properties.
- In comparison with the reference reinforced concrete beams, the hybrid elements had up to 63% higher flexural capacity with up to 40% less weight. However, the stiffness and ductility characteristics were more moderate and thus other designs should be explored.
- By laterally encasing the profile with concrete, the interface slip was reduced by half, the bending stiffness was increased, and the occurrence of partial interaction was hindered. Moreover, there was a post-failure recovery capacity of at least 50%. A stiffer mechanical connection or a combined joint could compensate for some of the confinement effects.

Overall, the bending tests have demonstrated the structural efficiency of the hybrid solution and have also highlighted the importance and effects of the shear connection flexibility.

6.1.2. Analytical procedure

The second objective of the investigation was to propose an analytical procedure for the design of hybrid FRP-concrete beams under short-term loading, where formulas and comments are provided for both serviceability and ultimate limit states. Complete and partial shear interaction assumptions were considered in the majority of the mathematical expressions which were later validated against gathered experimental data.

The following main observations are reported regarding the analytical procedure:

- A dimensionless parameter is introduced to quantify the effects of partial shear interaction in estimating flexural capacities, deflections, internal actions and stress distributions. From the perspective of the connection's flexibility, exact and simplified expressions were deduced for it. The parameter was found to be much more sensitive to the variation of the connection's shear stiffness than to the approximation error from using different formulations. However, after a certain increase in joint stiffness, the benefits of installing additional or more rigid shear connectors decrease considerably.
- An extensive parametric study highlighted that the basic expression of the introduced parameter derived from the Eurocode 5 relations is the most suitable for office design use due to its accuracy, simplicity and independence to load and supporting conditions.
- The presented analytical procedure is recommended for estimating the deformational behavior of the beams at the serviceability limit states or at intermediate load levels, where the connection and the slab have not experienced important plastic strains.
- In addition, it is possible to establish the order of failure causes and to easily implement changes in flexural stiffness due to slab cracking and concrete strength variation.

Several conclusions were drawn from the validation study against available experimental data from several published investigations of hybrid beams with mechanical joints, as discussed below:

- It was demonstrated that the analytical model accounting for interface slip is more accurate than the complete interaction model since the loss in flexural stiffness was higher than 30% even in beams with full shear connection. The relations from the major design codes for steel-concrete structures neglect this phenomenon when sufficient connectors are installed, which is noticeably incorrect for FRP-concrete beams. Effective flexural stiffness values were thus overestimated by the expressions specified in Eurocode 4 (draft version), AISC 360 and AS 2327.1.
- When partial interaction effects were considered, estimated flexural capacities and deflections were more precise and the model fitted better the experimental axial strain variations and shear

stress distributions. Furthermore, there was an insignificant difference between using the slip strain or the simple dimensionless parameter in calculating ultimate bending moments.

- Ignoring the angular deformations in the concrete slab was found to be unconservative at the serviceability limit states as it diminishes the bending stiffness and shear stress values, leading therefore to inefficient designs and poor use of material properties. At the ultimate limit states, however, only the shear contribution of the profile's web should be considered, if the concrete slab carries less than half of the induced shear load.
- There were some discrepancies noticed in estimating properly the flexural response for a couple of hybrid specimens, which were most probably caused by the empirical nature of the expression employed for calculating the connection's shear stiffness.

The accuracy of the analytical procedure was finally checked against the results of the laboratory campaign performed by the author. The distinctive conclusions of the research are stated beneath:

- Overall, the flexural responses of the hybrid beams were captured appropriately, including the transition from complete interaction to partial interaction as well as the decrease in bending stiffness due to the cracking of the top slab.
- Flexural and shear capacities were predicted within 5% of the experimental results when partial interaction effects were considered. Initial axial strains and deflections highlighted also a positive match for all the tested specimens.
- Due to severe plastic deformations at higher loads, the stiffness degradation caused by concrete crushing was not captured by the elastic analytical model. Late experimental slip strains and relative displacements at the GFRP-concrete interface were also difficult to reproduce because of the yielding of the connectors.
- Regarding the flexural stiffness of the beams which had a low degree of shear connection, the Eurocode 5, Eurocode 4 (draft version) and the AISC 360 specifications offered the closest results to the laboratory observations.

Given all these points, due to the improved precision of the expressions accounting for shear connection flexibility, the proposed analytical procedure is capable of capturing in a proper way the structural behavior and performance of hybrid FRP-concrete beams. Moreover, the viability of using simplified or approximate formulas to account for shear interaction effects has also been confirmed.

Lastly, it was concluded that in order to model effectively both fully and partially composite hybrid beams with mechanical joints, the relations should be based on the shear stiffness of the connectors and not on their capacity, as connections in hybrid beams are found to be substantially more flexible than in conventional steel-concrete composite beams.

6.1.3. Numerical models

The third main objective of the thesis was to develop a predictive finite element model capable of simulating the fundamental behavior of FRP-concrete beams with shear connectors. In this regard, a series of models with increasing definition complexity was studied and the computed outcomes were compared against analytical estimations and experimental data from laboratory tests.

From the initial numerical models, the following conclusions were obtained:

- The general flexural behavior of the pultruded GFRP profiles was properly replicated with the effective homogenous elastic constants determined from the static characterization tests. In exchange, the in-plane shear and transverse compressive responses were matched only during initial loads due to the nonlinear inherent characteristics of the composite material.
- Linear elastic computer analyses were determined to be better suited for serviceability checks, similar to the analytical formulations presented in advance. For higher load levels, where significant plastic deformations took place, the initial numerical data diverged drastically from the experimental observations. Therefore, it is essential to model especially the nonlinear behavior of the concrete slab and shear connectors. For hybrid beams with a low degree of composite action, it may be advisable to define also the post-elastic response of the connectors. Furthermore, because of the high flexural deformability of FRP-concrete beams, nonlinear geometry effects should also be considered.

In the subsequent finite element model which had more advanced characteristics, all of the above indications were followed, and thus the concrete crushing, cracking and stiffness degradation effects were simulated. To state, the constitutive behavior of the connectors was defined using an exponential elasto-plastic force-displacement law, and nonlinearities from contact friction, second order effects and concrete-rebar interaction were also implemented. From the validation process, the subsequent conclusions were drawn:

- The advanced nonlinear model was able to reproduce in a very accurate manner the experimental flexural behavior of the investigated hybrid beams. The obtained load-deflection responses were captured well even outside of the serviceability domain.
- Axial strain and stress predictions displayed a high level of agreement with the experimental results. Moreover, the dispersion and direction of the tensile cracks in the concrete slabs and the inward slip of the profiles were properly predicted by the finite element model.
- The variations and distributions of slip and slip strain along the interface were appropriately estimated even toward failure loads.

- There were slight discrepancies in the validation process regarding the computed deflections after concrete crushing had occurred. By this cause, concrete strains at failure were also more dissimilar. Lastly, significant differences were observed for the numerical distributions of the in-plane shear stress and transverse compressive stress in the web of the profiles.
- The finite element model was able to point out the region of the failure initiation in the composite material, near the top web-flange junction, in the central part of the shear span.

To summarize, the proposed finite element model with advanced nonlinear characteristics is capable of predicting the global flexural response of FRP-concrete hybrid beams, offering more precise data than the analytical estimations. Nevertheless, because the method is time-consuming and involves a great deal of complexity, the advanced models may be more suited for validating novel hybrid solutions or assessing individual cases.

6.2. Future lines of investigation

The carried investigation has also highlighted possible future lines of research which are discussed in the present section.

Material characterization tests have revealed that a reliable value for the in-plane shear strength of pultruded FRP profiles is challenging to be obtained. Furthermore, the current methods employed for determining the property offer dissimilar results. Hence, research should be done to propose consistent standardized testing methods. In direct correlation, alternative layouts of fiber reinforcements should be explored for open section composite profiles in order to strengthen the web-flange junction region.

The prospect of changing the type of concrete so as to improve the ductility of hybrid beams should be investigated. For the same purpose, different shear connection configurations could also be trialed, where cost-effective solutions could be identified.

Since the present work has studied the influence of partial interaction effects over the short-term static response of flexural members, the impact of the same effects should be assessed also for hybrid beams subjected to cyclic loads or dynamic loading regimes. Moreover, it is highly important to validate further the proposed analytical procedure and numerical models for other static cases, determinate and indeterminate, and for other load configurations.

Regarding the connection system, a rigorous analytical method for estimating the stiffness of mechanical joints is crucial to be developed, as this property greatly influences the predicted results considering interface slip. To achieve this objective, standardized design methods for bolted connections should be established. In addition, experimental methodologies for determining the capacity and flexibility of mechanical shear connections in combined FRP-concrete beams are needed.

Lastly, finite element models coupled with parametric studies should be developed to study how different factors, such as bolt pretension, hole clearance, flange thickness, etc., affect the force-slip relationship and the connection stiffness describing the interface behavior.

References

- [1] Bank LC. Composites for construction: Structural design with FRP materials. Hoboken, New Jersey: John Wiley & Sons, Inc.; 2006.
- [2] Hollaway LC. A review of the present and future utilisation of FRP composites in the civil infrastructure with reference to their important in-service properties. *Constr Build Mater* 2010;24:2419–45. doi:10.1016/j.conbuildmat.2010.04.062.
- [3] Gay D, Hoa S V. Composite materials: Design and Applications. Second Edition. CRC Press; 2007.
- [4] Bernat-Maso E. Analysis of unreinforced and TRM-strengthened brick masonry walls subjected to eccentric axial load. Ph.D. thesis. Polytechnic University of Catalonia, 2014.
- [5] Escrig C. Estudio del comportamiento mecánico de vigas de hormigón armado reforzadas a flexión y a cortante con materiales compuestos de matriz cementítica. Ph.D. thesis. Polytechnic University of Catalonia, 2015.
- [6] Neagoie CA. Concrete beams reinforced with CFRP laminates. Master's thesis. Polytechnic University of Catalonia, 2011.
- [7] Hollaway L. The evolution of and the way forward for advanced polymer composites in the civil infrastructure. *Constr Build Mater* 2003;17:365–78. doi:10.1016/S0950-0618(03)00038-2.
- [8] Piggott M. Load bearing fibre composites. 2nd ed. Kluwer Academic; 2002.
- [9] Fiberline Design Manual. Kolding, Denmark: Fiberline Composites A/S; 2003.
- [10] The New and Improved Pultex® Pultrusion Design Manual of Standard and Custom Fiber Reinforced Polymer Structural Profiles. Vol. 4. Creative Pultrusions, Inc.; 2004.
- [11] Bedford Reinforced Plastics' Design Guide. 12th ed. Bedford Reinforced Plastics, Inc.; 2010.
- [12] Clarke JL, editor. Structural Design of Polymer Composites - EUROCOMP Design Code and Handbook. E & FN SPON; 1996.
- [13] Gay D. Composite Materials: Design and Applications. Third Edition. CRC Press; 2014.
- [14] European Committee for Standardization (CEN). EN 13706. Reinforced plastics composites – Specifications for pultruded profiles - Part 1: Designation. Brussels, Belgium: 2002.
- [15] European Committee for Standardization (CEN). EN 13706. Reinforced plastics composites – Specifications for pultruded profiles - Part 2: Method of test and general requirements. Brussels, Belgium: 2002.
- [16] European Committee for Standardization (CEN). EN 13706. Reinforced plastics composites – Specifications for pultruded profiles - Part 3: Specific requirements. Brussels, Belgium: 2002.
- [17] ASCE. Pre-Standard for Load & Resistance Factor Design (LRFD) of Pultruded Fiber Reinforced Polymer (FRP) Structures. American Society of Civil Engineers; 2010.
- [18] Correia JR, Almeida NM, Figueira JR. Recycling of FRP composites: reusing fine GFRP waste in concrete mixtures. *J Clean Prod* 2011;19:1745–53. doi:10.1016/j.jclepro.2011.05.018.

- [19] Sobrino JA, Pulido MDG. Towards Advanced Composite Material Footbridges. *Struct Eng Int* 2002;12:84–6. doi:10.2749/101686602777965568.
- [20] Boscato G. Numerical analysis and experimental tests on dynamic behaviour of GFRP pultruded elements for conservation of the architectural and environmental. Ph.D. thesis. University of Nova Gorica, 2009.
- [21] Russo S. Experimental and finite element analysis of a very large pultruded FRP structure subjected to free vibration. *Compos Struct* 2012;94:1097–105. doi:10.1016/j.compstruct.2011.10.003.
- [22] Chen D, El-Hacha R. Hybrid FRP-Concrete Structural Member: Research and Development in North America. In: Ye L, Feng P, Yue Q, editors. 5th Int. Conf. FRP Compos. Civ. Eng. (CICE 2010), Beijing, China: Springer & Tsinghua University Press; 2011, p. 185–90.
- [23] Chen D, El-Hacha R. Hybrid FRP-Concrete Structural Member: Research and Development in Europe and Asia. In: Ye L, Feng P, Yue Q, editors. 5th Int. Conf. FRP Compos. Civ. Eng. (CICE 2010), Beijing, China: Springer & Tsinghua University Press; 2011, p. 191–6.
- [24] Keller T. Recent all-composite and hybrid fibre-reinforced polymer bridges and buildings. *Prog Struct Eng Mater* 2001;3:132–40. doi:10.1002/pse.66.
- [25] Cheng L, Karbhari VM. New bridge systems using FRP composites and concrete: A state-of-the-art review. *Prog Struct Eng Mater* 2006;8:143–54. doi:10.1002/pse.221.
- [26] Diego Villalón A, Gutiérrez Jiménez JP, Arteaga Iriarte A, López Hombrados C. Utilización de materiales compuestos en la construcción de nuevos puentes. II Jornadas Investig. en Construcción, Madrid, Spain: 2008, p. 1583–92.
- [27] Bernard Potyrala P. Use of fibre reinforced polymer composites in bridge construction. State of the art in hybrid and all-composite structures. Master's thesis. Universitat Politècnica de Catalunya, 2011.
- [28] Bansal A, Monsalve Cano JF, Osorio Muñoz BO, Paulotto C. Examples of Applications of Fibre Reinforced Plastic Materials in Infrastructure in Spain. *Struct Eng Int* 2010;20:414–7. doi:10.2749/101686610793557726.
- [29] Areiza Hurtado M, Bansal A, Paulotto C, Primi S. FRP girder bridges: Lessons learned in Spain in the last decade. 6th Int. Conf. FRP Compos. Civ. Eng. (CICE 2012), Rome, Italy: 2012.
- [30] Correia JR, Branco FA, Ferreira JG. Structural solutions for floors of buildings with GFRP-concrete hybrid beams. Fourth Int. Conf. FRP Compos. Civ. Eng., Zurich, Switzerland: 2008.
- [31] Nguyen H, Mutsuyoshi H, Zatar W. Push-Out Tests for Shear Connections between UHPFRC Slabs and FRP Girder. *Compos Struct* 2014;118:528–47. doi:10.1016/j.compstruct.2014.08.003.
- [32] Albiol Ibáñez JR. Estudio experimental de la adherencia entre laminados de GFRP y el hormigón. Ph.D. thesis. Universitat Politècnica de València, 2015.
- [33] Fardis MN, Khalili H. Concrete Encased in Fiberglass-Reinforced Plastic. *ACI J Proc* 1981;78:440–6.
- [34] Karbhari VM, Seible F, Burgueño R, Davol A, Wernli M, Zhao L. Structural characterization of fiber-reinforced composite short-and medium-span bridge systems. *Appl Compos Mater* 2000;7:151–82.
- [35] Fam AZ, Rizkalla SH. Flexural Behavior of Concrete-Filled Fiber-Reinforced Polymer Circular Tubes. *J Compos Constr* 2002;6:123–32. doi:10.1061/(ASCE)1090-0268(2002)6:2(123).
- [36] Fam AZ, Schnerch DA, Rizkalla SH. Rectangular FRP tubes filled with concrete for beam and column applications. 6th Int. Conf. FRP Compos. Civ. Eng. (CICE 2012), Singapore: 2003.

- [37] Li W, Wu Z. Flexural performance of newly developed hybrid FRP – concrete beams. In: Seracino R, editor. *Second Int. Conf. FRP Compos. Civ. Eng. (CICE 2004)*, London: Taylor & Francis Group; 2005, p. 819–26.
- [38] Teng J, Yu T, Wong Y. Hybrid FRP-Concrete-Steel Double-Skin Tubular Structural Members. In: Ye L, Feng P, Yue Q, editors. *5th Int. Conf. FRP Compos. Civ. Eng. (CICE 2010)*, Beijing, China: Springer; 2011, p. 16–32.
- [39] Chakraborty A, Khennane A, Kayali O, Morozov E. Performance of outside filament-wound hybrid FRP-concrete beams. *Compos Part B Eng* 2011;42:907–15. doi:10.1016/j.compositesb.2011.01.003.
- [40] Hillman JR, Murray TM. Innovative lightweight floor systems for steel framed buildings. *IABSE Symp. Mix. Struct. Incl. New Mater. Rep.*, Brussels, Belgium: 1990, p. 671–6. doi:http://dx.doi.org/10.5169/seals-46563.
- [41] Saiidi M, Gordaninejad F, Wehbe N. Behavior of Graphite/Epoxy Concrete Composite Beams. *J Struct Eng* 1994;120:2958–76. doi:10.1061/(ASCE)0733-9445(1994)120:10(2958).
- [42] Hall JE, Mottram JT. Combined FRP Reinforcement and Permanent Formwork for Concrete Members. *J Compos Constr* 1998;2:78–86. doi:10.1061/(ASCE)1090-0268(1998)2:2(78).
- [43] Sekijima K, Miyata K, Ihara T, Hayashi K. Study on Flexural Behavior of Fiber Reinforced Plastic-Concrete Composite Beam. *Third Int. Symp. Non-Metallic Reinf. Concr. Struct.*, Sapporo, Japan: Japan Concrete Institute; 1997, p. 543–50.
- [44] Sekijima K, Ogisako E, Miyata K, Hayashi K. Analytical study on flexural behavior of GFRP-concrete composite beam. In: Teng JG, editor. *Int. Conf. FRP Compos. Civ. Eng.*, vol. II, Hong Kong, China: Elsevier Science Ltd.; 2001, p. 1363–70.
- [45] Biddah A. Experimental investigation of pultruded FRP section combined with concrete slab. In: Tan KH, editor. *Sixth Int. Symp. FRP Reinf. Concr. Struct.*, Singapore: World Scientific Publishing Co. Pte. Ltd.; 2003.
- [46] Fam A, Skutezky T. Composite T-Beams Using Reduced-Scale Rectangular FRP Tubes and Concrete Slabs. *J Compos Constr* 2006;10:172–81. doi:10.1061/(ASCE)1090-0268(2006)10:2(172).
- [47] Nordin H, Täljsten B. Testing of hybrid FRP composite beams in bending. *Compos Part B Eng* 2004;35:27–33. doi:10.1016/j.compositesb.2003.08.010.
- [48] Correia JR, Branco FA, Ferreira J. GFRP-concrete hybrid cross-sections for floors of buildings. *Eng Struct* 2009;31:1331–43. doi:10.1016/j.engstruct.2008.04.021.
- [49] Correia JR, Branco F a., Ferreira JG. Flexural behaviour of multi-span GFRP-concrete hybrid beams. *Eng Struct* 2009;31:1369–81. doi:10.1016/j.engstruct.2009.02.004.
- [50] Manalo AC, Aravinthan T, Mutsuyoshi H, Matsui T. Composite Behaviour of a Hybrid FRP Bridge Girder and Concrete Deck. *Adv Struct Eng* 2012;15:589–600. doi:10.1260/1369-4332.15.4.589.
- [51] Mutsuyoshi H, Hai ND, Aravinthan T, Manalo A. Experimental investigation of HFRP composite beams. *10th Int. Symp. Fiber Reinf. Polym. Reinf. Concr. Struct.*, Tampa, FL, United States: 2011.
- [52] Mendes PJD, Barros JAO, Sena-Cruz JM, Taheri M. Development of a pedestrian bridge with GFRP profiles and fiber reinforced self-compacting concrete deck. *Compos Struct* 2011;93:2969–82. doi:10.1016/j.compstruct.2011.05.005.
- [53] Gonilha JA, Correia JR, Branco FA. Structural behaviour of a GFRP-concrete hybrid footbridge prototype: Experimental tests and numerical and analytical simulations. *Eng Struct* 2014;60:11–22. doi:10.1016/j.engstruct.2013.12.018.

- [54] Nguyen H, Mutsuyoshi H, Zatar W. Hybrid FRP-UHPFRC composite girders: Part 1 – Experimental and numerical approach. *Compos Struct* 2015;125:631–52. doi:10.1016/j.compstruct.2014.10.038.
- [55] Kavlicoglu BM, Gordaninejad F, Saiidi M, Jiang Y. Analysis and Testing of Graphite/Epoxy Concrete Bridge Girders under Static Loading. 9th Int. Conf. Retrofit Repair Bridg., London, England: 2001.
- [56] Kavlicoglu BM, Saiidi M, Gordaninejad F. Fatigue Response of New Graphite/Epoxy-Concrete Girder. *J Compos Constr* 2003;7:50–7. doi:10.1061/(ASCE)1090-0268(2003)7:1(50).
- [57] Elmahdy A, El-Hacha R, Shrive N. Flexural behavior of hybrid composite girders for bridge construction. Fourth Int. Conf. FRP Compos. Civ. Eng., Zurich, Switzerland: 2008.
- [58] El-Hacha R, Chen D. Behaviour of hybrid FRP-UHPC beams subjected to static flexural loading. *Compos Part B Eng* 2012;43:582–93. doi:10.1016/j.compositesb.2011.07.004.
- [59] Deskovic N, Triantafillou TC, Meier U. Innovative Design of FRP Combined with Concrete: Short-Term Behavior. *J Struct Eng* 1995;121:1069–78. doi:10.1061/(ASCE)0733-9445(1995)121:7(1069).
- [60] Deskovic N, Meier U, Triantafillou TC. Innovative Design of FRP Combined with Concrete: Long-Term Behavior. *J Struct Eng* 1995;121:1079–89. doi:10.1061/(ASCE)0733-9445(1995)121:7(1079).
- [61] Canning L, Hollaway L, Thorne AM. An investigation of the composite action of an FRP/concrete prismatic beam. *Constr Build Mater* 1999;13:417–26. doi:10.1016/S0950-0618(99)00050-1.
- [62] Hulatt J, Hollaway L, Thorne A. The use of advanced polymer composites to form an economic structural unit. *Constr Build Mater* 2003;17:55–68. doi:10.1016/S0950-0618(02)00093-4.
- [63] Hulatt J, Hollaway L, Thorne A. Short Term Testing of Hybrid T Beam Made of New Prepreg Material. *J Compos Constr* 2003;7:135–44. doi:10.1061/(ASCE)1090-0268(2003)7:2(135).
- [64] Bloodworth AG, Szczerbicki JR. Advanced polymer composite and concrete beam and slab systems. In: Hollaway LC, Chryssanthopoulos MK, Moy SSJ, editors. *Adv. Polym. Compos. Struct. Appl. Constr. Int. Conf. Adv. Polym. Compos. Struct. Appl. Constr. (ACIC 2004)*, Cambridge, England: Woodhead Publishing Limited; 2004, p. 327–34.
- [65] Euring HN. The use of advanced composite materials in long span civil engineering infrastructure. In: Hollaway LC, Chryssanthopoulos MK, Moy SSJ, editors. *Adv. Polym. Compos. Struct. Appl. Constr. Int. Conf. Adv. Polym. Compos. Struct. Appl. Constr. (ACIC 2004)*, Cambridge, England: Woodhead Publishing Limited; 2004, p. 343–52.
- [66] Li T, Feng P, Ye L. Experimental study on FRP-concrete hybrid beams. In: Mirmiran A, Nanni A, editors. *Third Int. Conf. Compos. Civ. Eng. (CICE 2006)*, Miami, Florida, USA: 2006.
- [67] Mieres JM, Calvo I, Miravete A, Gutiérrez E, Shahidi E, López C, et al. Descripción de paso superior vehicular de la Autovía del Cantábrico realizado con materiales compuestos. *Mater Construcción* 2006;56:81–6. doi:10.3989/mc.2006.v56.i284.20.
- [68] Gutiérrez E, Primi S, Mieres JM, Calvo I. Structural Testing of a Vehicular Carbon Fiber Bridge: Quasi-Static and Short-Term Behavior. *J Bridg Eng* 2008;13:271–81. doi:10.1061/(ASCE)1084-0702(2008)13:3(271).
- [69] Ziehl PH, Engelhardt MD, Fowler TJ, Ulloa F V, Medlock RD, Schell E. Design and Field Evaluation of Hybrid FRP/Reinforced Concrete Superstructure System. *J Bridg Eng* 2009;14:309–18. doi:10.1061/(ASCE)BE.1943-5592.0000002.
- [70] Honickman H, Fam A. Investigating a Structural Form System for Concrete Girders Using Commercially Available GFRP Sheet-Pile Sections. *J Compos Constr* 2009;13:455–65. doi:10.1061/(ASCE)CC.1943-5614.0000039.

- [71] Fam A, Honickman H. Built-up hybrid composite box girders fabricated and tested in flexure. *Eng Struct* 2010;32:1028–37. doi:10.1016/j.engstruct.2009.12.029.
- [72] Kim YJ, Fam A. Numerical analysis of pultruded GFRP box girders supporting adhesively-bonded concrete deck in flexure. *Eng Struct* 2011;33:3527–36. doi:10.1016/j.engstruct.2011.07.016.
- [73] ASCE. *Structural Plastics Design Manual (MOP 63)*. New York, NY, USA: 1984.
- [74] Italian National Research Council. *Guide for the Design and Construction of Structures made of FRP Pultruded Elements (CNR-DT 205/2007)*. 2008.
- [75] *Strongwell Design Manual*. Strongwell Corporation; 2013.
- [76] Mosallam A. *Design Guide for FRP Composite Connections (MOP 102)*. Reston, VA: American Society of Civil Engineers; 2011. doi:10.1061/9780784406120.
- [77] International Federation for Structural Concrete (fib). *fib Model Code for Concrete Structures 2010*. vol. 53. Wilhelm Ernst & Sohn; 2013.
- [78] Johnson RP. *Composite Structures of Steel and Concrete*. Third Edition. Oxford, UK: Blackwell Publishing Ltd; 2004. doi:10.1002/9780470774625.
- [79] Cosenza E, Zandonini R. *Composite Construction*. In: Chen W-F, editor. *Struct. Eng. Handb.*, CRC Press; 1999.
- [80] European Committee for Standardization (CEN). EN 1994-1-1:2004. *Eurocode 4: Design of composite steel and concrete structures – Part 1-1: General rules and rules for buildings*. Brussels, Belgium: 2004.
- [81] European Committee for Standardization (CEN). DD EN 1994-1-1:1994. *Eurocode 4: Design of composite steel and concrete structures – Part 1-1: General rules and rules for buildings*. Brussels, Belgium: 1994.
- [82] British Standards Institution (BSI). BS 5950-3.1:1990. *Structural use of steelwork in building – Part 3: Design in composite construction – Section 3.1 Code of practice for design of simple and continuous composite beams*. London, England: 1990.
- [83] Johnson R, May I. Partial-interaction design of composite beams. *Struct Eng* 1975;53:305–11.
- [84] AISC. *ANSI/AISC 360-10. Specification for Structural Steel Buildings*. Chicago, IL, USA: 2010.
- [85] Standards Australia. AS 2327.1-2003. *Composite structures, Part 1: Simply supported beams*. Sydney, Australia: 2003.
- [86] European Committee for Standardization (CEN). EN 1995-1-1:2004. *Eurocode 5: Design of timber structures – Part 1-1: General – Common rules and rules for buildings*. Brussels, Belgium: 2004.
- [87] Ministry of Construction of the People’s Republic of China. GB 50017-2003. *Code for Design of Steel Structures*. Beijing, China: China Architecture & Building Press; 2003.
- [88] Santos Neto ABDS, La Rovere HL. Composite concrete/GFRP slabs for footbridge deck systems. *Compos Struct* 2010;92:2554–64. doi:10.1016/j.compstruct.2010.02.005.
- [89] Correia JR, Branco F a., Ferreira JG. Flexural behaviour of GFRP–concrete hybrid beams with interconnection slip. *Compos Struct* 2007;77:66–78. doi:10.1016/j.compstruct.2005.06.003.
- [90] Knowles PR. *Composite Steel and Concrete Construction*. Wiley; 1973.
- [91] Wang YC. Deflection of Steel-Concrete Composite Beams with Partial Shear Interaction. *J Struct Eng* 1998;124:1159–65. doi:10.1061/(ASCE)0733-9445(1998)124:10(1159).

- [92] Nguyen H, Zatar W, Mutsuyoshi H. Hybrid FRP–UHPFRC composite girders: Part 2 – Analytical approach. *Compos Struct* 2015;125:653–71. doi:10.1016/j.compstruct.2014.12.001.
- [93] Grant JA, Fisher JW, Slutter RG. Composite Beams With Formed Steel Deck. *Eng J* 1977;14:24–43.
- [94] Crisinel M. Partial-interaction analysis of composite beams with profiled sheeting and non-welded shear connectors. *J Constr Steel Res* 1990;15:65–98. doi:10.1016/0143-974X(90)90043-G.
- [95] Stüssi F. Zusammengesetzte Vollwandträger (Composed beams). *Int Assoc Bridg Struct Eng* 1947:249–69.
- [96] Granholm H. On composite beams and columns with special regard to nailed timber structures. Technical Report 88. 1949.
- [97] Newmark NM, Siess CP, Viest IM. Test and analysis of composite beams with incomplete interaction. *Proc Soc Exp Stress Anal* 1951;9:75–92.
- [98] Pleshkov PF. Theoretical studies of composite wood structures. Moscow: 1952.
- [99] Girhammar UA. A simplified analysis method for composite beams with interlayer slip. *Int J Mech Sci* 2009;51:515–30. doi:10.1016/j.ijmecsci.2009.05.003.
- [100] Girhammar UA, Gopu VKA. Composite Beam-Columns with Interlayer Slip—Exact Analysis. *J Struct Eng* 1993;119:1265–82. doi:10.1061/(ASCE)0733-9445(1993)119:4(1265).
- [101] Girhammar UA, Pan DH. Exact static analysis of partially composite beams and beam-columns. *Int J Mech Sci* 2007;49:239–55. doi:10.1016/j.ijmecsci.2006.07.005.
- [102] Girhammar UA, Pan DH, Gustafsson A. Exact dynamic analysis of composite beams with partial interaction. *Int J Mech Sci* 2009;51:565–82. doi:10.1016/j.ijmecsci.2009.06.004.
- [103] Nie J, Cai CS. Steel–Concrete Composite Beams Considering Shear Slip Effects. *J Struct Eng* 2003;129:495–506. doi:10.1061/(ASCE)0733-9445(2003)129:4(495).
- [104] Nie J, Fan J, Cai CS. Stiffness and Deflection of Steel–Concrete Composite Beams under Negative Bending. *J Struct Eng* 2004;130:1842–51. doi:10.1061/(ASCE)0733-9445(2004)130:11(1842).
- [105] Nie J, Fan J, Cai CS. Experimental study of partially shear-connected composite beams with profiled sheeting. *Eng Struct* 2008;30:1–12. doi:10.1016/j.engstruct.2007.02.016.
- [106] Faella C, Martinelli E, Nigro E. Steel and concrete composite beams with flexible shear connection: “exact” analytical expression of the stiffness matrix and applications. *Comput Struct* 2002;80:1001–9. doi:10.1016/S0045-7949(02)00038-X.
- [107] Faella C, Martinelli E, Nigro E. Shear Connection Nonlinearity and Deflections of Steel–Concrete Composite Beams: A Simplified Method. *J Struct Eng* 2003;129:12–20. doi:10.1061/(ASCE)0733-9445(2003)129:1(12).
- [108] McCutcheon WJ. Stiffness of Framing Members with Partial Composite Action. *J Struct Eng* 1986;112:1623–37. doi:10.1061/(ASCE)0733-9445(1986)112:7(1623).
- [109] Ban H, Bradford M a. Flexural behaviour of composite beams with high strength steel. *Eng Struct* 2013;56:1130–41. doi:10.1016/j.engstruct.2013.06.040.
- [110] Frangi A, Fontana M. Elasto-Plastic Model for Timber–Concrete Composite Beams with Ductile Connection. *Struct Eng Int* 2003;13:47–57. doi:10.2749/101686603777964856.
- [111] Persaud R, Symons D. Design and testing of a composite timber and concrete floor system. *J Struct Eng Soc New Zeal* 2006;19:30–43.

- [112] Schnabl S, Saje M, Turk G, Planinc I. Analytical Solution of Two-Layer Beam Taking into account Interlayer Slip and Shear Deformation. *J Struct Eng* 2007;133:886–94. doi:10.1061/(ASCE)0733-9445(2007)133:6(886).
- [113] Xu R, Wu Y. Static, dynamic, and buckling analysis of partial interaction composite members using Timoshenko's beam theory. *Int J Mech Sci* 2007;49:1139–55. doi:10.1016/j.ijmecsci.2007.02.006.
- [114] Xu R, Wang G. Bending Solutions of the Timoshenko Partial-Interaction Composite Beams Using Euler-Bernoulli Solutions. *J Eng Mech* 2013;139:1881–5. doi:10.1061/(ASCE)EM.1943-7889.0000614.
- [115] Martinelli E, Nguyen QH, Hjjaj M. Dimensionless formulation and comparative study of analytical models for composite beams in partial interaction. *J Constr Steel Res* 2012;75:21–31. doi:10.1016/j.jcsr.2012.02.016.
- [116] Deskovic N. Innovative design of FRP composite members combined with concrete. Ph.D. thesis. Massachusetts Institute of Technology, 1993.
- [117] Correia JR. GFRP pultruded profiles in civil engineering: hybrid solutions, bonded connections and fire behaviour. Ph.D. thesis. Instituto Superior Técnico, Technical University of Lisbon, 2008.
- [118] Liang QQ, Uy B, Bradford MA, Ronagh HR. Strength Analysis of Steel–Concrete Composite Beams in Combined Bending and Shear. *J Struct Eng* 2005;131:1593–600. doi:10.1061/(ASCE)0733-9445(2005)131:10(1593).
- [119] Ollgaard JG, Slutter RG, Fisher JW. Shear Strength of Stud Connectors in Lightweight and Normal-Weight Concrete. *AISC Eng J* 1971:55–64.
- [120] Queiroz FD, Vellasco PCGS, Nethercot DA. Finite element modelling of composite beams with full and partial shear connection. *J Constr Steel Res* 2007;63:505–21. doi:10.1016/j.jcsr.2006.06.003.
- [121] Tahmasebinia F, Ranzi G. Three-Dimensional FE Modelling of Simply-Supported and Continuous Composite Steel-Concrete Beams. *Procedia Eng* 2011;14:434–41. doi:10.1016/j.proeng.2011.07.054.
- [122] Prakash A, Anandavalli N, Madheswaran CK, Rajasankar J, Lakshmanan N. Three Dimensional FE Model of Stud Connected Steel-Concrete Composite Girders Subjected to Monotonic Loading. *Int J Mech Appl* 2012;1:1–11. doi:10.5923/j.mechanics.20110101.01.
- [123] Liu X, Bradford MA, Chen QJ, Ban H. Finite element modelling of steel-concrete composite beams with high-strength friction-grip bolt shear connectors. *Finite Elem Anal Des* 2016;108:54–65. doi:10.1016/j.finela.2015.09.004.
- [124] Wang AJ, Chung KF. Integrated analysis and design of composite beams with flexible shear connectors under sagging and hogging moments. *Steel Compos Struct* 2006;6:459–77. doi:10.12989/scs.2006.6.6.459.
- [125] Wang AJ, Chung KF. Advanced finite element modelling of perforated composite beams with flexible shear connectors. *Eng Struct* 2008;30:2724–38. doi:10.1016/j.engstruct.2008.03.001.
- [126] Titoum M, Tehami M, Achour B, Jaspert J-P. Analysis of semi-continuous composite beams with partial shear connection using 2D finite element approach. *Asian J Appl Sci* 2008;1:185–205.
- [127] Chiorean CG. A computer method for nonlinear inelastic analysis of 3D composite steel–concrete frame structures. *Eng Struct* 2013;57:125–52. doi:10.1016/j.engstruct.2013.09.025.
- [128] Buru ŞM, Miculaş CV, Şelariu MD, Milchiş T, Chiorean CG. Advanced Nonlinear Inelastic Analysis of Composite Beams with Partial Shear Connection. In: Chiorean CG, editor. *Proc. Second Int. Conf. PhD Students Civ. Eng. Archit. (CE-PhD 2014)*, Cluj-Napoca, Romania: UTPRESS; 2014, p. 148–56.

- [129] Oudjene M, Meghlat E-M, Ait-Aider H, Batoz J-L. Non-linear finite element modelling of the structural behaviour of screwed timber-to-concrete composite connections. *Compos Struct* 2013;102:20–8. doi:10.1016/j.compstruct.2013.02.007.
- [130] European Committee for Standardization (CEN). EN 1992-1-1:2004. Eurocode 2: Design of concrete structures – Part 1-1: General rules and rules for buildings. Brussels, Belgium: 2004.
- [131] Hognestad E. A Study of Combined Bending and Axial Load in Reinforced Concrete Members. University of Illinois at Urbana Champaign, College of Engineering, Engineering Experiment Station.; 1951.
- [132] Miculaş CV. Nonlinear analysis of steel-concrete composite beams with full and partial shear connection. Master's thesis. Polytechnic University of Catalonia, 2015.
- [133] Rüsç H. Researches Toward a General Flexural Theory for Structural Concrete. *ACI J Proc* 1960;57:1–28. doi:10.14359/8009.
- [134] Nie J, Tao M, Cai CS, Chen G. Modeling and investigation of elasto-plastic behavior of steel–concrete composite frame systems. *J Constr Steel Res* 2011;67:1973–84. doi:10.1016/j.jcsr.2011.06.016.
- [135] Carreira DJ, Chu K-H. Stress-Strain Relationship for Plain Concrete in Compression. *J Am Concr Inst* 1985;82:797–804.
- [136] Hsu LS, Hsu C-TT. Complete stress — strain behaviour of high-strength concrete under compression. *Mag Concr Res* 1994;46:301–12. doi:10.1680/mac.1994.46.169.301.
- [137] Simulia. Abaqus 6.13 Documentation. Internet User's Man 2013. <http://129.97.46.200:2080/v6.13/>.
- [138] Lubliner J, Oliver J, Oller S, Oñate E. A plastic-damage model for concrete. *Int J Solids Struct* 1989;25:299–326. doi:10.1016/0020-7683(89)90050-4.
- [139] Fenves JL and GL. Plastic-Damage Model for Cyclic Loading of Concrete Structures. *J Eng Mech* 1998;124:892–900.
- [140] Jankowiak T, Lodygowski T. Identification of parameters of concrete damage plasticity constitutive model. *Found Civ Environ Eng* 2005:53–69.
- [141] Birtel V, Mark P. Parameterised Finite Element Modelling of RC Beam Shear Failure. *Abaqus User's Conf* 2006:95–108.
- [142] Kmiecik P, Kamiński M. Modelling of Reinforced Concrete Structures and Composite Structures with Concrete Strength Degradation Taken into Consideration. *Arch Civ Mech Eng* 2011;XI:623–36. doi:10.1016/S1644-9665(12)60105-8.
- [143] Baskar K, Shanmugam NE, Thevendran V. Finite-Element Analysis of Steel–Concrete Composite Plate Girder. *J Struct Eng* 2002;128:1158–68. doi:10.1061/(ASCE)0733-9445(2002)128:9(1158).
- [144] Liang QQ, Uy B, Bradford MA, Ronagh HR. Ultimate strength of continuous composite beams in combined bending and shear. *J Constr Steel Res* 2004;60:1109–28. doi:10.1016/j.jcsr.2003.12.001.
- [145] Wang T, Hsu TT. C. Nonlinear finite element analysis of concrete structures using new constitutive models. *Comput Struct* 2001;79:2781–91. doi:10.1016/S0045-7949(01)00157-2.
- [146] Kwon G, Hungerford B, Kayir H, Schaap B, Ju YK, Klingner R, et al. Strengthening Existing Non-Composite Steel Bridge Girders Using Post-Installed Shear Connectors. Austin, TX, United States: 2007.
- [147] Gilbert R, Warner R. Tension stiffening in reinforced concrete slabs. *J Struct Div* 1978;104:1885–900.

- [148] Vecchio FJ, Collins MP. The modified compression-field theory for reinforced concrete elements subjected to shear. *ACI J Proc* 1986;83:219–31. doi:10.14359/10416.
- [149] Belarbi A, Hsu TTC. Constitutive laws of concrete in tension and reinforcing bars stiffened by concrete. *ACI Struct J* 1994;91:465–74.
- [150] Bentz EC. Sectional analysis of reinforced concrete members. Ph.D. thesis. University of Toronto, 2000.
- [151] Wahalathantri BL, Thambiratnam DP, Chan THT, Fawzia S. A material model for flexural crack simulation in reinforced concrete elements using ABAQUS. *First Int Conf Eng Des Dev Built Environ Sustain Wellbeing* 2011:260–4.
- [152] Nayal R, Rasheed HA. Tension Stiffening Model for Concrete Beams Reinforced with Steel and FRP Bars. *J Mater Civ Eng* 2006;18:831. doi:10.1061/(ASCE)0899-1561(2006)18:6(831).
- [153] Shim C-S, Lee P-G, Yoon T-Y. Static behavior of large stud shear connectors. *Eng Struct* 2004;26:1853–60. doi:10.1016/j.engstruct.2004.07.011.
- [154] Neagoie CA. Design and analysis of PFRP and concrete hybrid beams. In: Pérez MA, editor. *Adv. Appl. Compos. Mater. Civ. Work. Build., OmniaScience Monographs*; 2014, p. 205–36. doi:10.3926/oms.207.
- [155] European Committee for Standardization (CEN). EN ISO 14125. Fibre-reinforced plastic composites – Determination of flexural properties. Brussels, Belgium: 1998.
- [156] European Committee for Standardization (CEN). EN ISO 527-1. Plastics – Determination of tensile properties. Part 1: General principles. Brussels, Belgium: 2012.
- [157] European Committee for Standardization (CEN). EN ISO 527-4. Plastics – Determination of tensile properties. Part 4: Test conditions for isotropic and orthotropic fibre-reinforced plastic composites. Brussels, Belgium: 1997.
- [158] European Committee for Standardization (CEN). EN ISO 14126. Fibre-reinforced plastic composites – Determination of compressive properties in the in-plane direction. Brussels, Belgium: 1999.
- [159] European Committee for Standardization (CEN). EN ISO 14130. Fibre-reinforced plastic composites – Determination of apparent laminar shear strength by short-beam method. Brussels, Belgium: 1997.
- [160] ASTM International. ASTM D 3846 – 02. Standard Test Method for In-Plane Shear Strength of Reinforced Plastics. vol. 03. West Conshohocken, PA: 2002.
- [161] Yokoyama T, Nakai K. Interlaminar and In-Plane Shear Strengths of a Unidirectional Carbon/Epoxy Laminated Composite under Impact Loading. *SEM Annu. Conf. Expo. Exp. Appl. Mech.*, St. Louis, MO, United States: 2006.
- [162] Correia JR, Branco F, Gonilha J, Silva N, Camotim D. Glass Fibre Reinforced Polymer Pultruded Flexural Members: Assessment of Existing Design Methods. *Struct Eng Int* 2010;20:362–9. doi:10.2749/101686610793557771.
- [163] Pierron F, Vautrin A. The 10° off-axis tensile test: A critical approach. *Compos Sci Technol* 1996;56:483–8. doi:10.1016/0266-3538(96)00004-8.
- [164] Vargas G, Mujika F. Determination of In-plane Shear Strength of Unidirectional Composite Materials Using the Off-axis Three-point Flexure and Off-axis Tensile Tests. *J Compos Mater* 2010;44:2487–507. doi:10.1177/0021998310369601.
- [165] Fernandes LA, Gonilha J, Correia JR, Silvestre N, Nunes F. Web-crippling of GFRP pultruded profiles. Part 1: Experimental study. *Compos Struct* 2015;120:565–77. doi:10.1016/j.compstruct.2014.09.027.

- [166] Hodgkinson JM, editor. *Mechanical testing of advanced fibre composites*. Cambridge, England: Woodhead Publishing Limited; 2000. doi:10.1533/9781855738911.
- [167] Ministerio de Fomento. Comisión Permanente del Hormigón. *EHE-08 Instrucción de Hormigón Estructural*. 5ª Edición. 2011.
- [168] Shi Y, Sol H, Hua H. Transverse shear modulus identification by an inverse method using measured flexural resonance frequencies from beams. *J Sound Vib* 2005;285:425–42. doi:10.1016/j.jsv.2004.03.074.
- [169] Larsson PO. Determination of young's and shear moduli from flexural vibrations of beams. *J Sound Vib* 1991;146:111–23. doi:10.1016/0022-460X(91)90525-O.
- [170] Larsson D. Using Modal Analysis for Estimation of Anisotropic Material Constants. *J Eng Mech* 1997;123:222–9. doi:10.1061/(ASCE)0733-9399(1997)123:3(222).
- [171] Gibson RF. Modal vibration response measurements for characterization of composite materials and structures. *Compos Sci Technol* 2000;60:2769–80. doi:10.1016/S0266-3538(00)00092-0.
- [172] Harris CM, Piersol AG. *Harris' Shock and Vibration Handbook*. 5th Edition. Mc-Graw-Hill; 2002.
- [173] He J, Fu Z-F. *Modal Analysis*. Butterworth-Heinemann; 2001. doi:10.1007/978-0-387-09645-2.
- [174] Awad ZK, Aravinthan T, Zhuge Y, Gonzalez F. A review of optimization techniques used in the design of fibre composite structures for civil engineering applications. *Mater Des* 2012;33:534–44. doi:10.1016/j.matdes.2011.04.061.
- [175] Pagnotta L. Recent progress in identification methods for the elastic characterization of materials. *Int J Mech* 2008;2:129-140.
- [176] Euler E, Sol H, Dascotte E. Identification of Material Properties of Composite Beams: Inverse Method Approach. 2006 SEM Annu. Conf. Expo. Exp. Appl. Mech., St. Louis, MO, USA: 2006, p. 9.
- [177] Chakraborty S, Mukhopadhyay M, Sha OP. Determination of Physical Parameters of Stiffened Plates using Genetic Algorithm. *J Comput Civ Eng* 2002;16:206–21. doi:10.1061/(ASCE)0887-3801(2002)16:3(206).
- [178] Cunha J, Cogan S, Berthod C. Application of genetic algorithms for the identification of elastic constants of composite materials from dynamic tests. *Int J Numer Methods Eng* 1999;45:891–900. doi:10.1002/(SICI)1097-0207(19990710)45:7<891::AID-NME610>3.0.CO;2-1.
- [179] Cunha J, Piranda J. Application of model updating techniques in dynamics for the identification of elastic constants of composite materials. *Compos Part B Eng* 1999;30:79–85. doi:10.1016/S1359-8368(98)00050-X.
- [180] Boscatto G, Russo S. Free Vibrations of Pultruded FRP Elements: Mechanical Characterization, Analysis, and Applications. *J Compos Constr* 2009;13:565–74. doi:10.1061/(ASCE)1090-0268(2009)13:6(565).
- [181] Hajianmaleki M, Qatu MS. Vibrations of straight and curved composite beams: A review. *Compos Struct* 2013;100:218–32. doi:10.1016/j.compstruct.2013.01.001.
- [182] Bai Y, Keller T. Modal parameter identification for a GFRP pedestrian bridge. *Compos Struct* 2008;82:90–100. doi:10.1016/j.compstruct.2006.12.008.
- [183] Gonilha JA, Correia JR, Branco FA, Caetano E, Cunha Á. Modal identification of a GFRP-concrete hybrid footbridge prototype: Experimental tests and analytical and numerical simulations. *Compos Struct* 2013;106:724–33. doi:10.1016/j.compstruct.2013.07.003.
- [184] Allemang R. The modal assurance criterion – Twenty years of use and abuse. *Sound Vib* 2003;1:14–21.

- [185] Pérez MA, Gil L, Oller SH. Evaluación del daño por impacto en laminados de material compuesto mediante la respuesta dinámica (Monografía CIMNE M128). Barcelona, Spain: Centro Internacional de Métodos Numéricos en Ingeniería (CIMNE); 2012. doi:10.1017/CBO9781107415324.004.
- [186] ANSYS Mechanical User's Guide. Canonsburg, CA, USA: ANSYS, Inc.; 2013.
- [187] ANSYS Design Exploration User's Guide. Canonsburg, CA, USA: ANSYS, Inc.; 2013.
- [188] ME'scopeVES (Visual Engineering Series). Scotts Valley, CA, USA: Vibrant Technology, Inc.
- [189] Corder GW, Foreman DI. Nonparametric Statistics: A Step-by-Step Approach. Second Edition. Wiley; 2014.
- [190] Bank LC. Shear coefficients for thin-walled composite beams. *Compos Struct* 1987;8:47–61. doi:10.1016/0263-8223(87)90015-8.
- [191] Barbero EJ, Lopez-Anido R, Davalos JF. On the Mechanics of Thin-Walled Laminated Composite Beams. *J Compos Mater* 1993;27:806–29. doi:10.1177/002199839302700804.
- [192] Omidvar B. Shear Coefficient in Orthotropic Thin-Walled Composite Beams. *J Compos Constr* 1998;2:46–56. doi:10.1061/(ASCE)1090-0268(1998)2:1(46).
- [193] Roberts T., Al-Ubaidi H. Influence of shear deformation on restrained torsional warping of pultruded FRP bars of open cross-section. *Thin-Walled Struct* 2001;39:395–414. doi:10.1016/S0263-8231(01)00009-X.
- [194] Hutchinson JR. Shear Coefficients for Timoshenko Beam Theory. *J Appl Mech* 2001;68:87. doi:10.1115/1.1349417.
- [195] Roberts TM, Al-Ubaidi H. Flexural and Torsional Properties of Pultruded Fiber Reinforced Plastic I-Profiles. *J Compos Constr* 2002;6:28–34. doi:10.1061/(ASCE)1090-0268(2002)6:1(28).
- [196] Mottram JT. Shear Modulus of Standard Pultruded Fiber Reinforced Plastic Material. *J Compos Constr* 2004;8:141–7. doi:10.1061/(ASCE)1090-0268(2004)8:2(141).
- [197] Chan K, Lai K, Stephen N, Young K. A new method to determine the shear coefficient of Timoshenko beam theory. *J Sound Vib* 2011;330:3488–97. doi:10.1016/j.jsv.2011.02.012.
- [198] Gere JM, Timoshenko SP. *Mechanics of Materials*. 3rd ed. Pws Pub Co; 1990.
- [199] AISC. ANSI/AISC 360-05. Specification for Structural Steel Buildings. Chicago, IL, USA: 2005.
- [200] Neagoe CA, Gil L. Evaluation of Deflections for PFRP-RC Hybrid Beams with Complete and Partial Shear Connection. In: Chiorean CG, editor. Proc. Second Int. Conf. PhD Students Civ. Eng. Archit. (CE-PhD 2014), Cluj-Napoca, Romania: UTPRESS; 2014, p. 57–64.
- [201] Oehlers DJ, Coughlan CG. The shear stiffness of stud shear connections in composite beams. *J Constr Steel Res* 1986;6:273–84. doi:10.1016/0143-974X(86)90008-8.
- [202] Bärtschi R. Load Bearing Behaviour of Composite Beams in Low Degrees of Partial Shear Connection. Zurich: vdf Hochschulverlag AG; 2005.
- [203] Murray TM, Allen DE, Ungar EE. Steel Design Guide Series No. 11: Floor vibrations due to human activity. Chicago IL, USA: American Institute of Steel Construction (AISC); 1997.
- [204] Crețu D, Tulei E, Ghindea C, Cruciat R. Vibrations Induced By Human Activities in Composite Steel Floor Decks . Case Study. Int. Symp. "Steel Struct. Cult. Sustain. 2010," Istanbul, Turkey: 2010.
- [205] International Organization for Standardization (ISO). ISO 10137:2007. Bases for design of structures - Serviceability of buildings and walkways against vibrations. 2007.

- [206] Allen DE, Pernica G. Control of Floor Vibration. *Constr Technol Updat* 1998;22.
- [207] AF&PA/ASCE. Standard for Load and Resistance Factor Design (LRFD) for Engineered Wood Construction (16-95). 1996.
- [208] ANSYS Workbench User's Guide. Canonsburg, CA, USA: ANSYS, Inc.; 2013.
- [209] CSI. CSI Analysis Reference Manual. Berkeley, California, USA: Computers & Structures, Inc.; 2015.
- [210] Cowper GR. The Shear Coefficient in Timoshenko's Beam Theory. *J Appl Mech* 1966;33:335.
doi:10.1115/1.3625046.
- [211] International Organization for Standardization (ISO). ISO 2602. Statistical interpretation of test results – Estimation of the mean – Confidence interval. 1980.
- [212] European Committee for Standardization (CEN). EN ISO 527-1. Plastics – Determination of tensile properties. Part 1: General principles. Brussels, Belgium: 1996.
- [213] ASTM International. ASTM D 2344/D 2344M – 00e1. Standard Test Method for Short-Beam Strength of Polymer Matrix Composite Materials and Their Laminates. West Conshohocken, PA: 2000.



Profile characterization tests

A.1. Introduction

The present appendix compiles the experimental reports that describe the testing procedures and results of the mechanical characterization tests performed on samples of the GFRP composite pultruded profiles used in the experimental investigation. The mechanical properties were determined following the recommendations of specific CEN, ISO and ASTM International standards. The following tests were carried out: flexural, tensile, compressive, interlaminar and in-plane shear tests as well as full-section characterization tests.

All the experiments were performed by the author at the Laboratory for the Technological Innovation of Structures and Materials (LITEM) from Universitat Politècnica de Catalunya – BarcelonaTech, under room temperature and normal relative humidity conditions.

A.2. Flexural characterization tests

A.2.1. Scope and principle

The first report presents the experimental procedure and results of the flexural characterization tests performed on extracted GFRP profile samples. The recommendations of European Standard EN ISO 14125:1998 [155] were followed, as the method described therein is suited for determining the flexural properties of fiber-reinforced thermosetting plastic composites.

According to the norm, the method is not appropriate for the determination of design parameters although it may be used instead for screening materials or quality-control tests. This is because, for example, the evaluation of the modulus of elasticity does not account for the shear contribution to deformation and thus the resulting value is lower than in reality. However, the standard suggests various test span/specimen dimension ratios, in function of the composite material being tested, that minimize

this effect and inhibit the development of an interlaminar shear failure. It should also be noted that due to the internal lay-up structure of the GFRP, the flexural properties tend to differ from tensile properties.

The prescribed method is used to investigate the flexural behavior of test specimens and for determining the flexural strength, flexural modulus and other aspects of the flexural/strain relationship under the conditions defined in the standard. To obtain these properties, simply-supported coupons from the GFRP pultruded profile were deflected in a three-point bending configuration setup (Method A) at a constant rate until they fractured. During the procedure, the force applied to the specimens and the bottom longitudinal strains were measured.

Due to the anisotropy of the composite material in the GFRP profiles, flexural properties should be evaluated in both longitudinal and transversal direction to the pultrusion process; however, because of the reduced height of the investigated profile, adequate crosswise coupons were not possible to be sampled.

A.2.2. Testing procedure

For the flexural characterization tests, 6 coupons were cut lengthwise from a GFRP I-profile: 2 from the top flange (designated F1 and F2), two from the web (W1 and W2), and two from the bottom flange (F1'' and F2''). Since the inherent thickness of the specimens was larger than the preferred dimensions, recommendations from normative Annex A of the same standard were used. Hence, for a Class III material made of a glass-fiber system the overall length to thickness ratio to be respected is 30, the test span/thickness ratio is 20 and the width of the specimen should be 15 mm. Thus, based on a thickness value of 8 mm all specimens had the following nominal dimensions: 250 mm in length, 160 mm for test span and 15 mm in width. The nominal dimensions and sampling area from the GFRP I-profile are illustrated in Figure A.1.

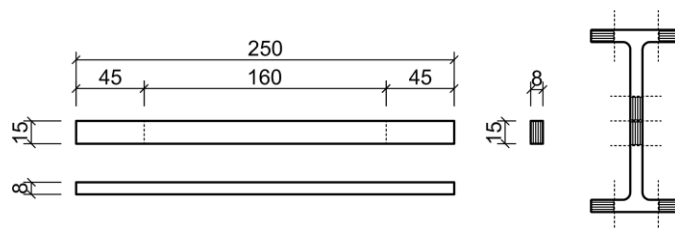


Figure A.1: Specimen nominal dimensions and sampling area for flexural tests (mm).

In the first part of the procedure, each specimen's mean thickness and mean width was determined by performing several measurements along the center cross-section with the help of a micrometer with a precision of 0.01 mm. HBM strain gauges model 1-LY41-6/350 were installed at the middle sections to measure the axial strain variations on the bottom face of the coupons. After the gauge bonding agents had hardened to an adequate degree, the specimens were simply supported on a pair of U80 steel profile

edges over a span distance of 160 mm. The edges were rounded to conform to the standard's recommendations and the radius of the loading member was equal to 5 mm. The schematic of the flexural characterization test setup is displayed in Figure A.2.

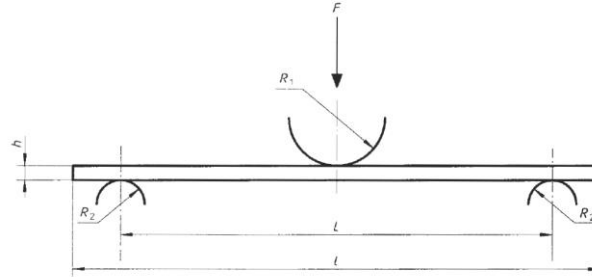


Figure A.2: Test setup scheme for flexural characterization tests [155].

The midspan load was applied monotonically under the displacement control method at a standard speed of 5 mm/min by an electromechanical Suzpecar press. The force was measured by a 50 kN force transducer, model TC4, from AEP transducers. All the data were registered automatically by an HBM MGCplus data acquisition system at a sampling rate of 50 Hz. Figure A.3 displays the experimental test setup configuration.



Figure A.3: Experimental test setup configuration for flexural characterization tests.

The flexural strength of the composite material σ_{fM} was calculated using the following expression:

$$\sigma_{fM} = \frac{3 \cdot F_M \cdot L}{2 \cdot b \cdot h^2} \quad (\text{A2.1})$$

where F_M is the maximum (failure) load, L the test span, b the width of the specimen and h is the thickness of the specimen.

The flexural modulus of elasticity E_f was determined using the chord slope method for a specified strain interval. Its value was calculated from the equation below:

$$E_f = \frac{\sigma_2 - \sigma_1}{\varepsilon_f'' - \varepsilon_f'} \quad (\text{A2.2})$$

where σ_2 is the flexural stress at $\varepsilon_f'' = 0.0025$ and σ_1 is the flexural stress at $\varepsilon_f' = 0.0005$. If no strain gauges are applied, EN ISO 14125:1998 recommends the following expression for determining E_f :

$$E_f = \frac{L^3}{4 \cdot b \cdot h^3} \cdot \left(\frac{\Delta F}{\Delta s} \right) \quad (\text{A2.3})$$

where ΔF is the difference in load F'' and load F' at mid-point deflections s'' and s' respectively, which in their turn correspond to the above-given values of flexural strain ε_f'' and ε_f' . The difference between the mid-point displacements is expressed as:

$$\Delta s = s'' - s' = \frac{\varepsilon_f'' \cdot L^2}{6 \cdot h} - \frac{\varepsilon_f' \cdot L^2}{6 \cdot h} \quad (\text{A2.4})$$

The flexural failure strain ε_{fM} was taken as the longitudinal strain corresponding to the maximum load as measured by the electrical strain gauge. Alternatively, it can be obtained from:

$$\varepsilon_{fM} = \frac{6 \cdot s_M \cdot h}{L^2} \quad (\text{A2.5})$$

where s_M is the mid-point displacement corresponding to the maximum load F_M .

If large deflections are registered in the tests ($> 0.1 \cdot L$), the standard recommends using the following equations for calculating the flexural stress σ_f and flexural strain ε_f , in the case of specimens subjected to three-point bending (Method A):

$$\sigma_f = \frac{3 \cdot F \cdot L}{2 \cdot b \cdot h^2} \cdot \left[1 + 6 \cdot \left(\frac{s}{L} \right)^2 - 3 \cdot \left(\frac{s \cdot h}{L^2} \right) \right] \quad (\text{A2.6})$$

$$\varepsilon_f = \frac{h}{L} \cdot \left[6.00 \cdot \frac{s}{L} - 24.37 \cdot \left(\frac{s}{L} \right)^3 + 62.17 \cdot \left(\frac{s}{L} \right)^5 \right] \quad (\text{A2.7})$$

where, as stated before, s is the mid-point deflection, F is the applied load and the rest of the parameters represent geometric characteristics of the specimen and test setup.

A.2.3. Results

All tests were considered valid since there were no failures initiated by interlaminar shear stresses. The failure modes observed were tensile-initiated for all coupons except W1 which had a compression type of failure. Figure A.4 illustrates the two failure modes registered by the GFRP specimens.



Figure A.4: Tensile fracture and compression fracture of fibers due to flexure [155].

In the experimental evaluations there were no large deflections registered. Moreover, failures were caused remotely from the supporting points, under the midspan load, and thus deemed as acceptable.

The failure sequence started with the tensile fracture of the surface layer made of non-woven fibers and continued with the rupture of the subsequent lay-up structure of glass fiber rovings and woven fabrics. Figure A.5 and Figure A.6 illustrate the failed coupons from two different perspectives. It is clearly noticeable that all specimens broke in a similar manner, at the midspan cross-section.



Figure A.5: Bottom-up view of the flexural failure of the GFRP specimens.

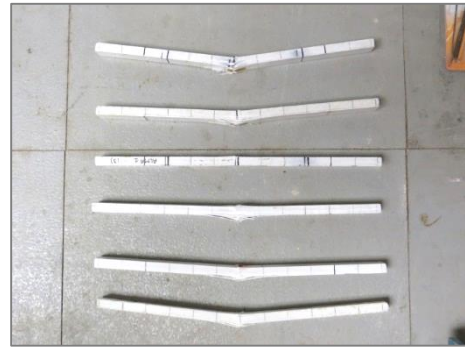


Figure A.6: Lateral view of the failed specimens in flexure.

Regarding the computed results, Figure A.7 plots the flexural stress values versus the strains measured in the longitudinal direction of the fiber rovings.

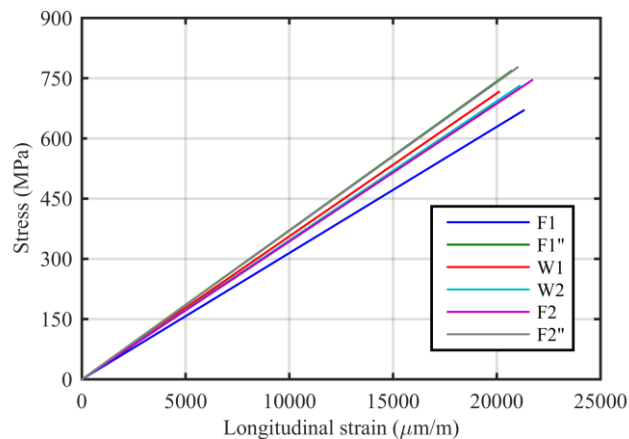


Figure A.7: Stress-strain curves of the longitudinal flexural characterization tests.

As expected for a composite material, the flexural behavior was linear-elastic up to failure, for all specimens. Furthermore, the mechanical response of the specimens that were extracted from the flanges did not differ significantly from that of the specimens extracted from the web.

Based on the experimental data registered, the following flexural properties summarized in Table A.1 were calculated. The mean, standard deviation (SD), coefficient of variation (CV) and 95% confidence interval (CI) of each property was evaluated according to ISO 2602:1980 [211] and reported.

Table A.1: Main results and statistical interpretation of the flexural characterization tests.

Specimen	Dimensions		F_M (kN)	ε_{fM} (%)	σ_{fM} (MPa)	E_f (GPa)
	b (mm)	h (mm)				
F1	14.13	7.96	2.50	2.13	669.8	31.49
F2	15.32	7.98	3.03	2.17	745.4	34.36
W1	14.91	7.97	2.83	2.01	716.0	35.58
W2	15.10	7.91	2.88	2.11	730.8	34.68
F1''	15.84	8.02	3.26	2.07	768.0	37.05
F2''	15.20	8.01	3.16	2.10	776.7	36.99
			Mean	2.10	734.4	35.02
			SD	0.05	38.90	2.06
			CV	2.5%	5.3%	5.9%
			CI	2.10 ± 0.06	734.4 ± 40.82	32.02 ± 2.17

To conclude, the average value of the flexural failure strain, flexural strength and flexural modulus of elasticity to be used in analytical and numerical simulations is 2.10%, 734.4 MPa, respectively 35.02 GPa. The value obtained for the flexural strength was higher than the minimum value specified by European Norm EN 13706-3:2002 for structural pultruded profiles of grade E17. In fact it was closer to the value given by the manufacturer for the GFRP bars than for the GFRP profiles.

A.3. Tensile characterization tests

A.3.1. Scope and principle

The following subsection reports the experimental procedure and results of the tensile characterization tests performed on GFRP coupons. Test principles were adopted from the European Standard EN ISO 527-1:2012 [212] which specifies general principles for determining the tensile properties of plastics and plastic composites under particular conditions. Due to the nature of the pultruded material, recommendations from EN ISO 527-4:1997 [157] were also followed since they further detail the procedure for the determination of tensile properties of isotropic and orthotropic fiber-reinforced plastic composites, and more specifically of thermosetting composites incorporating both unidirectional and multidirectional reinforcements.

The method found in the standards is used to investigate the tensile behavior of the test specimens and determine the tensile strength, tensile modulus and other aspects of the tensile stress-strain relationship, under the conditions defined. Essentially, from an experimental point of view, a test specimen is extended along its major longitudinal axis at a constant speed until it fractures. During the procedure, the load sustained by the specimen and the lengthwise and crosswise elongations are measured.

Due to the anisotropy of the composite material of the profile, the tensile properties should be evaluated in both longitudinal and transversal direction to the pultrusion process; however, because of the reduced height of the investigated shape, adequate coupons from the profile's web were not possible to be sampled.

It should be noted that the stacking sequence of the different reinforcement formats (*e.g.* rovings, fabrics) produces a “sandwich type” layered structure which results in different properties being obtained in flexural and tensile coupon tests.

A.3.2. Testing procedure

In order to perform the tensile characterization tests, 7 coupons were cut lengthwise from the flanges and web of a GFRP I-profile – 2 from the top flange (designated F1 and F2), three from the web (designated W1 to W3), and two from the bottom flange (designated F1'' and F2''). Initially all coupons were of Type 2 category and had the following nominal standard dimensions: 250 mm in overall length, 25 mm in width, and 50 mm for the gripping distance. The inherent thickness of the specimens, h , was 8 mm. A milling machine was used to minimize the irregularities of the cut surfaces. The nominal dimensions and sampling area from the GFRP I-profile are illustrated in Figure A.8.

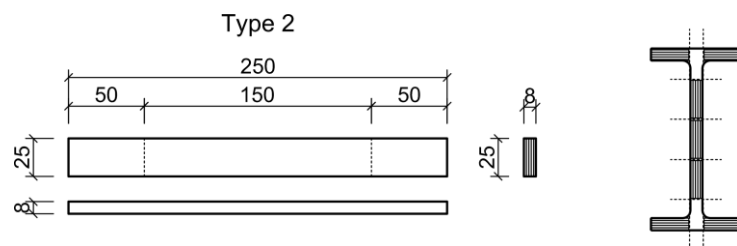


Figure A.8: Nominal dimensions of Type 2 specimens and sampling area for tensile tests (mm).

After an initial tensile test that served to check the alignment of the specimens with the loading setup, the specimen type was changed due to the registered type of failure. As the norm states, the specimens have to fail at a point sufficiently distanced from the grips, failure which in that case did not comply, as it can be observed from Figure A.9.



Figure A.9: Tensile failure of specimen W1 in the proximity of one of the action grips.

Therefore, it was opted to use Type 1B specimens in the following tensile tests because of its hourglass shape and reduced middle cross-section area. These new specimens were machined from the initial ones and respected the standard nominal dimensions with a few amendments: the width at the

ends was kept to 25 mm for adherence reasons and the width of the narrow portion b_1 was set to 15 mm, as opposed to the recommended 10 mm, so as to properly accommodate strain gauges in the transverse direction. The initial distance between the grips was also kept to 150 mm, similar to the case of Type 2 coupons. The nominal dimensions for specimens Type 1B are presented in Figure A.10.

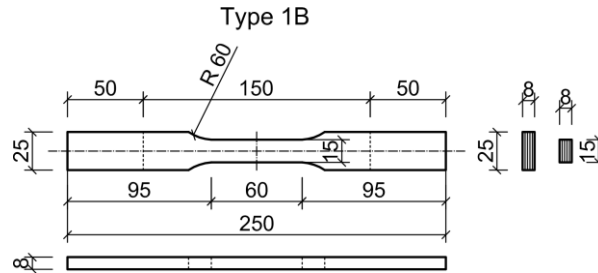


Figure A.10: Nominal dimensions of Type 1B specimens used for the tensile tests (mm).

In the first part of the test procedure, each specimen's mean thickness and mean width was determined by performing several measurements along the center cross-section with a micrometer with a precision of 0.01 mm. Strain gauges model 1-LY41-6/350 from HBM were installed at the middle section in order to measure the axial and transverse strains on the two main faces of the coupon. After the gauge bonding agents had hardened to an adequate degree, the specimens were placed in a pair of MTS Advantage Mechanical Wedge Grips, taking care to align the longitudinal axis of the coupons with the axis of the testing machine. The grips were tightened firmly by hand to avoid slippage of the test specimen and movement of the grips during the experiment. Figure A.11 and Figure A.12 illustrate the experimental setup and a close-up of the mechanical action grips.



Figure A.11: Experimental test setup configuration for tensile characterization tests.



Figure A.12: Tensile GFRP specimen positioned in the action grips.

Loading was applied monotonically, under the displacement control method at a standard speed of 2 mm/min by an MTS model 244.22 hydraulic actuator with a maximum capacity of 100 kN. The vertical displacement of the setup was registered by the actuator's internal LVDT and the force by an MTS 661.20F-03 force transducer mounted on the actuator's head. All the data were registered

automatically by an HBM MGCplus data acquisition system at a sampling rate of 50 Hz and the instruments had a measurement error under $\pm 1\%$.

The tensile failure strain ε_{tM} was taken as the longitudinal strain corresponding to the maximum load.

The tensile strength of the composite material σ_{tM} was calculated using the following expression:

$$\sigma_{tM} = \frac{F_M}{A} \quad (\text{A3.1})$$

where F_M is the maximum (failure) load, and A is the initial cross-section area of the specimen ($b_1 \cdot h$).

The tensile modulus of elasticity E_t was determined using the chord slope method for a specified strain interval. Its value is obtained from the ratio:

$$E_t = \frac{\sigma_2 - \sigma_1}{\varepsilon_2 - \varepsilon_1} \quad (\text{A3.2})$$

where σ_2 is the tensile stress at $\varepsilon_2 = 0.0025$ and σ_1 is the tensile stress at $\varepsilon_1 = 0.0005$.

EN ISO 527-1:2012 states that in order to overcome the difficulties related to the precise determination of the lateral contraction at small values of the longitudinal strain, the strain interval for calculating Poisson's ratio should be chosen beyond the strain region of the modulus determination. Thus, as recommended, Poisson's ratio was evaluated at higher strains than 0.3% and it is expressed as the negative ratio of the strain increment in transverse direction $\Delta\varepsilon_n$ to the corresponding strain increment in longitudinal direction $\Delta\varepsilon_l$:

$$\mu_{12} = -\frac{\Delta\varepsilon_n}{\Delta\varepsilon_l} \quad (\text{A3.3})$$

A.3.3. Results

During all tensile tests there were no premature fractures observed and no squashing of the specimens in the grips. In addition, there was no important prestress present in the material at the beginning of the experiments.

All coupons experienced a brittle tensile failure within the gauge length, as illustrated in Figure A.13. Although failure took place in an instance, the surface layer made of non-woven fibers ruptured first and then in a second phase, the glass fiber rovings from the inside started splintering, as depicted in Figure A.14.



Figure A.13: Tensile failure of a Type 1B GFRP specimen.

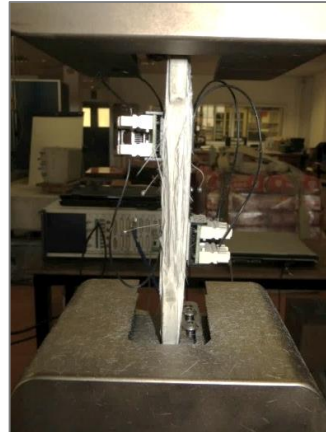


Figure A.14: Tensile splintering of GFRP fibers.

Figure A.15 illustrates part of the failed Type 1B specimens. It was observed that all specimens failed in a similar manner, close to the necking of the cross-section.

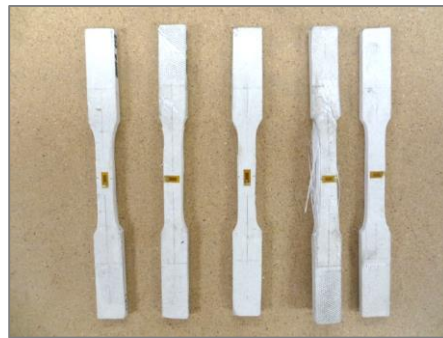


Figure A.15: Type 1B specimens after tensile testing.

The experimental load-displacement curves registered for the lengthwise extracted specimens are displayed below in Figure A.16, except for W1 which had a different cross-section.

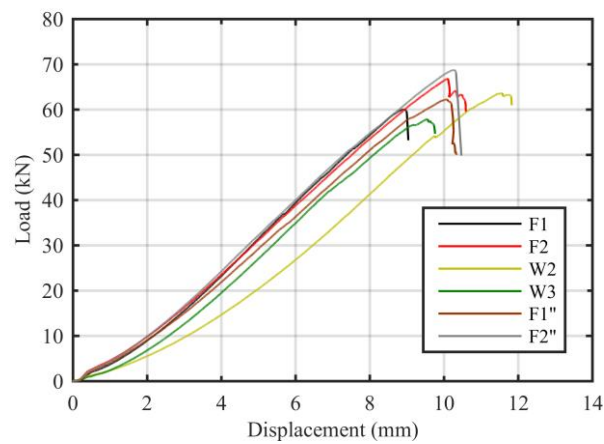


Figure A.16: Load-displacement curves of the longitudinal tensile characterization tests.

Even though the initial part of the tensile behavior was nonlinear due to the settlement of the loading arrangement, the rest of the response was linear up to failure. Maximum registered load values were close, independent of the coupon's sampling location from the profile.

In Figure A.17, the calculated tensile stress values are plotted versus the strains measured in longitudinal and transverse direction of the fiber rovings (positive – tension; negative – compression). It is clearly noticeable that the behavior of the specimens that were extracted from the flanges does not differ from that of the specimens extracted from the web.

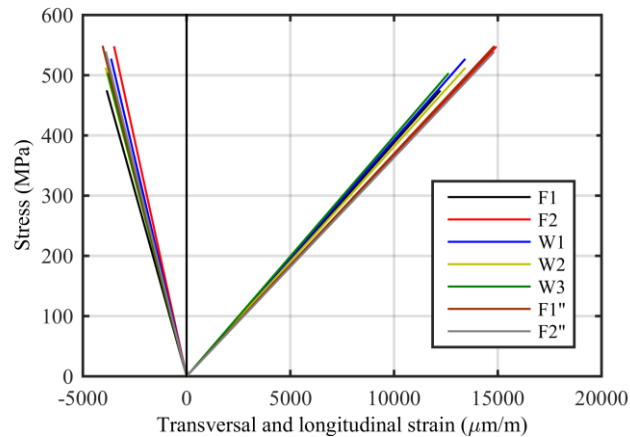


Figure A.17: Stress-strain curves of the longitudinal tensile characterization tests.

Based on the experimental data registered, the tensile properties reported in Table A.2 were calculated for the GFRP pultruded profile specimens. The mean, standard deviation (SD), coefficient of variation (CV) and 95% confidence interval (CI) of each property was evaluated according to ISO 2602:1980 and reported in the same table.

Table A.2: Main results and statistical interpretation of the longitudinal tensile tests.

Specimen	Dimensions		F_M (kN)	ε_{tM} (%)	σ_{tM} (MPa)	μ_{12}	E_t (GPa)
	b_1 (mm)	h (mm)					
F1	15.85	8.00	60.02	1.22	473.0	0.30	38.7
F2	15.30	8.00	66.88	1.49	546.0	0.24	36.6
W1	21.66	7.96	90.67	1.34	526.0	0.27	39.2
W2	15.70	7.93	63.62	1.34	511.0	0.27	38.2
W3	14.52	7.94	57.89	1.26	502.0	0.30	39.9
F1''	14.40	7.90	62.25	1.48	547.0	0.25	37.0
F2''	16.18	7.90	68.74	1.48	538.0	0.26	36.4
			Mean	1.37	520.4	0.27	38.0
			SD	0.11	27.01	0.02	1.36
			CV	8.1%	5.2%	8.2%	3.6%
			CI	1.37 ± 0.10	520.4 ± 24.98	0.27 ± 0.02	38.0 ± 1.26

In conclusion, the average value of the tensile failure strain, tensile strength, Poisson's ratio and tensile modulus of elasticity to be used in analytical and numerical simulations is 1.37%, 520.4 MPa, 0.27, respectively 38.0 GPa. The values obtained for the tensile strength and tensile elastic modulus were higher than the minimum values specified by European Norm EN 13706-3:2002 for structural pultruded profiles of grade E17. They were in fact closer to the values given by the manufacturer for the GFRP bars than for the GFRP profiles.

A.4. In-plane compressive characterization tests

A.4.1. Scope and principle

The current subsection presents the experimental procedure and results of the in-plane compressive characterization tests performed on GFRP coupons. The utilized test method was adopted from the International Standard ISO 14126:1999 [158] which is suitable for determining the compressive properties in directions parallel to the lamination plane of fiber-reinforced plastic composites that have a thermoset or thermoplastic matrix.

The standard's test principle describes that an axial force is applied to the unsupported length of a rectangular specimen held in a loading fixture, while the applied load and axial strain are measured. It is also mentioned that the test method concentrates on the quality of the axial deformation experienced by the specimen and that any loading fixture can be used provided that the failure of the specimen occurs below a 10% bending strain in the material.

Due to the anisotropy of the composite material in the GFRP profile, the compressive properties were evaluated both in the longitudinal and transversal direction of the pultrusion process.

A.4.2. Testing procedure

Loading method 2 was chosen from the norm since it is specified for the end loading or mixed loading case. Method 1 on the other hand provides only a shear loading of the specimen. Regarding the specimen model, type B2 was selected mainly because of the allowed range of thickness and because it can be tested in an untabbed manner.

For the compression tests 7 specimens were cut lengthwise from a GFRP pultruded I-profile, 4 from the flanges (designated as F1 to F4) and 3 from the web (designated as W1 to W3). Another batch of 6 specimens (CW1 to CW6) were extracted in transverse direction only from the web due to the dimensional requirements. The nominal dimensions of the lengthwise coupons were as specified in the standard: 125 mm for the overall length, 25 mm for the width and free test distance, and 50 mm for the grip length. The inherent thickness of the specimens was 8 mm. The crosswise specimens had a shorter

length constrained by the web's depth, of 90 mm. In order to minimize the irregularities of the cut surfaces a milling machine was used. The nominal dimensions and sampling areas from the GFRP IPE 120 profile are shown in Figure A.18.

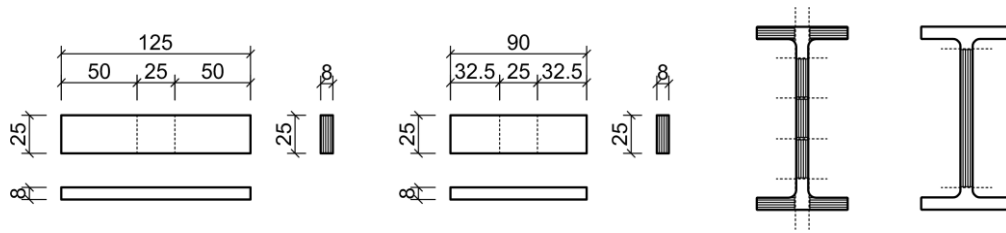


Figure A.18: Lengthwise and crosswise coupon nominal dimensions and sampling areas for in-plane compressive tests (mm).

For the compressive characterization tests, an end loading fixture was designed by the author and fabricated at the facilities of Fundació CIM from UPC-BarcelonaTech. The schematics of the compressive jig are illustrated in Figure A.19, and were based on the design suggestions presented in the informative Annex C of ISO 14126:1999. The specified annex references similar compressive fixtures from ISO 8515:1991 and ASD-STAN prEN 2850. The equipment made can accommodate specimens with a thickness up to 15 mm and a maximum overall length of 140 mm. It has a fixed bottom plate and a sliding top part that can be mounted on an actuator head. The clamps were manufactured from hardened steel and had $\pm 45^\circ$ grooves machined onto the contact surfaces. One half of the clamps were built as mobile so they can be tighten manually on the specimens with a torque wrench.

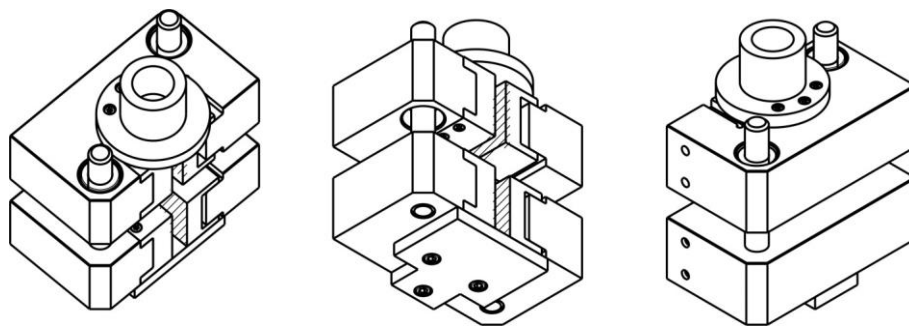


Figure A.19: Isometric views of the designed compressive supporting jig.

In the first part of the test procedure, each specimen's thickness and width was determined with a micrometer with a precision of 0.01 mm. Strain gauges model 1-LY41-6/350 from HBM were installed at the middle section in order to measure the axial compressive strains on the two main faces of the coupon. The two strain gauges positioned in a back-to-back configuration were required to ascertain that column bending was not occurring. Euler buckling is detected if the strain on one face reverses (decreases) while the strain on the opposite face increases rapidly. After the gauge bonding agents had hardened, the specimens were placed and fixed in upright position in the loading jig previously described. Due to the reduced length of crosswise specimens CW1 to CW2, aluminum plates were placed at the loading ends.

The load was applied monotonically under the displacement control method at a standard speed of 1 mm/min by an MTS model 244.22 hydraulic actuator with a maximum capacity of 100 kN. The vertical displacement of the setup was registered by the LVDT mounted in the actuator and the force by the MTS 661.20F-03 force transducer installed on the actuator's head. All the data were registered automatically by an HBM MGCplus data acquisition system at a sampling rate of 50 Hz, and the instruments had a measuring error under 1%. The schematic of the loading fixture and the test setup configuration are shown in Figure A.20 and Figure A.21.

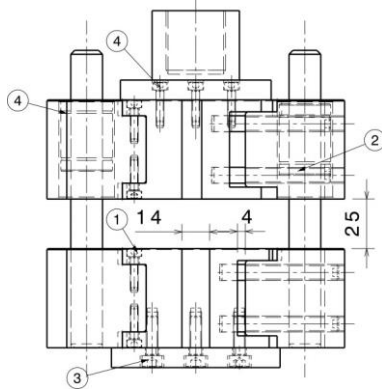


Figure A.20: Schematic of the loading fixture for compressive characterization tests (mm).



Figure A.21: Experimental test setup configuration for compressive tests.

Bending is considered acceptable by the standard if the difference between the strains recorded on each face of the specimen throughout the duration of the test until failure remains smaller than 10%, as noted in the equation below:

$$\left| \frac{\varepsilon_{11b} - \varepsilon_{11a}}{\varepsilon_{11b} + \varepsilon_{11a}} \right| \leq 0.1 \quad (\text{A4.1})$$

where ε_{11a} and ε_{11b} are the longitudinal strains on opposing faces of the specimen.

The in-plane compressive strength of the composite material σ_{CM} was calculated using the following expression:

$$\sigma_{CM} = \frac{F_{max}}{b \cdot h} \quad (\text{A4.2})$$

where F_{max} is the failure or maximum load, b is the width of the test specimen, and h is the thickness of the test specimen.

The modulus of elasticity in compression E_c was determined from:

$$E_c = \frac{\sigma_c'' - \sigma_c'}{\varepsilon_c'' - \varepsilon_c'} \quad (\text{A4.3})$$

where σ_c'' is the compressive stress at $\varepsilon_c'' = 0.0025$ and σ_c' is the compressive stress at $\varepsilon_c' = 0.0005$. For the calculation, the strain values on opposing faces were averaged.

The compressive failure strain ϵ_{cM} was taken as the mean of the longitudinal strains, ϵ_{11a} and ϵ_{11b} , at failure.

A.4.3. Results

Longitudinal specimens failed in compression by delamination of the layers, although in most cases the compressive failure was preceded by significant crushing of the loaded ends. The delamination, as found in ISO 14126:1999, is illustrated in Figure A.22.

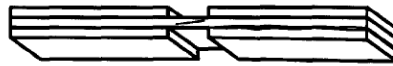


Figure A.22: Acceptable compressive failure mode: delamination [158].

All experimental tests were valid for the specimens extracted crosswise from the profile's web, the only failure mode observed being the through-thickness shear failure represented in Figure A.23, with the existence of either one or two shear planes.



Figure A.23: Acceptable compressive failure mode: through-thickness shear failure [158].

Failed specimens F1 to F4 and W1 to W3 that were extracted lengthwise from the profile's flanges and web are depicted in Figure A.24. The crushed ends are clearly visible for all coupons.

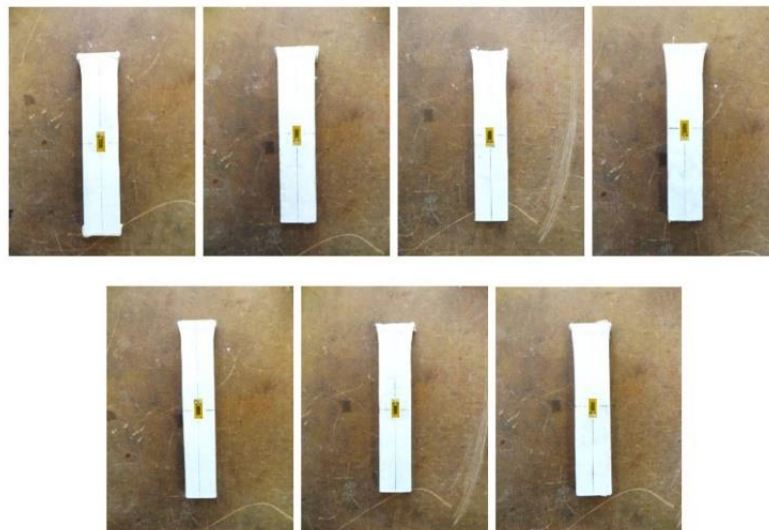


Figure A.24: Compressive failure of the GFRP lengthwise specimens.

Figure A.25 presents the compressive failure of specimen CW1 after the test had stopped. Failed specimens CW1 to CW6 are shown in Figure A.26, with the inclined cracks noticeable in all cases.

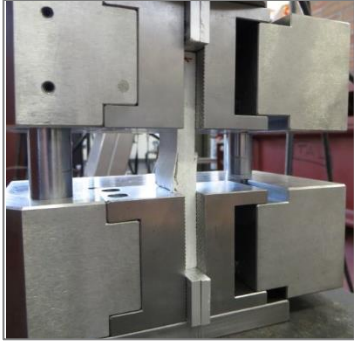


Figure A.25: Through-thickness shear failure of a crosswise GFRP specimen.



Figure A.26: Compressive failure of the GFRP crosswise specimens.

The experimental load-displacement curves registered for the lengthwise and crosswise extracted specimens are displayed below in Figure A.27 and Figure A.28.

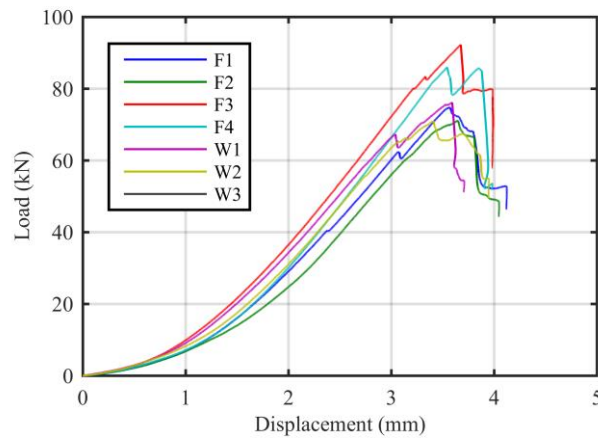


Figure A.27: Load-displacement curves of the longitudinal compressive tests.

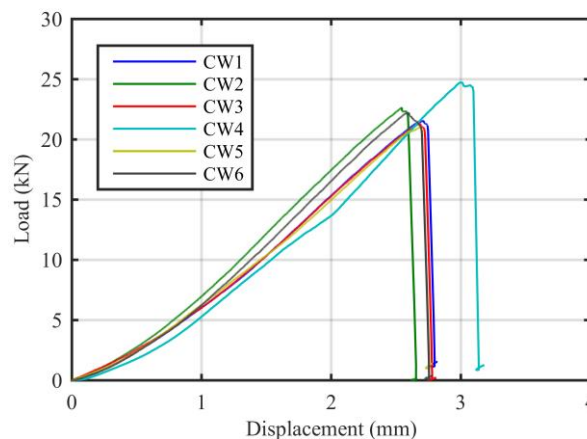


Figure A.28: Load-displacement curves of the transverse compressive tests.

The initial part of the compressive responses is nonlinear probably because of the settlement of the loading arrangement (or loading jig). In the longitudinal tests, sudden drops in load before failure

suggested that part of the extremity fibers in contact with the top end plate started crushing. In contrast, the transverse coupons failed sooner due to the anisotropy of the composite material and no end crushing incidents were observed.

Figure A.29 and Figure A.30 plot the calculated compressive stress values versus the averaged axial strains measured in the tests, for the lengthwise and crosswise extracted coupons. It is noteworthy that due to a couple of strain gauge malfunctions strain data were not available for specimens CW1 and CW4.

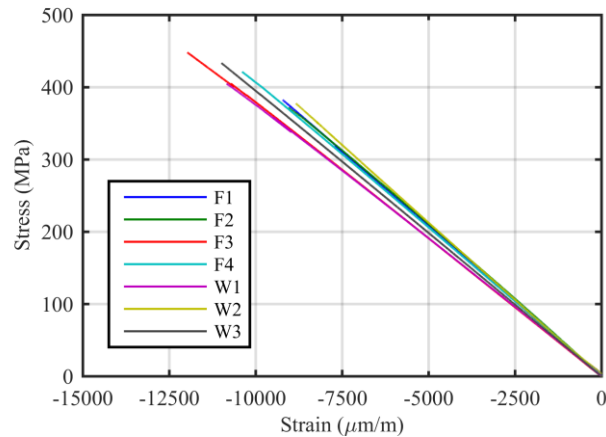


Figure A.29: Stress-strain curves of the longitudinal compressive tests.

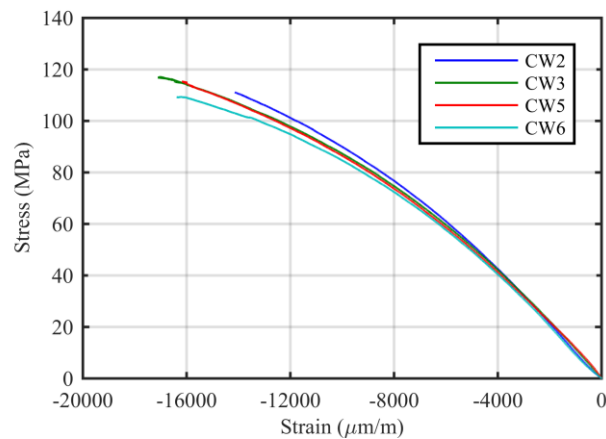


Figure A.30: Stress-strain curves of the transverse compressive tests.

Whereas the longitudinal test responses were linear up to failure, the crosswise specimens exhibited a nonlinear compressive behavior especially for high strain deformation levels. Nonetheless, the compressive modulus of elasticity was evaluated in both cases as specified in the standard, at low stress-strain values. Another observation made was that the experimental responses were similar for coupons extracted from the flanges or the web of the profile.

Based on the experimental data registered for the two test cases, the in-plane compressive properties were calculated for the GFRP pultruded profile specimens. The mean value, standard deviation (SD), coefficient of variation (CV) and 95% confidence interval (CI) were evaluated according to ISO 2602:1980 and are reported for the discussed properties in Table A.3 and Table A.4.

Table A.3: Main results and statistical interpretation of the longitudinal compressive tests.

Specimen	Dimensions		F_{max} (kN)	$\varepsilon_{cM,L}$ (%)	$\sigma_{cM,L}$ (MPa)	$E_{c,L}$ (GPa)
	b (mm)	h (mm)				
F1	24.60	7.95	74.82	0.92	382.6	41.74
F2	24.00	7.97	71.10	0.94	371.7	42.98
F3	26.00	7.92	92.29	1.20	448.2	38.38
F4	25.70	7.94	86.00	1.04	421.5	41.63
W1	23.90	7.87	76.18	1.08	405.0	38.45
W2	23.80	7.90	71.00	0.88	377.6	41.54
W3	22.70	7.89	77.66	1.10	433.6	39.72
			Mean	1.02	405.7	40.63
			SD	0.11	29.75	1.79
			CV	11.1%	7.3%	4.4%
			CI	1.02 ± 0.10	405.7 ± 27.52	40.63 ± 1.66

Table A.4: Main results and statistical interpretation of the transverse compressive tests.

Specimen	Dimensions		F_{max} (kN)	$\varepsilon_{cM,T}$ (%)	$\sigma_{cM,T}$ (MPa)	$E_{c,T}$ (GPa)
	b (mm)	h (mm)				
CW1	23.80	7.93	21.56		114.3	
CW2	24.90	7.92	22.65	1.41	114.9	11.26
CW3	22.90	7.95	21.32	1.70	117.1	10.83
CW4	26.20	7.98	24.75		118.4	
CW5	23.00	7.93	21.04	1.62	115.3	10.17
CW6	25.70	7.90	22.22	1.65	109.5	10.80
			Mean	1.60	114.9	10.77
			SD	0.13	3.07	0.45
			CV	7.9%	2.7%	4.2%
			CI	1.60 ± 0.20	114.9 ± 3.22	10.77 ± 0.72

In conclusion, the average value of the compressive failure strain, strength and modulus of elasticity in longitudinal and transverse directions, to be used in analytical and numerical simulations is 1.02%, 405.6 MPa, 40.63 GPa, respectively 1.60%, 114.9 MPa, 10.77 GPa. European Norm EN 13706-3:2002 does not specify a minimum value for these particular mechanical properties of structural pultruded profiles. Once again, the values obtained for the elastic moduli were closer to the values given by the manufacturer for the GFRP bars than for the GFRP profiles.

A.5. Interlaminar shear strength characterization tests

A.5.1. Scope and principle

The current appendix subsection discusses the experimental procedure and results of the interlaminar shear strength characterization tests performed on GFRP specimens. The employed test method was adopted from the European Standard EN ISO 14130:1997 [159] which is suitable for determining the apparent interlaminar shear strength of fiber-reinforced plastic composites that are both symmetric and balanced and have a thermoset or thermoplastic matrix.

The method presented in the standard, known also as the short-beam method, is similar to the one suggested by ASTM D 2344 [213] in which a bar of rectangular cross-section is loaded over a small test span as a simple beam in flexure, so that interlaminar failure occurs in the matrix layer. It is not suitable for the determination of design parameters but may be used for screening materials or as a quality-control test.

It is emphasized that the result obtained is not an absolute value due to the fact that the shear stress distribution in this case is significantly different than the parabolic distribution described by the elasticity theory in cross-sections sufficiently distanced from the supports and load-application areas. For this reason the term “apparent interlaminar shear strength” is used to define the quantity measured and no other differently-sized specimens or testing conditions are directly comparable.

A.5.2. Testing procedure

In the short-beam method the bar rests on two supports and the load is applied by means of a loading member midway between the supports. For these tests six coupons were cut lengthwise from the web of a GFRP IPE 120 profile and named IL1 to IL6. The nominal dimensions to be obtained were determined based on the thickness of the composite material. The norm specifies the desirable ratios between the length and the thickness of the specimen and between the width and the thickness as $l = 10h$, respectively $b = 5h$. Therefore, all specimens were cut to be 80 mm long and 40 mm wide considering their inherent thickness of 8 mm. The nominal dimensions and sampling area from the GFRP profile are illustrated in Figure A.31.

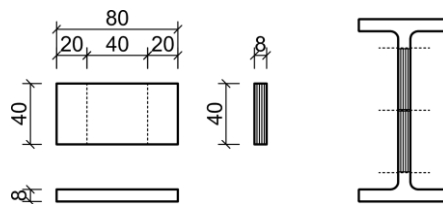


Figure A.31: Coupon nominal dimensions and sampling area for interlaminar shear tests (mm).

The specimens were simply supported on two rounded edges of U40 steel profiles over a span distance of 40 mm ($L = 5h$), and loaded by an electromechanical Suzpecar press with a maximum capacity of 50 kN. The force was applied monotonically at the midspan under the displacement control method at a standard speed of 1 mm/min. The radius of the loading member was 5 mm and of the supports 2 mm, as recommended by the norm. The test setup scheme is illustrated in Figure A.32.

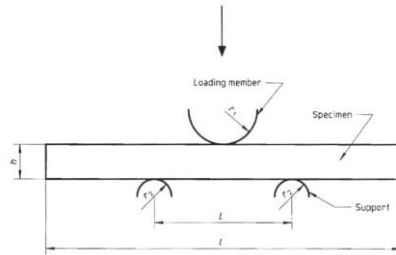


Figure A.32: Test setup scheme for interlaminar shear tests [159].

With respect to the instrumentation, the force was measured by a 50 kN force transducer model TC4 from AEP transducers and the vertical displacement was recorded by the Suzpecar press. All the data were registered automatically by an HBM MGCplus data acquisition system at a sampling rate of 50 Hz, and the instruments had a measuring error under 1%. The loading machine and test arrangement are shown in Figure A.33 and Figure A.34.



Figure A.33: Test setup configuration for interlaminar shear tests.



Figure A.34: Loading and support arrangement for interlaminar shear tests.

The apparent interlaminar shear strength, τ , was determined using the following equation specified in the standard:

$$\tau = \frac{3}{4} \cdot \frac{F}{b \cdot h} \quad (\text{A5.1})$$

where F is the failure or maximum load, b is the width of the test specimen, and h is the thickness of the test specimen.

A.5.3. Results

Before testing commenced, the width and thickness of each specimen was measured at its mid-point using a micrometer with a precision of 0.01 mm and then the specimen to be tested was placed with the unmachined, flat face on the round supports.

All coupons failed in an acceptable interlaminar shear failure mode due to a single shear delamination plane that appeared at the median layer near the non-woven, multi-directional continuous fiber strand mat. After a maximum load value, failure planes continued to develop in the adjacent matrix layers of the lay-up system, leading to a multiple shear crack failure mode as shown in Figure A.35.



Figure A.35: Single shear and multiple shear interlaminar failure modes [159].

There were no unacceptable modes of failure from mixed, plastic or non-shear causes. The captured moment of a single shear failure is depicted in Figure A.36 and a side-view of all the tested coupons is presented alongside in Figure A.37.

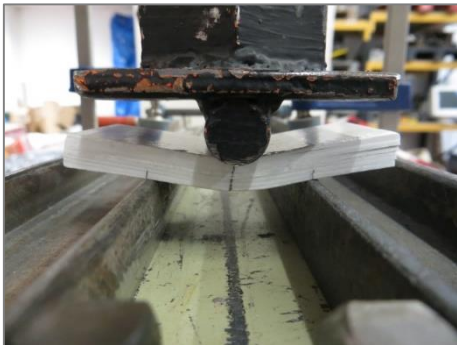


Figure A.36: Interlaminar single shear failure at the right end of a GFRP web specimen.



Figure A.37: Lateral view of the interlaminar shear failure of all coupons.

The experimental load-midspan deflection charts registered for specimens IL1 to IL6 are displayed in Figure A.38. All shear responses can be divided in three parts: a first nonlinear part (up to ~2 kN) characterized by the settling of the load-application system which does not reflect a nonlinear behavior of the composite material; a second, linear part (between 2 and ~11 kN) that lasted until the first interlaminar shear failure of the specimens; and finally, a third part where multiple interlaminar shear cracks started to develop in adjacent layers. The maximum load measured in all tests was used to calculate the interlaminar shear strength from the equation mentioned before.

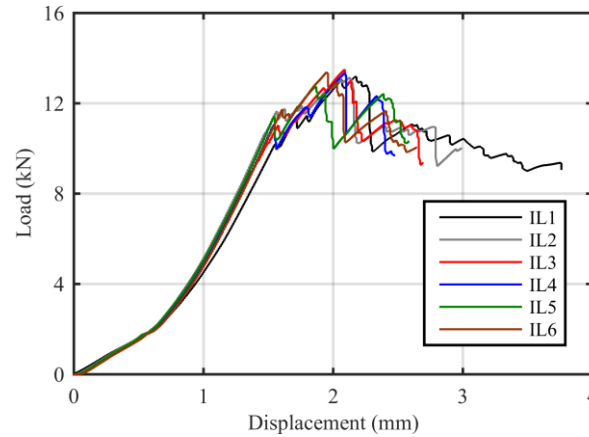


Figure A.38: Load-midspan displacement curves of the interlaminar shear tests.

Based on the experimental data registered, the following interlaminar shear strength values were obtained for the GFRP pultruded profile specimens. The mean value, standard deviation (SD), coefficient of variation (CV) and 95% confidence interval (CI) were also evaluated according to ISO 2602:1980 and are reported Table A.5.

Table A.5: Main results and statistical interpretation of the interlaminar shear tests.

Specimen	Dimensions		F (kN)	τ (MPa)
	b (mm)	h (mm)		
IL1	39.88	7.92	13.18	31.30
IL2	40.60	7.95	13.13	30.51
IL3	39.74	7.94	13.50	32.09
IL4	40.11	7.94	13.37	31.49
IL5	39.78	7.93	12.72	30.24
IL6	40.75	7.92	13.40	31.14
			Mean	31.13
			SD	0.67
			CV	2.2%
			CI	31.13 ± 0.70

Thus, the average value of the interlaminar shear strength to be used in analytical and numerical simulations is 31.13 MPa, which is higher than the value specified for the profiles by EN 13706-3:2002 for E17 grade structural profiles. Even so, it must be reminded that the precision of this test method is not well known.

A.6. In-plane shear strength characterization tests

A.6.1. Scope and principle

The experimental procedure and results of the in-plane shear strength characterization tests performed on GFRP profile coupons is treated in the following. The test method used herein was adapted from the ASTM D 3846-08 standard [160] since the European EN ISO 14129:1997 $\pm 45^\circ$ tensile test method covers only composites with continuously aligned fiber reinforcements. The in-plane shear strength is a key factor in the failure of GFRP members at web-flange junctions, subjected to combined flexural and shear loads.

In the standard employed, the in-plane shear strength is defined as the shear strength at rupture in which the plane of fracture is located along the longitudinal axis of a specimen, between two centrally positioned notches machined halfway through its thickness on opposing faces.

A.6.2. Testing procedure

The in-plane shear strength is measured by applying a compressive load to a notched specimen of uniform width. Because the specified standard supporting jig is the same as the one used in compressive strength characterization tests, the fixture previously designed by the author on the recommendations of ISO 14126:1999 was used once more.

A number of 5 specimens were prepared for the characterization tests and named IP1 to IP5. The specimens were extracted from the web of a GFRP profile, in the lengthwise direction, and had the following nominal dimensions: 125 mm in length, 15 mm in width and an inherent thickness of 8 mm. Two parallel cuts (1.5 mm wide), one on each opposite face of the specimen and 8 mm apart, were sawed across the entire width of the specimen and centrally located along its length. The cuts were made sufficiently deep to sever the center plane of the reinforcement located midway between the two faces of the coupon. Gripping distances were set to 50 mm as for the compressive tests.

The nominal dimensions and sampling area from the GFRP profile are illustrated in Figure A.39. Specimens IP1 to IP5 prior to testing are presented in Figure A.40.

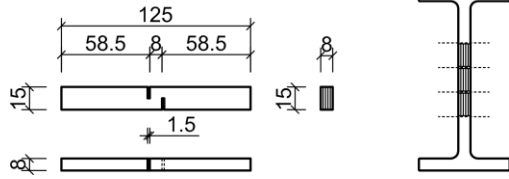


Figure A.39: Coupon nominal dimensions and sampling area for in-plane shear tests (mm).

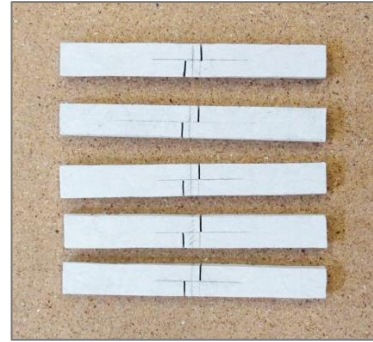


Figure A.40: GFRP profile coupons used for in-plane shear characterization tests.

At start, each specimen was measured with a micrometer that has a precision of 0.01 mm and then mounted in an upright position in the steel supporting fixture. The force was applied then monotonically by an electromechanical Suzpecar press under the displacement control method at a standard specified speed of 1.3 mm/min.

Regarding the instrumentation, the force was measured by a 50 kN force transducer model TC4 from AEP transducers and the vertical displacement was recorded by the Suzpecar press. All the data were registered automatically by an HBM MGCplus data acquisition system at a sampling rate of 50 Hz, and the instruments had a measuring error under 1%. The test setup and loading jig are shown in Figure A.41 and Figure A.42.



Figure A.41: Test setup configuration for in-plane shear tests.

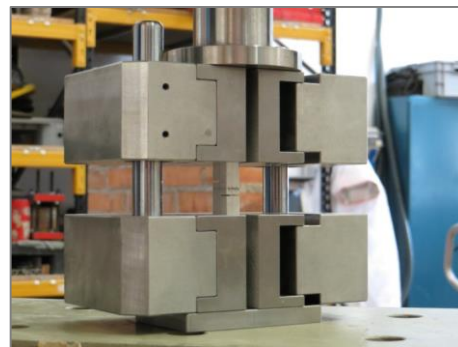


Figure A.42: Loading jig and specimen for in-plane shear tests.

The in-plane shear strength, τ , was determined using the following equation specified in the norm:

$$\tau = \frac{F}{w \cdot l} \quad (\text{A6.1})$$

where F is the failure or maximum load, w is the width of the test specimen, and l is the length of the failed (sheared) area which has to be measured with respect to either half of the ruptured specimen.

A.6.3. Results

All coupons failed in an acceptable in-plane shear failure mode due to a single shear failure plane that developed at the center. The captured moment of a single shear failure is depicted in Figure A.43 and an example of a ruptured tested coupon is presented alongside in Figure A.44. It is noticeable that the sheared surface is flat so in consequence the standard's formulation can be correctly applied.

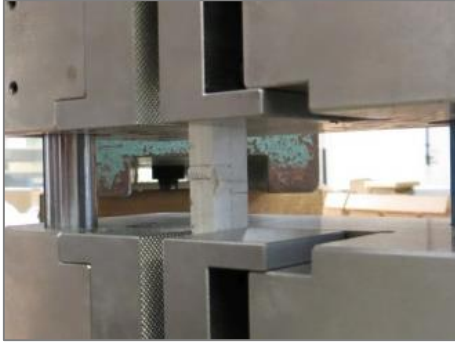


Figure A.43: In-plane shear failure of a GFRP specimen.

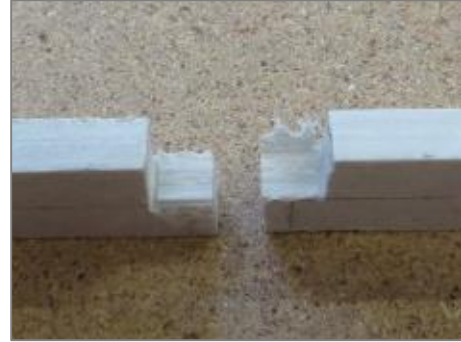


Figure A.44: Post-failure image of a ruptured GFRP specimen.

The experimental load-displacement chart registered for specimens IP1 to IP5 is displayed below in Figure A.45. Shear responses can be divided in two parts: first a nonlinear part up to 0.2 kN characterized by the settling of the load-application system, which does not reflect a nonlinear behavior of the composite material, and then a second, linear part, until shear failure occurred. The maximum load measured in all tests was used to calculate the in-plane shear strength.

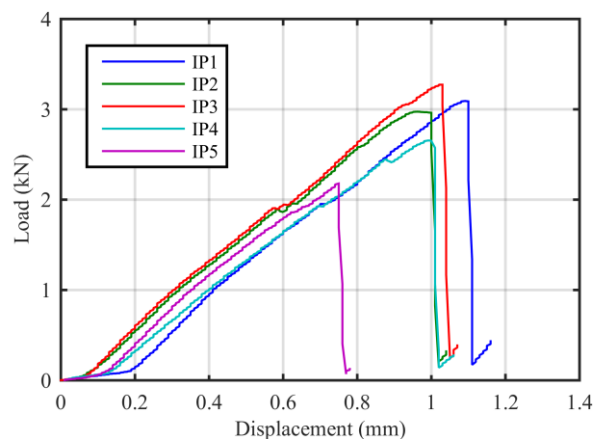


Figure A.45: Load-displacement curves of the in-plane shear tests.

Based on the experimental data registered, the following in-plane shear strength values were obtained for the GFRP pultruded profile specimens. The mean value, standard deviation (SD), coefficient of variation (CV) and 95% confidence interval (CI) were also evaluated according to ISO 2602:1980 and are reported together with the other properties in Table A.6.

Table A.6: Main results and statistical interpretation of the in-plane shear tests.

Specimen	Dimensions		F (kN)	τ (MPa)
	w (mm)	l (mm)		
IP1	7.33	7.92	3.09	53.28
IP2	7.89	7.92	2.97	47.59
IP3	7.84	7.94	3.27	52.58
IP4	6.69	7.93	2.65	50.06
IP5	6.65	7.87	2.18	41.64
			Mean	49.03
			SD	4.70
			CV	9.6%
			CI	49.03 ± 5.84

In conclusion, the average value of the in-plane shear strength to be used in analytical and numerical simulations is 49.03 MPa, which is higher than the value specified for the profiles by the manufacturer and 57% higher than the interlaminar shear strength that was determined previously for the same product. European Norm EN 13706-3:2002 does not specify a minimum value for this particular mechanical property as it does for others.

Obtaining a reliable design value of the in-plane shear strength of inhomogeneous GFRP pultruded profiles remains a difficult challenge that demands future research and standardized testing methods.

A.7. Full-section characterization tests

A.7.1. Scope and principle

The experimental procedure and results of the full-section characterization tests performed on the GFRP profiles employed in the hybrid beam designs are reported below. The method used for determining the effective flexural and shear stiffness properties was adopted from the informative Annex G (method A) of European Standard EN 13706-2:2002 [15] which is suitable for symmetrical thin walled pultruded profiles.

It should be noted that due to the lay-up configuration of the profile in webs and flanges, results differ between coupon tests and full-section tests. Also it is not possible to predict any of the values from data obtained from a different test mode or test direction.

As test principle, a pultruded profile of regular cross-section is repeatedly loaded (elastically) as a simple beam in three-point flexure at a number of different span lengths. The shear and bending contributions to the overall beam deflection vary with each test span. During the iterative procedure, the force applied to the specimen and the resulting deflection are measured.

A.7.2. Testing procedure

From the methods available in the standard, method A from Annex G was preferred over the one in Annex D since it can lead to obtaining both flexural and shear moduli, and not just a flexural modulus that compensates for angular deformations. The tested profiles were loaded in a decreasing series of span lengths, at a set strain rate and to a set strain level, as illustrated in the following scheme in Figure A.46.

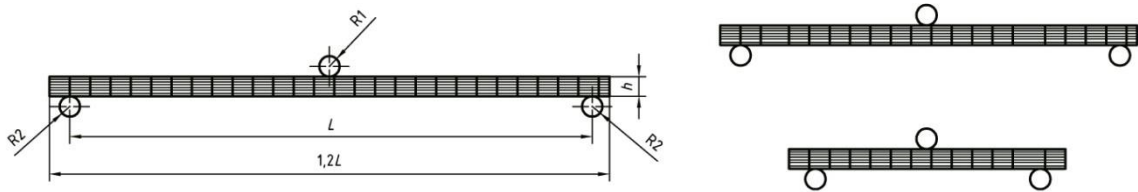


Figure A.46: Loading configuration for method A [15].

Three GFRP profiles were selected and measured with a micrometer in order to determine the second moment of inertia and cross-sectional area of their sections. The length was then established based on the fact that it has to be 1.2 times greater than the testing span which in its turn has to be close to the critical length where the shear deformation contributes about 12% to the total deflection.

A number of 8 spans were chosen varying from 2500 mm to 1800 mm with decrements of 100 mm, considering that the critical length was estimated to around 2300 mm for this particular shape and material. Each specimen was supported on two steel cylinders with a diameter of 120 mm and subjected to bending by a loading head with a diameter of 50 mm, until a maximum deflection value was reached equal to the test span divided by 200. The loading apparatus was set to the largest span of the picked range and after each subsequent test the span was decreased and the specimen's length was adjusted by removing equal lengths from both ends of the profile so as to keep the same midspan position. Pictures of the test setup are presented below in Figure A.47 and A.48 for two different span lengths.



Figure A.47: Profile bending setup for a test span of 2500 mm.

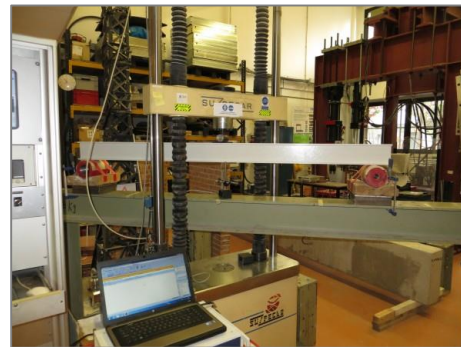


Figure A.48: Profile bending setup for a test span of 1800 mm.

All specimens were loaded over a constant time period of 60 seconds taking into account the maximum deflection value to be attained. The force was applied by a Suzpecar universal testing machine and measured by a 50 kN TC4 force transducer from AEP transducers. The midspan displacement was registered by an HBM WA20 LVDT with a measuring range of 20 mm. Data were recorded automatically by an HBM MGCplus data acquisition system, at a sampling rate of 50 Hz. All instruments had a measuring error under 1%.

The effective values of the mechanical properties were estimated using a linear regression analysis of the three-point bending equation which characterizes the deflection test shown in Figure A.49.

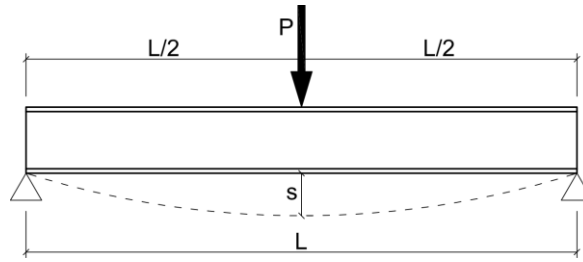


Figure A.49: Flexural test scheme used for determining the elastic properties of the GFRP profiles.

The deflection of a simply supported beam with a concentrated center load can be modeled by the following equation:

$$s = \frac{P \cdot L^3}{48 \cdot E_{eff} \cdot I} + \frac{P \cdot L}{4 \cdot G_{eff} \cdot \kappa \cdot A} \quad (A7.1)$$

where P is the applied load; L – beam span; E_{eff} – effective longitudinal modulus of elasticity; I – moment of inertia about the axis being tested; G_{eff} – effective shear modulus; κ – Timoshenko shear coefficient; and A – cross section area. The sheared area $\kappa \cdot A$ was approximated as equal to the web area of the profile A_w .

By rearranging the previous equation into a slope-intercept form and by using the method of superposition to split it into separate terms, the effective moduli of the GFRP profile could be obtained. Firstly, the flexural stiffness D was calculated from the slope of the linear trend line of the data points of L^2 vs. $s/P \cdot L$, and then the effective modulus of elasticity E_{eff} was obtained from D/I . Secondly, the shear stiffness Q was calculated from the slope of the linear trend line of the data points of $1/L^2$ vs. $s/P \cdot L^3$, and then the effective shear modulus G_{eff} was determined from Q/A_w .

As a double-check, the slope of L^2 vs. $s/P \cdot L$ was verified with the intercept of $1/L^2$ vs. $s/P \cdot L^3$, and the intercept of L^2 vs. $s/P \cdot L$ was compared with the slope of $1/L^2$ vs. $s/P \cdot L^3$.

A.7.3. Results

All results were considered valid since there was no local failure or loss of stability phenomenon observed. The next cumulative chart in Figure A.50 presents the flexural responses of the three tested specimens in terms of load-midspan deflection values, ranging from the maximum test span conditions to the minimum.

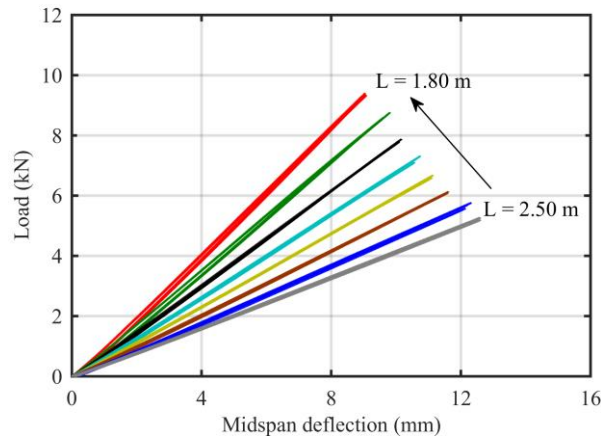


Figure A.50: Load-midspan deflection curves of the tested GFRP profiles.

There's a clear linear-elastic behavior exhibited by each one of the specimens both in the loading and unloading stage, under all test span conditions. Furthermore, their flexural responses are overlapped thus proving an adequate repeatability of the experiments. Individual values of L^2 , $s/P \cdot L$, $1/L^2$ and $s/P \cdot L^3$ are reported in Tables A.7-9 for each GFRP profile specimen. So as to eliminate any errors in the data that may have had been produced by the initial settlement of the test setup configuration, the values were calculated for a midspan deflection value s between $L/500$ and $L/200$.

Table A.7: Registered and calculated data values for GFRP profile P1.

L (mm)	s (mm)	P (kN)	L^2 (m ²)	$s/P \cdot L$ (MN ⁻¹)	$1/L^2$ (m ⁻²)	$s/P \cdot L^3$ (MN ⁻¹ ·m ⁻²)
1800	3.60	3.62	3.240	0.525	0.309	0.162
1800	9.00	9.33				
1900	3.80	3.34	3.610	0.582	0.277	0.161
1900	9.50	8.49				
2000	4.00	2.99	4.000	0.631	0.250	0.158
2000	10.00	7.75				
2100	4.20	2.78	4.410	0.687	0.227	0.156
2100	10.50	7.15				
2200	4.40	2.55	4.840	0.753	0.207	0.156
2200	11.00	6.54				
2300	4.60	2.36	5.290	0.808	0.189	0.153
2300	11.50	6.07				
2400	4.80	2.11	5.760	0.883	0.174	0.153
2400	12.00	5.51				
2500	5.00	2.05	6.250	0.943	0.160	0.151
2500	12.50	5.23				

Table A.8: Registered and calculated data values for GFRP profile P2.

L (mm)	s (mm)	P (kN)	L^2 (m ²)	$s/P \cdot L$ (MN ⁻¹)	$1/L^2$ (m ⁻²)	$s/P \cdot L^3$ (MN ⁻¹ ·m ⁻²)
1800	3.60	3.64	3.240	0.535	0.309	0.165
1800	9.00	9.24				
1900	3.80	3.34	3.610	0.582	0.277	0.161
1900	9.50	8.50				
2000	4.00	3.04	4.000	0.642	0.250	0.161
2000	10.00	7.71				
2100	4.20	2.78	4.410	0.688	0.227	0.156
2100	10.50	7.14				
2200	4.40	2.56	4.840	0.744	0.207	0.154
2200	11.00	6.60				
2300	4.60	2.36	5.290	0.817	0.189	0.154
2300	11.50	6.04				
2400	4.80	2.18	5.760	0.875	0.174	0.152
2400	12.00	5.61				
2500	5.00	2.03	6.250	0.942	0.160	0.151
2500	12.50	5.22				

Table A.9: Registered and calculated data values for GFRP profile P3.

L (mm)	s (mm)	P (kN)	L^2 (m ²)	$s/P \cdot L$ (1/MN)	$1/L^2$ (1/m ²)	$s/P \cdot L^3$ (1/MN·m ²)
1800	3.60	3.58	3.240	0.527	0.309	0.163
1800	9.00	9.28				
1900	3.80	3.32	3.610	0.581	0.277	0.161
1900	9.50	8.49				
2000	4.00	2.99	4.000	0.635	0.250	0.159
2000	10.00	7.72				
2100	4.20	2.74	4.410	0.696	0.227	0.158
2100	10.50	7.05				
2200	4.40	2.56	4.840	0.756	0.207	0.156
2200	11.00	6.53				
2300	4.60	2.37	5.290	0.816	0.189	0.154
2300	11.50	6.04				
2400	4.80	2.17	5.760	0.875	0.174	0.152
2400	12.00	5.60				
2500	5.00	2.02	6.250	0.958	0.160	0.153
2500	12.50	5.15				

The graphical representation of the tabular data is plotted in the following Figures A.51-56 together with the slope-intercept form of the fitting trend line equation and its corresponding coefficient of determination (R^2), for all three profiles. The high coefficients prove that the trendlines fit the statistical data very well: $R^2 > 0.999$ for the determination of E_{eff} and $R^2 > 0.96$ for the estimation of G_{eff} .

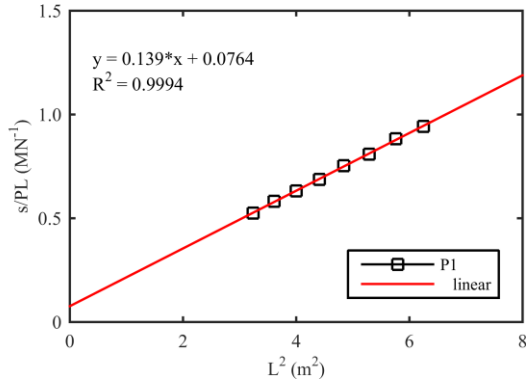


Figure A.51: Slope-intercept form for the evaluation of the effective flexural stiffness of P1.

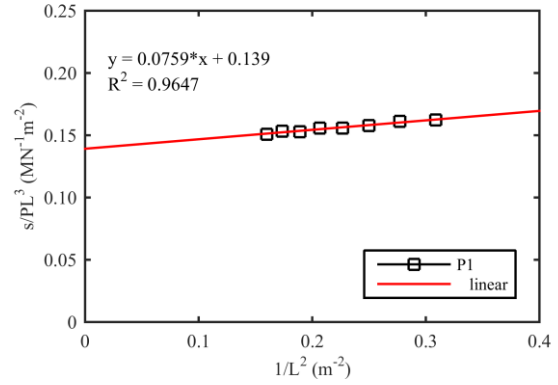


Figure A.52: Slope-intercept form for the evaluation of the effective shear stiffness of P1.

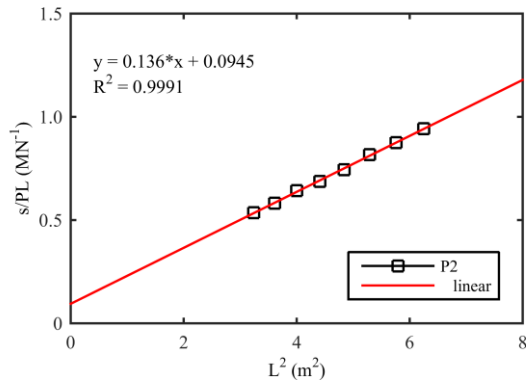


Figure A.53: Slope-intercept form for the evaluation of the effective flexural stiffness of P2.

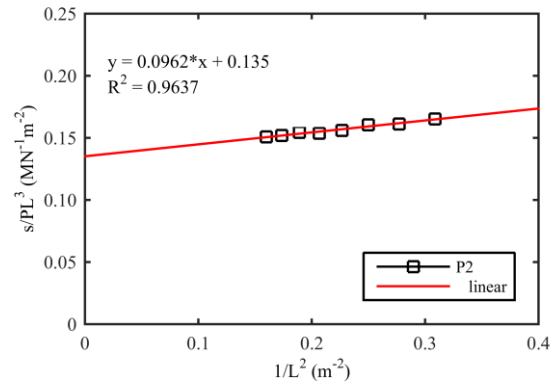


Figure A.54: Slope-intercept form for the evaluation of the effective shear stiffness of P2.

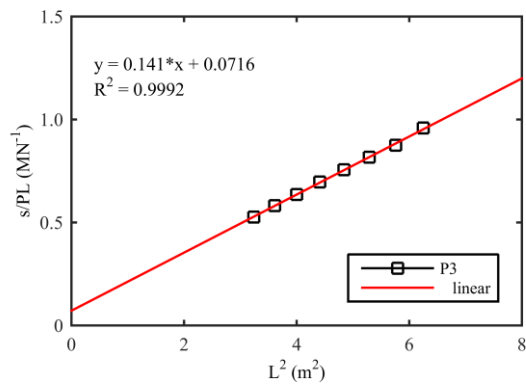


Figure A.55: Slope-intercept form for the evaluation of the effective flexural stiffness of P3.

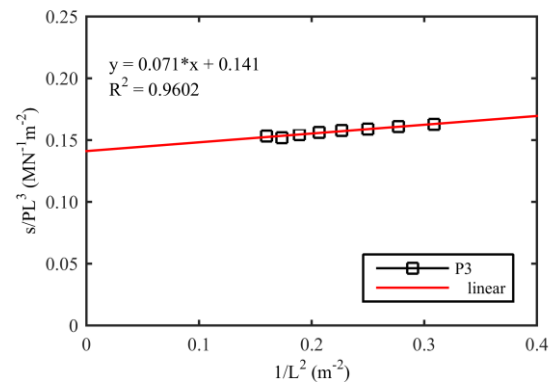


Figure A.56: Slope-intercept form for the evaluation of the effective shear stiffness of P3.

Based on the linear regression analysis of the experimental data, the following effective flexural and shear moduli were obtained for the three GFRP pultruded profile specimens. The mean value, standard deviation (SD), coefficient of variation (CV) and 95% confidence interval (CI) were also evaluated according to ISO 2602:1980 and are reported together with the other properties in Table A.10.

Table A.10: Main results and statistical interpretation of the full-section tests.

Specimen	L^2 vs. $s/P \cdot L$		$1/L^2$ vs. $s/P \cdot L^3$		E_{eff} (GPa)	G_{eff} (GPa)
	D	Q	D	Q		
	(kN·mm ²)	(N)	(kN·mm ²)	(N)		
P1	149.55	3.33	149.68	3.45	39.15	4.14
P2	149.90	3.33	149.42	3.43	39.24	4.13
P3	148.83	3.24	149.75	3.06	38.96	3.68
				Mean	39.11	3.98
				SD	0.14	0.26
				CV	0.4%	6.6%
				CI	0.35	0.65

Thus, the effective values to be used in analytical and numerical simulations are 39.11 GPa for flexural modulus and 3.98 GPa for shear modulus. The effective properties are higher than the values specified for the GFRP profiles by the manufacturer and closer to the values reported by the same source for GFRP bars. The average values are also greater than the ones specified in EN 13706-3:2002 for E17 grade structural profiles.

B

Additional experimental data

B.1. Introduction

The following appendix illustrates additional information regarding the instrumentation and configuration of the bending setups and presents in a comparative manner supplementary results gathered during the laboratory flexural tests. Results are included for the control/reference specimens as well as for the hybrid GFRP-concrete beams. The graphics complement the information in Chapter 3 and clarify some of the observations that were made.

B.2. Test setups

As commented before, in test setup I the beams were supported on elastomeric pads to prevent the occurrence of local crushing failure at the reaction points. The central vertical displacement of the pads was measured by linear potentiometers, and served to compensate the general deflections measured by the laser triangulation sensors. The average deformation behavior of a pair of elastomeric pads is displayed in Figure B.1.

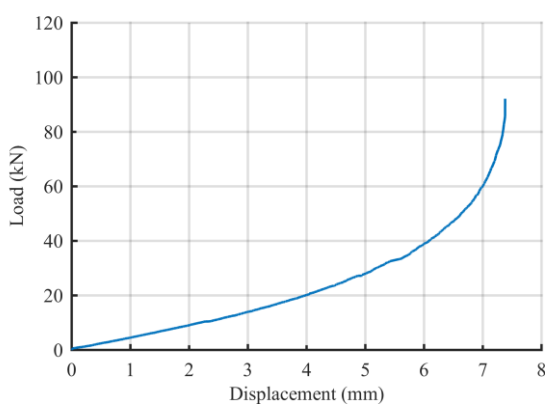
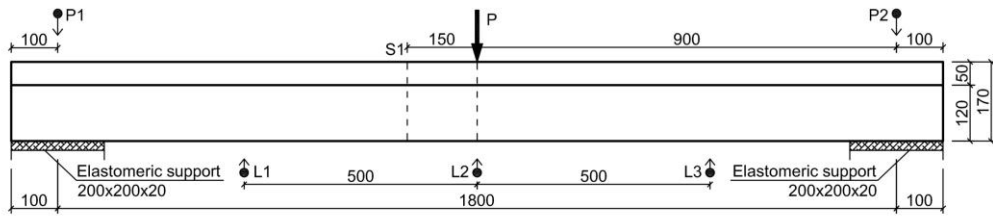


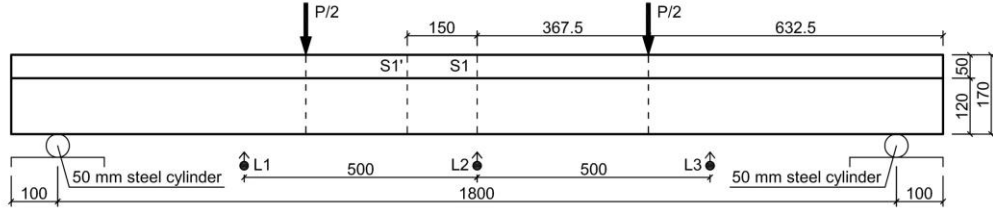
Figure B.1: Deformation behavior of elastomeric supports.

Previously not shown test setups of several reference specimens are depicted in Figure B.2.

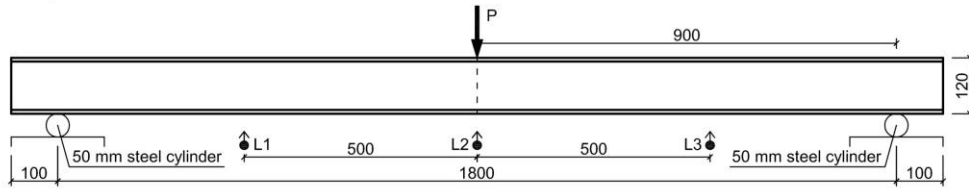
Test setup I - M0-RCB1



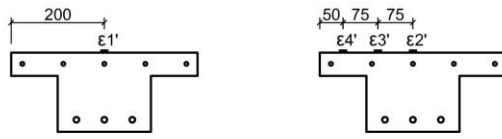
Test setup II - M0-RCB2



Test setup I - Profile 1



Section instrumentation



M0-RCB1 & M0-RCB2 - Section S1

M0-RCB2 - Section S1'

●→ displacement transducer
 — strain gauge

Figure B.2: Schematic of load arrangements and instrumentation of reference specimens (mm).

B.3. Reference specimens

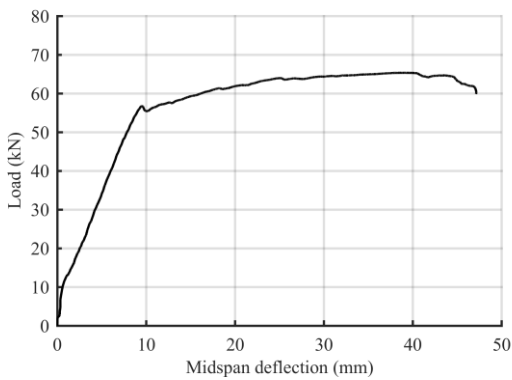


Figure B.3: Flexural behavior of M0-RCB1: load-midspan deflection curve.

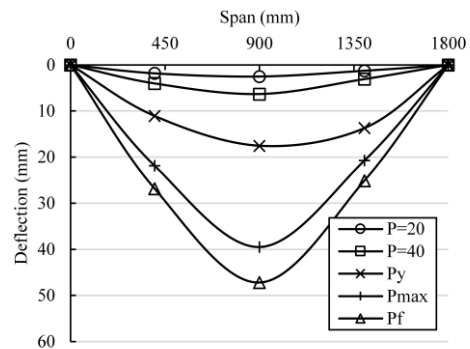


Figure B.4: Deflection profile of M0-RCB1 at different load levels (kN; P_y – yielding load; P_{max} – maximum load; P_f – final load).

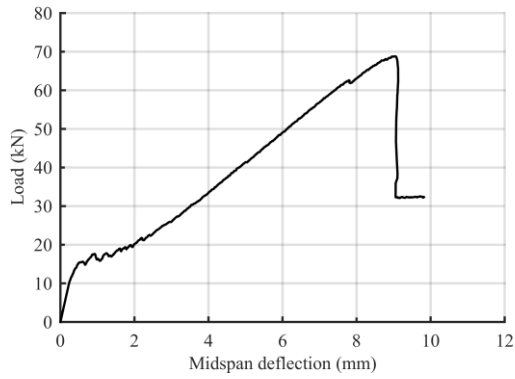


Figure B.5: Flexural behavior of M0-RCB2: load-midspan deflection curve.

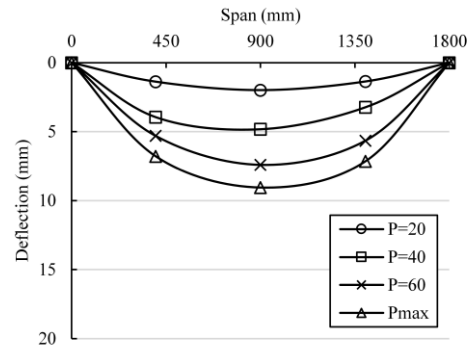


Figure B.6: Deflection profile of M0-RCB2 at different load levels (kN).

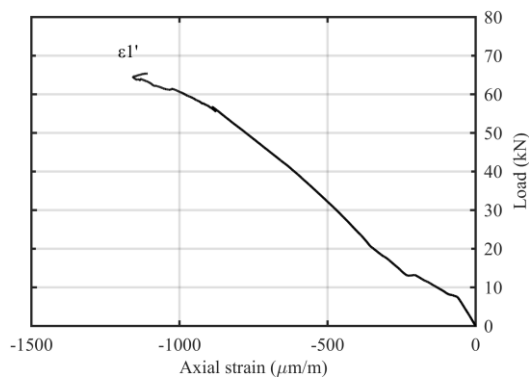


Figure B.7: Reference beam M0-RCB1: variation of axial compressive strain in section S1.

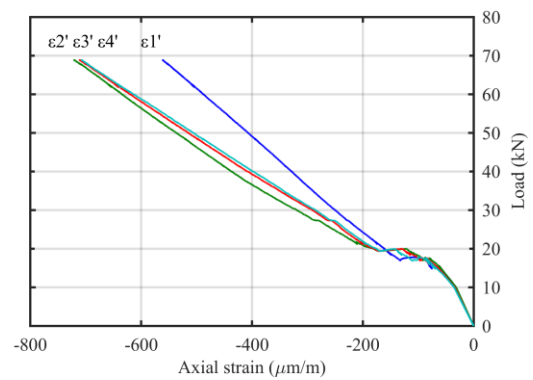


Figure B.8: Reference beam M0-RCB2: variation of axial compressive strains in section S1 and S1'.

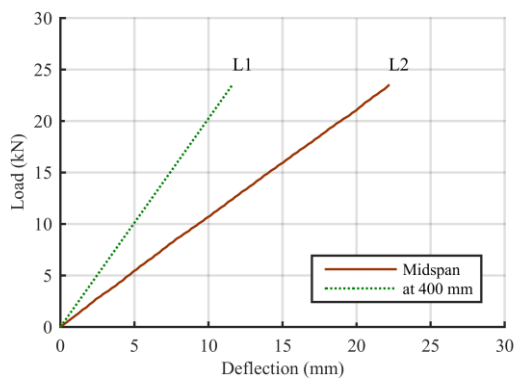


Figure B.9: Flexural behavior of reference beam Profile 1: load-midspan deflection curve.

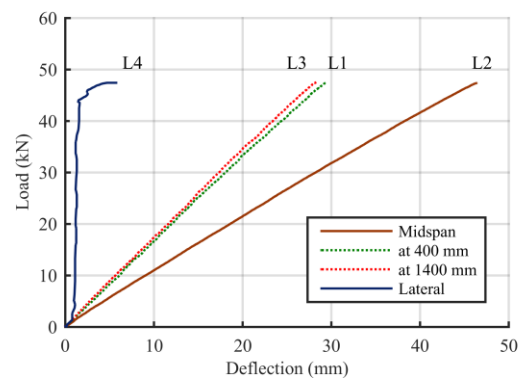


Figure B.10: Flexural behavior of reference beam Profile 2: load-midspan deflection curve.

Appendix B | Additional experimental data

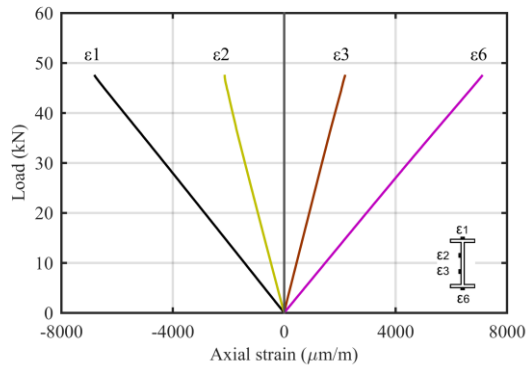


Figure B.11: Reference beam Profile 2: variation of axial strains in section S1.

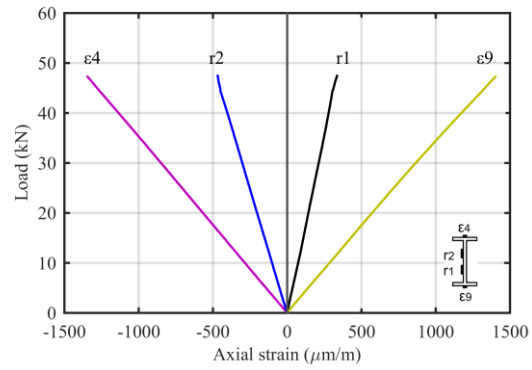


Figure B.12: Reference beam Profile 2: variation of axial strains in section S2.

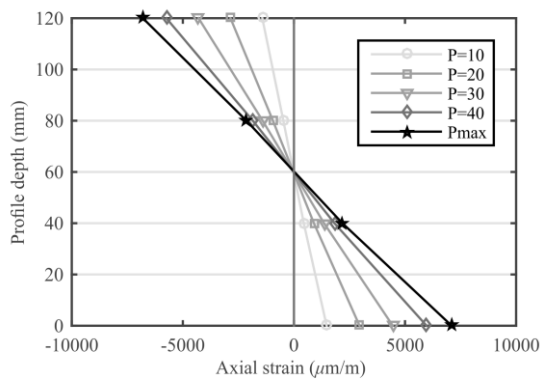


Figure B.13: Reference beam Profile 2: axial strain distribution at different load levels (kN), in section S1.

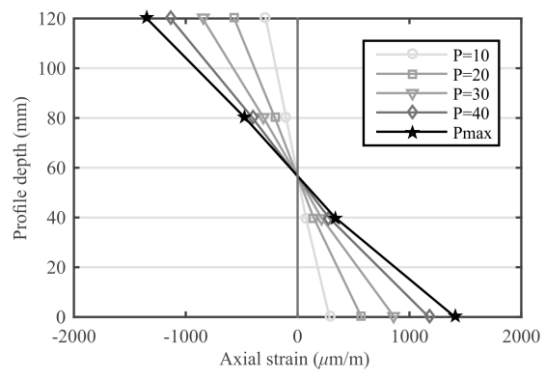


Figure B.14: Reference beam Profile 2: axial strain distribution at different load levels (kN), in section S2.

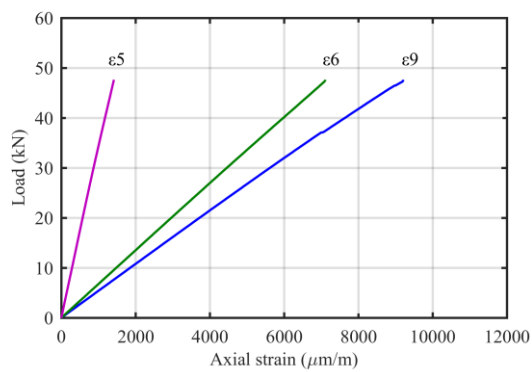


Figure B.15: Reference beam Profile 2: bottom flange axial strain variations.

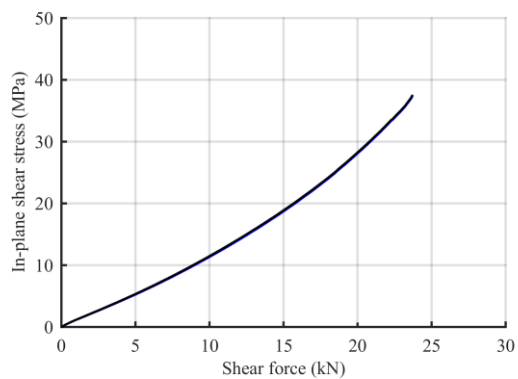


Figure B.16: Reference beam Profile 2: in-plane shear stress variation.

B.4. GFRP-concrete hybrid beams

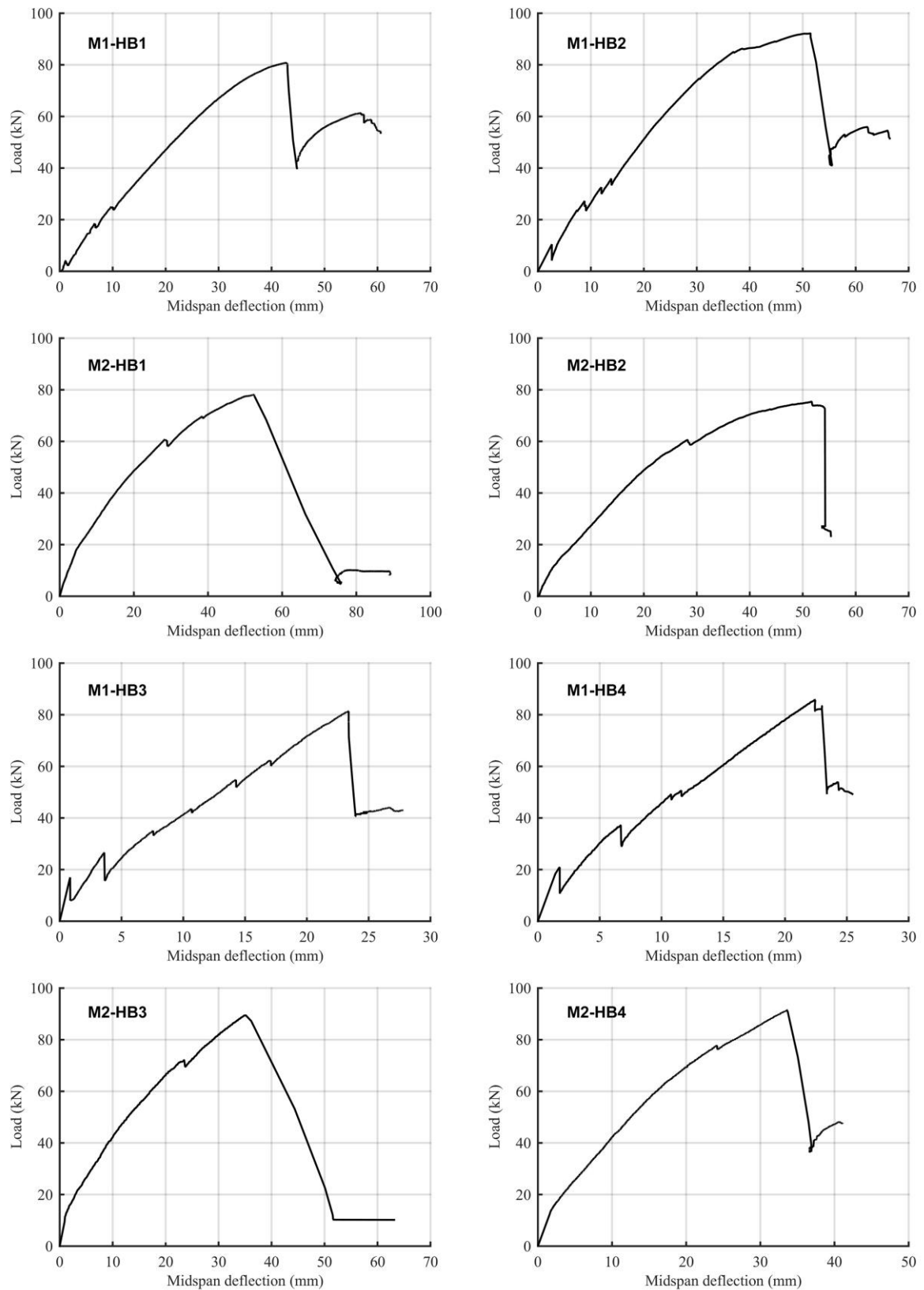


Figure B.17: Flexural behavior of hybrid beams: complete load-midspan deflection curves until final collapse.

Appendix B | Additional experimental data

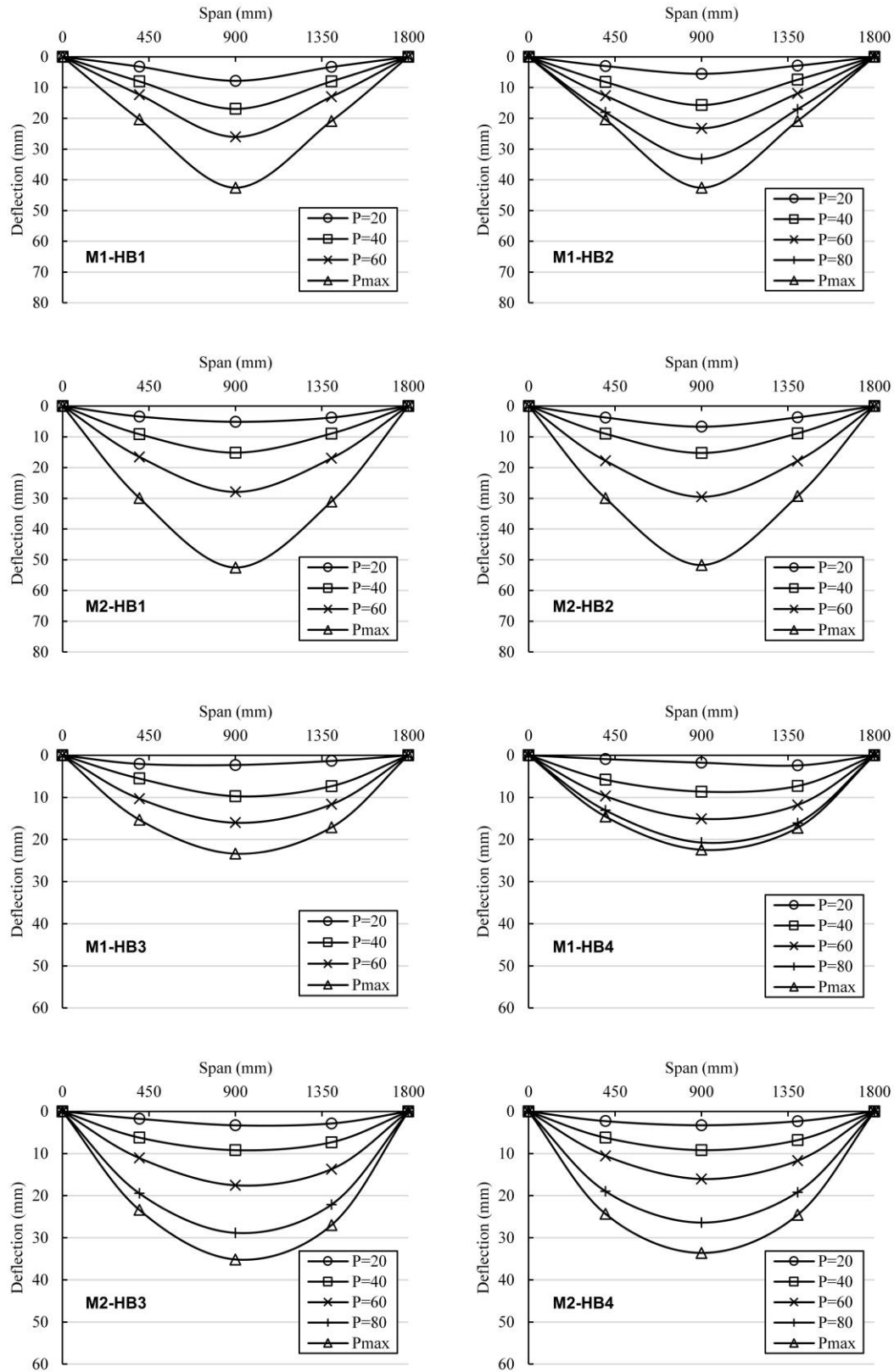


Figure B.18: Deflection profiles of hybrid beams at different load levels until failure (kN).

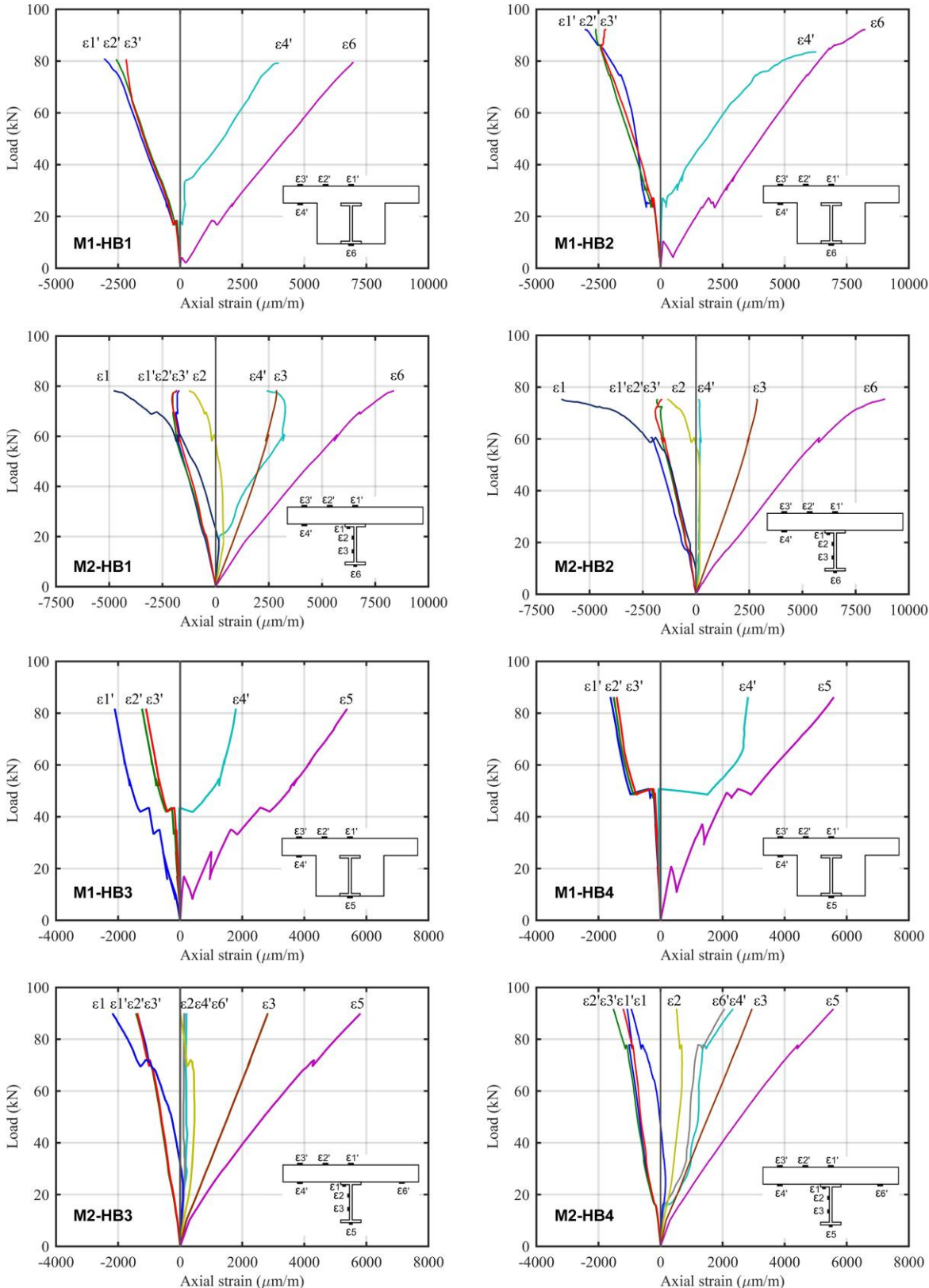


Figure B.19: Axial strain variations of hybrid beams in section S1 until failure.

Note: a few of the strain gauges especially on the concrete slab may have malfunctioned due to occurrence of cracks in their vicinity or due to debonding.

Appendix B | Additional experimental data

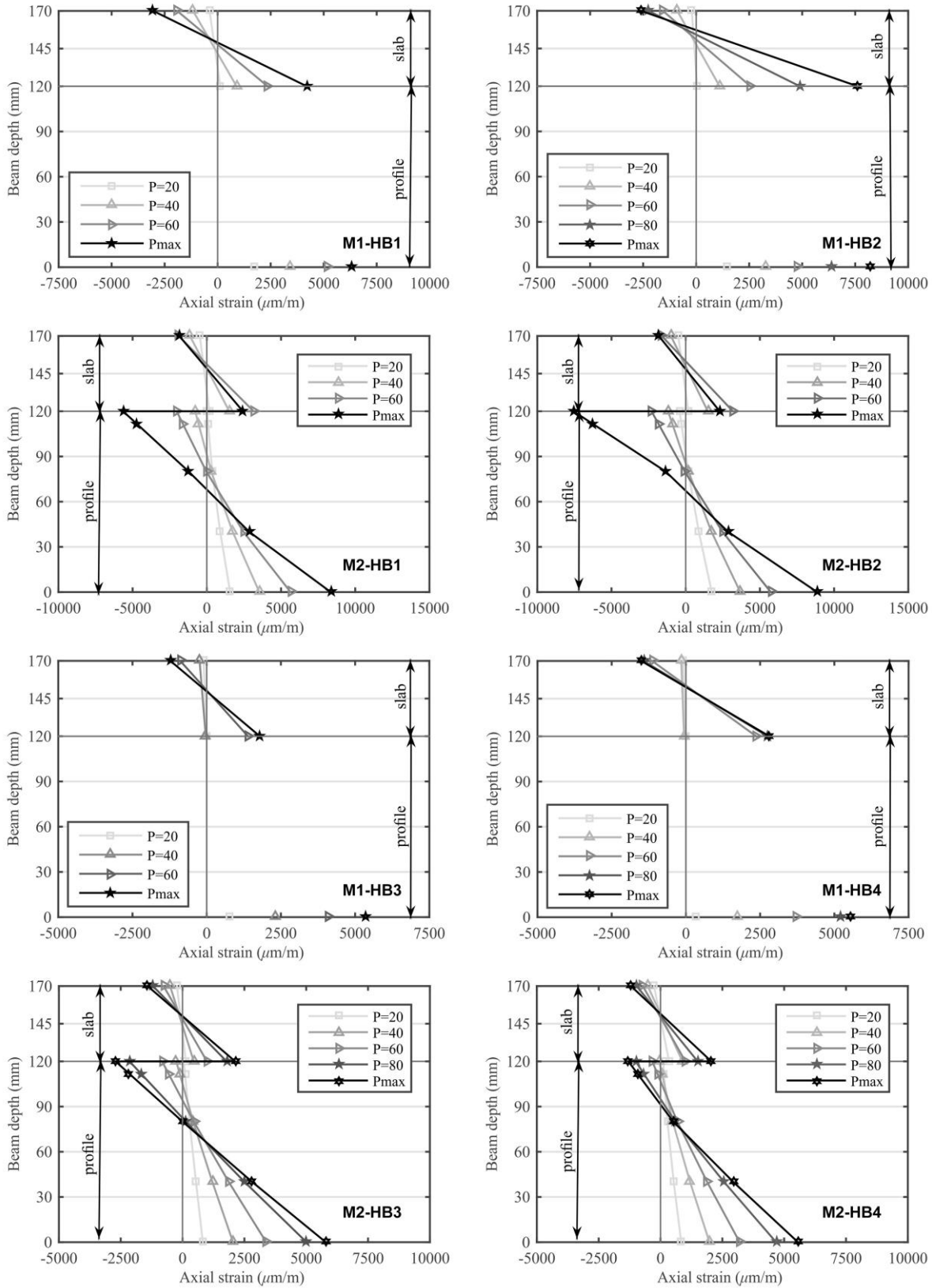


Figure B.20: Axial strain distributions of hybrid beams in section S1 at different load levels until failure (kN).

Note: in a couple of cases where the concrete tensile strain measurements were faulty (M2-HB2 and M2-HB3), their values were corrected considering the hypothesis that both the slab and the profile have the same curvature during bending.

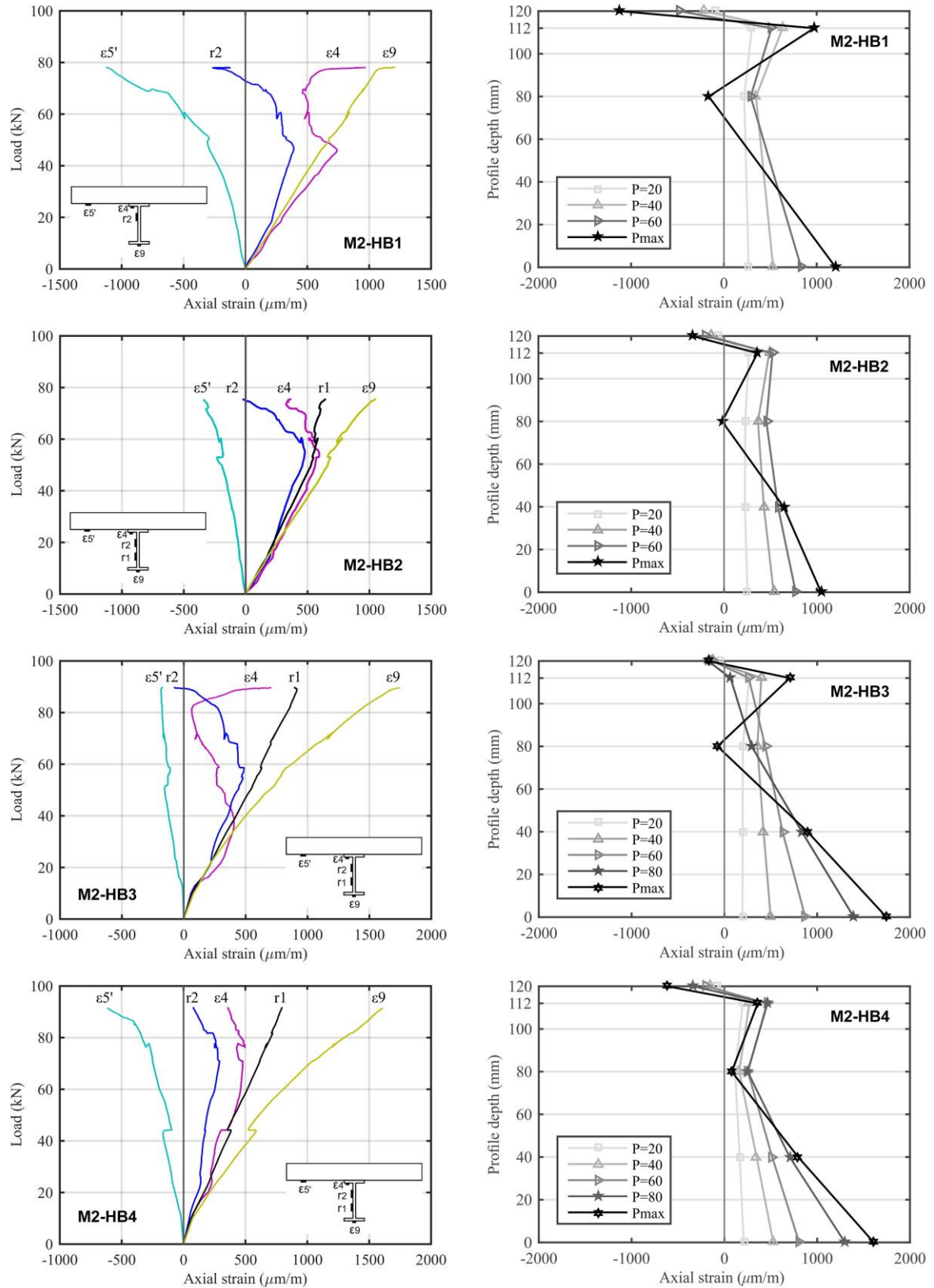


Figure B.21: Axial strain variations and axial strain distributions of the M2 hybrid beams in section S2 until failure (kN).

Note: a few of the strain gauges such as ϵ_5' or ϵ_4 may have malfunctioned in some cases due to occurrence of cracks or debonding.

Appendix B | Additional experimental data

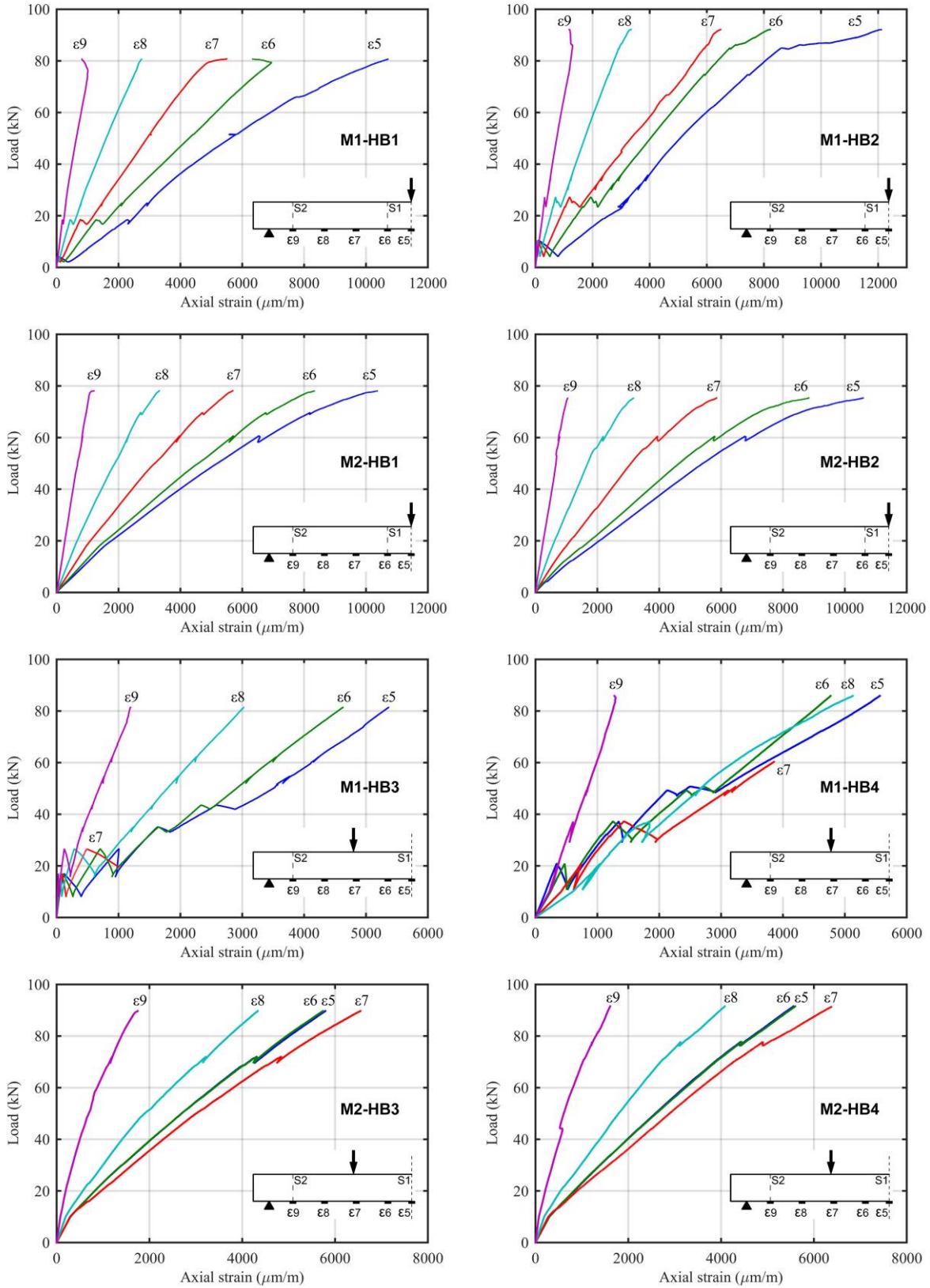


Figure B.22: Bottom flange axial strain variations of hybrid beams until failure.

Note: a couple of strain gauges placed on the bottom flange of M1-HB3 and M1-HB4 may have failed sooner due to debonding.

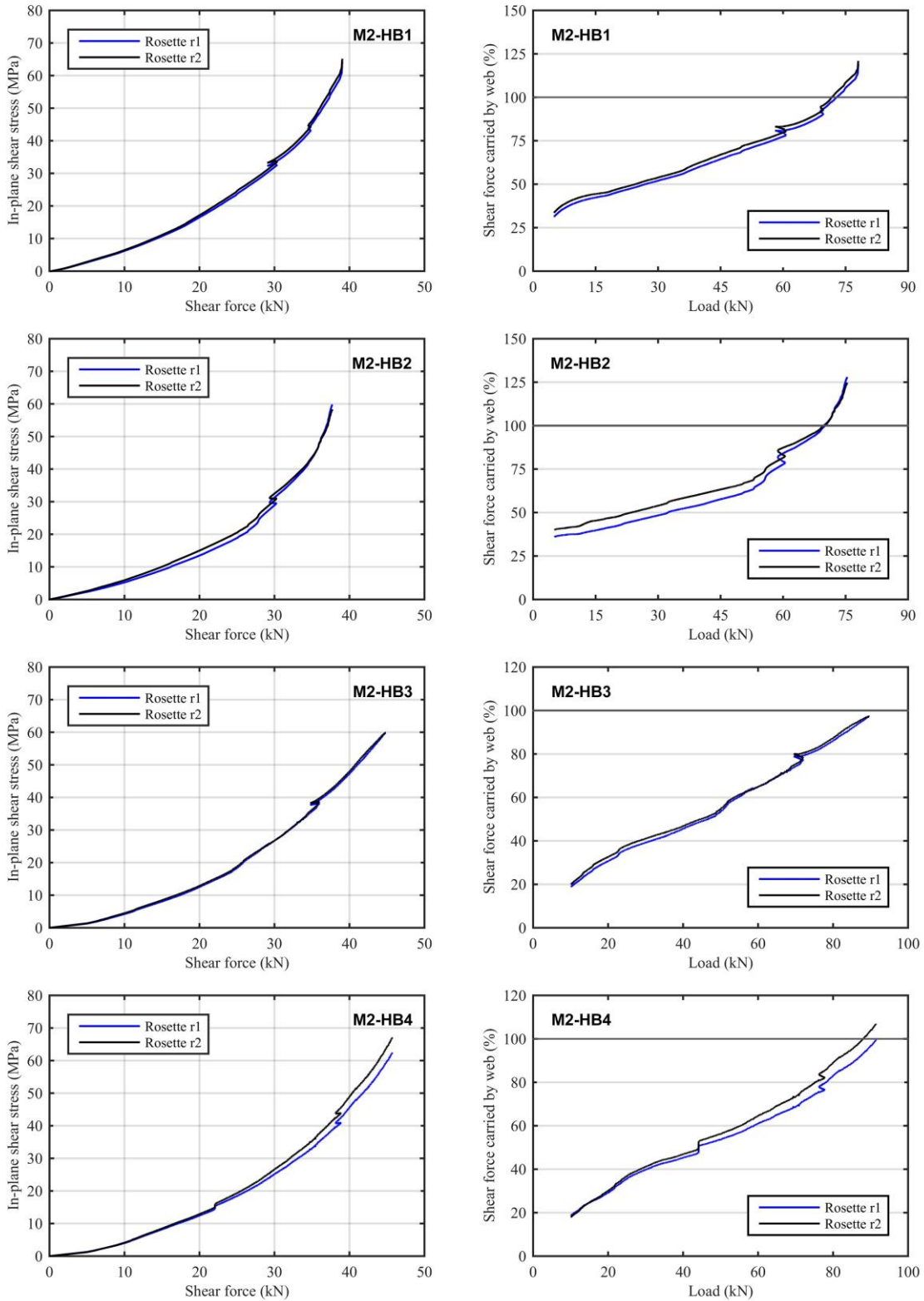


Figure B.23: In-plane shear stress variation and shear force percentile carried by the profile in function of the applied shear load or total load, for the M2 hybrid beams.

Note: the shear force percentile was computed considering a uniform shear stress distribution in the profile and that the entire shear load applied on the hybrid beam is carried just by the profile's web. These assumptions indicate why some of the percentiles reached at failure are above unity.

Appendix B | Additional experimental data

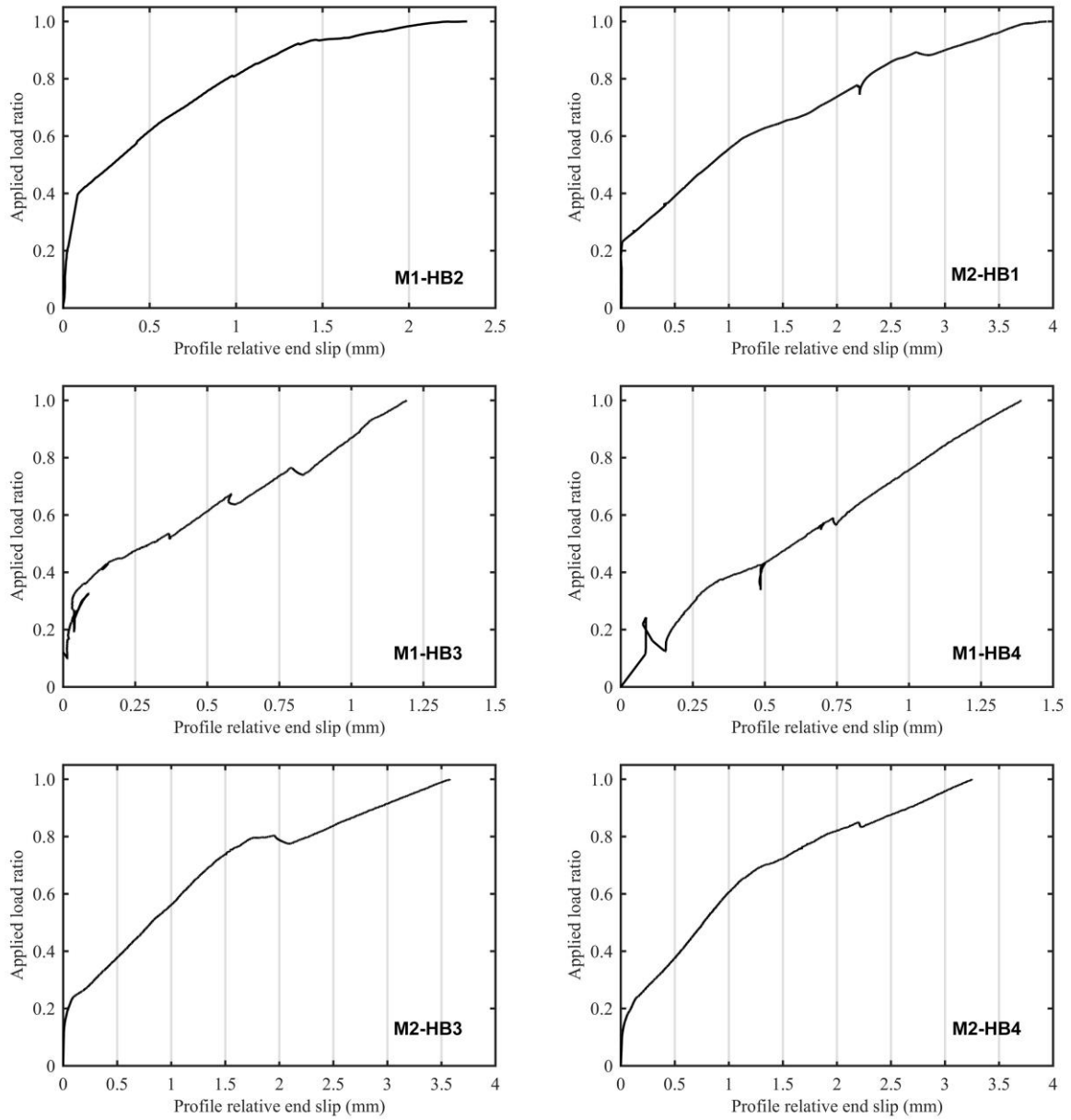


Figure B.24: Relative profile end slip variation of the hybrid beams in function of the applied load ratio, until failure.

Note: for hybrid beam M1-HB1 and M2-HB2 there were no valid slip measurements performed during the tests.

Additional analytical results

C.1. Introduction

Supplementary results obtained during the validation of the analytical expressions from Chapter 4 are included in the present appendix in the form of experimental-analytical comparative charts, for the two reference profiles and for all four model M2 hybrid beams used in the investigation. The plots accompany the information given in the cited chapter and justify some of the observations that were reported.

C.2. Validation of analytical results for reference profiles

The analytical prediction in the following graphics was performed for an applied force equal to the maximum load registered during the flexural tests.

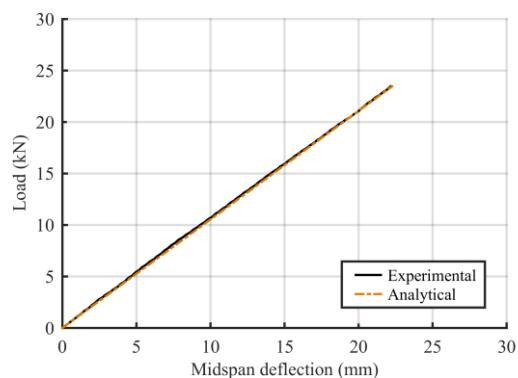


Figure C.1: Load-midspan deflection response of Profile 1: experimental and analytical curves.

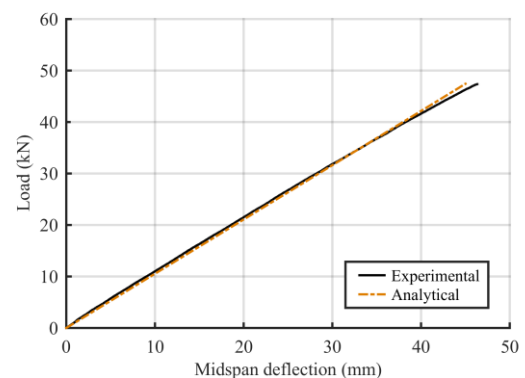


Figure C.2: Load-midspan deflection response of Profile 2: experimental and analytical curves.

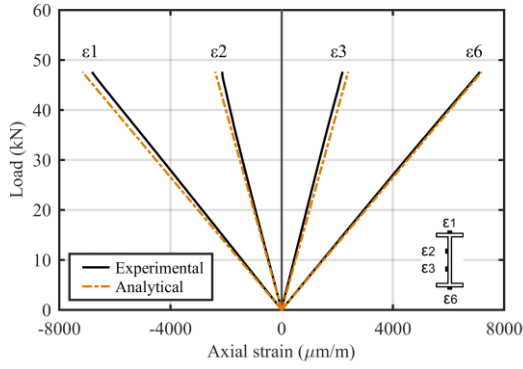


Figure C.3: Axial strain variations of Profile 2 in section S1: experimental and analytical curves.

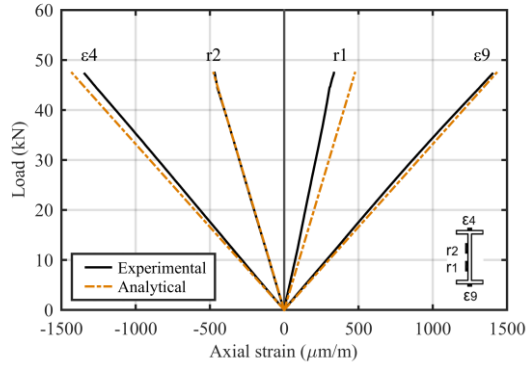


Figure C.4: Axial strain variations of Profile 2 in section S2: experimental and analytical curves.

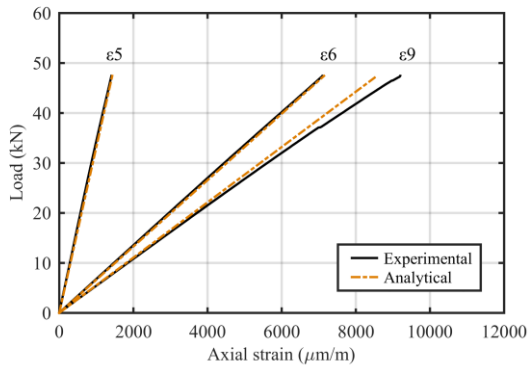


Figure C.5: Bottom flange axial strain variations of Profile 2: experimental and analytical curves.

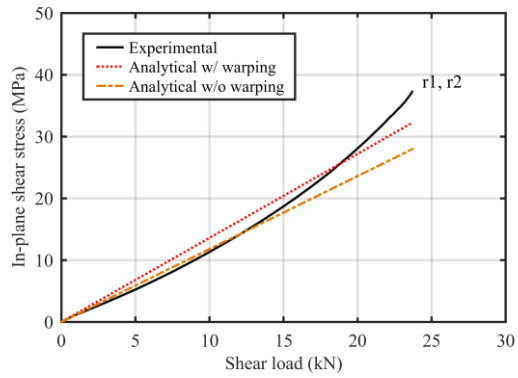


Figure C.6: In-plane shear stress variation in Profile 2, section S2, in function of the applied shear load: experimental and analytical curves with or without warping.

C.3. Validation of experimental campaign results

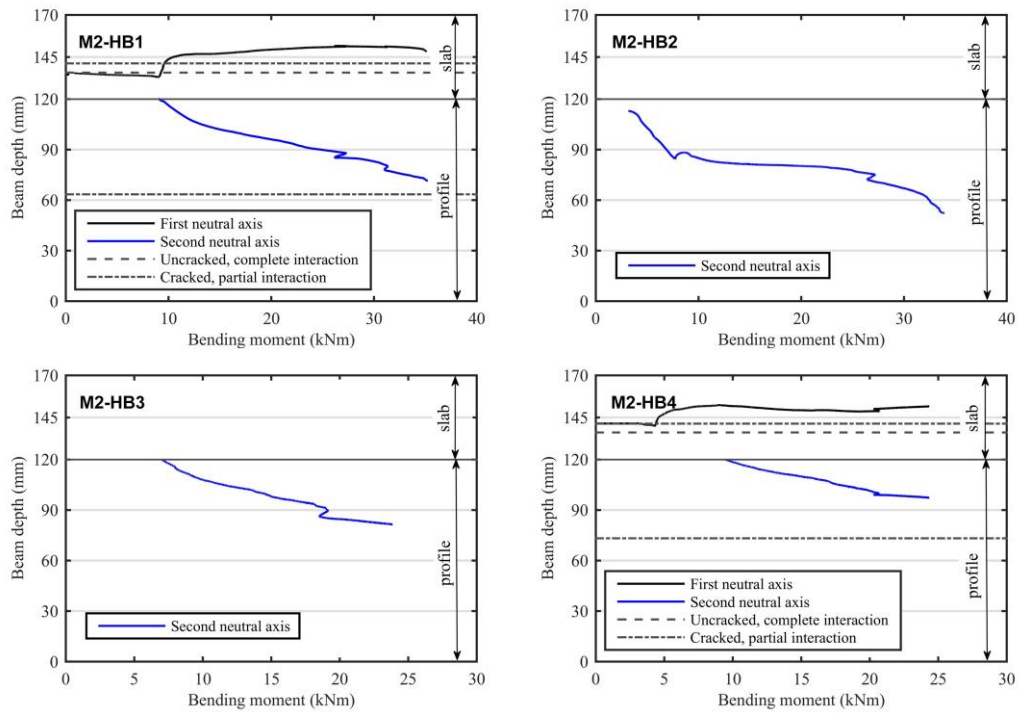


Figure C.7: Neutral axis depth variation in function of the applied load for hybrid beams M2 in section S1. Experimental curves and analytical predictions.

Note: a couple of strain gauge malfunctions explain the missing top neutral axis information for M2-HB2 and M2-HB3.

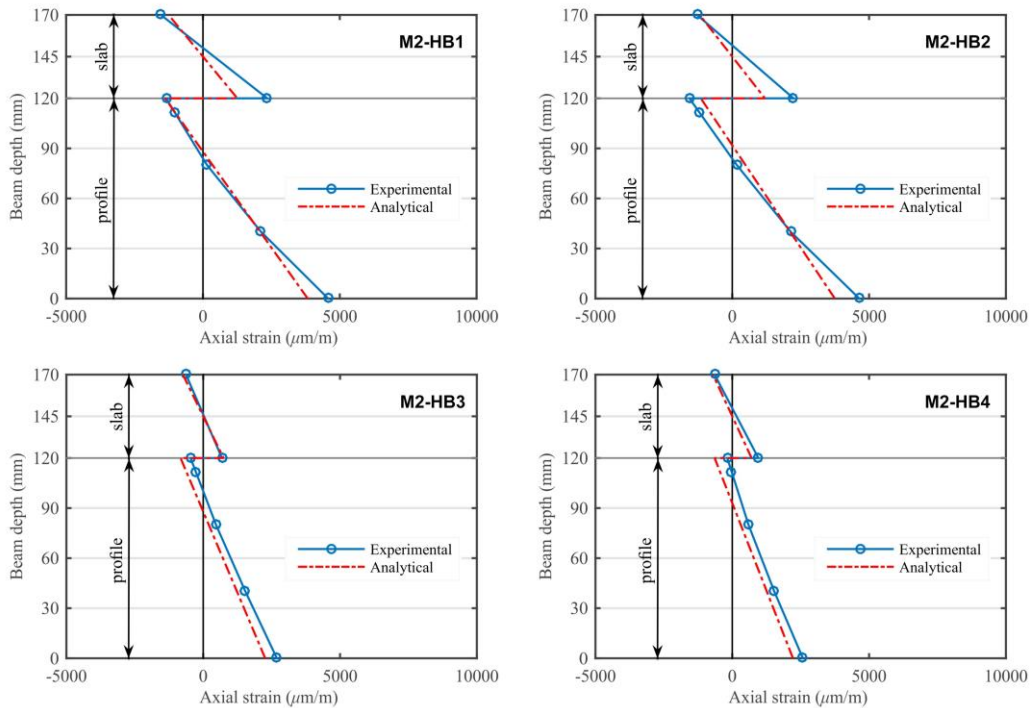


Figure C.8: Experimental and analytical axial strain distributions of hybrid beams M2 in section S1, at an intermediate load level of 50 kN.

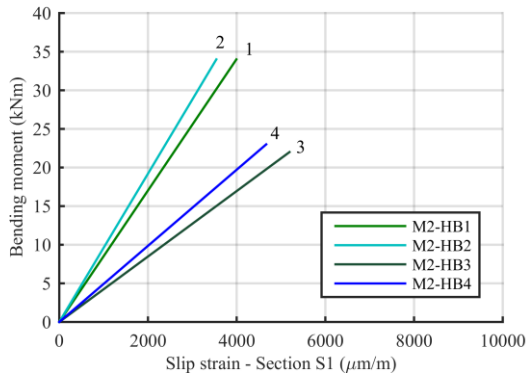


Figure C.9: Analytical estimation of the slip strain variation in hybrid beams M2, in function of the applied bending moment.

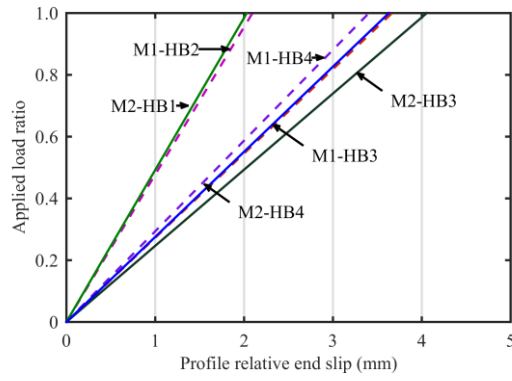


Figure C.10: Analytical estimation of the interlayer slip variation in hybrid beams M2, in function of the applied bending load ratio.

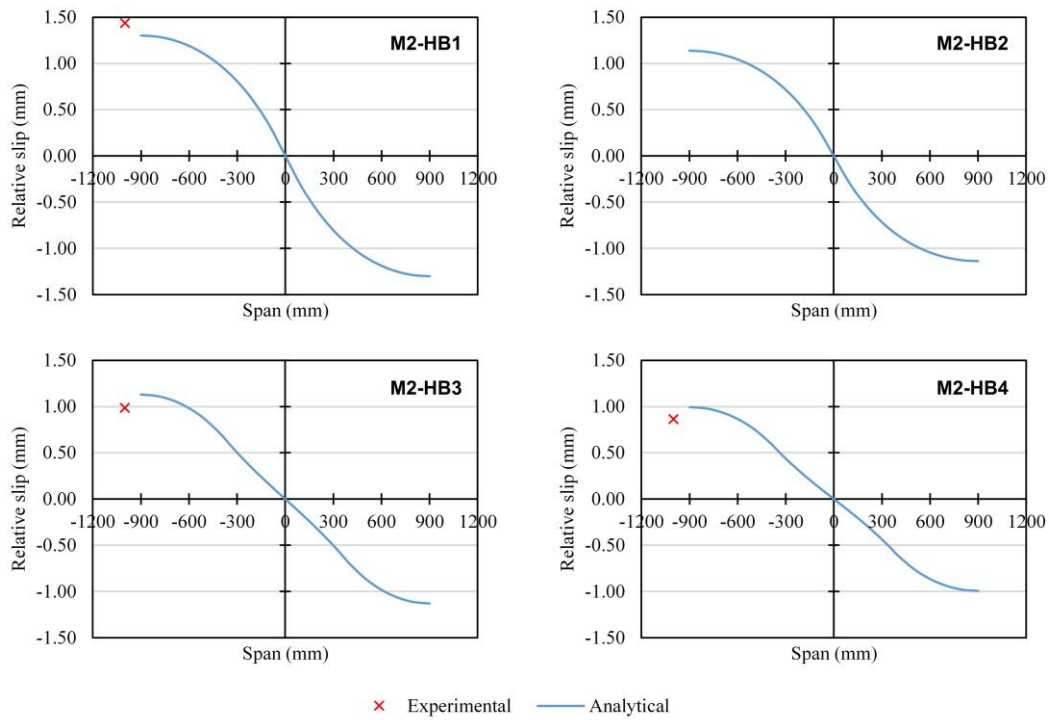


Figure C.11: Analytical longitudinal slip distributions in hybrid beams M2, at an intermediate load level of 50 kN, versus registered experimental data points.

Note: experimental slip data were not available for M2-HB2.

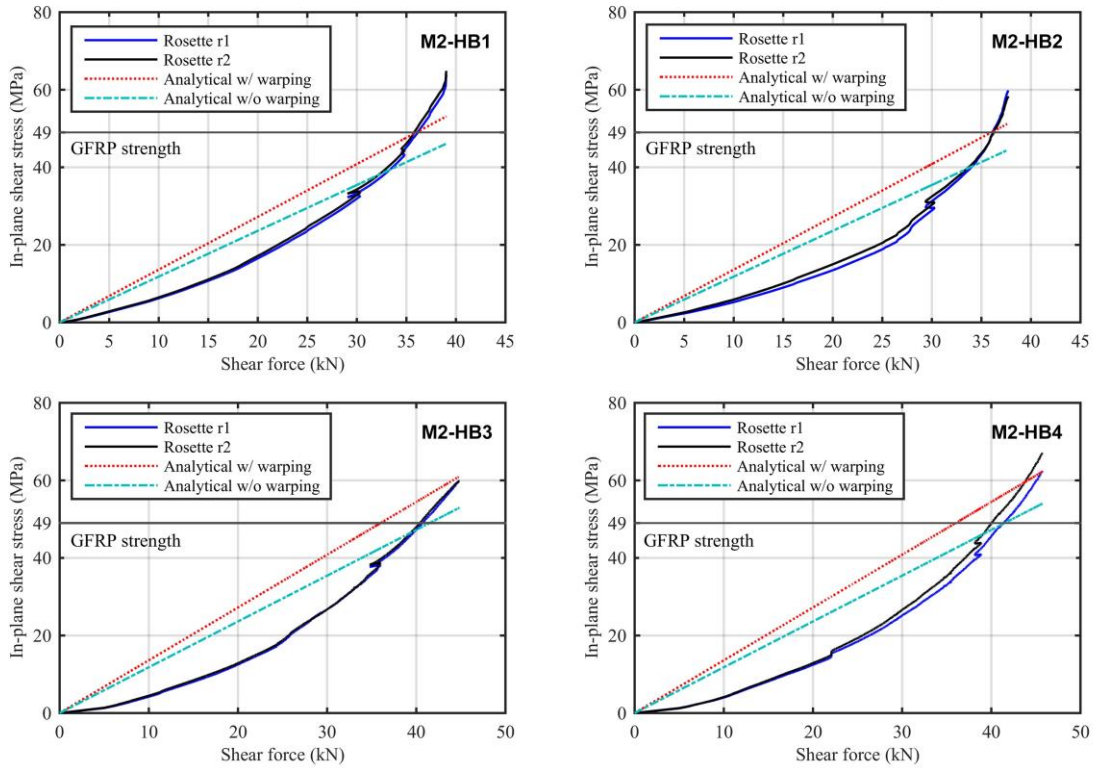


Figure C.12: In-plane shear stress variation in hybrid beams M2 section S2 in function of the applied shear load: experimental and analytical curves with or without warping.

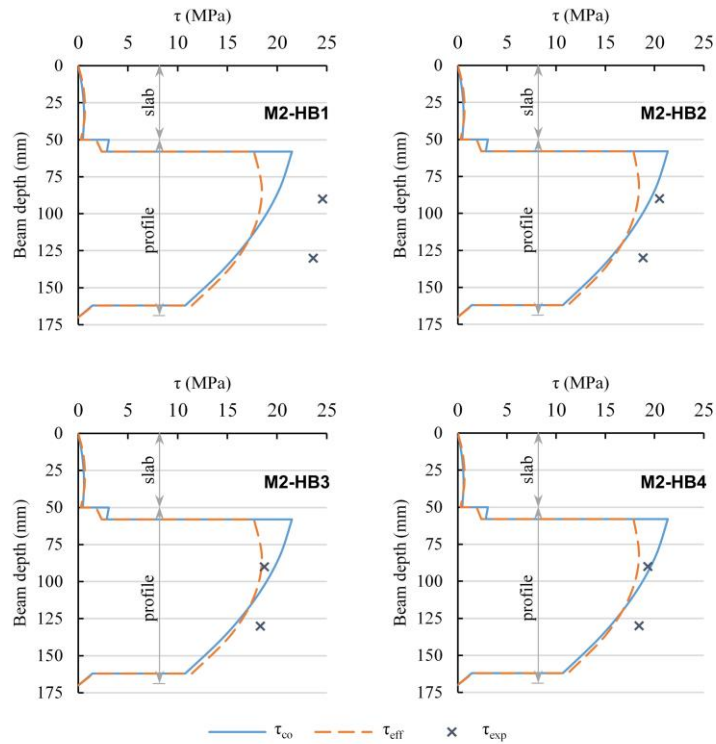


Figure C.13: In-plane shear stress distributions in hybrid beams M2, in section S2, at an intermediate load of 50 kN. Analytical curves under complete (τ_{co}) and partial (τ_{eff}) shear interaction assumptions versus experimental data points (τ_{exp}).

